



V6 Ground-Motion Model (GMM) for Induced Seismicity in the Groningen Field With Assurance Letter

Julian J Bommer¹, Benjamin Edwards¹, Pauline P Kruiver², Adrian Rodriguez-Marek¹, Peter J Stafford¹, Bernard Dost³, Michail Ntinalexis¹, Elmer Ruigrok³ and Jesper Spetzler³

- 1. Independent consultant,**
- 2. Deltares,**
- 3. Royal Netherlands Meteorological Institute (KNMI)**

Datum December 2019

Editors Jan van Elk & Dirk Doornhof

General Introduction

The hazard in Groningen, due to earthquakes induced by the production of gas, is primarily presented by the ground motions to which buildings and people are subjected. The prediction of these ground motions is therefore critical for hazard and risk assessment.

This research was started in 2012 and is continuing with ever more ground motion data from Groningen earthquakes being collected. The Ground Motion Prediction Model (GMM) was therefore updated and progress documented regularly. In the Technical Addendum to Winningsplan 2013, a Ground Motion Prediction methodology based on a catalogue of tectonic earthquakes in southern Europe, was presented (Ref. 1). This methodology was inherently conservative, in the sense that it predicted ground motions, which in future would more likely to be adjusted downwards than upwards.

In the report “Development of GMPEs for Response Spectral Accelerations and for Strong-Motion Durations (Version 1)” the status in May 2015 was documented (Ref. 2). An update of this document was issued in November 2015 which presented version 2 of the GMPE methodology (Ref. 3). This version of the Ground Motion Prediction Model was tailored to the Groningen situation (Ref. 4 to 7). In general, this update led to downward adjustment of assessed ground motions for larger earthquakes, resulting in a reduction of the assessed hazard. After incorporating some adjustments, this version of the GMM was used for the hazard and risk assessment supporting Winningsplan 2016, issued in April 2016 (Ref. 8).

Originally, an update of the GMM (version 3) was planned for July 2016, in support of the hazard and risk assessment for Winningsplan 2016. However, when early 2016 the deadline of submission for the Winningsplan was brought forward from July 2016 to April 2016, version 3 of the GMM could not be ready in time to be implemented in the hazard and risk assessment for this winningsplan.

Version 4 of the Ground Motion Model (GMM) was completed mid-2017 and shared with experts for an assurance review (Ref. 9). Based on the comments of the assurance panel, version 5 of the Ground Motion Model was developed and documented in a report issued in November 2017 (Ref. 10). This version was used in Hazard, Building Damage and Risk Assessment of November 2017 (Ref. 12), the Hazard and Risk Assessment for production forecast Basispad Kabinet of August 2018 (Ref. 13) and the Hazard and Risk Assessment for the production forecast prepared by GTS (GTS-raming) of March 2019 (Ref. 14). The report on GMM V5 was later re-issued (Ref. 11) with the addition of the Assurance Letter and short resumes of the Assurance Panel members (Appendix I), and the full set of written comments on the first versions of the V4 and V5 GMM reports (Ref. 9 and 10), together with the detailed responses from the GMM development team (Appendices IX and X).

A number of improvements were incorporated in the development of the current Ground Motion Model (V6). The most important change is the switch from using the G4 geophones recordings acquired at 200 m depth to the G0-station accelerograms acquired at surface. This change was made possible by expansion of the database of ground motion recordings.

References:

- 1 Technical Addendum to the Winningsplan Groningen 2013; Subsidence, Induced Earthquakes and Seismic Hazard Analysis in the Groningen Field, Nederlandse Aardolie Maatschappij BV (Jan van Elk and Dirk Doornhof, eds), November 2013.
- 2 Development of Version 1 GMPEs for Response Spectral Accelerations and for Strong-Motion Durations, Julian J Bommer, Peter J Stafford, Benjamin Edwards, Michail Ntinalexis, Bernard Dost and Dirk Kraaijpoel, March 2015.
- 3 Development of Version 2 GMPEs for Response Spectral Accelerations and Significant Durations for Induced Earthquakes in the Groningen field, Julian J Bommer, Bernard Dost, Benjamin Edwards, Adrian Rodriguez-Marek, Pauline P Kruiver, Piet Meijers, Michail Ntinalexis & Peter J Stafford, October 2015
- 4 Geological schematisation of the shallow subsurface of Groningen (For site response to earthquakes for the Groningen gas field) – Part I, Deltares, Pauline Kruiver and Ger de Lange.
- 5 Geological schematisation of the shallow subsurface of Groningen (For site response to earthquakes for the Groningen gas field) – Part II, Deltares, Pauline Kruiver and Ger de Lange.
- 6 Geological schematisation of the shallow subsurface of Groningen (For site response to earthquakes for the Groningen gas field) – Part III, Deltares, Pauline Kruiver and Ger de Lange.
- 7 Modifications of the Geological model for Site response at the Groningen field, Deltares, Pauline Kruiver, Ger de Lange, Ane Wiersma, Piet Meijers, Mandy Korff, Jan Peeters, Jan Stafleu, Ronald Harting, Roula Dambrink, Freek Busschers, Jan Gunnink
- 8 Winningsplan Groningen 2016, NAM, April 2016.
- 9 V4 Ground-motion Model (GMM) for Response Spectral Accelerations, Peak Ground Velocity and Significant Duration in the Groningen field, Julian Bommer, Bernard Dost, Benjamin Edwards, Pauline Kruiver, Pier Meijers, Michail Ntinalexis, Adrian Rodriguez-Marek, Elmer Ruigrok, Jesper Spetzler and Peter Stafford, Independent Consultants, Deltares and KNMI, June 2017 with Parameter files - V4 Ground-Motion Model (GMM) for Response Spectral Accelerations, Peak Ground Velocity, and Significant Durations in the Groningen Field, Supplement to V4 GMM, Julian Bommer and Peter Stafford, Independent Consultants, June 2017
- 10 V5 Ground-Motion Model (GMM) for the Groningen Field, Julian J Bommer, Benjamin Edwards, Pauline P Kruiver, Adrian Rodriguez-Marek, Peter J Stafford, Bernard Dost, Michail Ntinalexis, Elmer Ruigrok and Jesper Spetzler, October 2017
- 11 V5 Ground-Motion Model (GMM) for the Groningen Field re-issued with assurance letter, Julian J Bommer, Benjamin Edwards, Pauline P Kruiver, Adrian Rodriguez-Marek, Peter J Stafford, Bernard Dost, Michail Ntinalexis, Elmer Ruigrok and Jesper Spetzler, March 2018
- 12 Hazard, Building Damage and Risk Assessment, NAM (Jan van Elk and Dirk Doornhof), November 2017.
- 13 Hazard and Risk Assessment for production forecast Basispad Kabinet, NAM, Jan van Elk and Dirk Doornhof, July 2018.
- 14 Hazard and Risk Assessment for production forecast GTS-raming 2019, NAM, Jan van Elk and Dirk Doornhof, March 2019.

These reports are also available at the study reports page of the website www.nam.nl.



NAM

Title	V6 Ground-Motion Model (GMM) for Induced Seismicity in the Groningen Field With Assurance Letter	Date	December 2019
		Initiator	NAM
Autor(s)	Julian J Bommer ¹ , Benjamin Edwards ¹ , Pauline P Kruiver ² , Adrian Rodriguez-Marek ¹ , Peter J Stafford ¹ , Bernard Dost ³ , Michail Ntinalexis ¹ , Elmer Ruigrok ³ and Jesper Spetzler ³	Editors	Jan van Elk & Dirk Doornhof
Organisation	1. Independent consultant, 2. Deltares, 3. Royal Netherlands Meteorological Institute (KNMI)	Organisation	NAM
Place in the Study and Data Acquisition Plan	<p><u>Study Theme:</u> Ground Motion Prediction</p> <p><u>Comment:</u> The hazard in Groningen, due to earthquakes induced by the production of gas, is primarily presented by the ground motions to which buildings and people are subjected. The prediction of these ground motions is therefore critical for hazard and risk assessment.</p> <p>This research was started in 2012 and is continuing with ever more ground motion data from Groningen earthquakes being collected. The Ground Motion Prediction Model (GMM) was therefore updated and progress documented regularly. In the Technical Addendum to Winningsplan 2013, a Ground Motion Prediction methodology based on a catalogue of tectonic earthquakes in southern Europe, was presented. This methodology was inherently conservative, in the sense that it predicted ground motions, which in future would more likely to be adjusted downwards than upwards.</p> <p>In the report “Development of GMPEs for Response Spectral Accelerations and for Strong-Motion Durations (Version 1)” the status in May 2015 was documented. An update of this document was issued in November 2015 which presented version 2 of the GMPE methodology. This version of the Ground Motion Prediction Model was tailored to the Groningen situation. In general, this update led to downward adjustment of assessed ground motions for larger earthquakes, resulting in a reduction of the assessed hazard. After incorporating some adjustments, this version of the GMM was used for the hazard and risk assessment supporting Winningsplan 2016, issued in April 2016.</p> <p>Originally, an update of the GMM (version 3) was planned for July 2016, in support of the hazard and risk assessment for Winningsplan 2016. However, when early 2016 the deadline of submission for the Winningsplan was brought forward from July 2016 to April</p>		

	<p>2016, version 3 of the GMM could not be ready in time to be implemented in the hazard and risk assessment for this winningsplan.</p> <p>Version 4 of the Ground Motion Model (GMM) was completed mid-2017 and shared with experts for an assurance review. Based on the comments of the assurance panel, version 5 of the Ground Motion Model was developed and documented in a report issued in November 2017. This version was used in Hazard, Building Damage and Risk Assessment of November 2017, the Hazard and Risk Assessment for production forecast Basispad Kabinet of August 2018 and the Hazard and Risk Assessment for the production forecast prepared by GTS of March 2019. The report on GMM V5 was later re-issued with the addition of the Assurance Letter and short resumes of the Assurance Panel members (Appendix I), and the full set of written comments on the first versions of the V4 and V5 GMM reports, together with the detailed responses from the GMM development team (Appendices IX and X).</p> <p>A number of improvements were incorporated in the development of the current Ground Motion Model (V6). The most important change is the switch from using the G4 geophones recordings acquired at 200 m depth to the G0-station accelerograms acquired at surface. This change was made possible by expansion of the database of ground motion recordings.</p>
Directly linked research	<p>(1) Hazard Assessment.</p> <p>(2) Fragility assessment of buildings in the Groningen region.</p>
Used data	<p>Accelerograms from the accelerometers placed in the Groningen field.</p> <p>P- and S-wave velocity model sub-surface Groningen.</p> <p>Description of the shallow geology of Groningen.</p>
Associated organisation	KNMI
Assurance	External assurance team has reviewed the report for GMM version 4, 5 and 6. Comments from the assurance team on GMM version 4, 5 and 6 are included in these reports as appendices.

V6 Ground-Motion Model for Induced Seismicity in the Groningen Gas Field

A report prepared for NAM

**Julian J Bommer¹, Benjamin Edwards¹, Pauline P Kruiver², Adrian Rodriguez-Marek¹,
Peter J Stafford¹, Bernard Dost³, Michail Ntinalexis¹, Elmer Ruigrok³, Jesper Spetzler³,**

1. Independent consultant, 2. Deltares, 3. Royal Netherlands Meteorological Institute (KNMI)

Revision 1

19 December 2019

TABLE of CONTENTS

Acknowledgements	ii
1. INTRODUCTION	1
1.1. Evolution of the Groningen GMMs and motivation for a V6 model	1
1.2. Error in the V5 GMM database: Slochteren event recordings	2
1.3. The G-network surface accelerograph calibration issue	7
1.4. Overview of the V6 GMM report	11
2. V6 GMM DATA and FRAMEWORK	12
2.1. Modelling approach for the V6 GMM	12
2.2. Ground-motion database	16
2.3. Updated site response models	21
2.4. Linear TFs and AFs from NS_B to surface	29
3. GROUND-MOTION AMPLITUDES at NS_B	32
3.1. Inversion of NS_B motions for source, site & path parameters	32
3.2. Logic-tree for ground-motion simulations	37
3.3. Regression on NS_B simulated motions	43
3.4. Aleatory variability model	45
4. SITE RESPONSE ZONATION	52
4.1. Input rock motions and site response analyses	52
4.2. Zonation and amplification factors	54
5. MODEL SUMMARY and IMPLEMENTATION	63
5.1. Complete GMM logic-tree	63
5.2. Sampling of variance components	70
6. CONCLUDING REMARKS	75
6.1. Comparison between V5 and V6 GMM	75
6.2. Possible future refinements of the GMM	83
7. REFERENCES	88
APPENDIX I AFs from measured and modelled V_s profiles	91
APPENDIX II Median predictions of motion at NS_B	104
APPENDIX III Station vs zone linear AFs	118
APPENDIX IV Residuals of surface recordings	149
APPENDIX V Median predictions of motion at surface	159
APPENDIX VI Geophone amplitudes	183
APPENDIX VII Review Panel report from V6-to-V7 workshop	189

Acknowledgements

The report on the V4 ground-motion model (GMM) included almost three full pages of acknowledgements to the numerous individuals who have contributed in many important ways to the development of this work. Those expressions of gratitude and appreciation were reiterated in the V5 report and remain equally valid with regards to the V6 model.

In view of their critical role in providing detailed feedback on the model development from V2 through to V5, we reiterate our debt of gratitude to the international GMM review panel, chaired by Jonathan Stewart and comprising Norm Abrahamson, Gail Atkinson, Hilmar Bungum, Fabrice Cotton, John Douglas, Ivan Wong and Bob Youngs. We cannot overstate the enormous value that has been added to the GMM development through the technical challenges and insightful observations that have been put forward by this illustrious panel of experts in the fields of ground-motion prediction and site response modelling. While the GMM review panel was not engaged during the development of the V6 GMM, a Workshop was held in September 2019 to discuss the development of the V7 GMM and through this engagement extensive feedback was provided on the first version of the V6 GMM report issued on 30 March 2019. The report has been modified to take account of many of these comments although the majority of the more substantial comments have been taken on board in the scope of work for the V7 GMM development.

We also acknowledge the interactions with researchers from KEM-02 and KEM-04 projects funded by the Dutch Ministry of Economic Affairs. The KEM researchers were invited to participate in the September 2019 Workshop and subsequently invited the GMM development team to participate in a meeting at which their findings were presented in December 2019. Valuable insights were obtained from some of these discussions, particularly with regard to apparent differences between the recordings from B-station and G-stations and the possible limitations of 1D site response analyses, both of which will be explored during the V7 GMM development. We thank in particular Gabriele Ameri, Floris Besseling and Jacob Chacko for their willingness to engage in an open and constructive exchange and for the insights we obtained from our interactions. We also extend our gratitude to Karin van Thienen-Visser and Bastiaan Jaarsma for facilitating these interactions.

We also add a note of thanks to the reviewers of the various journal papers that have been published from the work on the Groningen GMM. Their comments and challenges have also been very valuable in assisting with the continued improvement of the GMM.

Renewed thanks are also due to Stephen Bourne, Steve Oates, Pourya Omid and Tomas Storck for the invaluable feedback and testing of the model through implementation in the Groningen hazard and risk engine, and to Assaf Mar-Or for generating hazard and risk results that have provide very helpful insights into the performance of the GMM and changes from previous versions. We also thank Helen Crowley and Rui Pinho for keeping us informed of the ground-motion input needs for the derivation of building fragility functions for Groningen.

Finally, we must express our debt to Jan van Elk for continuing to provide the space and conditions to undertake this work and supporting for us in so many ways. The continued assistance of Dirk Doornhof and Jeroen Uilenreef in supporting Jan is also gratefully acknowledged.

1. Introduction

Induced seismicity associated with gas production from the Groningen gas field in the Netherlands has caused serious societal and regulatory concern, especially following the magnitude (M_L) 3.6 Huizinge earthquake in August 2012, the largest event to date. In response to this situation, NAM has engaged in a major endeavour of data acquisition and model development to quantify the risk due to these induced earthquakes and to inform decision-making regarding alternative risk mitigation strategies (van Elk *et al.*, 2019). A critical component of the model for the hazard and risk estimation is a ground-motion model (GMM) for the prediction of parameters characterising the shaking at the surface due to each earthquake scenario considered.

1.1. Evolution of the Groningen GMM and motivation for a V6 model

The Groningen GMM has been developed in successive stages, with the work beginning in the first half of 2013 when a very preliminary model was produced for the 2013 Winningsplan. Subsequently, over a period of six years, a much more sophisticated model has been developed in five successive and iterative stages, culminating in the V6 model presented in this report. The derivation of the previous five versions of the model were all documented in great detail in reports that collectively have a total length of 2,144 pages, supported by numerous other documents of even greater length presenting the underlying data collection activities to characterise the near-surface soil profiles across the Groningen field and the database of ground-motion recordings that have underpinned the model development. Additionally, several papers on different aspects of the model development process have been published in peer-reviewed journals (Bommer *et al.*, 2016; Bommer *et al.*, 2017a; Bommer *et al.*, 2017c; Kruiver *et al.*, 2017a,b; Rodriguez-Marek *et al.*, 2017; Stafford *et al.*, 2017; Noorlandt *et al.*, 2018; Edwards *et al.*, 2019; Stafford *et al.*, 2019). In view of the extensive documentation already available, this report presents a more succinct overview of the V6 model, a trend that was already adopted for the V5 GMM report: the main body of that report was succinct although the overall length ran to almost 300 pages because of several appendices, including 116 pages devoted to the multi-stage review of the model by an international panel of experts (Bommer *et al.*, 2018). The intention with the V6 model is to present the essential features of the model and the differences with regard to earlier versions of the Groningen GMM, referencing earlier reports and published papers to guide the reader who seeks more detailed information.

The review panel consisted of several eminent figures in the fields of ground-motion modelling and site response: Dr Norm Abrahamson (USA), Professor Gail Atkinson (Canada), Dr Hilmar Bungum (Norway), Professor Fabrice Cotton (Germany), Dr John Douglas (UK), Professor Jonathan Stewart (USA), Mr Ivan Wong (USA), and

Dr Bob Youngs (USA). The closure letter from the review panel, issued on 15 January 2018, concluded with the following statement regarding the V5 GMM: “*Our overall assessment of the modelling effort to date is that it has produced a state-of-the-art model that is well-suited for its purpose of regional ground motion prediction to support hazard and risk studies in the Groningen field.*” In view of this positive assessment of the V5 GMM model, it is reasonable to ask why there is a need for a V6 model. The answer to this question has several facets, which include the following considerations:

1. There is an intention and desire to continually refine and improve the model, and the V6 hazard and risk calculations present an opportunity to re-visit the GMM and enhance some of its features through the current revision. This new development phase also provided an opportunity to explore some of the suggestions put forward by the international review panel, particularly with regards to the model for aleatory variability (including alternative branches for the inter-event variability and distance dependence in the within-event standard deviation).
2. Work conducted by Deltares has refined the model for the dynamic characteristics of the soil profiles across the Groningen field, also incorporating new measurements from deep logs obtained by NAM. In parallel, analyses were performed by KNMI using the borehole geophone array (G-network) to revise the damping estimates for Groningen soils. Consequently, the changes in the site response model (Section 2.3) warrant new site response analyses to derive update amplification factors for the field.
3. Two earthquakes with $M_L \geq 2.5$ have occurred since the V5 database was compiled, which together have yielded ~150 recordings, the addition of which had led to a 40% increase with respect to the V5 database. This significant expansion of the database, including recordings from an event of M_L 3.4 among which is the highest recorded PGA (0.11g) obtained in the field to date, also justify an update of the ground-motion model.
4. During the preparation of the ground-motion database for the derivation of the V6 GMM it was discovered that there had been an error in the processing of the recordings from the Slochteren earthquake. Although the decision had already been taken to develop the V6 model, the discovery of this error in the data from this event—discussed in detail in Section 1.2 below—made it necessary to provide an updated version of the GMM.

1.2. Error in the V5 GMM database: Slochteren event recordings

Before explaining the nature of the error in the V5 GMM database, it is worthwhile describing the context in a cycle of GMM development for the Groningen seismic hazard and risk assessment. The deadline for each cycle is fixed by the due date for delivery of the hazard and risk results by NAM, which in turn determines the time—

usually 2 to 3 months ahead of that deadline—for delivery of the GMM for implementation in the hazard and risk engine. The V5 GMM was delivered at the beginning of September 2017 in order to allow sufficient time for the execution of the hazard and risk calculations. The first version of the report on the V5 model was issued almost two months later (and a revised version another four months after that following the final review by the international panel of experts) but the documentation is performed in parallel with the model implementation.

The full process of developing the GMM, from estimation of linear transfer and amplification functions to transform the recorded motions to the reference rock horizon through to estimation of non-linear amplification factors and zonation of the field, requires several months of work. The Slochteren earthquake, with magnitude M_L 2.6, occurred on 27 May 2017, just over three months before the due date to hand over the V5 GMM to the hazard and risk analysts. At this time the work on the V5 model had already begun but it was decided to pause the process briefly while the recordings from the event were added to the database. This decision was taken in view of the fact that this was the first earthquake in the magnitude range of relevance to the model development ($M_L \geq 2.5$) since the M_L 3.1 Hellum event in September 2015. As can be appreciated from Figure 1.1, the Slochteren earthquake added considerably to the database that had been used to derive the V3 and V4 models.

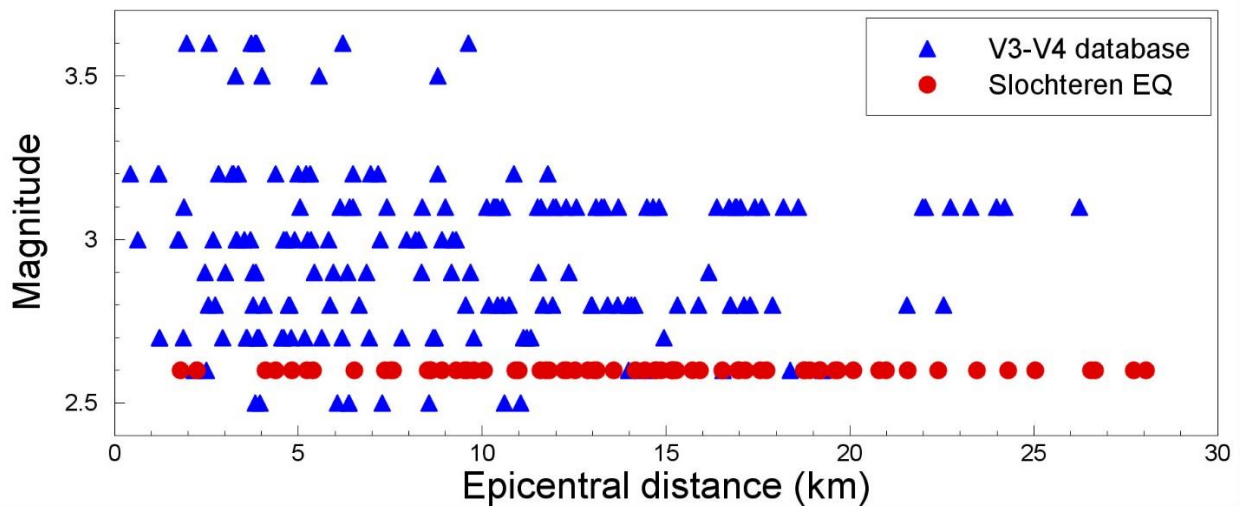


Figure 1.1. Distribution of the V5 Groningen ground-motion database in terms of local magnitude, M_L , and epicentral distance, R_{epi} .

A regrettable consequence of the speed with which the Slochteren recordings were processed and added to the database is that errors were made in the application of the instrument deconvolution that converts the raw data from the G-network geophones to velocity (prior to differentiation against time to obtain acceleration

traces). The processing of the G4-station (borehole geophones at 200 m) was performed independently by two different members of the GMM development team, one to obtain Fourier amplitude spectra (FAS) and the other to generate acceleration response spectra (Sa); the error affected the generation of the Sa ordinates but not the FAS. The ratios of Sa ordinates used to those from the correctly processed records are plotted in Figure 1.2, from which it can be seen that at oscillator periods beyond about 0.15 seconds, the accelerations were severely underestimated.

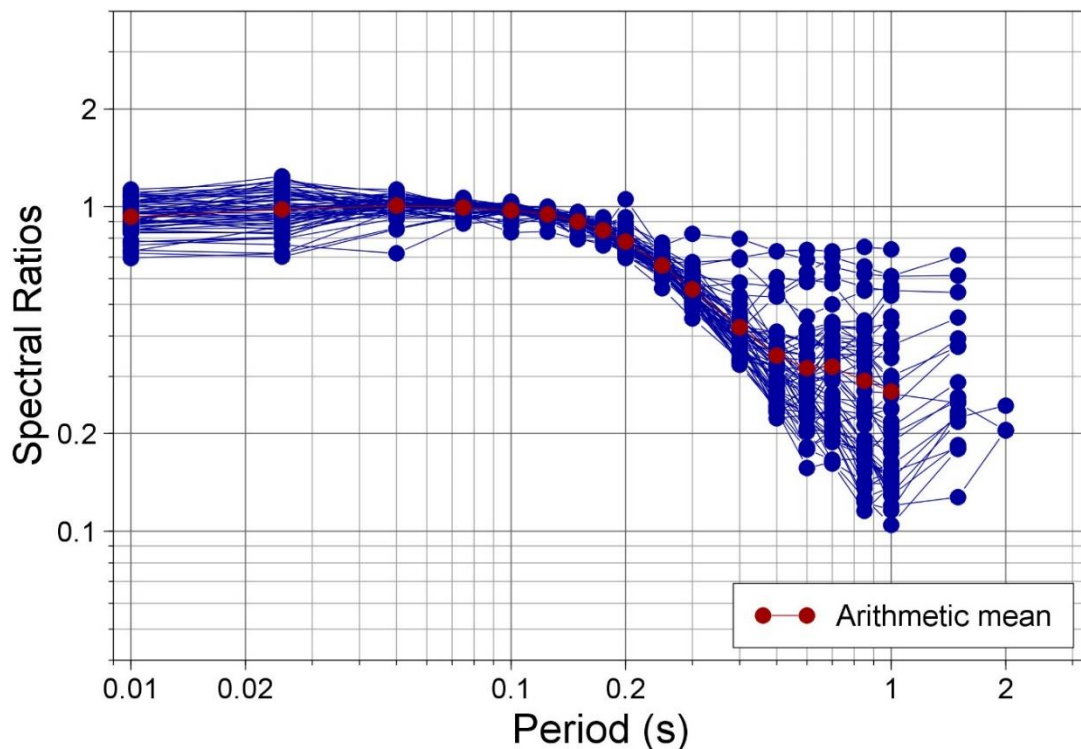


Figure 1.2. Ratios of erroneous to corrected response spectra of the records of the Level 4 G-station geophone recordings obtained during the Slochteren earthquake

Since the FAS were unaffected, the inversions to estimate the source, path and site parameters for the motions at the NS_B horizon were unaffected. The error impacted the model derivation in only two ways, both related to use of the Sa values transferred to the NS_B reference rock. The first of these was calibration of the optimal values of the stress parameter ($\Delta\sigma$) and site kappa (κ_0) by comparison of simulations with the actual motions. The consequence of the inclusion of the erroneous amplitudes led to a decrease in both $\Delta\sigma$ and site kappa (κ_0), as illustrated in Figure 1.3. The consequence of the underestimated stress parameter combined with the underestimated kappa was to lead to overestimation of the predictions at very short oscillator periods and underestimation at intermediate response periods (0.1 – 1.0 second), as shown in Figure 1.4. The patterns were observed and documented in the V5 GMM report but it was assumed that this was due to the

characteristics of the Slochteren earthquake and the recordings from the G-network stations, rather than the result of a data error.

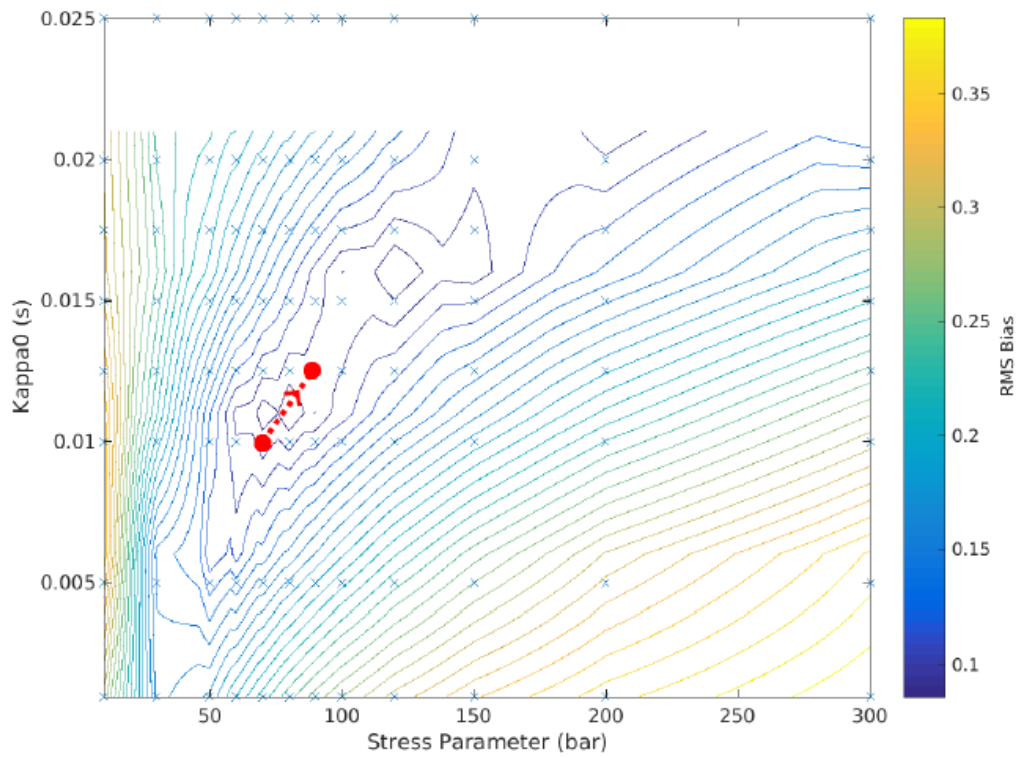


Figure 1.3. Change in optimal model parameters caused by removal of Slochteren data (Figure A2.7 in Bommer *et al.*, 2018)

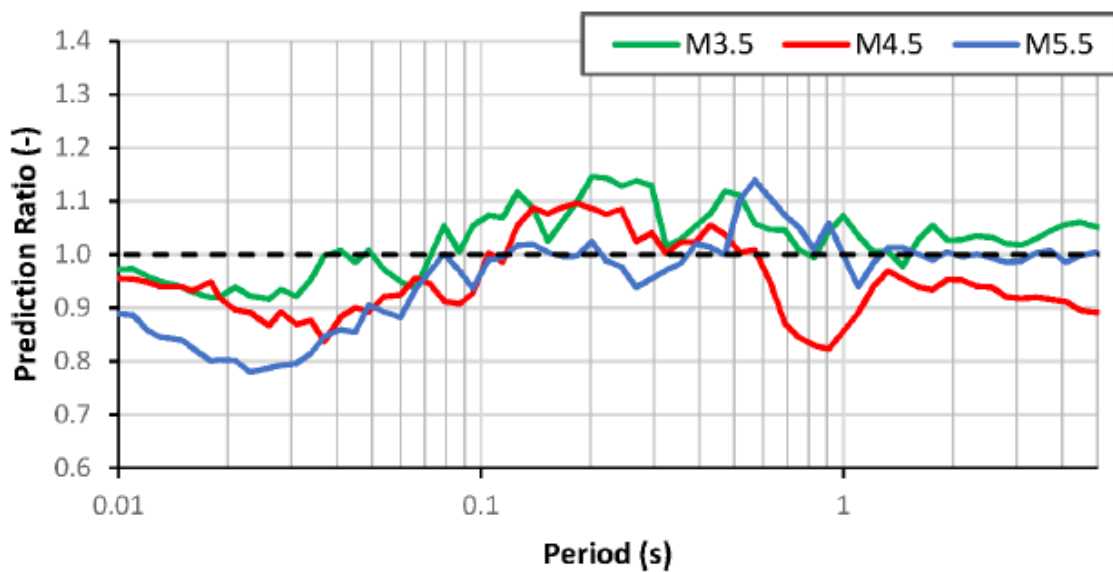


Figure 1.4. Ratios of simulated motions from V5 inversions excluding the recordings of the Slochteren event to those from the original inversions (Figure A2.8 in Bommer *et al.*, 2018)

A point that is worth emphasising is that while the processing error affected a large number of records in the V5 database, the optimisation of the stress parameter and kappa was based on the average residual for each earthquake rather than those of individual recordings (*i.e.*, 1-in-23 earthquakes rather than 1-in-4 records). The same holds for the second consequence of the data error, which was to lead to an overestimation of the between-earthquake variability (Figure 1.5). As these plots clearly show, at very short periods the inter-event variability (τ) was underestimated.

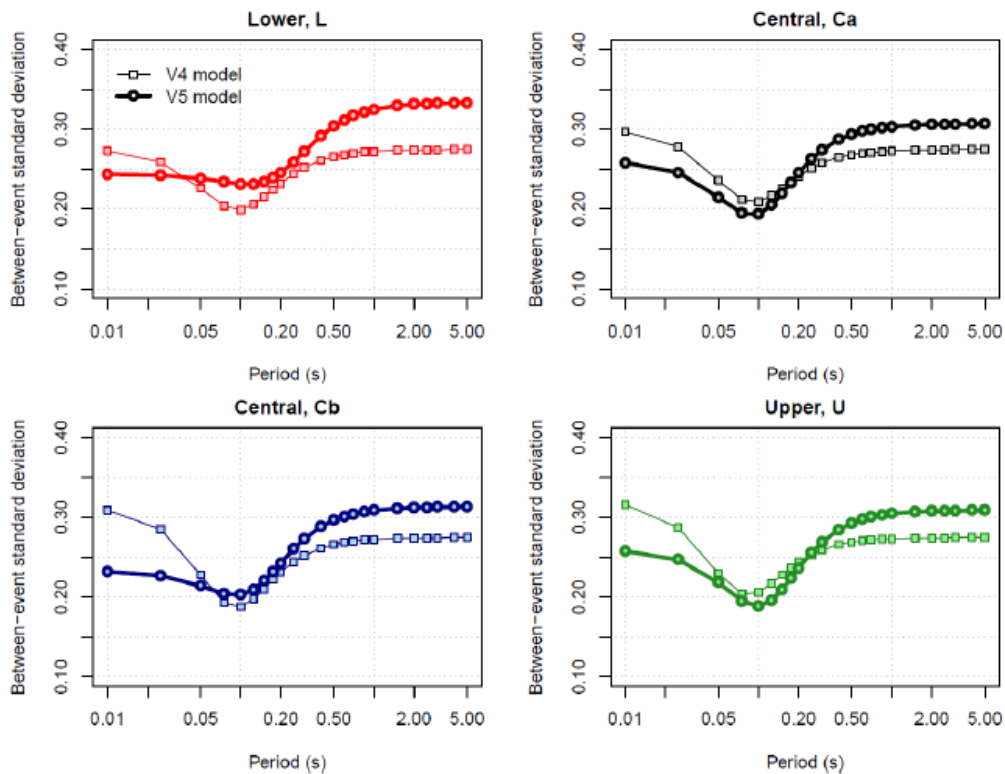


Figure 1.5. Comparison of the between-event standard deviations for the V4 and V5 models (Figure 3.16 in Bommer *et al.*, 2018).

Consequently, the effect on τ was the opposite of the effect on the median predictions. In the hazard and risk modelling, for each earthquake scenario, the ground-motion field is first generated by predicting the median amplitudes plus a randomly selected sample from the inter-event variability. Therefore, there will have been a tendency for the two errors to cancel one another out to some extent, and the overall impact on the hazard and risk results is unlikely to have been very large. Since this error was only discovered during the assembly of the V6 database, a decision has been taken to correct the mistake within the development of the V6 model and not to undertake a detailed assessment of the impact of the error on the hazard and risk results. This would entail repeating the derivation of the V5 GMM and then running new hazard and risk calculations, all of which would served only to delay the delivery of the V6 hazard and risk assessment.

1.3. The G-network surface accelerograph calibration issue

The error discussed in the previous section was related to the processing of ground-motion recordings from the Groningen field. Another error has been identified since the issue of the V5 model, which was an error in the calibration of the surface accelerographs of the G-network (G0 stations). That there might be a problem with one of the two networks of surface accelerographs had been suspected for some time, mainly related to the observation of trends in the event terms for recent earthquakes calculated as part of the development of an empirical GMPE for the prediction of PGV, which is used by NAM only for estimating the impact of events in the range M_L 1.8 to 3.6. An observation had been made that for recent earthquakes, the event terms were consistently negative (Figure 1.6). This would imply a trend towards much lower amplitudes of motion, which could, for example, reflect a tendency towards lower stress parameters. However, a persistent feature of these recent events is that the recordings they have generated predominantly come from the G-network, which was installed between late 2014 and 2015 (Dost *et al.*, 2017). Separating the recordings from the two networks during the most recent period, and calculating the apparent event-terms separately from the two sets of recordings, clearly indicates a systematic difference, with the G0-stations yielding lower amplitudes of motion (Figure 1.6).

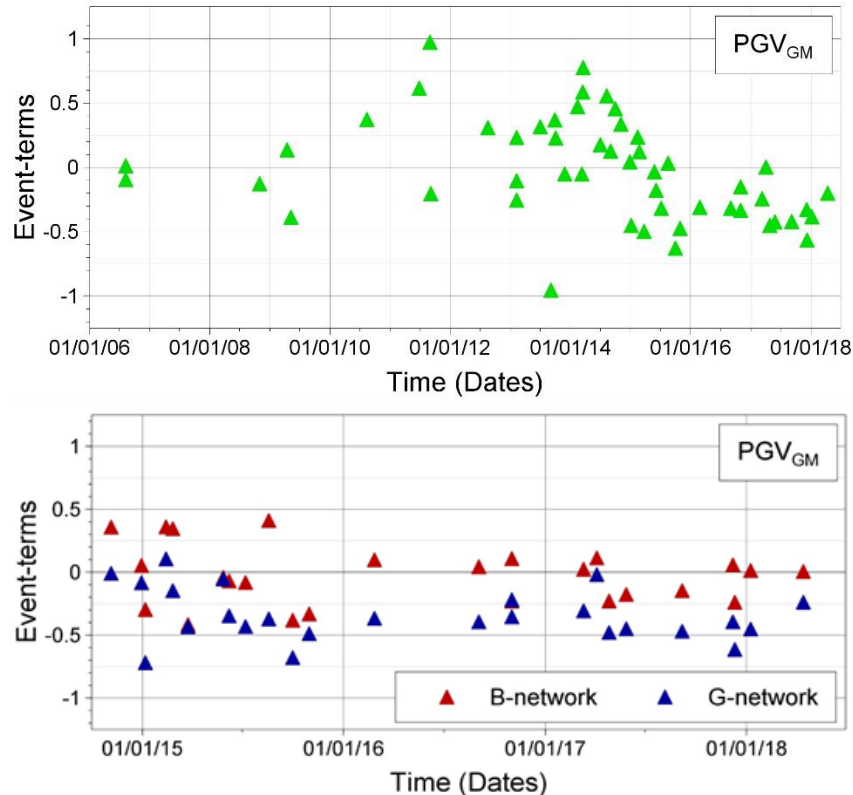


Figure 1.6. Upper: Event-terms from the derivation of an empirical GMPE for PGV, plotted against date of the earthquake; lower: Zoom-in on the more recent events, with event-terms calculated separately for the B-stations and G0-stations.

This prompted further investigations, including comparisons between recordings from G0- and B-stations installed in close proximity to one another (Figure 1.7). These consistently revealed higher amplitudes on the B-stations than the G0-stations. Additional evidence of a systematic difference came through analyses conducted at KNMI in which template matching was used to identify waveforms from an earthquake in Fiji, for which the vertical component peak velocities are about twice as high on the B-station recordings as those from the G0-stations (Figure 1.8).

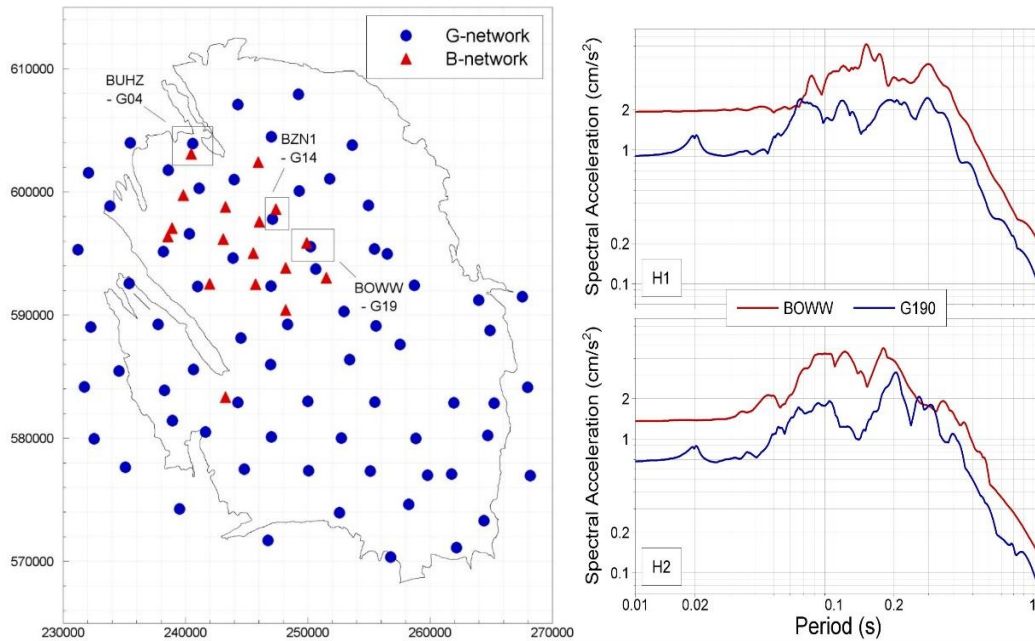


Figure 1.7. *Left*: Accelerograph stations in the Groningen field, highlighting co-located pairs of B- and G-network stations; *right*: comparison of horizontal component spectra from recordings on the BOWW and G190 accelerographs during the 2015 Hellum event.

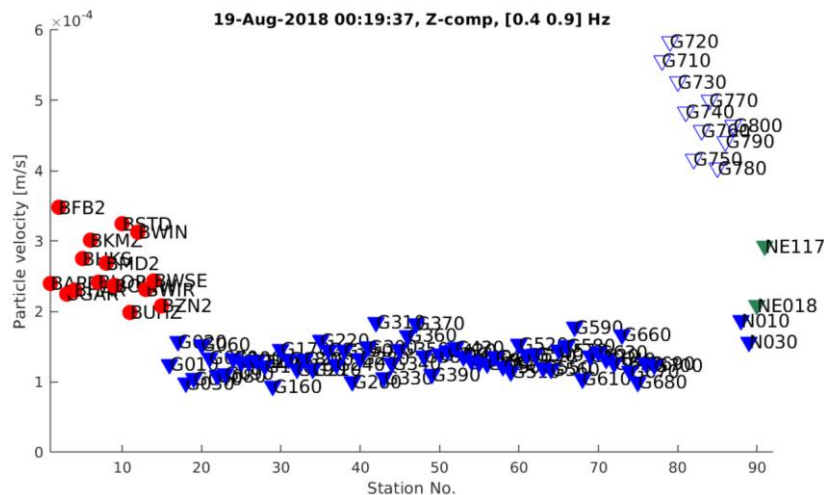


Figure 1.8. Vertical component PGV values from waveforms for an earthquake in Fiji, recorded on B-stations (red circles) and G0-stations (solid blue triangles)

In late 2018, field inspection of the instruments identified that an error had been made in the settings and that consequently the G0 accelerographs of the G01-G70 stations had been recording half of the actual ground-motion amplitudes (whereas the G71-G80 instruments were recording double the true amplitudes). The instrument calibration data was immediately corrected on the KNMI web portal and work began on assessing the impact that this error may have had on the V5 GMM. While this work was underway, comparisons similar to that shown in Figure 1.7 were performed by researchers in one of the SodM-funded KEM projects, who then approached KNMI and were informed of the instrument calibration error and its correction. One of the participants in that project then put out of blog regarding the issue on their web site (<https://www.hanze.nl/eng/blog/knmi-earthquake-motion-recording-mistake>), which included the following assertions: “*There are direct and indirect effects of this mistake. The direct effect is on the Ground Motion Model (GMM) v5, and maybe on the v3 & v4. The indirect effects are spread on the products that used the GMM v5, such as the Hazard and Risk Model (HRA), Seismic Hazard Map and thus the NPR-related studies. Because the GMM and the relevant hazard map are the base and the first step of all kinds of safety assessments and risk calculations, the problem must have affected a large and important number of studies in the recent years.*” These statements are actually without any basis and entirely misleading since the impact of the G0-calibration error on the derivation of the V5 GMM was effectively null, as explain by the following bullet points:

1. **Median predictions at NS_B.** The model for PGA, PGV and spectral accelerations is derived from analyses of the surface recordings of the B-network and recordings on the 200-m borehole geophones of the G-network (G4 stations), as illustrated in Figure 1.9. This approach was adopted because of the lack of measured near-surface velocity profiles at the G-stations. Consequently, the model for median amplitudes at the NS_B horizon is entirely unaffected by the G0-station calibration issue.
2. **Model for durations.** The derivation of the model for durations does make use of the G0 recordings but the duration definition used is based on the accumulation of Arias intensity in the time-series, which is entirely insensitive to the scaling of the record amplitude. Therefore, the duration model is entirely immune to the correction of the G0 instrument gain.
3. **Magnitude conversions.** The GMM derivation makes use of the assumption of equivalence of local magnitude M_L and moment magnitude M_w , which has been confirmed for the magnitude range of relevance to the GMM ($M \geq 2.5$) in a study published in *Seismological Research Letters* in 2018 (Dost *et al.*, 2018). Some of the seismic moment values used in that study were calculated using G0 recordings as well as B-station recordings; the re-calculation of the moment magnitudes after application of the calibration correction leads to a small change in the M_L - M_w relationship at smaller magnitudes, but the change in the magnitude range for which the GMM is derived was found to be negligible. The change in moment magnitude values and the resulting modification of the M_L - M_w relationship at small magnitudes has been communicated in an erratum submitted to *Seismological Research Letters*.

4. **Site amplification model.** The only part of the site response modelling that uses G0-station recordings were calculations of site kappa at the surface and at the 200 m horizon in order to verify the damping used in the uppermost part of site response profiles. This was last done during the V4 GMM development since the same damping model was used in V5. The kappa values are estimated from analyses of the shape of the Fourier amplitude spectrum and therefore insensitive to the scaling of the recording.
5. **Component-to-component variability.** The component-to-component variability, which is used in the risk calculations to transform the geometric mean component to the arbitrary horizontal component of motion, is calculated using surface recordings, including those from G0 stations. However, the variability is calculated from the logarithmic of ratios of the amplitudes from the two horizontal components of each accelerogram, which is clearly insensitive to any scaling error applied to the record.
6. **Correlation models.** Two correlation models are used in the risk calculations, one being the period-to-period correlation of spectral accelerations and the other the correlation of spectral accelerations and duration. Although surface recordings from Groningen were analysed to explore these correlations, in both cases the modelling adopted global models derived for the full response period range and calibrated over larger magnitude ranges. Consequently, the G0-station error did not influence these elements of the model.

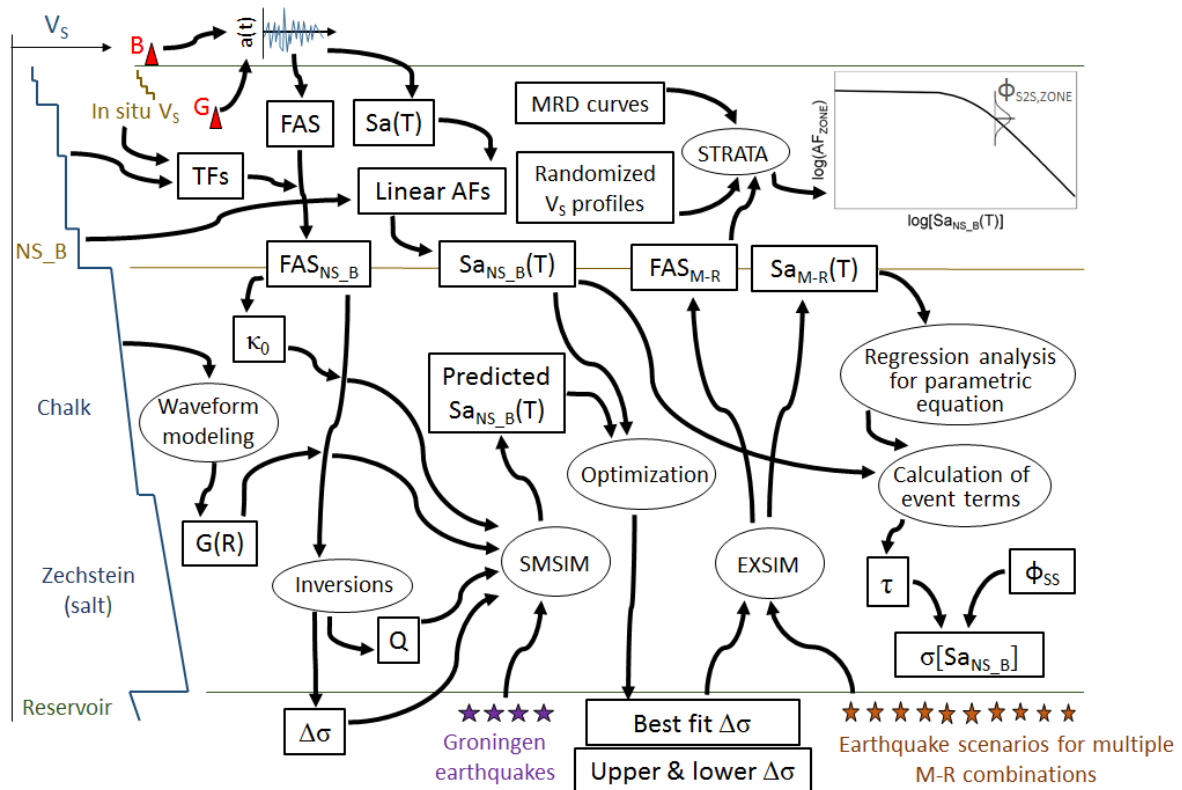


Figure 1.9. Schematic illustration of the derivation of the V4 and V5 ground-motion models, clearly indicating the use of surface accelerograms from the B-network and borehole recordings from the G-network (adapted from Bommer *et al.*, 2017a).

Consequently, were the derivation of the V5 GMM to be repeated using the same data and modelling procedures with the only change being the calibration correction to the G0 accelerographs, there would be no change at all to the model. An email clarifying the key points in the list above was communicated to the author of the blog by the lead author of this report, and was posted on the web site—but with none of the original text being modified. By the time the email was added, the original announcement had already caused widespread controversy and scandal in the Netherlands, which was unfortunate because while the calibration error in the instruments is a fact, the impact that this was claimed to have caused on the hazard and risk modelling was entirely inaccurate (despite the author of the blog having access to the report and papers published and having also participated in a workshop on the GMM development organised by NAM in May 2018).

1.4. Overview of the V6 GMM report

Following this introduction explaining the background to the V6 GMM model, Chapter 2 presents an overview of the framework for this latest version of the Groningen GMM and the ground-motion database available at this stage of the study. The updated site response model and the resulting linear transfer functions and amplification functions are also presented as essential building blocks. Chapter 3 presents the model for horizontal spectral accelerations and peak ground velocity (PGV) at the NS_B reference rock horizon, whereas Chapter 4 presents the site amplification factors that adjust the rock motions to the ground surface and the zonation of the Groningen field into areas for which a common amplification model applies. Chapter 5 summarises the complete guidance for implementing the GMM in terms of the logic-tree structure and the sampling of the variance components; for the user looking for a concise summary of the model without explanation of its derivation, this is fully self-contained in the Chapter 5. The report concludes with a discussion of the V6 model, including comparisons with the V5 GMM, and also potential future developments to be included in the V7 GMM.

In order to keep the main body of the report to an accessible length, series of plots are assigned to appendices, starting with Appendix I that compares amplification factors calculated with measured and modelled near-surface velocity profiles at the B-stations. This is followed by four appendices that contain diagnostic plots to illustrate the performance of the V6 model: Appendix II presents plots of median predictions in terms of response spectral accelerations at the NS_B horizon; Appendix III compares the NS_B to surface amplification factors calculated for the recording stations with the linear factors assigned to the zones in which they are located; Appendix IV presents the residuals of the surface recordings with respect to the model predictions; and Appendix V presents the predicted motions at the ground surface. A final Appendix (VI) summarises an analysis by KNMI to confirm the calibration of the G-network borehole geophones.

2. V6 GMM Data and Framework

This chapter begins with an overview of the modelling approach adopted for the derivation of the V6 GMM. This is followed by descriptions of the V6 ground-motion database and the modifications made to the site response model for the V6 model derivation, concluding with a summary of the linear transfer functions (TFs) and amplification functions (AFs) used to adjust the motions to NS_B.

2.1. Modelling approach for V6 the GMM

The overall procedure for deriving the V6 GMM is unchanged from that deployed in the V4 and V5 GMM development except in one regard, this being the change from using the G4-station geophone recordings to instead making direct use of the G0-station accelerograms. Another change in the framework for the model derivation is the fact that the V6 GMM does not include a model for the prediction of duration since this parameter is not required for the current fragility functions.

The original motivation for using the G4-station geophone records instead of the G0-station accelerograms was related to the calculation of the TFs and AFs to transform the recorded motions to the reference rock horizon, which was chosen as the base of the North Sea supergroup (NS_B) located at ~800 m depth. At the B-stations, the uppermost part of the V_s profiles, which can be expected to exert a very strong influence on the amplification characteristics, particularly at shorter response periods, were determined by a campaign of *in situ* measurements using multiple methods (Noorlandt *et al.*, 2018). Such measurements have not yet been made for the G-network stations, hence it was considered preferable to use the 200-metre borehole recordings since the TFs and AFs used to deconvolve the recordings to NS_B would not be affected by uncertainty in the uppermost part of the soil profiles, which were inferred from the GeoTop model (Kruiver *et al.*, 2017a), at these locations. A beneficial consequence of this decision was that more recordings could be included in the inversions because of the higher signal-to-noise ratios of the borehole recordings compared to those at the surface.

Following the discovery and resolution of the calibration issue with the G0-station accelerographs (Section 1.3), the GMM development team began new discussions regarding this modelling choice and whether it should be re-considered. One reason that motivated a re-evaluation of this modelling choice is that subsequent work has shown that the modelled near-surface V_s profiles based on the GeoTop model are actually a surprisingly good approximation to the measured profiles at the B-stations (Figure 2.1). Estimation of interval velocities over the upper 200 m at the G-stations, from analyses of the borehole recordings, also support the GeoTop-based model in terms of representing the actual V_s profiles (Figure 2.2).

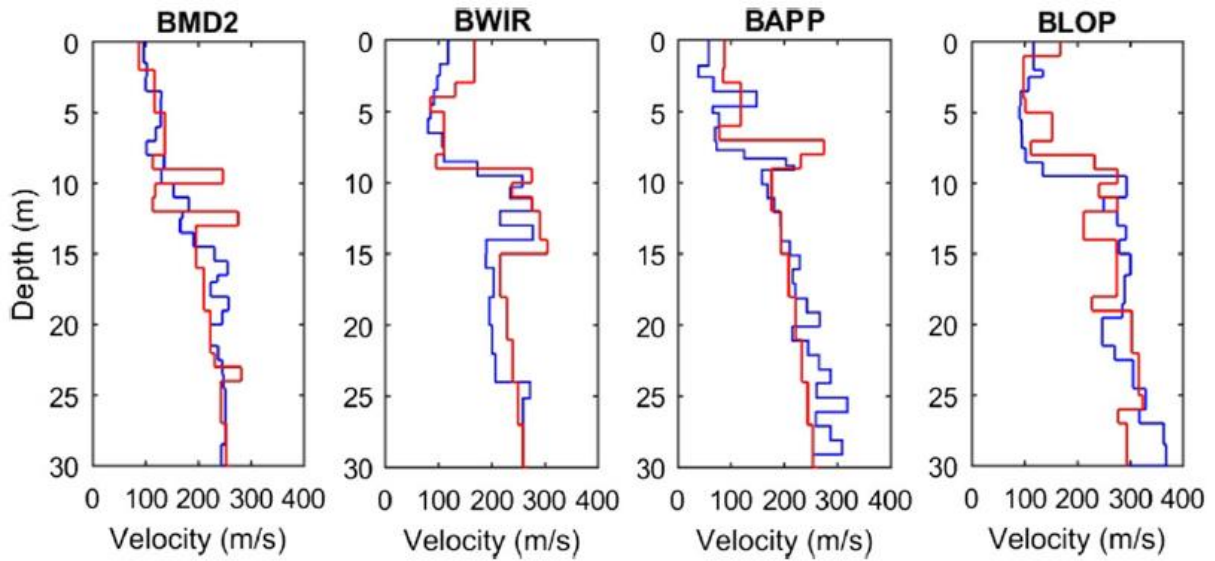


Figure 2.1. Examples of V_S profiles at selected B-stations: measured V_S in blue and modelled mean V_S in red (Noorlandt *et al.*, 2018).

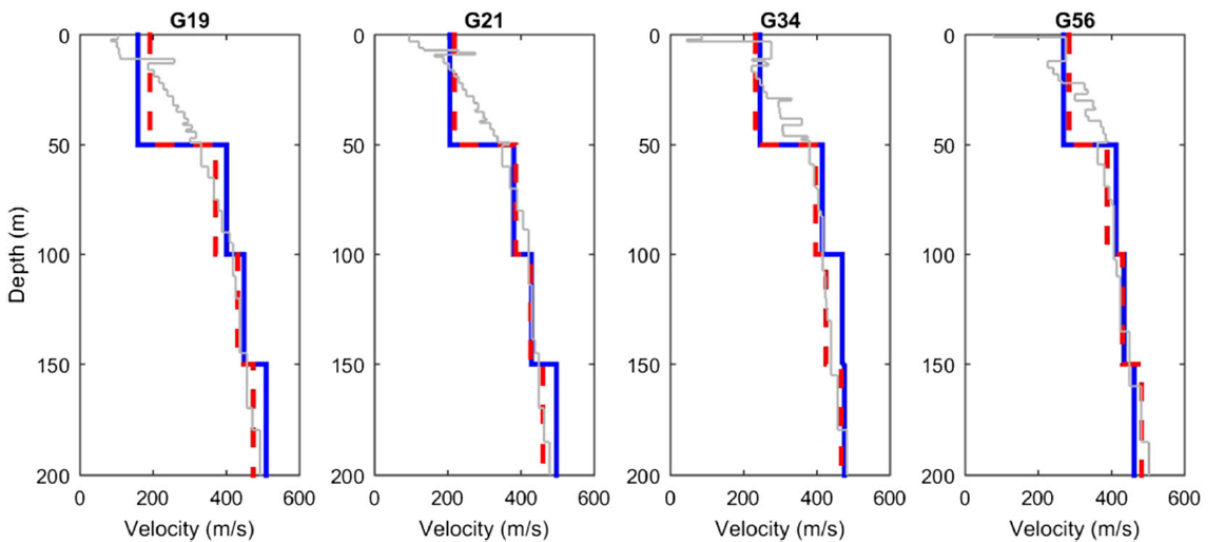


Figure 2.2. Examples of V_S profiles at selected G-stations: interval V_S from seismic interferometry in blue, modelled mean V_S in grey, and harmonic mean of modelled profiles in red (Noorlandt *et al.*, 2018).

Although these visual comparisons are very encouraging in terms of providing confidence in the field-wide velocity model, what ultimately matters is whether the calculated AFs obtained with this model are an accurate and reliable representation of the actual dynamic behaviour of the field. To this end, AFs have been calculated for the B-stations using the measured and modelled V_S profiles, and these are compared graphically in Appendix I. The AFs are calculated using the computer program STRATA (Kottke & Rathje, 2008) and the weakest set of input motions at the NS_B horizon (see Section 4.1). At 11 out of the 18 stations, there is a reasonably good agreement between the two sets of AFs, with excellent agreement

in some case (BMD2, BUHZ). At six of the remaining stations the AFs based on the measured profiles significantly exceed the modelled AFs over a limited period range but at BLOP the opposite is observed at another period and at the remaining BKAN station the modelled AFs are higher. No clear correlations have been identified between these patterns and any features of the profiles such as the V_{S30} values or the presence of certain lithological units. The resulting AF differences are not only a result of differences in V_s profiles, but also in the soil properties defining the shear-modulus and damping reduction (MRD) curves. Figure 2.3 shows the overall results in terms of residuals, calculated as the logarithmic difference between the AFs calculated from the measured profiles to those obtained from the modelled profiles. While there is considerable scatter, the average (over 18 stations and 10 motions applied at each location) trend is reasonably close to zero (implying a ratio of unity) across most of the period range.

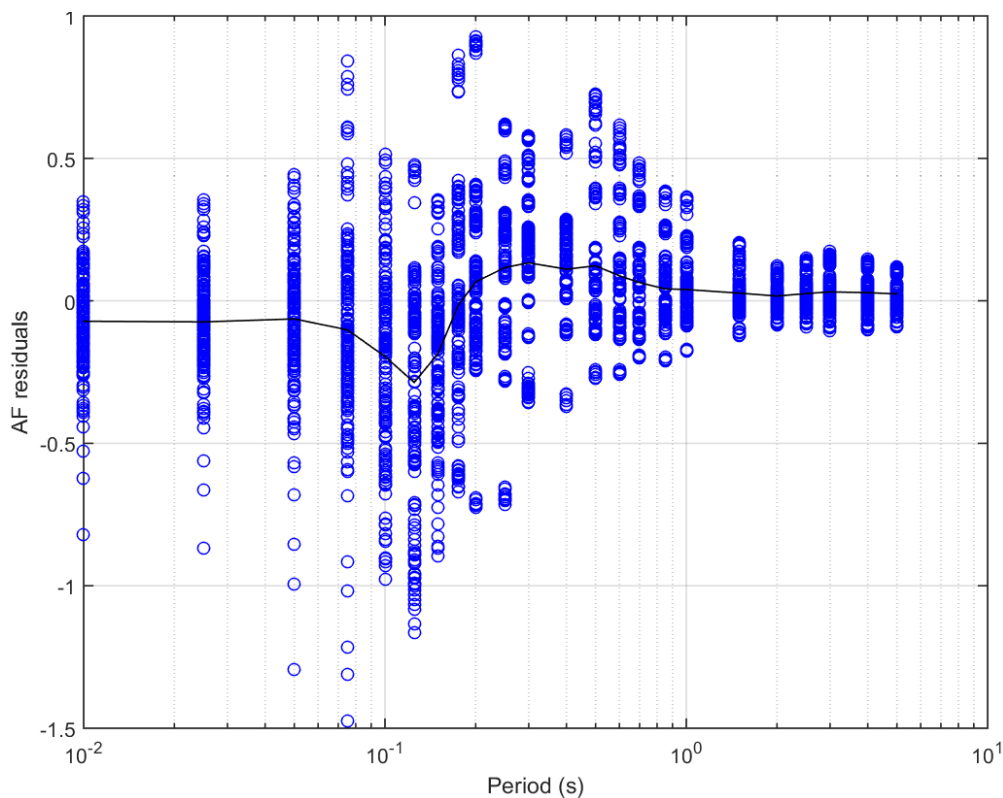


Figure 2.3. Residuals of AFs (in natural logarithms) obtained from modelled V_s profiles relative to the AFs obtained from the measured V_s at the B-stations.

Although these comparisons indicate that the AFs obtained from the modelled V_s profiles are not a perfect match with those obtained from measured profiles, the average agreement between the two is reasonable (at least in the northern part of the field where the B-stations are mainly located). In addition to this conclusion, there are a number of reasons why the use of the G0-station recordings may be preferable to the continued use of the geophone recordings, as follows:

1. The use of G0-station and B-station recordings alone means that the GMM is now derived exclusively from accelerograph recordings. There is no reason to believe that any major inaccuracies were introduced by using the geophone recordings especially since these have high sampling rates and can be differentiated with confidence to obtain accelerations (and extensive analyses were performed to conclude that the same filter parameters could be applied to B-station and G4-station recordings). However, deriving the model using recordings obtained from the same type of instruments at all locations may be more internally consistent.
2. A particular challenge associated with the use of the G4-station recordings is that it requires the calculations of TFs and AFs for a within-column horizon. There is some potential for inaccuracies in this process because theoretical constructive and destructive interference at depth may not be realised in the field due to deviations from 1D conditions. The calculation of TFs and AFs for the ground surface relative to the NS_B are not affected by these issues.
3. The model-building process involves deconvolving the recorded motions down to the NS_B horizon, whereas the application of the model involves transmitting NS_B motions to the ground surface. In this regard, using recorded motions obtained at the surface—rather than at a depth of 200 m—renders the model more internally consistent.

One consequence of using the surface motions is that a reduced proportion of the data can be used in the inversions as a result of poorer signal-to-noise ratios, but this is perhaps less of an issue now that the database has grown so much (Section 2.2). The issue is also slightly offset by the fact that a few G4 stations are not operational whereas the corresponding G0 accelerograph is yielding usable data.

The switch from using 200-m geophone recordings to using the surface accelerographs at the G-stations is a significant change in the way that the GMM is derived, and this needs to be considered when comparing the V6 model with previous versions (Section 6.1).

In terms of the predicted ground-motion parameters, the V6 GMM provides predictions for the $S_a(T)$ at the same 23 oscillator periods, T , ranging from 0.01 to 5 seconds, since these are the parameters used to characterise the fragility functions. The distribution of response periods in the V6 exposure database is very similar to that in the previous version (Figure 2.4) although the fragility functions are now defined in terms of average $S_a(T)$ over a range of periods. The fragility functions no longer include any dependence on duration of shaking and consequently, since there is no other application of that parameter, the V6 GMM does not include a duration model. Although PGV is not used in the risk calculations, it is still included since it is a useful parameter for mapping hazard (probably more so than PGA) and may also be of use to risk assessment of some utilities and lifelines.

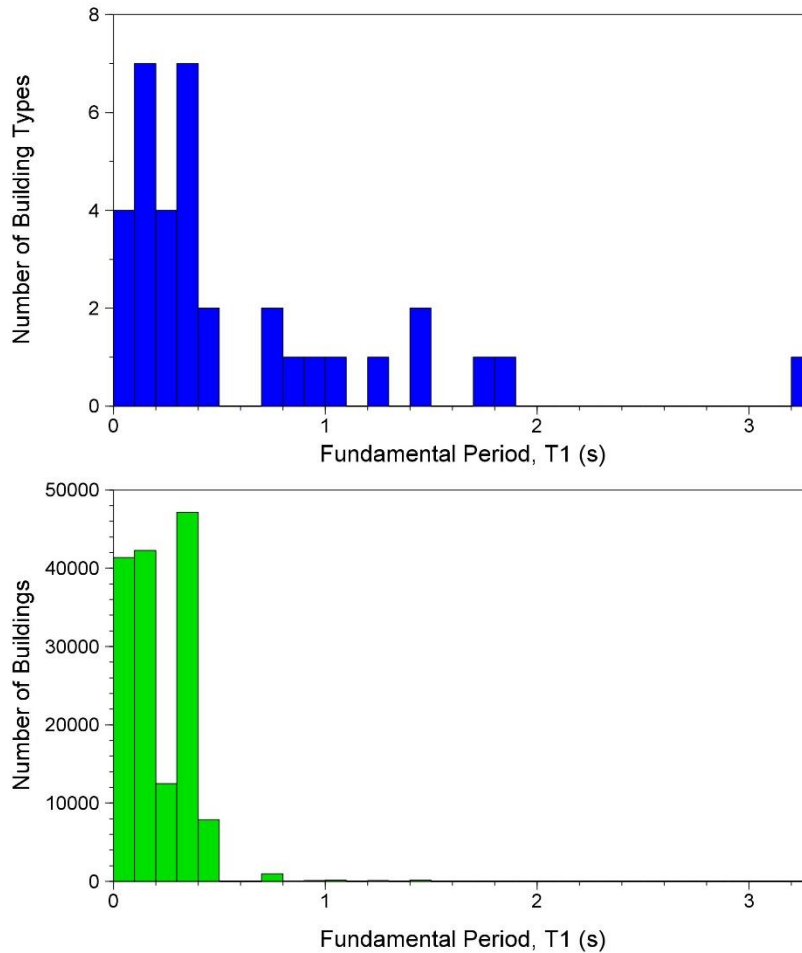


Figure 2.4. Distribution of natural periods of vibration in the exposure model by building type (*upper*) and by number of buildings (*lower*)

2.2. Ground-motion database

Since the V5 GMM database was compiled, two significant earthquakes occurred in early 2018, the M_L 3.4 Zeerijp event of 8 January and the M_L 2.8 Garsthuizen event on 13 April. The epicentres of these two earthquakes, relative to those of the 23 events in the V5 database, are shown in Figure 2.5. Both earthquakes contributed close to 80 recordings, a direct result of the installation of the G-network (Figure 2.6), resulting in an almost 60% increase in the total size of the database. The V6 database now consists of 414 recordings from 25 earthquakes; the earthquake characteristics are in Table 2.1 and their recordings in Table 2.2. The magnitude-distance distribution of the database is illustrated in Figure 2.7, which highlights the additions from the two recent earthquakes. Direct comparisons of numbers of records between the V5 and V6 databases, however, can be misleading since, as noted previously, a few of the G4 instruments are not operational hence the change to use of G0-station recordings has also increased the number of records coming from the 23 earthquakes already in the V5 database.

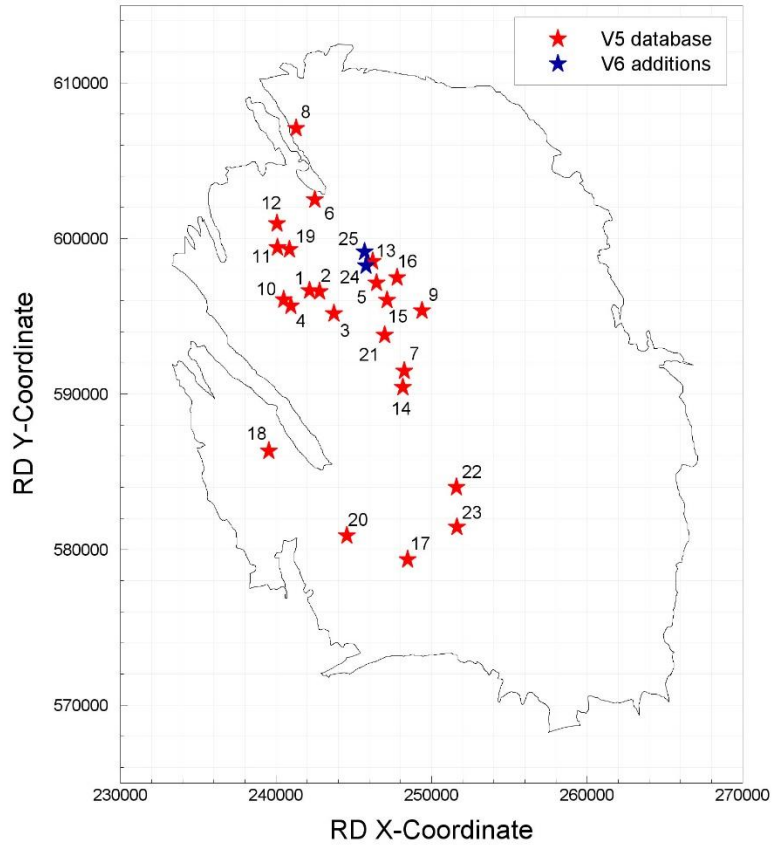


Figure 2.5. Epicentres of earthquakes in the V5 database

Table 2.1. Earthquakes included in the V6 Database

EQ-ID	M	RD-X (m)	RD-Y (m)	Date	Location
1	3.5	242159	596659	2006-08-08-05:04:00	Westeremden
2	2.5	242826	596579	2006-08-08-09:49:23	Westeremden
3	3.2	243740	595168	2008-10-30-05:54:29	Westeremden
4	2.6	240955	595673	2009-04-14-21:05:25	Huizinge
5	3	246479	597129	2009-05-08-05:23:11	Zeerjip
6	2.5	242496	602509	2010-08-14-07:43:20	Uithuizermeeden
7	3.2	248253	591487	2011-06-27-15:48:09	Garrelsweer
8	2.5	241305	607070	2011-08-31-06:23:57	Uithuizen
9	2.5	249399	595368	2011-09-06-21:48:10	Oosterwijtwerd
10	3.6	240504	596073	2012-08-16-20:30:33	Huizinge
11	2.7	240112	599405	2013-02-07-22:31:58	Zandeweer
12	3.2	240085	600945	2013-02-07-23:19:08	Zandeweer
13	2.7	246230	598516	2013-02-09-05:26:10	t Zandt'
14	3	248163	590446	2013-07-02-23:03:55	Garrelsweer
15	2.8	247166	596048	2013-09-04-01:33:32	Zeerjip
16	3	247804	597489	2014-02-13-02:13:14	Leermens
17	2.6	248489	579359	2014-09-01-07:17:42	Froombosch
18	2.8	239565	586336	2014-09-30-11:42:03	Garmerwolde
19	2.9	240890	599307	2014-11-05-01:12:34	Zandeweer
20	2.8	244561	580898	2014-12-30-02:37:36	Woudbloem
21	2.7	246987	593800	2015-01-06-06:55:28	Wirdum
22	3.1	251603	584016	2015-09-30-18:05:37	Hellum
23	2.6	251654	581456	2017-05-27-15:29:00	Slochteren
24	3.4	245790	598262	2018-01-08-14:00:52	Zeerjip
25	2.8	245706	599151	2018-04-13-21:31:35	Garsthuizen

Table 2.2. Numbers and features of records from each earthquake

EQ ID	M	Recs	Tot	Min. R_{epi} (km)	Max. R_{epi} (km)	Max. PGA (g)	Max. PGV (cm/s)
01	3.5	4	4	3.30	8.79	0.050	1.25
02	2.5	1	5	3.97	3.97	0.005	0.13
03	3.2	6	11	1.20	5.32	0.035	1.44
04	2.6	3	14	2.18	2.50	0.014	0.44
05	3.0	5	19	0.63	7.95	0.023	0.62
06	2.5	5	24	3.84	7.28	0.014	0.28
07	3.2	8	32	1.21	11.78	0.027	1.21
08	2.5	3	35	8.55	11.05	0.006	0.12
09	2.5	1	36	6.37	6.37	0.001	0.02
10	3.6	7	43	1.97	18.54	0.082	3.51
11	2.7	3	46	0.43	4.39	0.019	0.55
12	3.2	3	49	1.23	5.64	0.031	1.44
13	2.7	2	51	2.95	3.94	0.009	0.36
14	3.0	2	53	3.31	8.19	0.014	0.55
15	2.8	5	58	2.56	5.87	0.013	0.48
16	3.0	14	72	1.75	9.29	0.070	1.62
17	2.6	5	77	13.98	19.26	0.0003	0.02
18	2.8	12	89	4.78	17.29	0.002	0.11
19	2.9	18	107	2.46	16.16	0.077	1.78
20	2.8	19	126	2.60	22.54	0.017	0.35
21	2.7	19	145	1.22	14.94	0.013	0.45
22	3.1	42	187	1.90	26.24	0.033	1.08
23	2.6	70	257	1.81	28.05	0.070	0.85
24	3.4	77	334	1.41	31.71	0.111	3.21
25	2.8	80	414	1.59	32.51	0.042	0.94

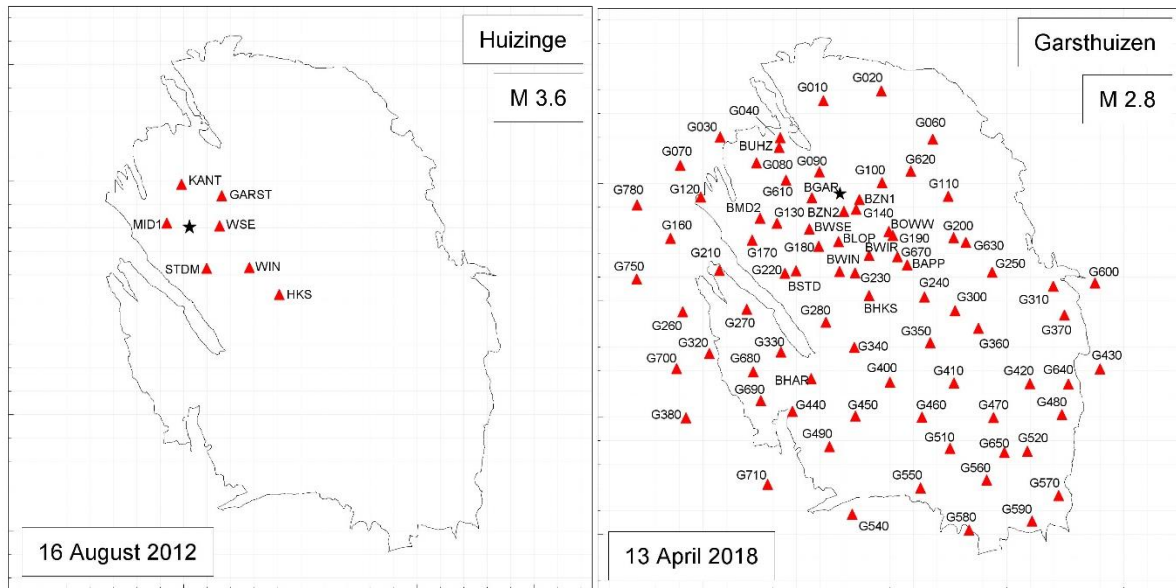


Figure 2.6. Contrast between stations yielding records from the 2012 Huizinge earthquake (left) and the 2018 Garsthuizen event (right)

The largest value of PGA in the database is now 0.11g, recorded during the 2018 Zeerijp earthquake, which is the first and only exceedance of the 0.08g PGA value obtained during the 2012 Huizinge earthquake. Figure 2.8 shows the geometric

mean PGA values as a function of distance, separated into two magnitude ranges. The largest horizontal component PGV recorded in the field, however, continues to be the 3.5 cm/s obtained from the Huizinge earthquake.

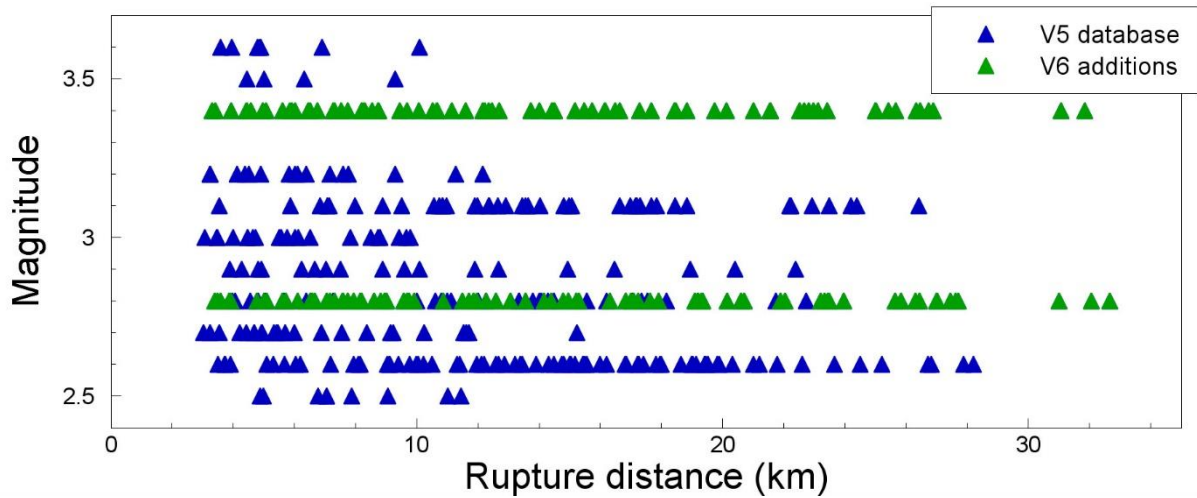


Figure 2.7. Magnitude-distance distribution of the V6 database; for these small events, rupture distances are taken as equivalent to hypocentral distances.

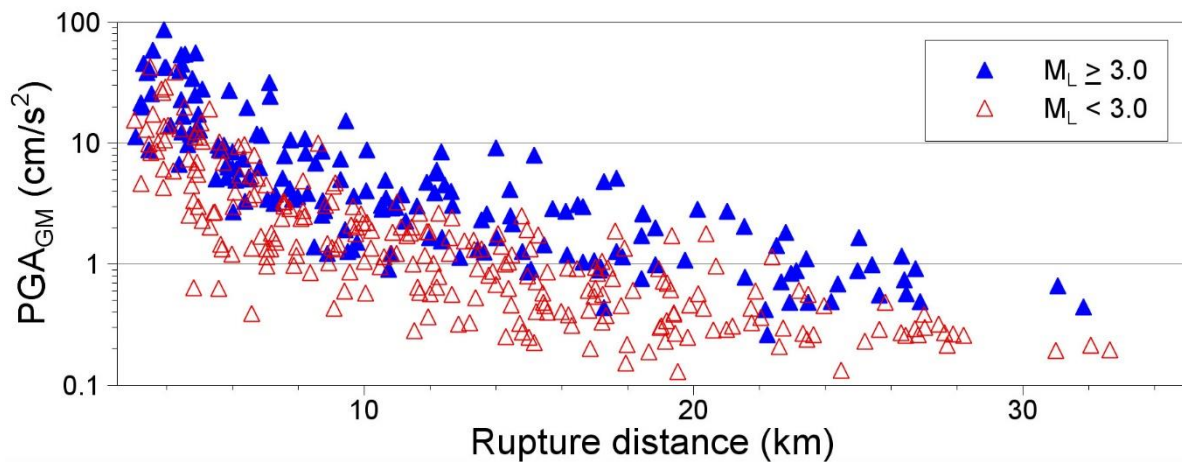


Figure 2.8. Geometric mean horizontal PGA values in the V6 database plotted against distance

The necessity of filtering the recordings leads to a maximum oscillator period at which the response spectral ordinates from each record can be reliably used, resulting in a rapid decay in the number of usable recordings for response periods in excess of about 0.9 seconds (Figure 2.9). At 1.4 seconds one half of the database is no longer usable and at 2 seconds only about 10% of the records still yield reliable spectral ordinates. As well as the number of usable records decreasing, the magnitude-distance distribution also changes, with fewer distant recordings contributing at longer oscillator periods (Figure 2.10).

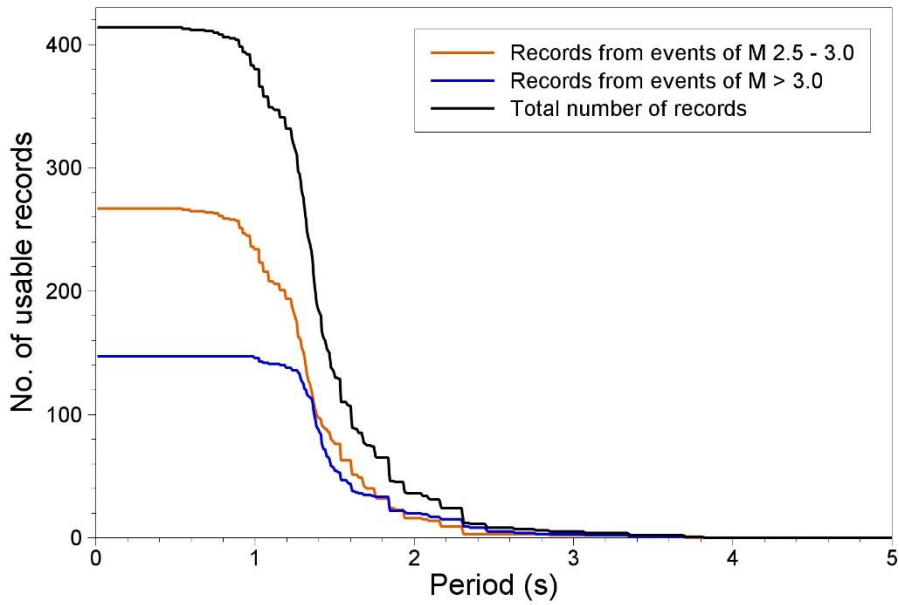


Figure 2.9. Number of usable records (for calculating spectral accelerations) as a function of oscillator period



Figure 2.10. Magnitude-distance distribution of usable records at different oscillator periods

2.3. Updated site response models

The site amplification model adjusts the ground-motion predictions at the NS_B horizon to the ground surface. The framework of the V6 site response model is identical to that of the V4 and V5 GMMs. Several inputs, however, have been updated: the input motions, the soil columns and the low-strain damping. The input motions are described in Chapter 4. The updated soil column and low-strain damping models are described below.

Soil columns

Two updates of the soil columns were made: the soil layering and the V_s values in the depths below the Modal Elastic Inversion (MEI) range (Kruiver *et al.*, 2017b). Borehole logs were obtained at the G station locations in the 200-m-deep boreholes before the geophone strings were installed. The borehole logs were interpreted in terms of lithology. The realisations of the geological model between 50 and 200 m depth were updated with the information from the borehole logs. The realisations were updated by adding scenarios, changing the depth of geological units, changing lithofacies and probabilities of occurrence. The zonation model of the deeper geology was not adjusted and remains identical to the model described in Kruiver *et al.* (2015). The deep zonation refers to Areas on the deep zonation map numbered from 1 to 63 (Figure 6.8 in Kruiver *et al.*, 2105).

An example of an adjustment of the scenarios in one deep zone (Area 16) is shown in Figure 2.11.

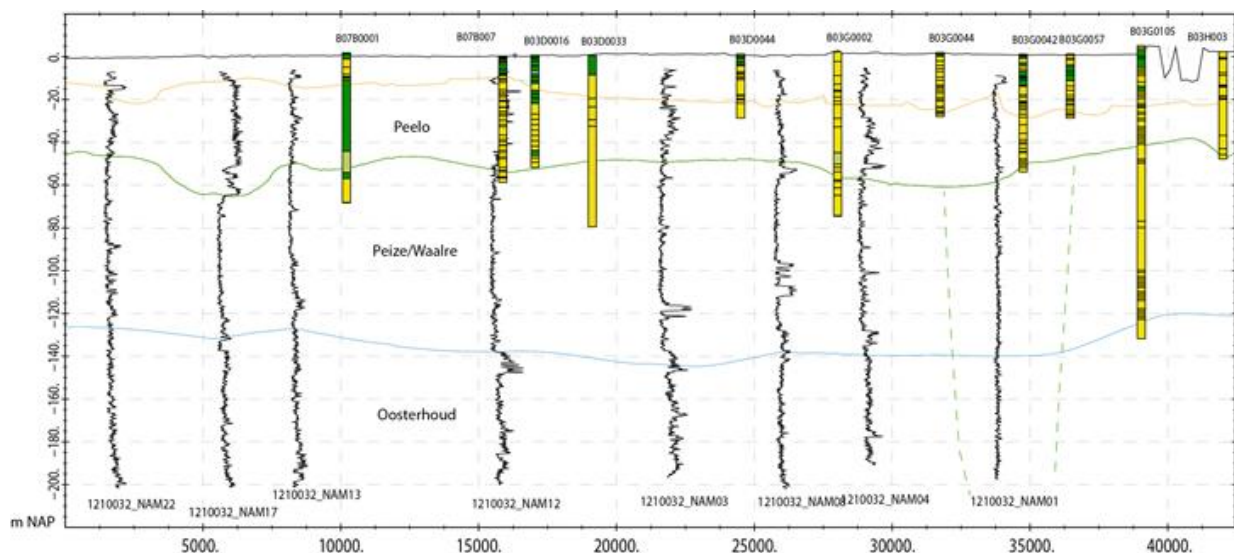


Figure 2.11. Cross-section through Area 16 showing the borehole logs (gamma, black lines), the DINOloket (<https://www.dinoloket.nl>) boreholes (green/yellow/brown lithology bars) and the Digital Geological Model surfaces. The green dashed line indicates the interpreted glacial valley of the Peelo Formation.

One of the borehole logs (1210032-NAM01) in Area 16 shows the presence of fine to medium sand all the way from -20 to at least -200 m NAP (Netherlands elevation datum) (Figure 2.11). We interpreted these fine-sand deposits as glacial tunnel-valley deposits of the Peelo Formation. In previous versions of the model, no Peelo Valley was included in the scenarios of Area 16. For V6, we added an extra scenario with a fine sand facies of glacial origin (Pgsf) with a probability of 20 % (Figure 2.12). This borehole is right on the boundary between Area 16, 22 and 46. Therefore, a Peelo Valley scenario was added to Areas 22 and 46 as well.

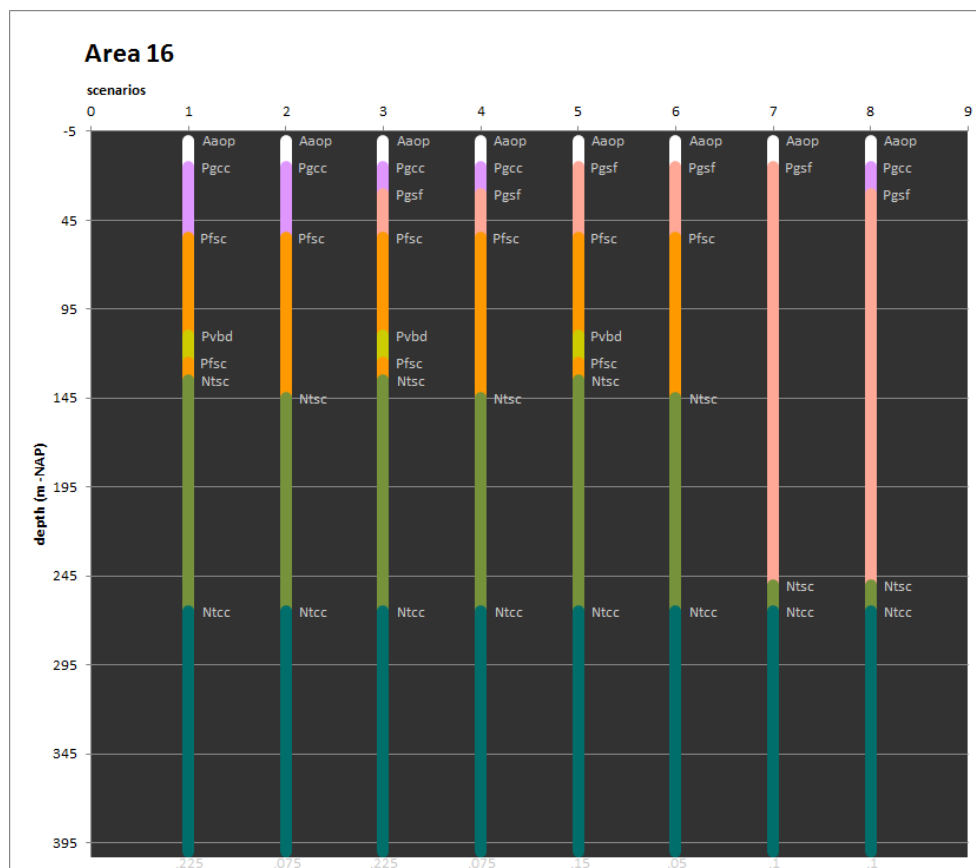


Figure 2.12. Example of scenarios in Area 16. Two scenarios were added (numbers 7 and 8) to account for the presence of a Peelo Valley as was evident from one of the borehole logs. The probabilities of the scenarios are shown in pale grey numbers at the bottom of each column. The codes indicate lithofacies, which were transformed to soil types for the soil response calculation input files.

The sonic V_s model (Kruiver *et al.*, 2017b) has been updated by NAM and is referred to as the "September2017" model (Romijn, 2017). Relative to the previous model (May 2015), the new model has been extended to the west, south and southeast. More importantly, the P-wave velocities (V_P) and the depths of the NU_B and NS_B horizons are based on the latest reprocessing and imaging of the seismic data. The velocity model is based on the Pre-stack Depth Migration (PSDM) model of the

northern part of the Netherlands, spanning the provinces of Groningen, Friesland and Drente. The various parts of the model were merged in the time domain (Romijn, 2017). During the conversion to depth, the PSDM model is transformed such that the mismatch between well markers and the horizons (e.g. NU_B and NS_B) in the model is minimized. As a result, the V_P distribution and depth levels of NU_B and NS_B are improved in the new model. The conversion from V_P to V_S uses the same equations as in Kruiver *et al.* (2017b). Figure 2.13 shows the difference in depth of the NU_B (left) and the NS_B (right) horizon between the two models. The difference is generally small, but can be up to 30 m at the edges of salt domes.

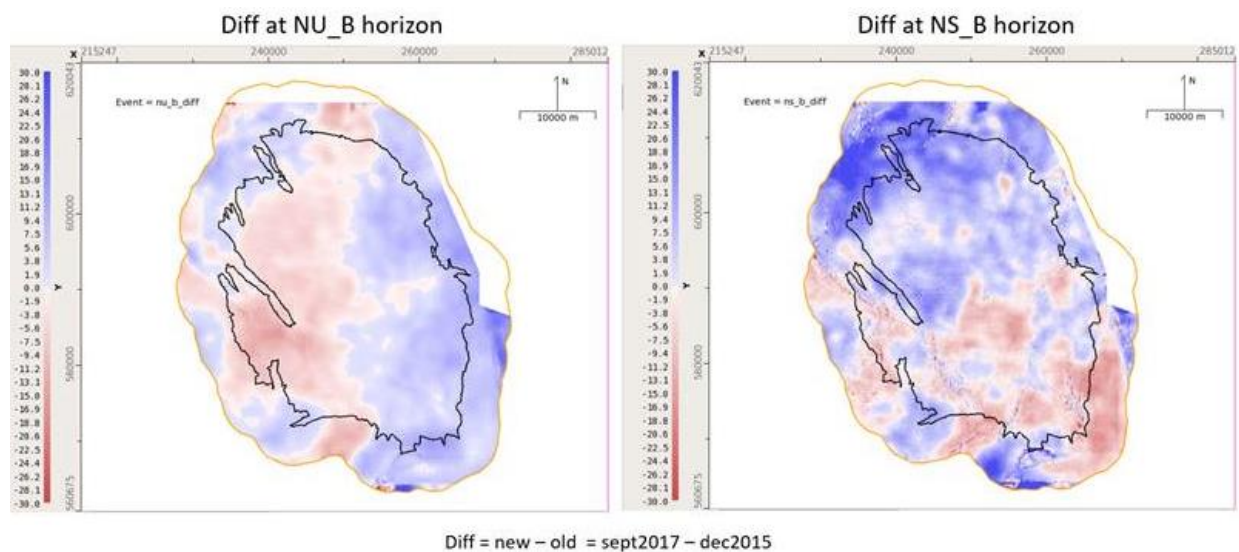


Figure 2.13. Difference in depth of NU_B and NS_B horizons between the May2015 (used in V4 and V5) and the September 2017 (used in V6) models. Courtesy Remco Romijn.

After updating the scenarios and the sonic V_S model, the three V_S models (GeoTOP, MEI and updated Sonic) were spliced again using the updated soil layers to create the V6 soil profiles serving as input for the site response calculations.

Low-strain damping

The same geomechanical lookup table was used in V6 as in V5 to obtain soil-type, index parameters, and V_S values. There is, however, one difference in the approach. In V5, the low-strain damping values (D_{min}) were computed by scaling the laboratory-based low-strain damping estimated from soil-type and index parameters using Menq (2003) and Darendeli (2001) by a constant factor. This factor was constrained using measurements of the attenuation parameter (or *quality factor*) Q in two boreholes located at the southern edge of the Groningen field (de Crook & Wassing, 1996; de Crook & Wassing, 2001). This approach ensured that the D_{min} model is consistent with local measurements, while retaining the confining-stress dependency and the dependency on soil index parameters that is well constrained from

laboratory measurements. More recently, estimations of the attenuation parameter Q were made for the G station boreholes located in the Groningen field. These new data were used to update the factor used to scale the laboratory-based D_{\min} estimates. The remainder of this section presents these results and the development of a new damping model for the Groningen field.

The attenuation parameter Q is estimated from borehole stations installed in the shallow subsurface (*i.e.*, the G stations). Low-strain damping or interval damping (D_{\min}) and the attenuation parameter Q can be correlated using $D_{\min}=0.5Q$, thus both are equivalent measures of attenuation. Each G-network station has an accelerometer at the earth's surface and geophones at 50, 100, 150 and 200 m depth (Figure 2.14a). From the Groningen seismicity, a near-surface response can be estimated using seismic interferometry (Figure 2.14b). This approach has been implemented in Hofman *et al.* (2017) to find interval velocity profiles, as shown in Figure 2.14c. Similarly, attenuation can be derived from this near-surface response. The derivation of interval damping profiles (Figure 2.14d) is described below.

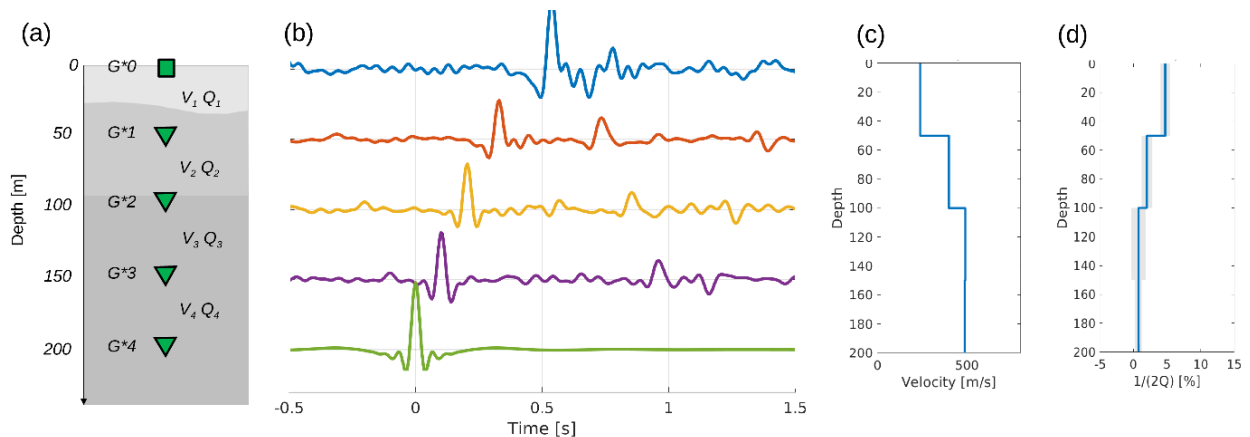


Figure 2.14. Different stages of attenuation (Q) estimation. (a) Setup of a G-network borehole station. (b) the local response over borehole station G36 estimated with seismic interferometry, with a virtual source constructed at 200 m depth. (c) The interval V_S profile extracted from (b). (d) Interval damping ($1/(2Q)$) profile extracted from (b) with mean damping per interval (blue line) and uncertainty (grey area).

For estimating attenuation, we largely follow the approach as introduced by Schneider & Safak (2006). In the first step, a local response is estimated from a multitude of local earthquake recordings using seismic interferometry by deconvolution. The main phase in the retrieved response (Figure 2.14b) is an up-going direct wave travelling from the virtual source at G*4 (at 200 m depth) along the borehole to the surface sensor G*0 (at the surface). This phase has the highest signal-to-noise ratio and is least affected by interference. Hence, this phase is used for deriving attenuation.

The near-surface response is corrected for the local impedance, geometrical spreading and the free-surface effect. Subsequently, the attenuation is estimated using the maximum method (Tonn, 1991). With this method, the attenuation is extracted from the decay of the maximum instantaneous amplitude and frequency of the direct wave, from one depth level to the next. This results in an estimate of the attenuation parameter Q for the upper three depth intervals. For obtaining an estimate for the deepest depth interval (Q_4 in Figure 2.14a), a local response is retrieved with a virtual source constructed at the Earth's surface.

The near-surface S-wave response as in Figure 2.14b is estimated from the radial and from the transverse component separately. The Q estimation is repeated for those two estimations of the S-wave response, and for 7 partly-overlapping frequency bands. This results in 14 estimates of each interval damping ($1/2Q$), from which the mean and standard deviation (σ) are determined. Figure 2.14d shows the mean damping for station G36 (blue line) and the confidence zone (minus one-sigma to plus one-sigma). This approach was used to estimate damping profiles at 43 stations (Figure 2.15).

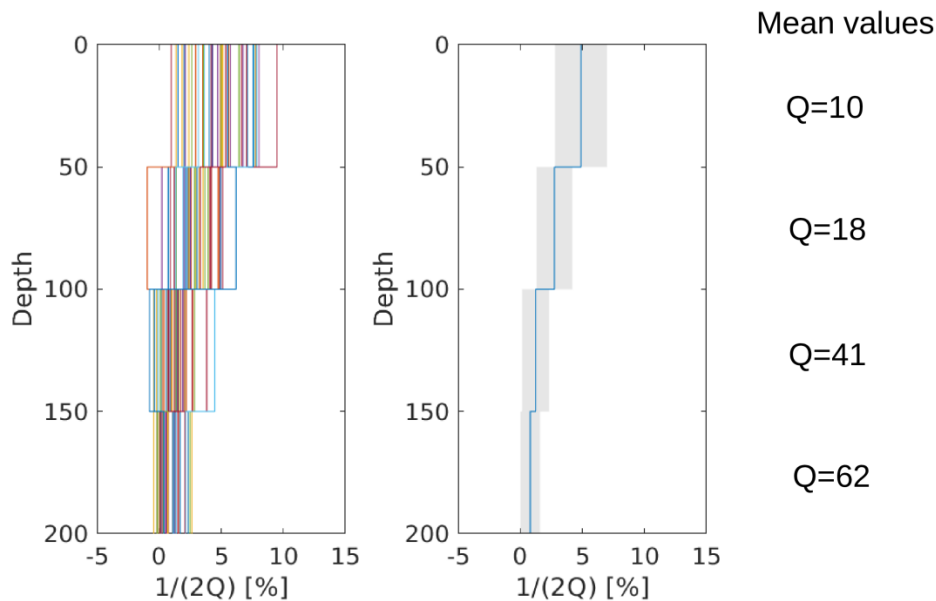


Figure 2.15. *Left*: Distribution of damping profiles at 43 different sites of the G-network; *right*: mean (blue line) and spread ($-\sigma$ to $+\sigma$) of damping values over the network. The corresponding mean Q values are listed on the right-hand side.

The damping measurements across the field were used to update the D_{\min} model for Groningen. The Q measurements for each station were converted into an equivalent $\Delta\kappa$ using:

$$(\Delta\kappa)_{\text{meas}} = \int_0^{z_{\text{rock}}} \frac{1}{Q(z)V_S(z)} dz \quad (2.1)$$

where the integration is from the base of the profile (*i.e.*, the NS_B boundary) to the surface. For layers below 200 m, a value of $Q=100$ was used. The value of $(\Delta\kappa)_{meas}$ is a single-valued parameter that represents the attenuation in the entire profile, which allows comparisons with previous versions of the model. Figure 2.16 shows the resulting $\Delta\kappa$ values for the stations where new Q measurements were conducted. Note that the new $\Delta\kappa$ values have a strong V_{S30} dependence. Also observe that a few stations appear to be outliers from the overall trend, indicated with the crosses. Figure 2.16 also shows the $\Delta\kappa$ computed using the D_{min} profiles from the V5 GMM. On average, the new Q measurements indicate higher levels of damping across the field.

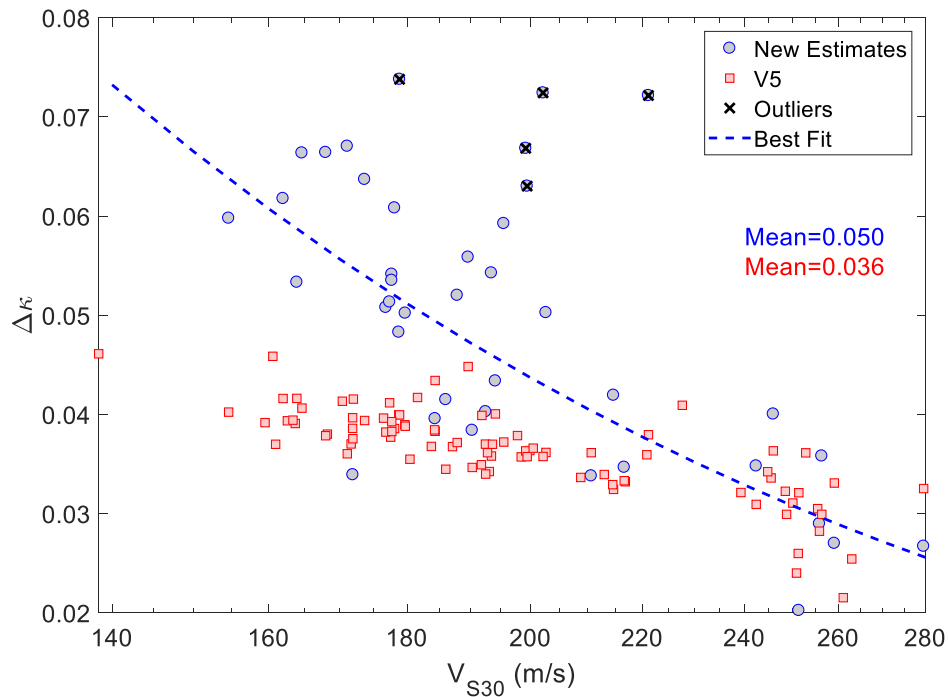


Figure 2.16. Full-profile attenuation ($\Delta\kappa$) computed from the measured Q profiles. The estimated $\Delta\kappa$ values from the D_{min} profiles in the GMM V5 are also shown for comparison.

The approach of scaling laboratory-based measurements, adopted in previous versions of the model, was retained. For this purpose, the $\Delta\kappa$ estimates at each station were used to compute a factor Γ with which the laboratory-based damping measured were scaled. The factor Γ was computed by equating the $(\Delta\kappa)_{meas}$ obtained from Eq.(2.1), with the $\Delta\kappa$ computed from laboratory-based measurements using:

$$\Delta\kappa = \int_0^{z_{rock}} \frac{\Gamma^2 (D_{min})_{lab}}{V_S(z)} dz \quad (2.2)$$

where the $(D_{min})_{lab}$ values were obtained from the Menq (2003) and Darendeli (2001) models, as described extensively in the GMM V4 report (Bommer *et al.*, 2017b). For the NS_B lithology, an unscaled value of $Q=100$ ($D_{min} = 0.005$) was used. By equating the $\Delta\kappa$ values from Eqs.(2.1) and (2.2) at each station, the scaling factor Γ was computed for each station. These values (excluding those for stations labelled as “outliers” in Figure 2.16) are shown as a function of V_{S30} in Figure 2.17. Note that there is a clear dependency on V_{S30} . For ease of implementation, the scaling factor Γ was then fitted to V_{S30} using a polynomial function:

$$\Gamma = 28.7912 - 6.6743 \ln V_{S30} + 0.3291 (\ln V_{S30})^2 \leq 3.5 \quad (2.3)$$

The limit of 3.5 was set to avoid over-estimating damping values. For comparison, the scaling factor Γ in the previous versions of the GMM was set to 2.11.

The low-strain damping (D_{min}) for use in the site response analyses was then obtained using:

$$D_{min} = \Gamma (D_{min})_{lab} \quad (2.4)$$

As indicated before, for the NS_B lithology a value of $D_{min}=0.005$ was used without any additional scaling. As in previous versions of the model, a limiting value of D_{min} was set for any soil in the model. This limit was set to $D_{min}=0.07$ (increased from 0.05 in the GMM V5). The increase was adopted, because values of D_{min} on the order of 0.07 were measured in various locations across the field (Figure 2.15). The values of the scaling factor Γ across the field are shown in Figure 2.18.

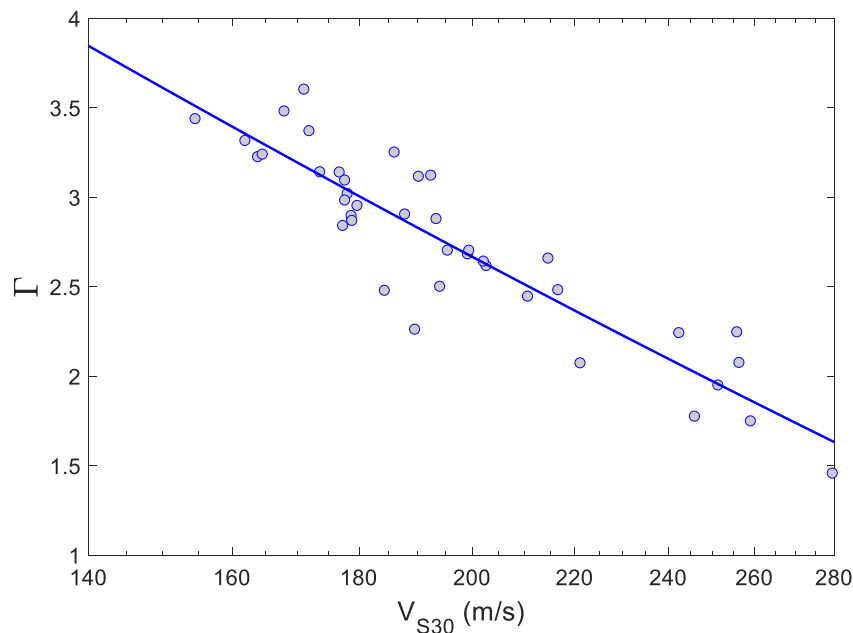


Figure 2.17. Scaling factor Γ as a function of V_{S30} .

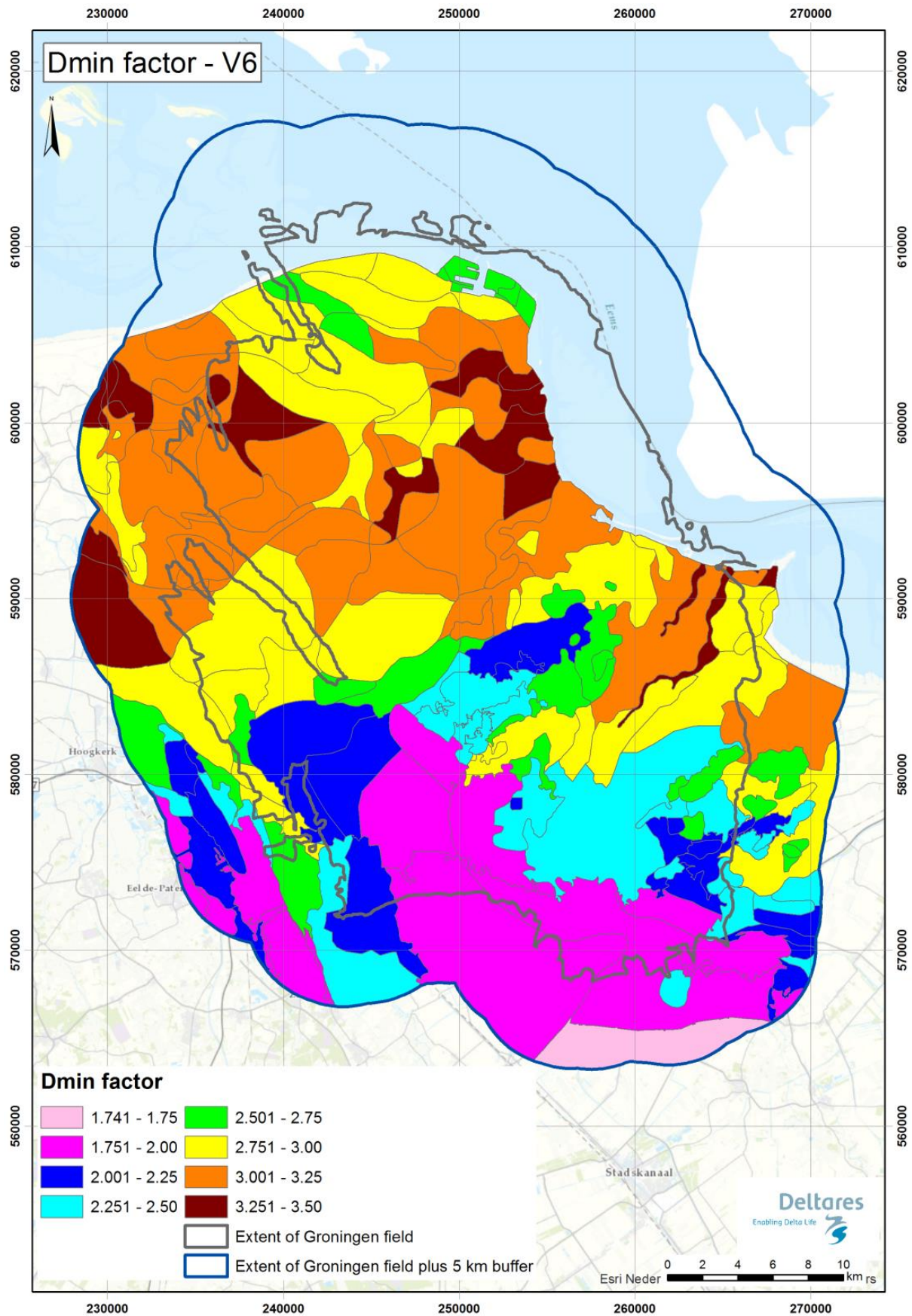


Figure 2.18. D_{\min} scaling factor Γ across the Groningen field.

2.4. Linear TFs and AFs from NS_B to surface

In order to apply the modelling approach described in Section 2.1, it is necessary to compute the motions at the NS_B level from the recordings at the surface. For different elements of the model-building process, both the FAS of acceleration and acceleration response spectra are required at the NS_B horizon. Following convention, the factors for converting the FAS are called Transfer Functions and those for response spectra are called Amplification Factors, and both are computed for all the recording stations. The approach to obtain these factors is the same that was adopted for previous versions of the GMM model (Bommer *et al.*, 2017b, Bommer *et al.*, 2018). The differences in this version of the model arise simply from the different inputs to the site response model, as discussed in Section 2.3. In particular, differences arise due to the differences in the low-strain damping profiles resulting from the adoption of a new damping model in the current version of the GMM. Input motions at the NS_B horizon are needed to compute the amplification factors (*i.e.*, in the response spectra domain). The same motions used to compute the amplification factors for the field (Section 4.1) are used to compute the factors for the stations.

An example of the TFs computed for the V6 model are shown in Figure 2.19. For comparison, the TF for the V5 model are also shown. The differences in the TF between the two models is primarily due to the differences in damping, and is seen in the high-frequency portion of the spectra. On the one hand, for stations where the D_{\min} scaling factor Γ (Section 2.3) is higher than that used in V5 (*i.e.*, stations with $V_{S30} < 238$ m/s), the newly computed TFs attenuate more rapidly (*e.g.*, station BAPP in Figure 2.19). On the other hand, for those stations where the scaling factor Γ is lower than in V5 (*i.e.*, stations with $V_{S30} > 238$ m/s), the high-frequency attenuation for the newly computed TFs is lower than that of V5 (*e.g.*, station BFB2 in Figure 2.19). Other than for high frequencies, the TFs are generally similar to those computed in previous versions of the model.

The spectral-domain AFs show clear magnitude and distance dependency (Figure 2.20). As discussed extensively in the GMM V5 report (Bommer *et al.*, 2018), their dependency is expected and has been observed in ground motion data (Stafford *et al.*, 2017). The AF model for the stations was fitted using only magnitudes lower than M_L 4.5, because this model was only needed to adjust the recording from the surface, and the maximum magnitude of the recorded motions is only M_L 3.6. The model used to capture distance and magnitude dependency is given by

$$\ln AF = [a_0 + a_1 \ln(R)] + [b_0 + b_1 \ln(R)][\min(M, M_{ref}) - M_{ref}] \quad (2.5)$$

where AF is the amplification factor, M is moment magnitude, R is closest distance, and $a_0, a_1, b_0,$ and b_1 are period-dependent parameters and M_{ref} is equal to 4.5. The

same model is also used for PGV. Figure 2.20 shows the computed AFs as well as the model in Eq.(2.5) for selected stations and periods. The model in Eq.(2.5) is a good fit to the computed AFs for most periods, but the bilinear functional form often results in under-predictions of the computed AFs for periods around 0.1 seconds and both large ($R > 40$ km) and short distances ($R < 10$ km).

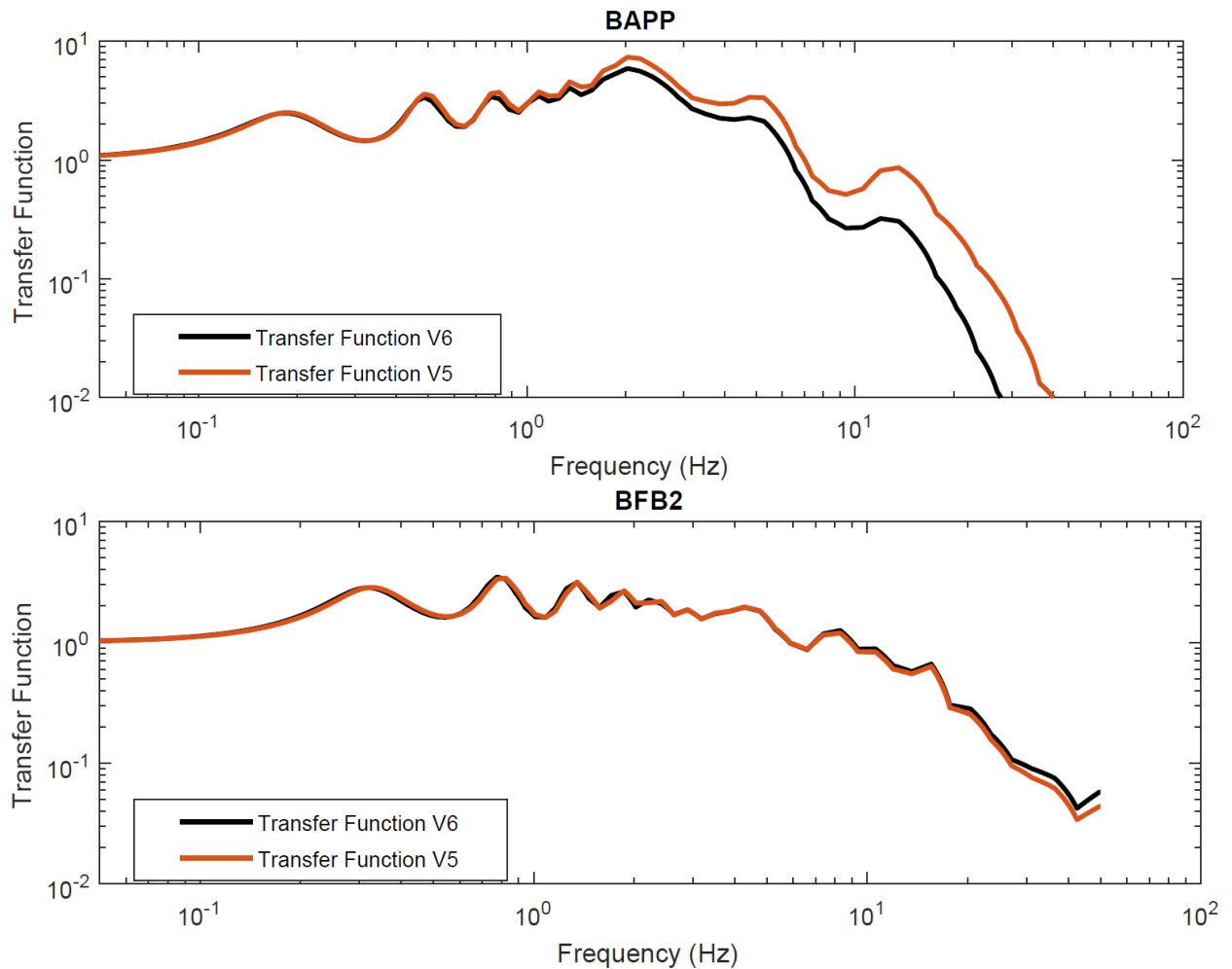


Figure 2.19. Transfer functions for two stations (BAPP and BFB2) for the V6 model (black line) and the V5 GMM model (orange line).

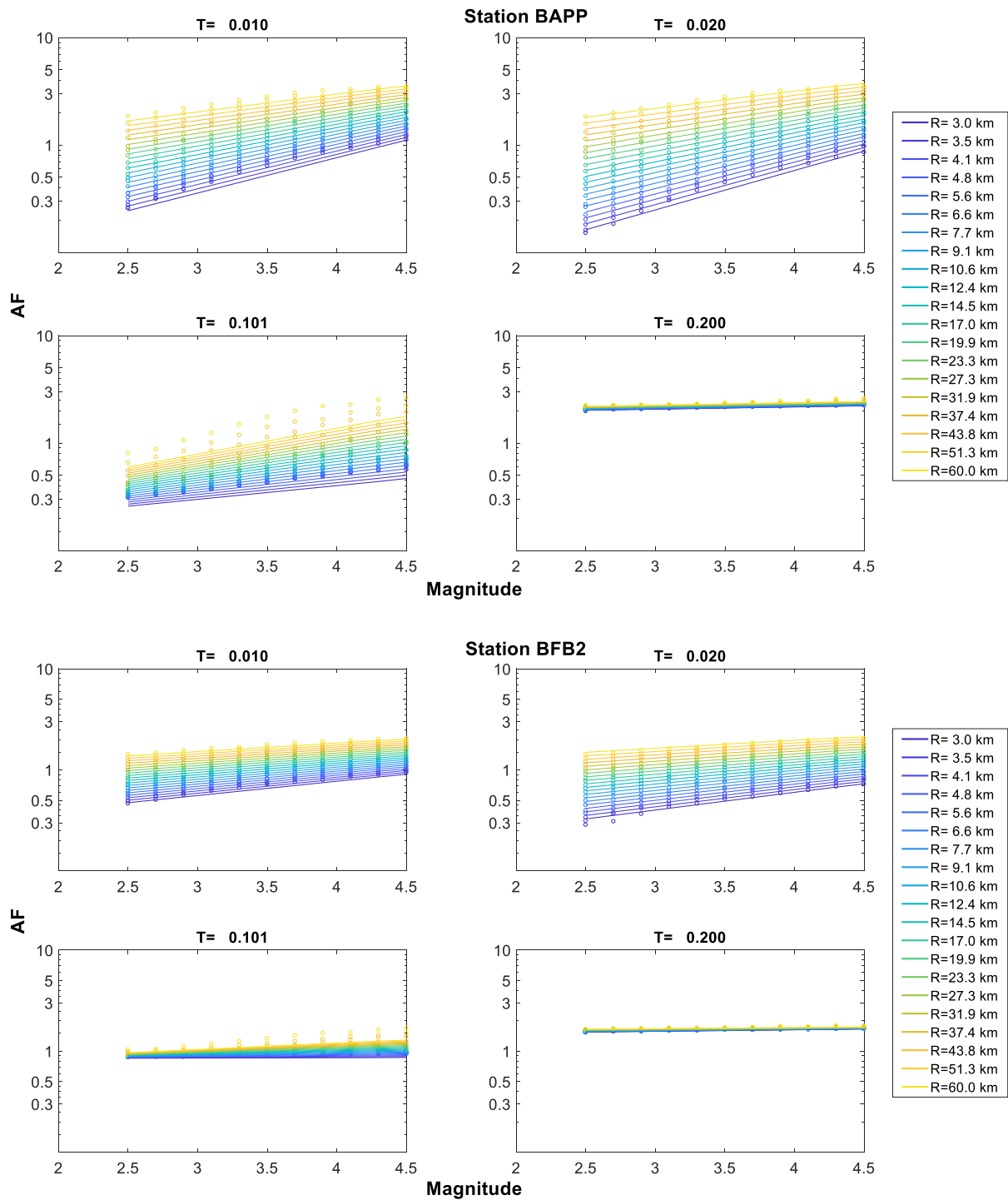


Figure 2.20. Computed AFs (small circles) and predictive model for selected stations and periods. The AFs are plotted versus magnitude and are color-coded for distance. Models for different distances are also plotted.

3. Ground-Motion Amplitudes at NS_B

The first part of the model for the prediction of $S_a(T)$ and PGV is a suite of ground-motion prediction equations (GMPEs) for the estimation of these parameters at the reference rock horizon (NS_B). The derivation of the V6 model for the motions at the rock horizon followed the same general procedures as used in the V3, V4 and V5 GMM development. However, three changes influenced the outcomes of this process as applied to the current model. The first of these changes is that now only recordings of ground motions obtained at the surface are used instead of a combination of surface accelerograph and borehole geophone records (see Section 2.1). Secondly, there has been an updating of the site response profiles (see Section 2.3) that led to minor modifications in the transfer functions used to translate the FAS of recordings at the surface to the NS_B horizon. Thirdly, the database has expanded with the inclusion of recordings from two earthquakes that occurred after the completion of the V5 database, adding a large number of additional records (see Section 2.2). This chapter briefly summarises the development of the V6 model for estimation of ground-motion amplitudes at the NS_B horizon, including the derivation of parametric equations for the prediction of $S_a(T)$ and PGV, as well as the model for the aleatory variability associated with the predictions.

3.1. Inversion of NS_B motions for source, path and site parameters

One of the key challenges in developing the GMM for the hazard and risk models has been the extrapolation from M_L 3.6 (the largest event that has occurred) to the largest magnitude considered possible, M 7.25. In order to accomplish this for the V6 Groningen GMM, motions are calculated using finite-fault, stochastic simulations. The method used is based on a discretised rupture model with dynamic corner-frequency (EXSIM: Motazedian & Atkinson, 2005; EXSIM_dmb: Boore, 2009). Each of the distributed sub-faults in this technique is assumed to be a point source (effectively a small magnitude earthquake), which can be characterised using the seismological parameters observed for events recorded in the Groningen gas field. More specifically, the seismological characteristics required for modelling ground motion using EXSIM are estimates of the source, path and site parameters that define the FAS and duration. This section presents an overview of the V6 inversions, with focus on updates with respect to the V5 model. In all other aspects the inversion methodology and results remain as per the V5 GMM.

Since the V5 GMM was developed the ground-motion database has been supplemented by two further events, and now includes 25 earthquakes. As discussed in Section 1.3, it was decided that the V6 GMM development would use only surface motions for inversions of source, path and site parameters at the reference horizon. The dataset includes 414 records, each of which has been

deconvolved (Figure 3.1) to the base of the North Sea supergroup (NS_B) horizon using the linear anelastic amplification functions corresponding to the V_s , density and Q profiles beneath each site. Of these records only 234 pass the signal-to-noise ratio (SNR) criteria necessary to be used in the inversions. The criteria are that $SNR > 3$ between at least 5 and 15 Hz and that the ratio of maximum to minimum usable frequencies exceeds 10, which remains unchanged since V5. The use of surface data introduces significantly more noise to the V6 dataset, however.

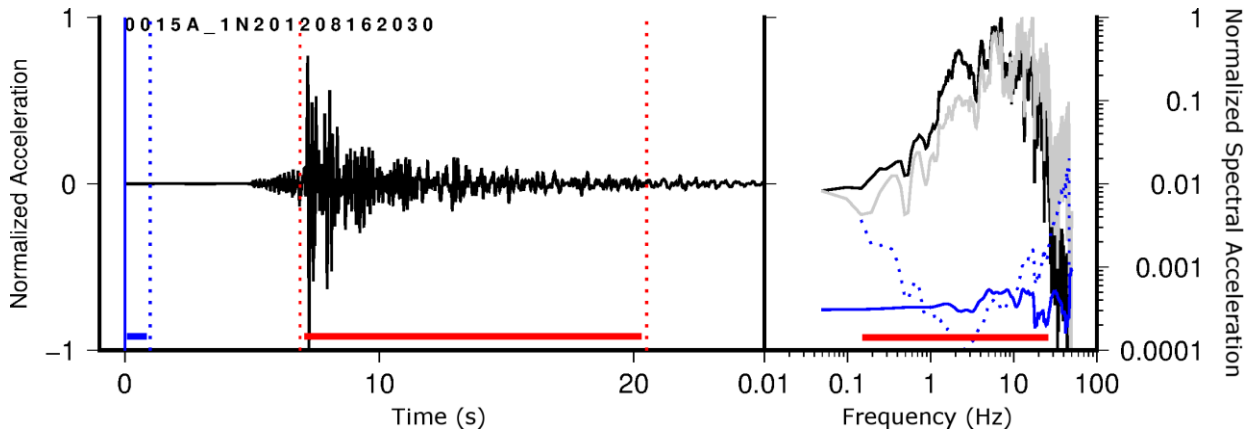


Figure 3.1. *Left:* example acceleration time series of the 2012 $M_L 3.6$ Huizinge earthquake recorded at station 15 (GARST), 14 km from the epicentre. The period highlighted in red indicates the signal and in blue the noise. *Right:* Fourier amplitude spectrum of the acceleration time series. Black: as recorded at the surface; grey: deconvolved to the NS_B; solid blue: recorded noise; dotted blue: noise after deconvolution to the NS_B and low frequency adjustment; the frequency range highlighted in red shows the FAS used in inversions ($SNR > 3$)

The FAS of all recordings, deconvolved to the NS_B horizon, are used to determine the source, path and NS_B rock parameters for use in subsequent forward simulations. A Bayesian-like approach was implemented to reduce the strong trade-off between the event stress-parameter (and equivalently, f_{oi}) and κ . A prior distribution for the stress-parameter was produced using a log-space median and standard-deviation ($\mu_{\log_{10} \Delta\sigma}$ and $\sigma_{\log_{10}(\Delta\sigma)}$). Alternative priors for the stress-parameter distribution can be tested with the aim being to reduce strong trade-offs and minimise the overall misfit between recorded FAS and model (Ω_d and Ω_m , respectively) over all frequencies (f) in a given passband between f_{low} and f_{high} . By using a wide prior we can achieve this, while at the same time minimising the influence on the median of the posterior distribution. The following function is minimised after selecting appropriate values for the prior (in which the normalisation within the sum of residuals gives log-based weighting to the FAS values, which, in turn, gives increased weighting to the fitting of the source corner frequency and spectral displacement plateau):

$$\chi = -2 \log_e \left\{ \frac{1}{2\pi\sigma_{\log_{10}(\Delta\sigma)}^2} \exp \left[-\frac{\log_{10}\left(\frac{\Delta\sigma}{\mu_{\Delta\sigma}}\right)^2}{2\sigma_{\log_{10}(\Delta\sigma)}^2} \right] \right\} \sum_{f_{low}}^{f_{high}} \left\{ \frac{\log_e[\Omega_d(f)] - \log_e[\Omega_m(f)]}{f} \right\} \quad (3.1)$$

Due to the limited distance range of available recordings (which is decreased with respect to the V5 GMM as a result of the noisier surface records now being used in place of the borehole records), the Q value was not robustly resolved. We therefore use $Q = 220$, as for the V5 model. This is consistent with analyses of t^* measurements of data in the Groningen gas field made by KNMI, which show that Q converges to around 200 when plotted against distance. For context, the median Q value measured in 44 boreholes between 150 and 200 m depth is $Q = 81$ according to analysis by KNMI. The Q values used in the inversions and throughout the analysis are therefore consistent with the general observation that Q increases with increasing V_s and depth. Using $Q = 220$, site-specific κ_0 were determined using a broadband fit of the linear-frequency log-acceleration FAS.

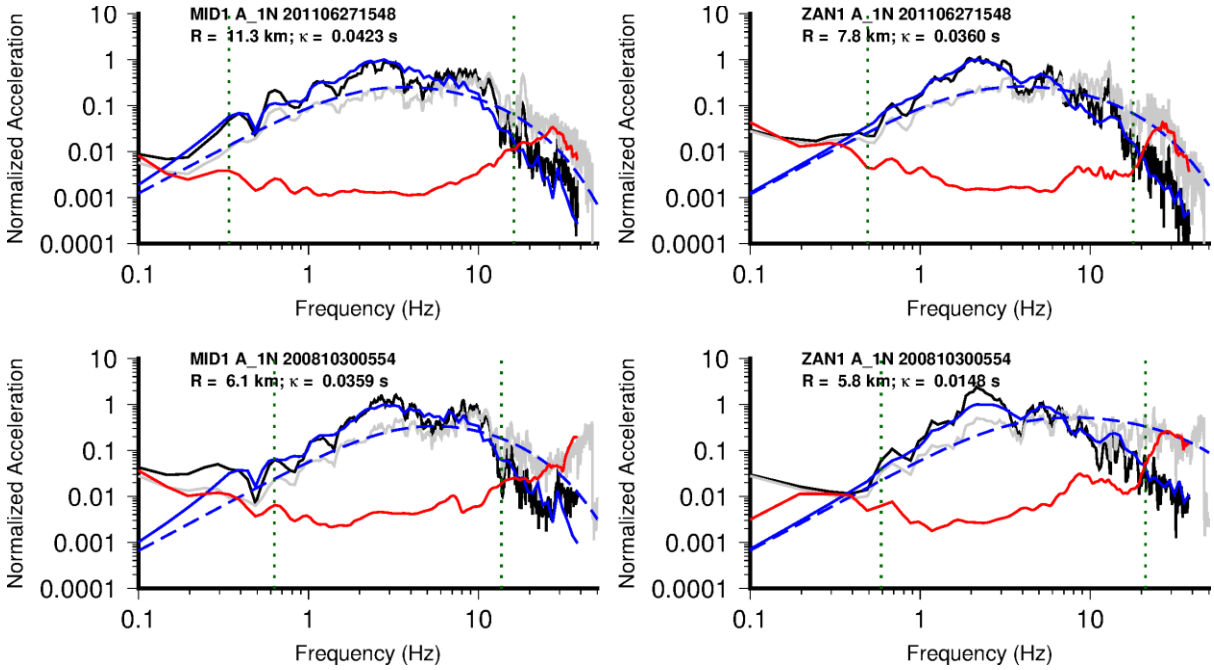


Figure 3.2. Comparison of observed (surface recordings at MID1 and ZAN1 accelerometers) and modelled FAS for two M_L 3.2 events. *Top*: 2011 Garrelsweer event ($f_0 = 3.0$ Hz); *Bottom*: 2008 Westeremden event ($f_0 = 4.9$ Hz). Note absolute amplitudes are normalized such that only spectral shape is fit. Black line: surface acceleration FAS; red: surface noise FAS; grey: FAS deconvolved to NS_B using site transfer function; blue: modelled FAS (dashed: at NS_B; and solid: at surface)

For the prior, the median stress-parameter was set to 7 MPa, as for the V5 GMM. A wide standard deviation (1 \log_{10} unit) was used so as not to bias the results, but to reduce the likelihood of trade-off between f_0 and κ . In a second step, both Q and κ_0 are fixed and a broadband inversion of the log-frequency log-acceleration FAS is

carried out (Figure 3.2). For f_0 the results are similar to those seen for the V5 GMM (for the comparable events, Figure 3.3). One event (2011-09-06) has a significantly increased f_0 ; however, only one usable FAS was available for this event. It is therefore poorly resolved and consequently controlled by the prior (in V5 it was a low outlier stress-parameter). The κ_0 at the B-stations are systematically lower (by an average of 0.0094 s) compared to the results presented in V5. The reduction in κ_0 is due to the increase in damping assigned in the linear site response analyses. The motions deconvolved to the NS_B horizon therefore have significantly more high-frequency content, which is reflected in the inverted NS_B reference κ_0 . The surface G-stations were not used in the V5 model development, so comparisons are not possible.

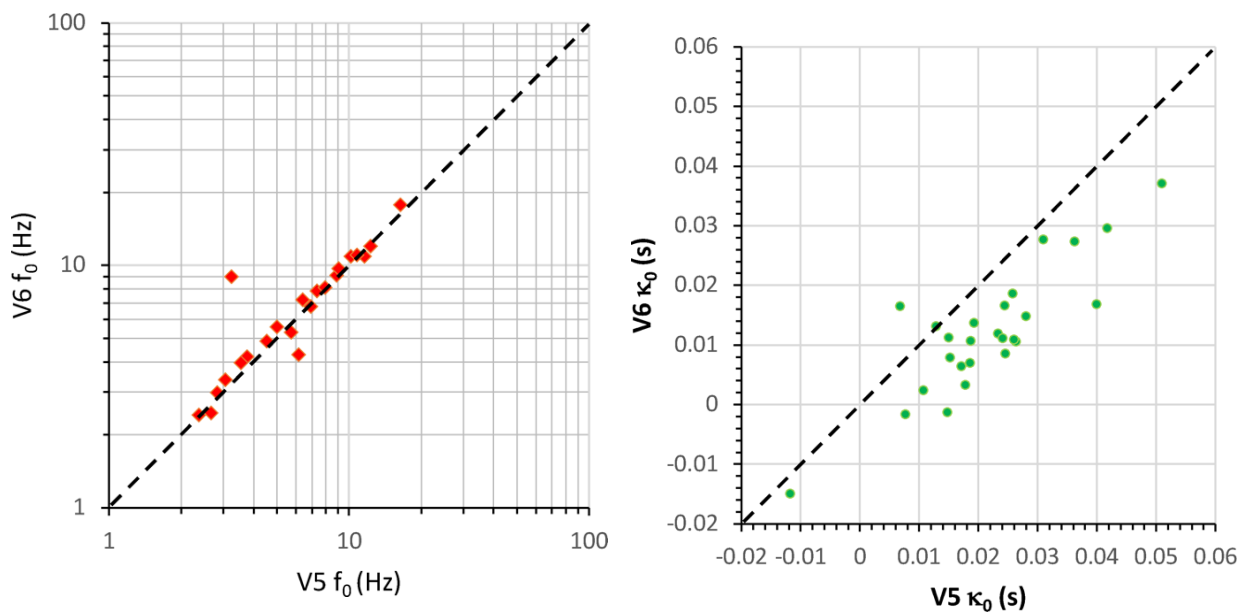


Figure 3.3. Comparison of inversion results (left f_0 and right κ_0) with those in V5

The Brune (1970, 1971) stress parameters calculated for the events are shown in Figure 3.4. The mean value was 65 bars (unweighted) or 70 bars (with a \log_{10} standard deviation of 0.38) when weighted by the square root of the number of records for each event, \sqrt{N} .

Using the long-period displacement plateau of the NS_B-corrected FAS, the geometrical decay function was inverted for along with average site amplification, fixing the moment magnitudes by assuming equivalence with M_L ($\mathbf{M} = M_L$). The hinge points of the geometrical spreading function were selected to coincide with the distances observed during the full waveform simulations undertaken at Shell: 7 km and 12 km, as presented in the V4 report. We assume that at hypocentral distances below 3 km (the minimum observed hypocentral distance), the rate of decay is the same as between 3 to 7 km.

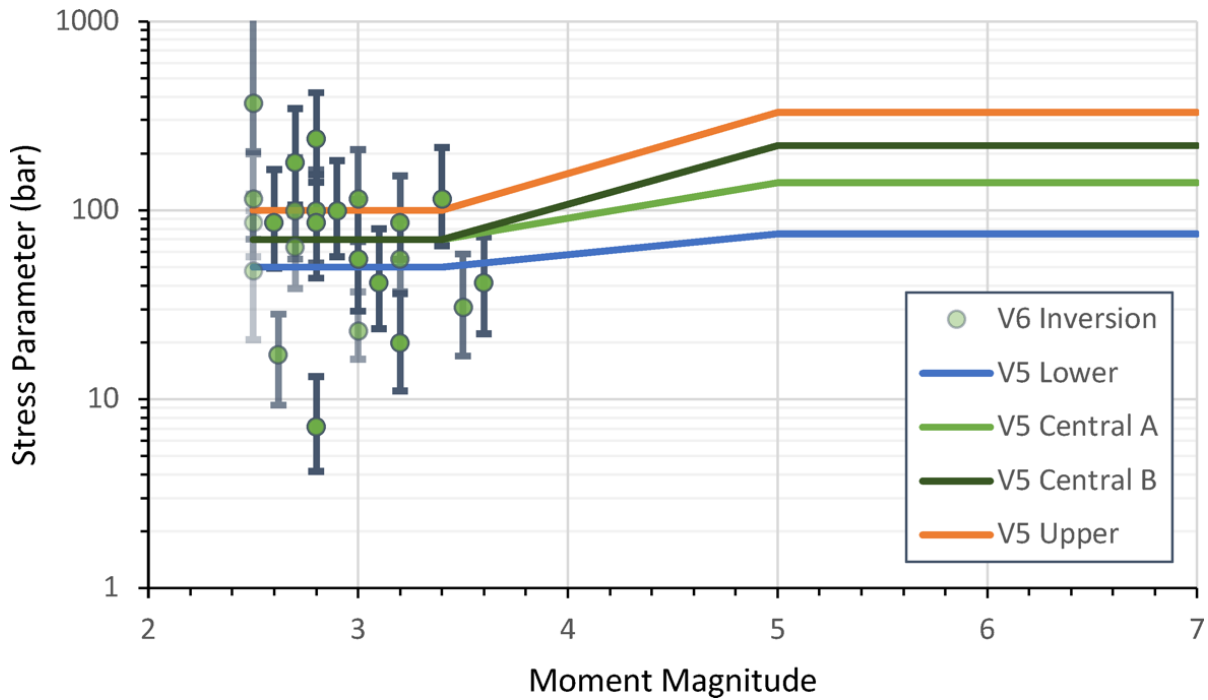


Figure 3.4. Inverted stress parameters plotted against moment magnitude. The V5 GMM stress parameter model is shown for comparison. Symbol transparency indicates the number of recordings used (darker indicates more records)

The shape of the decay observed is similar (although less pronounced) to that seen during the simulations, indicating that the velocity structure has a strong impact on the recorded amplitudes as a function of distance. The decay rates observed were: $R^{-1.55}$ up to 7 km, $R^{-0.51 \pm 0.25}$ from 7 to 12 km, and $R^{-0.69 \pm 0.38}$ from 12 to 25 km. There is no error assigned to the first rate of decay, as it is conditioned on the selected M values (and segmentation distances). Although there are no recordings beyond around 25 km, we assume R^{-1} , as indicated by the full waveform analyses. The use of surface data in the inversions leads to a smoother geometrical decay model than in V5. The results here show that decay between 7 to 25 km is similar (exponents of $R^{-0.51}$ and $R^{-0.69}$ before and after 12 km), while in the V5 model the decay showed a sharper transition at 12 km (with exponents changing from -0.23 to -1.43). In practice the differences are not large in the range where data exists (*i.e.*, $R < 30$ km). The decay rate in the first 7 km is, in fact, unchanged. However, the new decay rates at distances beyond 7 km will lead to systematically higher motions at distances greater than 25 km.

In order to define a field-average amplification at the NS_B level, the (geometric) average amplification (source to NS_B) of all sites was computed. As in previous GMMs, the amplification was found to be limited (compared to near-surface amplification) and broadly frequency-independent between ~ 0.5 and 30 Hz, fluctuating around 0.7-1.2 (albeit with a large standard deviation), suggesting that the effect of the velocity structure between the source (the reservoir) and the NS_B

interface results, overall, in no significant resonance. Weak de-amplifications between 0.8 and 2 Hz and 3 and 10 Hz may be indicative of velocity inversions present between the source and NS_B. The pronounced 0.6 Hz peak that existed in the V5 GMM is significantly reduced, which suggests it may have been an artefact of using borehole data (and/or corresponding ‘within’ motions in the deconvolution). At high frequency, the amplification increases, and plateaus at ~1.2 before dropping to unity. The overall amplification contrast (from low to high frequency) is consistent with expectations from quarter-wavelength modelling of the velocity profile.

3.2. Logic-tree for ground-motion simulations

Input ground motions are calculated using a finite-fault stochastic simulation methodology (EXSIM_dmb [version date: 17/10/2016]: Boore, 2009, based on EXSIM: Motazedian & Atkinson, 2005). This approach produces full time-histories and corresponding spectral ordinates by specifying a simplified seismological model (earthquake source, propagation and site effects).

The inversions discussed in Section 3.1 yield a range of source, path and site-specific parameters that are consistent with the recorded data. While there is therefore an estimate of the mean value of each of the parameters obtained from the inversion, a combination is sought that, when used in stochastic simulations, yields predicted spectral ordinates that best reproduce the recordings on average. Based on the initial observations in Section 3.1 and spanning the model space, we defined a range of stress-parameter and κ_0 values. In order to define a single characteristic NS_B κ_0 value a simulation grid-search was undertaken, with κ_0 values of 0.001, 0.005, 0.010 and 0.015 s; Brune stress parameter, $\Delta\sigma$, of 10, 20, 40, 80, 160 and 320 bars, and a Q value of 220. All simulations used the geometrical spreading model determined in Section 3.1 and based on the segmentation distances from full waveform modelling. Source to NS_B amplification, based on the network-average, was included for frequencies between 1 to 30 Hz. Below 1 Hz it was considered that insufficient data were available to constrain the amplification (below 1 Hz amplification is assumed to be equal to unity). The simulations were compared to the individual horizontal component response spectra at the NS_B horizon for all 20 spectral periods for which recorded data were available (0.01 to 2.5 s).

In order to assess the fit of each model, inter-event terms are calculated at each of the 20 periods. As for the V5 GMM, random-effect terms are calculated using the expression in Eq.(3.2) from Abrahamson & Youngs (1992) with arbitrary starting values of the intra-event term $\phi=0.5$ and inter-event term $\tau=0.5$ (\log_{10}) and iterating until convergence.

$$\eta_i = \frac{\tau^2 \sum_{j=1}^{n_i} y_{ij} - \mu_{ij}}{n_i \tau^2 + \phi^2} \quad (3.2)$$

In this equation, n_i is the number of records (y_{ij}) for the i^{th} event and μ_{ij} is the mean value of the j records for the i^{th} event. From the inter-event terms the average model bias is measured from the N events:

$$bias(T) = \frac{1}{N} \sum_{i=1}^N \eta_i(T) \quad (3.3)$$

As for the V5 GMM, the root-mean-square (RMS bias) and standard deviation [σ (RMS bias)] over the period-specific values is taken after each simulation to provide a simulation specific (period independent) measure of model bias. Note that the RMS misfit will only be 0 in the case that the model is perfectly unbiased at all periods. Low σ (RMS bias) indicates that the residual misfit is consistent (either consistently biased or unbiased), high values indicate period-to-period differences in the bias are present. EXSIM performs time-domain simulation, and is significantly slower than SMSIM, which can use random-vibration theory to speed up the process when only peak-amplitude ordinates (e.g., pseudo-spectral acceleration, PSA) are required. For small magnitude events, EXSIM_dmb has been shown to produce the same results as SMSIM (Boore, 2005; Boore, 2009), a fact verified during development of the earlier V4 GMM.

The results are shown in Figure 3.5 in terms of σ (RMS bias) versus stress parameter and κ_0 . After inspecting the residuals [$\eta_i(T)$, RMS bias and σ (RMS bias)] and considering the results of Section 3.1 the models with $\Delta\sigma = 60$ to 80 bar and with $\kappa_0 = 0.005$ s were deemed appropriate to model the recorded motions. Given the consistency with the spectral inversion (with weighted mean 70 bar and standard error limits of 50 to 100 bar, Figure 3.4), a central model with 70 bars was selected, as for the V5 GMM.

In order to refine the NS_B amplification function (which was based on the geometric mean across all sites), a subsequent step was introduced in this version. Since the inputs to the stochastic simulation of waveforms are in the Fourier domain, any remaining bias in $Sa(T)$ is apparent only in the response spectral domain, and it makes direct (re-)calibration difficult. However, inverse random vibration theory (iRVT, Rathje *et al.*, 2005) can be implemented to overcome this. The approach can generate response spectrum compatible FAS, and is implemented by the software STRATA. The steps taken here are as follows:

1. Generate response spectra using the simulation model described above ($\kappa_0 = 0.005$ s and $\Delta\sigma = 70$ bar) for a range of scenarios: $\mathbf{M} = 2.5, 3.0$ and 3.5 ; $R_{epi} = 0, 5, 10, 20$ and 30 km.
2. Remove any period-dependent $bias(T)$ (Eq. 3.3) from the simulated PSA.
3. Use STRATA to generate the response spectrum-compatible FAS for the simulated PSA (step 1) and bias-corrected PSA (step 2). Note – the ‘Limit Shape of FAS’ approach in STRATA should not be used.

- The ratio of FAS with and without bias correction provides the required modification to the input FAS to obtain unbiased (or reduced bias) PSA. The ratio is applied to the NS_B FAS amplification function to achieve this for subsequent simulations.

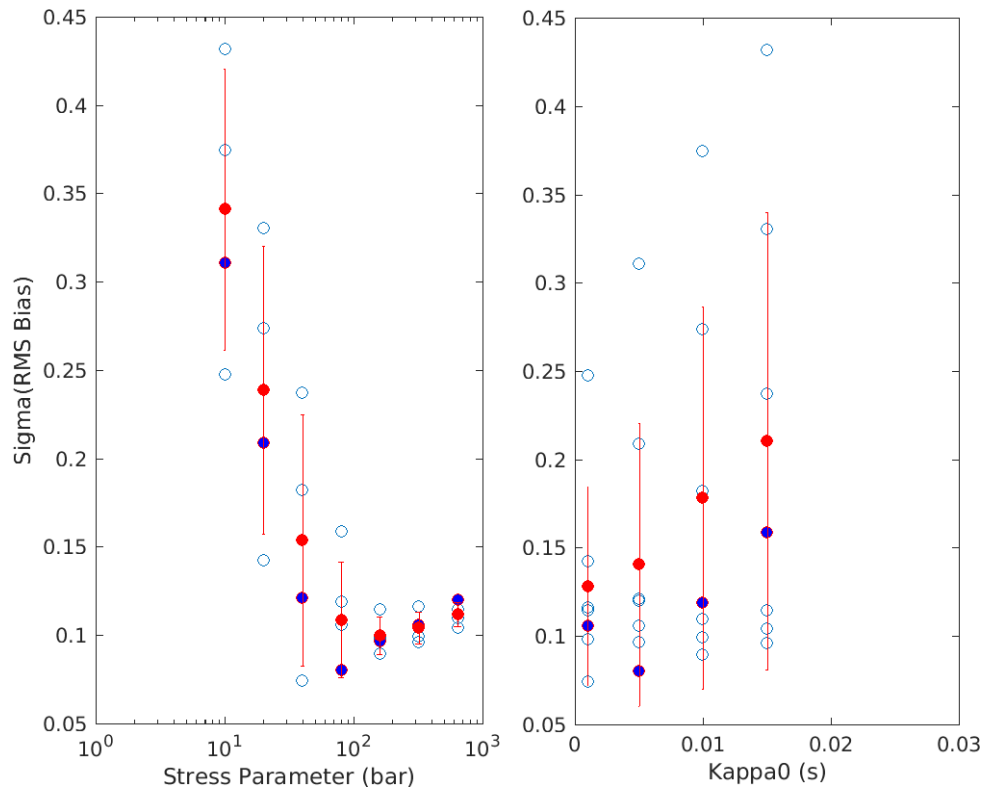


Figure 3.5. σ (RMS bias) plotted against *Left*: stress parameter and *Right*: κ_0 . $\kappa_0 = 0.005$ s in the stress parameter panel and $\Delta\sigma = 80$ bar in the κ_0 panel are indicated by the solid blue symbols

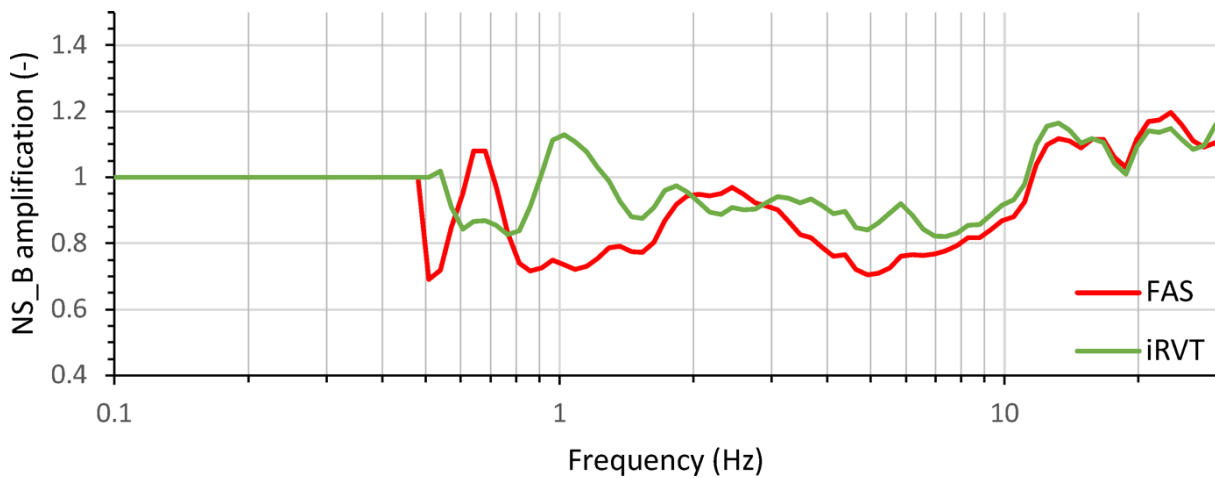


Figure 3.6. NS_B amplification functions based on the FAS analysis (Section 3.1) and iRVT analysis

Calibration to global GMPEs

The aim of the *upper* branch of the Groningen GMM is to reflect ground motions observed for small M events in the gas field, while producing ground motions comparable to global tectonic seismicity when extrapolating to larger M . In order to calibrate the model at large magnitudes, we have performed a similar process to that described above for matching models with locally observed events. However, we now set the target as the PSA at 6 spectral periods (PGA, 0.1, 0.2, 0.3, 1 and 2 s) at magnitudes $M = 5, 6$ and 7, for logarithmically spaced distances of 0, 2.5, 5, 10 and 20 km and with $V_{S30} = 1500$ m/s (consistent with NS_B rock velocities). Normal faulting is assumed, with a dip of 75° . Six GMPEs were used as the target: three NGA-W2 models (BSSA14: Boore *et al.*, 2014; CY14: Chiou & Youngs, 2014; CB14: and Campbell & Bozognia, 2014) in addition to the Eastern North America model YA15: Yenier & Atkinson (2015) and the European (RESORCE) models Aetal14: Akkar *et al.* (2014) and Betal14: Bindi *et al.* (2014). Due to the larger stress-parameters expected for typical tectonic events, the grid-search was expanded to include 20 values between 50 and 1600 bars. Based on the work of Boore (2009), who compared SMSIM against EXSIM_dmb, and the comparisons undertaken here, SMSIM (with the R_{EFF} distance metric used for finite-fault approximation) was again used for the calibration stage rather than the full EXSIM simulations.

Assessing the fit of the simulations to the GMPE predictions was somewhat subjective due to the low κ_0 (0.005 s) used at the NS_B reference, which is inconsistent with the spectral shape predicted by the GMPEs. The low κ_0 leads to much higher simulated short-period motions than typically observed in tectonic GMPEs (which, even at high V_{S30} as used here, are based on outcrop motions) (Figure 3.7).

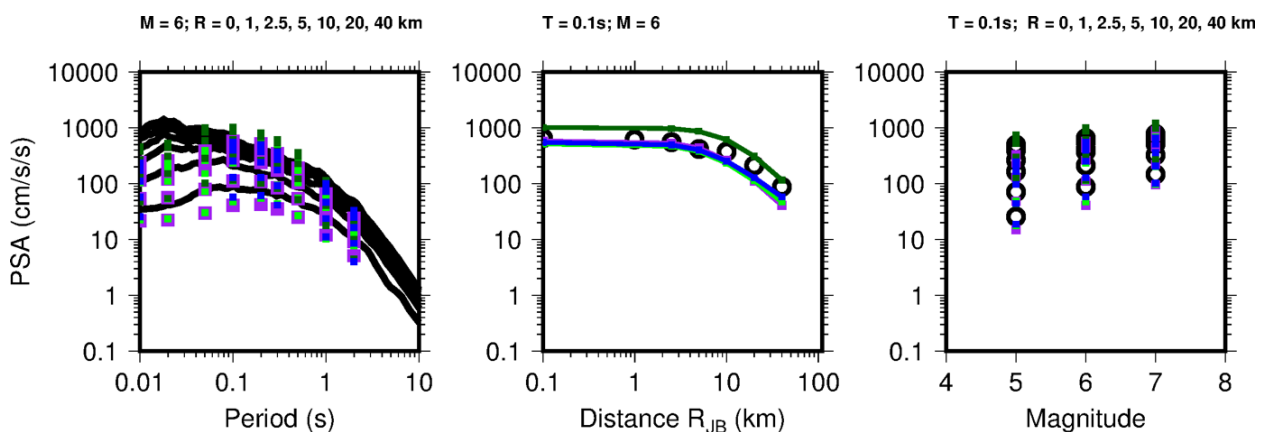


Figure 3.7. Comparison of simulated motions (EXSIM) against the calibration GMPEs for various scenarios. Blue: average of BSSA14, CY14 and CB14; dark green: YA15; purple: Aetal14; light green: Betal14 (see text for abbreviations)

To ensure capture of the full range of uncertainty, we retain the V5 model with 330 bars after inspection of the residual misfit plots, ensuring that predicted motions for the upper model are consistent with (or, if necessary, exceed) tectonic seismicity across the range of periods. As for previous GMMs, this means accepting a positive model bias (*i.e.*, overestimation at short and long periods) in order not to substantially underestimate the mid-period motions.

Selection of lower, central and upper models

As for previous GMMs, for the forward simulations it was decided to use alternative values of the stress parameter to reflect the considerable epistemic uncertainty associated with extrapolation to much larger magnitudes. In the magnitude range covered by data ($M \leq 3.6$) two central branches are proposed, and have a stress parameter of 70 bars (the ‘best-fit’ model to local data). The lower branch was set to 50 bars (one standard error below the mean from the analyses in section 3.1) and—reflecting the possibility of the motions being similar to those from typical tectonic earthquakes—the upper branch has 100 bars (one standard error above the mean). All models exhibit an increase of stress-parameter with magnitude, reflecting the belief that for larger events, increasingly sampling greater depths of the crust, the low $\Delta\sigma$ values observed in the reservoir at low M are unrealistic. For the two central models (central *a* and central *b*), $\Delta\sigma$ rises to 140 bars and 220 bars at M 5, respectively, then remains constant. Similarly, the lower and upper models rise to 75 bars and 330 bars, respectively. The latter is designed to produce motions, given the Groningen-specific attenuation and site characteristics, which are similar to those observed globally, as shown previously. The lower model, with stress drops increasing to 75 bars for $M \geq 5$, is designed to reflect the fact that we do not believe that median stress drops at moderate and large magnitude could be lower than those observed for local seismicity in the reservoir. The overall spread of the models is designed to be consistent—increasing by a factor ~ 1.5 for each branch, apart from the lowermost branch, where 75 bars is chosen as the upper level for the lower model—with a ‘self-similar’ magnitude scaling (*i.e.*, consistent with the central models at low magnitude). The only change to the V6 stress parameter model is therefore a shift of the lower hinge point from M 3.4 to 3.6 (*i.e.*, the maximum observed event magnitude). In the V5 model, the use of M 3.4 was based on the outdated assumption of $M = M_L - 0.2$ and had not been updated accordingly.

Table 3.1 summarises the full set of inputs to the simulations used to generate the motions at the NS_B reference for the derivation of the median GMPEs. For each of the model branches (lower, central *a/b*, and upper), response spectra were simulated using EXSIM_dmb for 2520 scenario events with M 2.0 to 7.0 in steps of 0.25. For each scenario event a random epsilon was selected to define the length and width and hypocentre of the rupture. Recording locations were placed radially above the centre of the fault’s top edge at 0 km and then 25 distances logarithmically spaced between 1.0 and 79.5 km. For each distance, 8 sites were located, at 0 to 315° (in 45° steps). In total 2.1 million response spectra were calculated, or 524,160

for each of the model branches. Examples of the simulated motions are plotted in Section 3.3 below, within the discussion of regression analyses to obtain parametric equations based on these simulations.

Table 3.1. EXSIM_dmb parameter values used in simulations for NS_B motions

Parameter	Symbol (units)	Value(s)	Notes
Density	ρ (g/cm ³)	2.6	
Shear-wave velocity	β (km/s)	2 3.5	M ≤ 4.5 (in reservoir) M ≥ 5.5 (Carboniferous) Linear interpolation between these magnitudes
Horizontal partition		0.707	
Radiation coefficient	θ	0.55	
Free surface	F	2	
Sub-fault source type		Brune (1970, 1971) ω^{-2}	
Top of rupture depth	Z_{top} (km)	3	
Seismogenic depth	Z_{seis} (km)	13	
Fault dip	Dip (degrees)	75	Average of observed 60 – 90 degrees.
Fault mechanism		Normal	
Fault width	W (km)	$\min(W(W\&C'94), [Z_{seis}-3]/\sin(\text{dip}))$	W(W&C'94): Width from Wells & Coppersmith (1994)
Fault length	L (km)	$L(W\&C'94)*(W/W\&C'94)$	L(W&C'94): Length from Wells & Coppersmith (1994) Conserve area of fault A given by LxW in case limited by Z_{seis}
Hypocentre location	H($\Delta L, \Delta W$) (km, km)	Random, 0	Located randomly along strike, at 3 km depth (top of fault).
Slip velocity	V_{slip} (km/s)	0.8 β	
Stress parameter (Lower, Central, Upper)	$\Delta\sigma$ [M ≤ 3.6] (bars)	50, 70, 70, 100	Linear interpolation of log($\Delta\sigma$) with M
	$\Delta\sigma$ [M ≥ 5.0] (bars)	75, 140, 220, 330	
Geometrical spreading distances (R_{hyp})	R1, R2, R3 (km)	7, 12, 25	
Geometrical decay rates	$\lambda_1, \lambda_2, \lambda_3, \lambda_4$	-1.55, -0.51, -0.69, -1.00	
Path attenuation	Q	220	
Site attenuation	κ_0 (s)	0.005	
Source duration	T_s (s)	$1/0.4906\beta(\Delta\sigma/M_0)^{1/3}$	SI units
Path duration for sub-fault signals	T_p [R (km)]	$T_{5,75}/0.383$	V3 Groningen $T_{5,75}$ model for M = 3.0, $V_{s30}=1500$.
Rise time	T_s (s)	1/ f_0	
Site amplification	A(f)	Network average NS_B modified by iRVT to reduce bias	
Dynamic, pulsing percentage		50%	
Sub-fault averaging		RMS	
Scaling		(Acceleration FAS) ²	

In terms of the logic-tree branch weights (summarised in Section 5.1), we found no reason to change the branch weights used in the V5 GMM since the rationale still holds. A small weight (10%) is assigned to the lowest branch, since there is relatively low confidence that such low values of the stress parameter would persist across the range of magnitudes considered, although the shallow focus of the events that would be expected to initiate within the gas reservoir means that such a possibility cannot be excluded. There is no real basis to then discriminate among the remaining three branches in terms of their likelihood of being the best representation of the nature of future earthquakes of magnitude greater than those that have been observed in the Groningen field to date. Consequently, the three upper branches are all treated as being equally likely and are each assigned a weight of 0.3.

3.3. Regressions on NS_B simulated motions

The parametric GMPEs for $S_a(T)$ and PGV at the NS_B were derived in exactly the same way as in the V5 model, performing simple regressions on the simulated motions. The functional form relating these ground-motion parameters to M_L and the rupture distance is identical to that used for the V5 model, including the values of the hinging magnitudes for the changes in scaling and the hinging distances that control the changes in spreading functions.

The functional forms and their coefficients are all presented in Section 5.1 of this report. The equations are presented only in Chapter 5 to avoid unnecessary inflation of the length of the report and to thus provide a complete description of the GMM in a single section, for the convenience of potential users. As noted in Section 5.1, the full set of coefficients for these equations—and all other numerical values required for the implementation of the model, including the site amplification zonation model described in Chapter 4—is provided in an electronic supplement to this report. For the reader looking for the information required to implement the V6 GMM, without explanation for its derivation or justification of the modelling choices, Chapter 5 provides a stand-alone summary.

Figures 3.8 and 3.9 show plots of the outcomes from the regression against the simulations, for $S_a(0.01s)$ and the lower central stress drop branch (the results for all other branches are very similar). The figures illustrate how well the regression fits the simulated motions at the NS_B horizon over the full range of magnitudes and distances for which the simulations were performed.

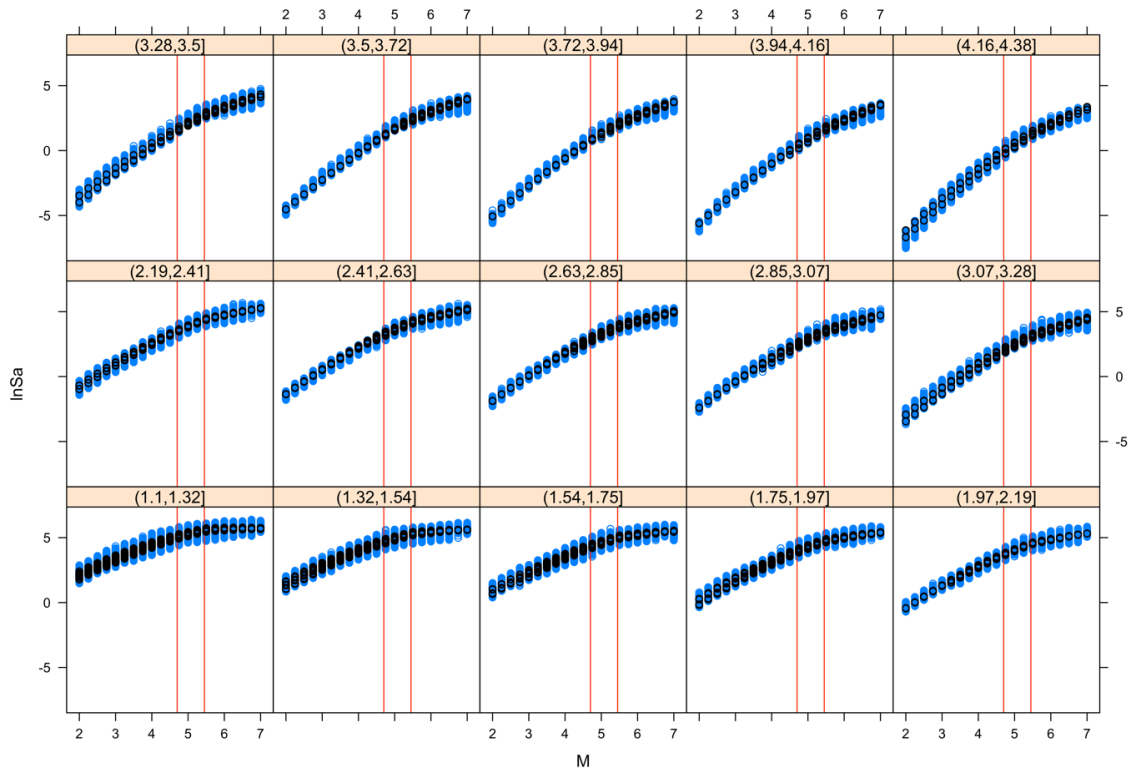


Figure 3.8. Comparison of regression results (*black*) with EXSIM simulations (*blue*) for PGA for different distances (ranges indicated by natural logarithmic values in the header of each frame) against magnitude. Results shown for the lower central branch.

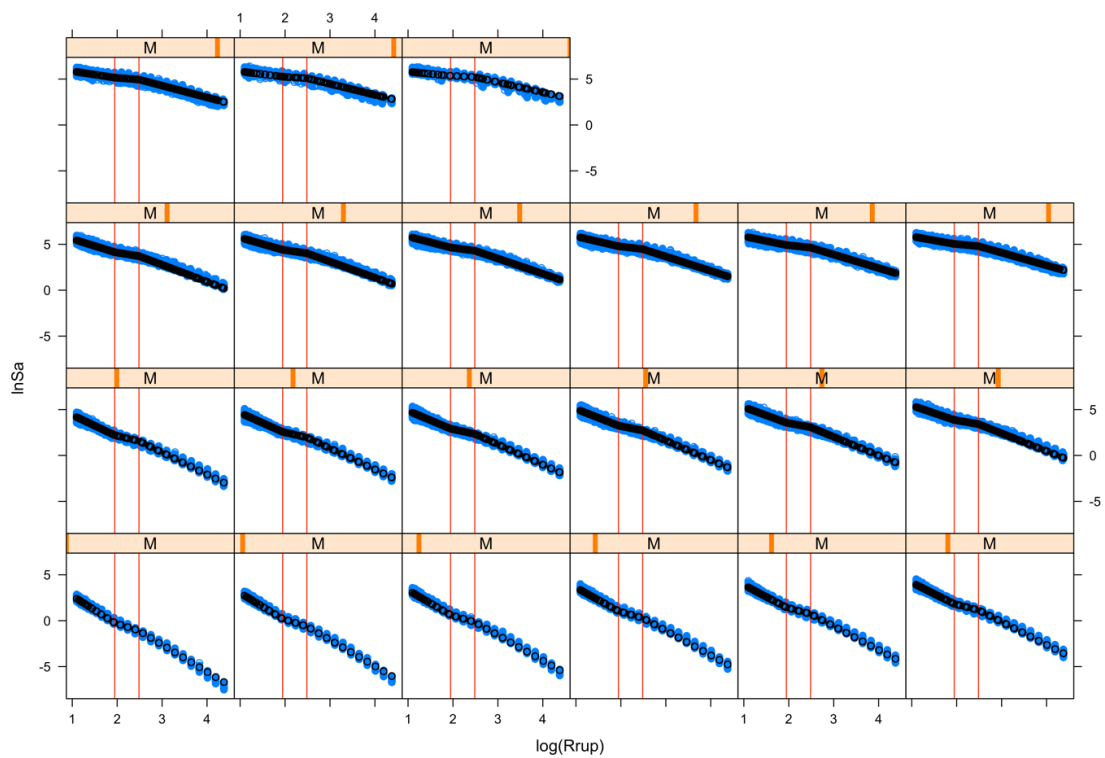


Figure 3.9. Comparison of regression results (*black*) with EXSIM simulations (*blue*) for PGA for different magnitudes (indicated by thick orange bars in header, with M increasing left to right) and $\ln(\text{distance})$; vertical lines indicate control point change of spreading function. Results shown for the lower central branch.

3.4. Aleatory variability model

The complete GMPEs for predicting ground-motion amplitudes at the NS_B horizon comprise the equations for the median values of these amplitudes, and the associated aleatory variability. As for the V5 model, the overall variability for Groningen motions is constructed using a combination of empirical constraint from data obtained in the Groningen field along with estimates of partially non-ergodic within-event variability based upon global tectonic databases; we note that the Groningen GMM is partially non-ergodic (single-station) at the NS_B horizon but fully ergodic at the surface because of the way site response uncertainty is currently modelled. The total variability that is computed for the hazard and risk calculations combines between-event variability (τ), within-event variability (ϕ_{SS}), component-to-component variability (σ_{c2c}) and between-site variability (ϕ_{S2S} , which includes the variability in site response). Rather than define epistemic uncertainty for each component of the variability model, we define branches on the single largest contributor, and this corresponds to the externally constrained branches on non-ergodic within-event variability. It is important to note that this does not imply that epistemic uncertainty is ignored in other components of the variability model, we just choose to represent epistemic uncertainty in the total variability through branching on ϕ_{SS} . The ϕ_{S2S} model is described in Section 4.2; the other three components of the variability model are presented in the following paragraphs.

The process followed to determine the between-event standard deviation is similar as that for the V5 model. Once the median model predictions at the NS_B horizon were determined, these model predictions were used to compute total residuals of the Groningen data. The total residuals are then partitioned into components using an advanced mixed effects regression approach that accounted for spatial correlation, as well as crossed random effects for repeatable event and site effects. The effect of magnitude uncertainty is then accounted for in a second step, by identifying the influence of propagating the magnitude uncertainty through the median NS_B ground-motion model, and then removing the associated variance from the between-event variance obtained in the regression analysis. This adjustment process is represented by the following equation:

$$\tau_{adj}^2 = \tau_{raw}^2 - \left(\frac{\partial \ln Sa}{\partial M}\right)^2 \sigma_M^2 \quad (3.4)$$

A more elaborate discussion of the approach taken, as well as the underlying mathematical framework, is provided in the V4 GMM report (Bommer *et al.*, 2017b, p.115).

The mixed-effects regression procedure was applied to each of the four model branches and the results obtained for the raw between-event variability (prior to making the magnitude correction) in each case are shown in Figure 3.10. The

required magnitude correction is period-dependent, and also depends upon each stress parameter branch. The computed magnitude correction is shown in Figure 3.11.

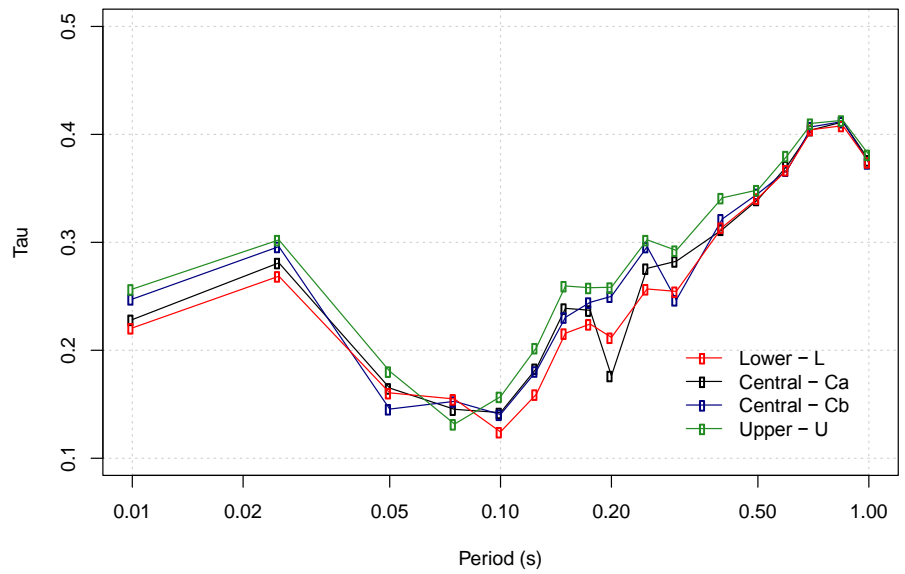


Figure 3.10. Estimates of the raw between-event standard deviation for each of the four branches at the NS-B horizon

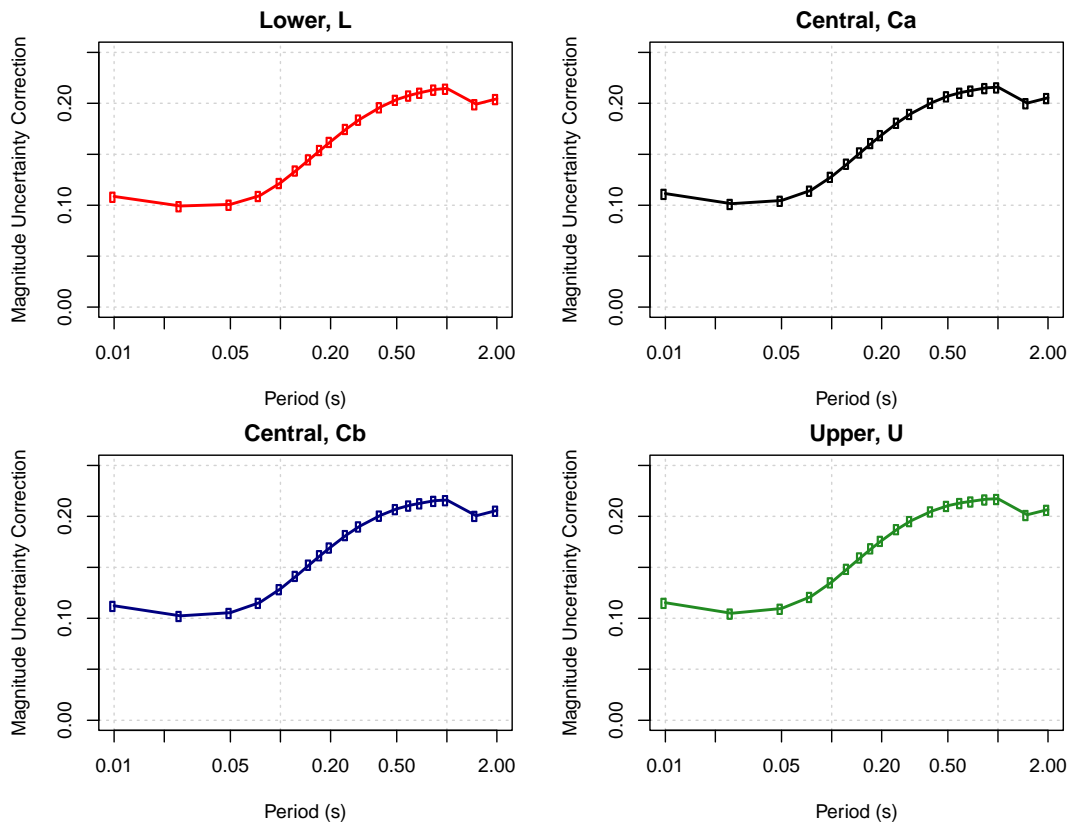


Figure 3.11. Standard deviation associated with magnitude uncertainties as a function of response period for each stress parameter branch.

The functional form for the between-event variability model in V5 was partly motivated by theoretical considerations regarding how stress parameter should influence between event variability. This leads to a period dependence of between-event variability that includes a localised reduction in between event variability at around 0.1 seconds. The regression analysis for the V6 model again reveals this period-dependence (as previously seen in Figure 3.10). However, as the NS-B median model has an implicit magnitude dependent stress parameter there is reason to believe that this reduction in the between-event variability will not remain localised at the position shown in Figure 3.10 for all magnitude scenarios relevant for the hazard and risk calculations. For that reason, in the V6 model, a new functional form for the between-event variability is adopted that starts from a relatively low value of τ at short periods, remains flat through the region where the localised reduction is empirically observed, and then increases at longer periods. This period-dependence is more aligned with models of τ from larger databases where a greater range of magnitudes (and stress drops) are represented.

The functional form for τ is a continuous function of response period as shown in Eq.(3.5):

$$\tau(T) = \tau_{LOW} + \frac{\Delta\tau}{1 + \exp\left[-\tau_S \ln\left(\frac{T}{\tau_C}\right)\right]} \quad (3.5)$$

To obtain the four parameters of this model, the functional form was fit to the magnitude-corrected τ_{adj} values using only periods $T \leq 0.025$ and $T \geq 0.15$ in order to ignore the effect of the localised reduction near $T \approx 0.1$ seconds. The resulting set of parameters is defined in Table 3.2.

Table 3.2. Parameters of the between-event standard deviation model

Branch	τ_{LOW}	$\Delta\tau$	τ_C	τ_S
Lower, L	0.1795	0.1522	0.4453	6.6849
Central, Ca	0.1810	0.1547	0.4510	5.8557
Central, Cb	0.2051	0.1271	0.4750	7.6859
Upper, U	0.2218	0.1169	0.4640	6.1842

The values of the between-event standard deviation for the V6 model have therefore changed from those in the V5 model, as shown in Figure 3.12. For most periods of primary interest in the risk model for Groningen, the between-event standard deviations have decreased (or are similar), while at the longest periods there is a slight increase.

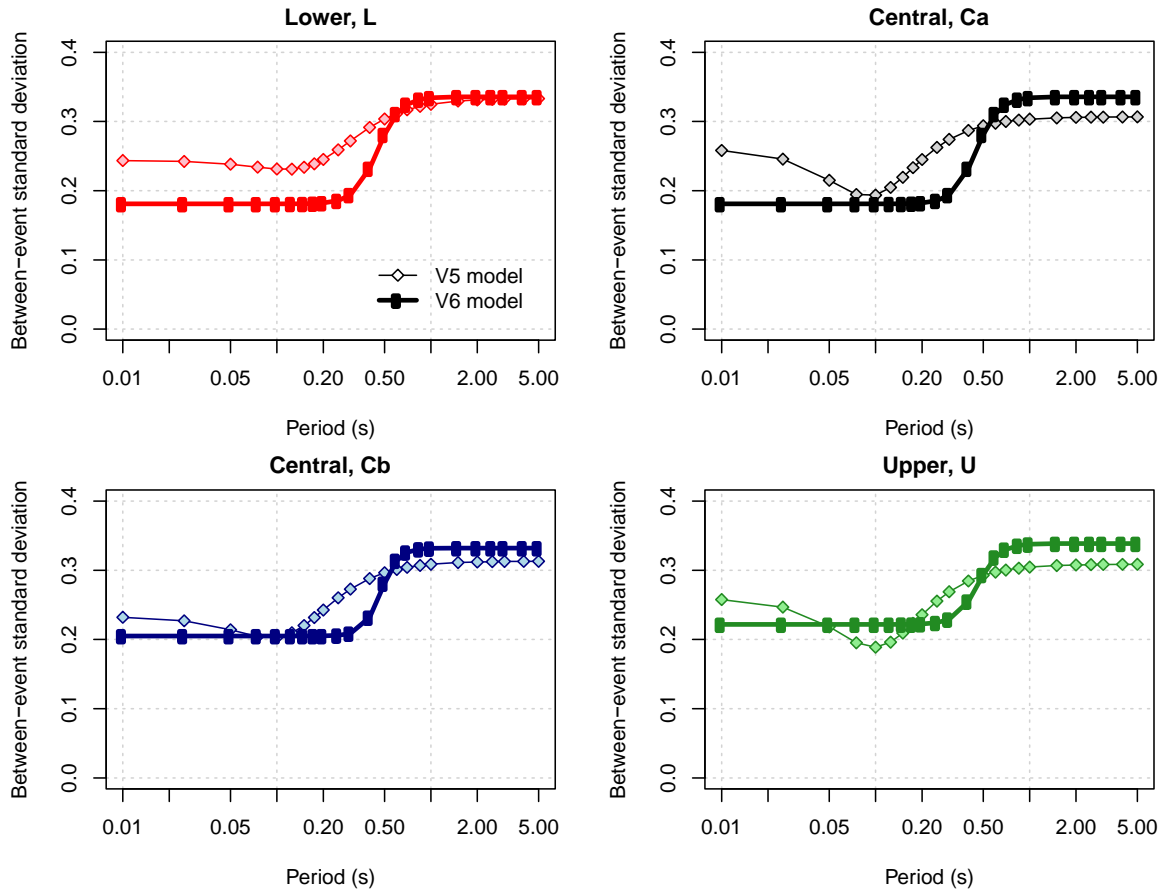


Figure 3.12. Comparison of the τ values for the V5 and V6 models

As noted previously, while estimates of the between-event variability are constrained directly using the empirical data from the Groningen field, the ϕ_{SS} values are constrained using externally-developed models, and branching is applied to this parameter in order to capture epistemic uncertainty in the overall variance model. The model for ϕ_{SS} remains unchanged from the V5 GMM; the original rationale for this model was presented in the V4 GMM report (Bommer *et al.*, 2017b). However, while we externally constrain these ϕ_{SS} values, we also check those values against empirical estimates derived from the Groningen data. Figure 3.13 shows a comparison between the values of ϕ_{SS} adopted for the V4 and V5 GMM (and retained again for the V6 model), and estimates obtained from the Groningen data using two different regression strategies. In Figure 3.13 the effect of either ignoring or considering spatial correlation during the variance decomposition is shown. Results referred to as ‘ES’ consider random effects for each earthquake and recording station, while those referred to as ‘ESX’ also consider the spatial correlation within the field. As ground motions are spatially-correlated and the empirical data includes a relatively large number of observations over a small spatial area, correlated motions spatially can appear as systematic event offsets. Considering the spatial correlation therefore reduces the apparent between-event variability as shown in the upper panel of the figure.

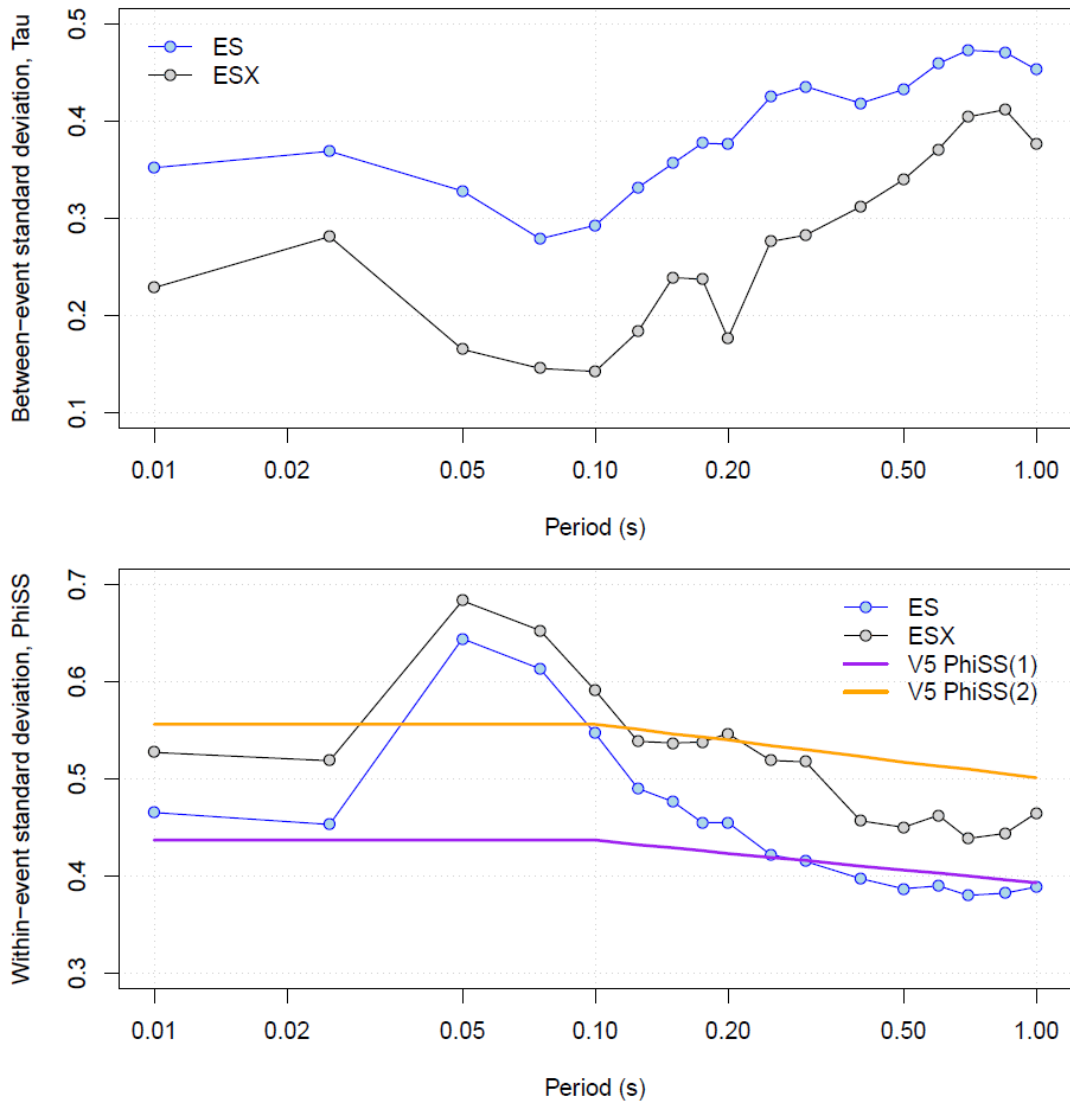


Figure 3.13. Comparison of estimates of variance components obtained using different regression strategies. The upper panel shows raw estimates of the between-event standard deviation, while the lower panel shows estimates of the event- and site-corrected within event standard deviations. The lower panel also compares these estimates with the externally-constrained values of ϕ_{SS} adopted in the V5 and V6 GMMs. Estimates labelled 'ES' correspond to crossed mixed effects formulations accounting for random event and site terms. Those labelled 'ESX' also consider spatial correlation in addition to the crossed random effects.

The lower panel of Figure 3.13 shows that the externally-constrained estimates of ϕ_{SS} are reasonably consistent with the cases where spatial correlation is either considered or ignored in the regression. As there is a trade-off between the event terms and the degree of spatial correlation (as noted above) the epistemic uncertainty assigned to ϕ_{SS} is partially accounting for our inability to truly know how much of the event-to-event variation is arising from systematic source effects versus spatially correlated ground-motions. It is also worth noting that where the empirical and externally-constrained ϕ_{SS} estimates diverge (at around 0.05 seconds) this is

probably related, at least in part, to the empirical estimates of the spatial correlation length (obtained directly within the regression analysis) being longer than the more robust results obtained in the more concerted study of spatial correlations undertaken by Stafford *et al.* (2019). This is shown in Figure 3.14. The greater correlation lengths lead to a greater apparent reduction in the aleatory variability and this needs to be offset by larger values of ϕ_{SS} – as seen in Figure 3.13.

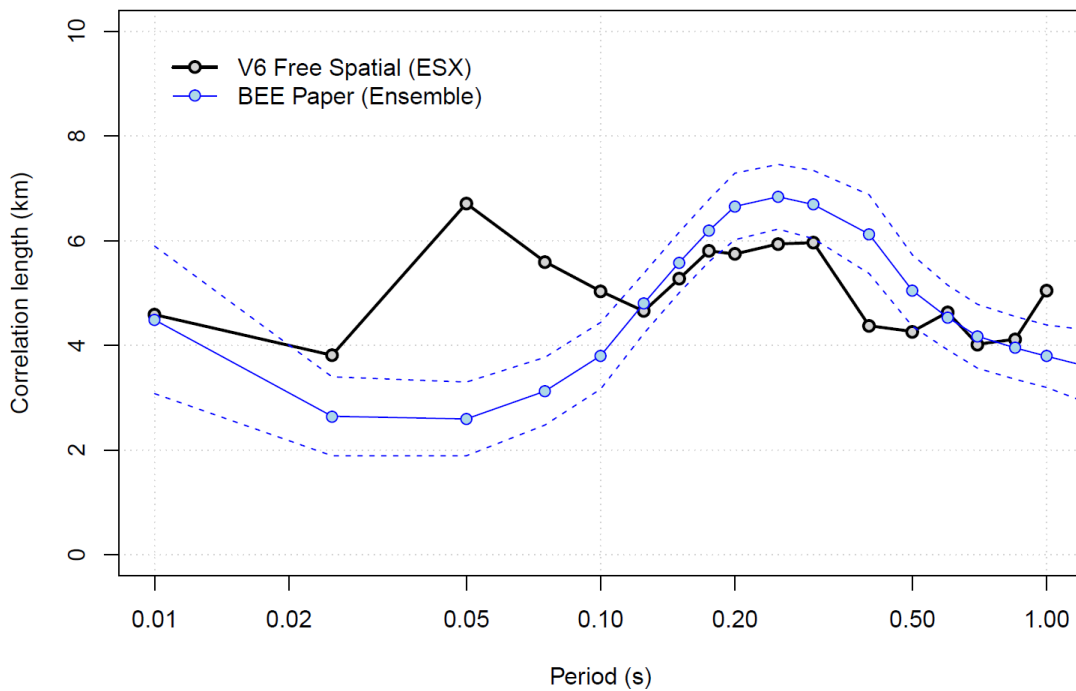


Figure 3.14. Comparison of the correlation lengths estimated directly within the variance decomposition of the Groningen data (V6 Free Spatial) with the model estimates obtained from an extended database and various methods in the study of Stafford *et al.* (2019).

The ϕ_{SS} values adopted for the V5, and now the V6, GMM have the advantage over the empirical estimates from the Groningen field that they are based upon much larger databases that cover a far wider range of magnitude and distance scenarios.

One of the observations of the international review panel regarding previous versions of the GMM was that there appeared to be evidence to support distance-dependence in the ϕ_{SS} model. Such a model was considered by Rodriguez-Marek *et al.* (2013) who observed that there might be larger values of ϕ_{SS} at short distances but also noted that the data at short distances was sparse and that the apparent increase in spatial variability could easily result from poorly constrained metadata. Distance-dependent models for ϕ_{SS} have not been widely adopted or applied in practice. Figure 3.15 shows a plot of decomposed residuals of Sa(0.1s) from the V5 GMM report, which does suggest greater variability at short distances, although it needs to be borne in mind that there is more data at short distances (an unusual

feature of the Groningen ground-motion dataset). A final decision was taken, however, not to introduce distance dependence into the ϕ_{SS} model, primarily because it is already accounted for, indirectly, through the model for component-to-component variability (σ_{c2c}).

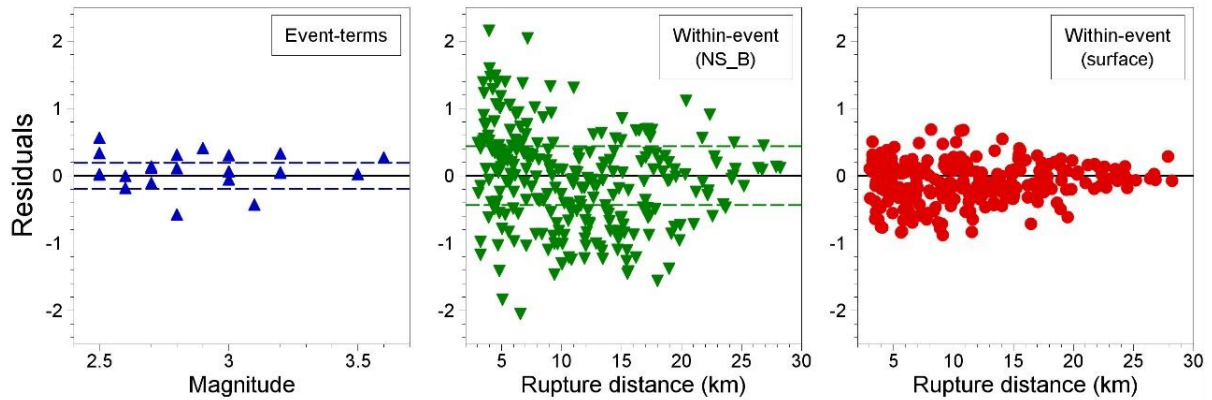


Figure 3.15. Total surface residuals of $Sa(0.1s)$ from the V5 study decomposed into event-terms (*left*), within-event residuals at the NS_B (*centre*) and within-event residuals at the surface (*right*)

The component-to-component variability model developed for the V5 GMM and summarised in Stafford *et al.* (2019) is required to transform the geometric mean horizontal component accelerations to the arbitrary horizontal component used in the risk calculations. This model includes a very pronounced dependence on distance, with large values of σ_{c2c} at short distances—for smaller magnitude earthquakes—and this component of variability is added to the within-event variability. Consequently, in the risk calculations, there is already an appreciable dependence on distance in the within-event variability.

4. Site Response Zonation

The site amplification model adjusts the ground-motion predictions at the NS_B horizon to the ground surface. The framework of the V6 site response model—including the field zonation—is very similar to that of the V5 model. The first section of this chapter summarises the input motions defined at the NS_B horizon and the execution of the site response calculations. The second section then presents the zonation of the field and the non-linear amplification factors for Sa(T) and PGV in each of the zones.

4.1. Input rock motions and site response analyses

A new set of 3,600 input motions at NS_B was used as input motions for the STRATA site response calculations. The site response analyses were conducted using random vibration theory (RVT) option. The input motions were defined by their FAS and their duration. These motions span a range from **M** 1.5 to 7.5 with steps of 0.1 up to **M** 5.0 (**M** 1.5-5.0) and then **M** 5.25, 5.5, 5.75, 6.0, 6.25, 6.5, 7.0, 7.25 and 7.5. The rupture distance ranges from 3.0 to 60 km in 20 log-spaced steps. These ranges enable the derivation of the magnitude and distance dependence of the AFs (Section 4.3). The derivation of the new FAS motions is described in Chapter 3.

The ground motion durations used in the STRATA analyses were adjusted from the duration of the simulated signals from EXSIM (D_{75-5}) such that the PGV of the input FAS motion in the RVT-FAS analysis using STRATA corresponded to the PGV of the simulated time signals. The corrected duration D_{corr} was derived for GMM V5 (Bommer *et al.*, 2018) and is given by:

$$D_{corr} = \frac{D_{75-5}}{0.64} \quad (4.1)$$

The significant durations for the corresponding magnitudes in V5 and V6 are practically identical. This correction produces PGVs in STRATA that are a few percent too low for low ranks (the FAS are ranked in order of their associated PGA) and a few percent too high for high ranks, apart from the strongest motions (maximum 16%). The median relative difference between PGVs from EXSIM and PGVs from corrected durations in STRATA for all ranks is 0%. As in previous versions of the GMM, the motions were ranked according to their PGA and subsequently divided into 10 groups. The FAS motions per group are shown in Figure 4.1. One motion per group of ranked motions was randomly selected as input motion for each voxel stack, corresponding to 10 STRATA calculations per voxel stack. All motions are sampled approximately evenly across the whole field (Figure 4.2). Each motion has been sampled 391 ± 19 on average.

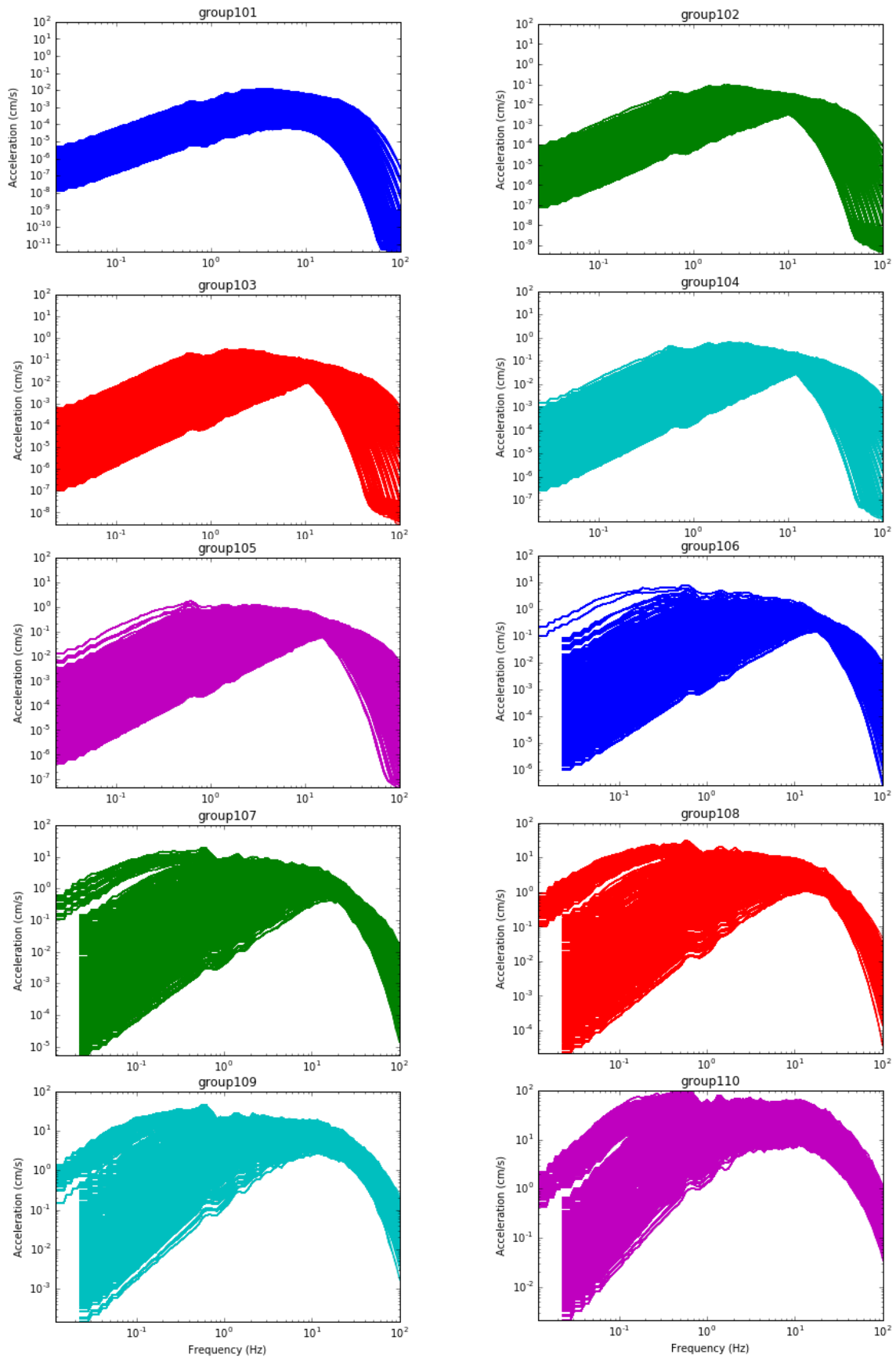


Figure 4.1. FAS generated at the NS_B horizon for use in RVT-based site response analyses.

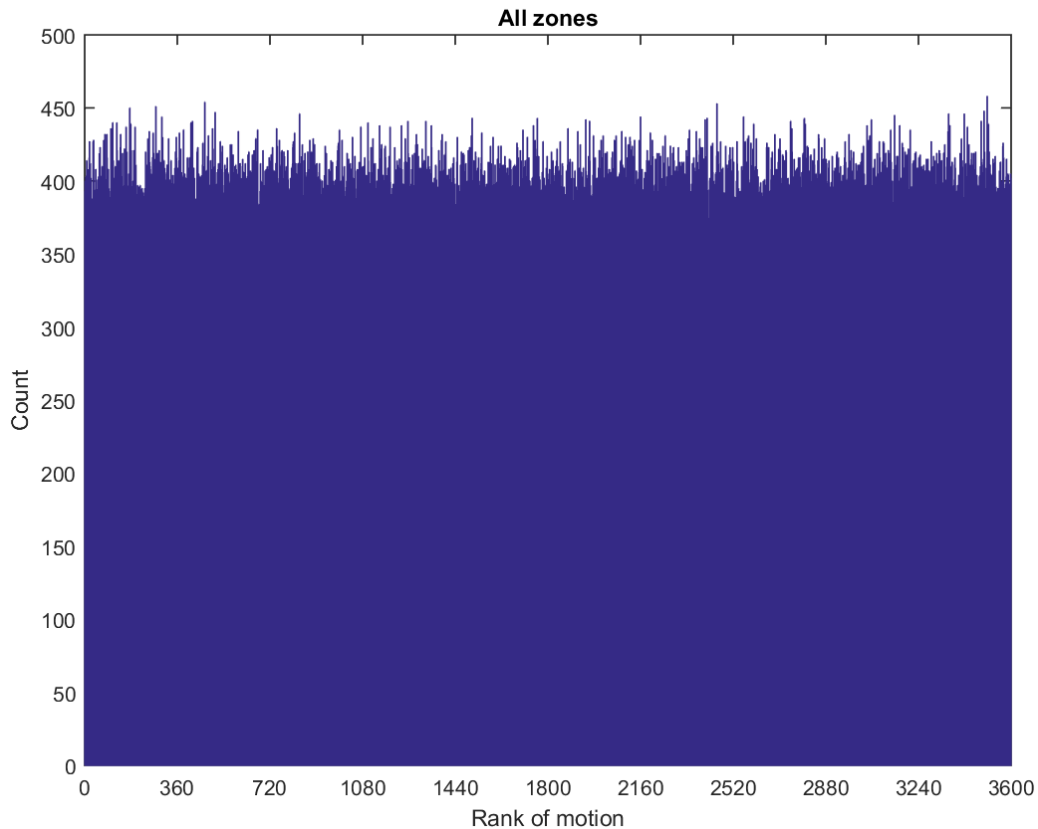


Figure 4.2. Histogram of sampling of the 3,600 NS_B FAS in the site response analyses over the whole field.

The site response analyses were performed according to the same set-up as for GMM V5 (Bommer *et al.*, 2018). The input parameters consisted of the updated soil columns and low-strain damping (Section 2.3), new input motions (Section 4.1) and the V5 geomechanical lookup table (Bommer *et al.*, 2018).

4.2. Zonation and amplification factors

The zonation of the Groningen region has been stable through the various versions of the GMM and only small adjustments were made. These adjustments are made based on the computed AFs for the voxel stacks. Two adjustments were made between V5 and V6: for V5 Zone 606 in the north is partitioned into Zones 631 and 632 in V6 and V5 Zone 3321 in the south is partitioned into Zones 3322 and 3323 in V6. The new zonation is shown in Figure 4.3 and the justification for these partitions is given in the following paragraphs, including detailed figures of the changed zones in Figures 4.4 and 4.5.

In the V5 Zone 606, there is a clear difference in AF behaviour between the east and the west part of this elongated zone (Figure 4.4). This division is consistent between

periods of 0.1 to 0.3 s and therefore present in the period range that is relevant for the types of buildings in Groningen. In this case, the dividing boundary between east and west is clear and easy to infer. Because of these reasons, the zone was split in two, creating two new V6 zones: 631 and 632.

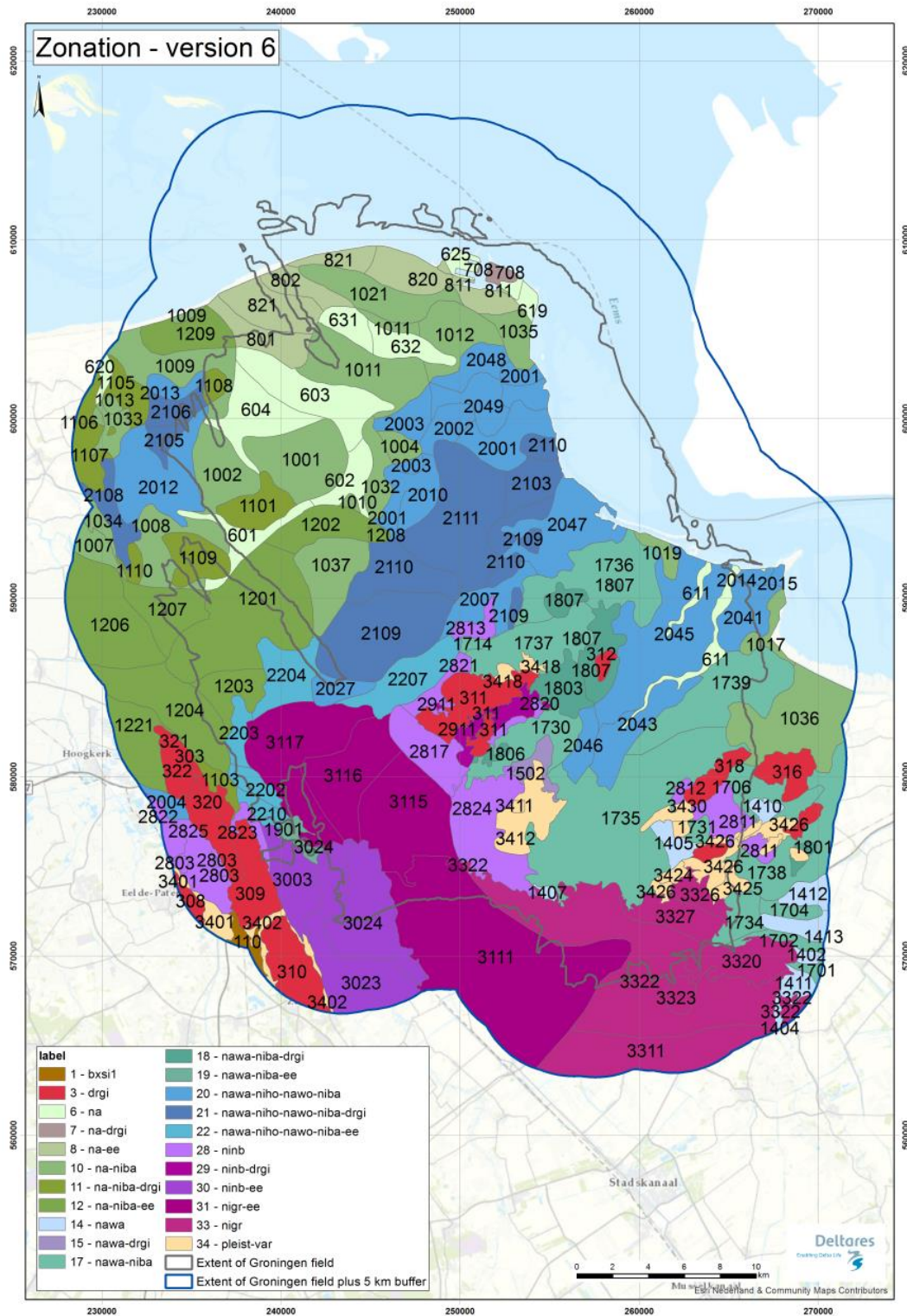


Figure 4.3. Updated zonation for V6.

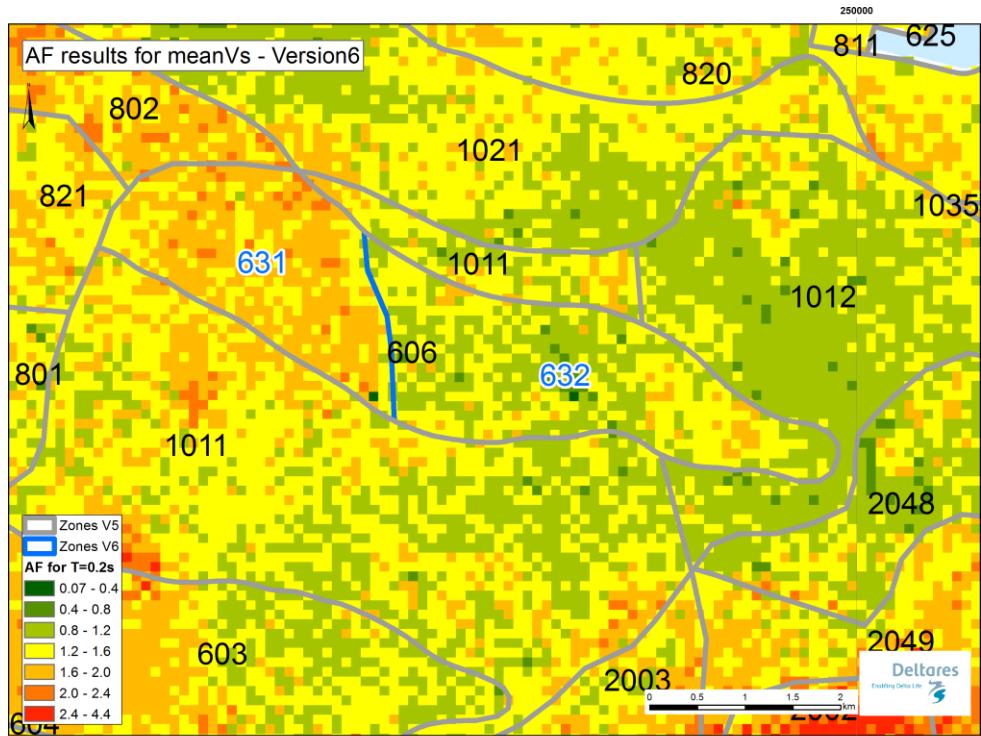


Figure 4.4. AFs for period $T = 0.2$ s for zones in the north of the Groningen field, focussing on V5 Zone 606. The V5 zonation is indicated by grey lines and black fonts, the new V6 split in blue lines and blue fonts. The colour scale shows the AF for each voxel stack for motions ranked 1 to 360 (group 101 motions) and mean V_s profiles.

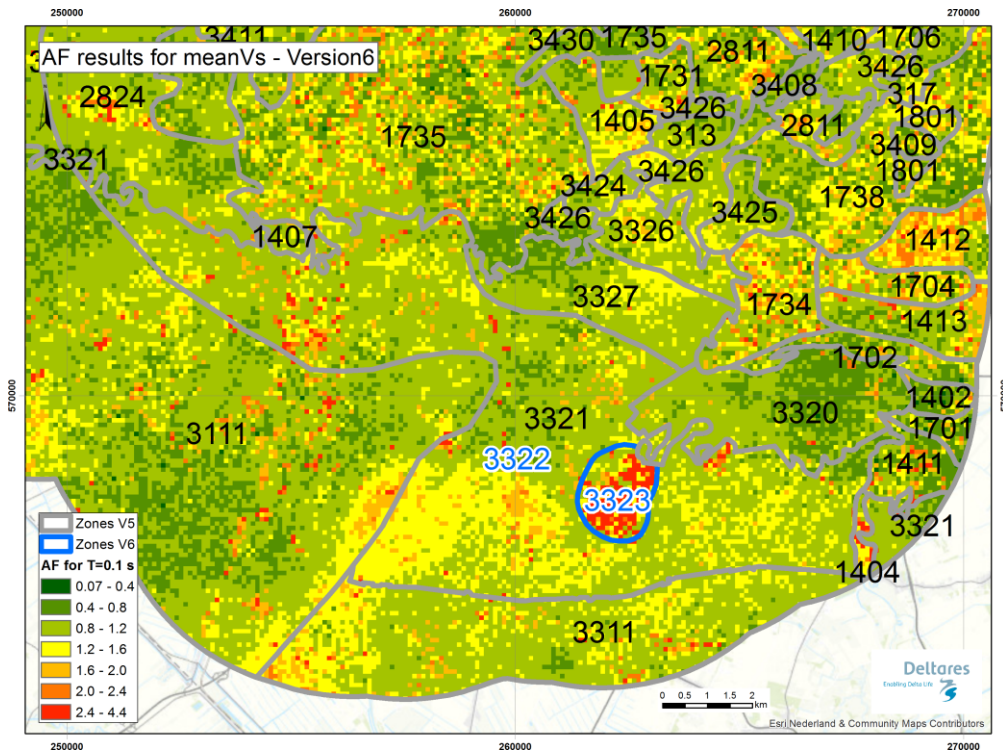


Figure 4.5 AF for period $T = 0.1$ s for zones in the south of the Groningen field, focussing on V5 Zone 3321. The V5 zonation is indicated by grey lines and black fonts, the new V6 split in blue lines and blue fonts. The colour scale shows the AF for each voxel stack for motions ranked 1 to 360 (group 101 motions) and mean V_s profiles.

In V5 Zone 3321, there is a distinct region of anomalously high AF relative to the surrounding voxels (Figure 4.5). This region had been identified before and was defined as a separate zone in previous versions of the model. However, in V4 and V5, the region was included in the large Zone 3321, because the AF behaviour was not consistent among periods. We revisited this decision in V6. The region stands out as a region of relatively low V_{S30} and relatively high AF for $T = 0.1$ s. There are buildings present in this zone and they are right on the border between the lower/higher V_{S30} and higher/lower AF. These are small buildings, probably sensitive to the shorter periods (~ 0.1 - 0.2 s). In order to avoid underestimation of AF in this small region, it was included as a separate zone in V6.

Although in the absence of a duration prediction model, V_{S30} is not a parameter that is directly used in the hazard and risk calculations, for completeness Figure 4.6 shows a map of median V_{S30} in the V6 zonation model.

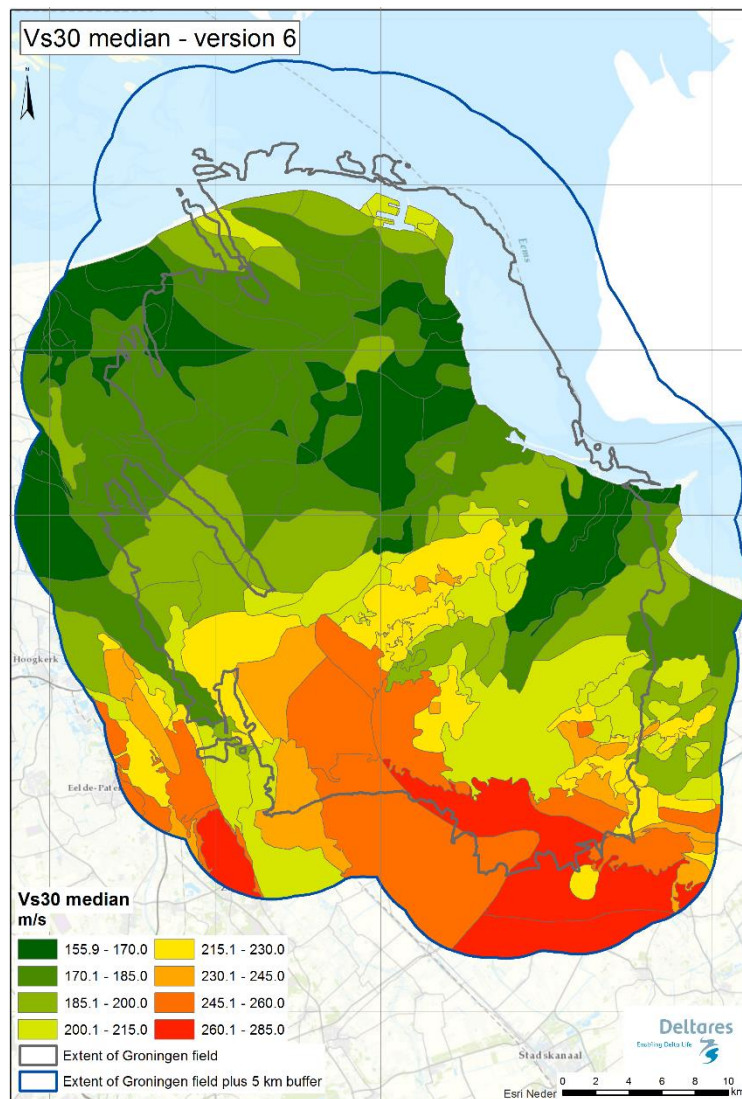


Figure 4.6. Median V_{S30} values in V6 zonation

The model for the AF for the zones is the same as the model used in GMM V5 (Bommer *et al.*, 2018). Magnitude and distance dependence is included for the elastic AFs, as suggested by Stafford *et al.* (2017). The model for the site-to-site variability (ϕ_{S2S}) is also the same as that used in the GMM V5 model. The regressions described in Bommer *et al.* (2018) were repeated using the newly computed AFs to compute the parameters of the AF and ϕ_{S2S} models. The upper and lower limits on the AFs and the ϕ_{S2S} were also maintained from the V5 model (these are explained in detail in the GMM V4 report; Bommer *et al.*, 2017b). Figure 4.7 shows the AFs for all the zones in the Groningen field for a fixed scenario (M 4.5 and R 5 km) and selected periods. These AFs can be compared with the V4 AFs shown in Figure 9.5 of the V4 GMM report (Bommer *et al.*, 2017b) and the V5 AFs shown in Figure 4.9 of the V5 GMM report (Bommer *et al.*, 2018). Figure 4.8 plots the ratios of AFs of the V6 and the AFs of the V5 model. In general, the AFs for V6 are slightly lower than those for the V5 GMM because of the overall increase in damping in the profiles (Section 2.3). An exception are AFs for very short periods ($T=0.025$ s and $T=0.05$ s) and a combination of low magnitude and short distance, which for are on average larger in the V6 model. Also, as expected, larger differences are seen at lower periods, which are more affected by damping.

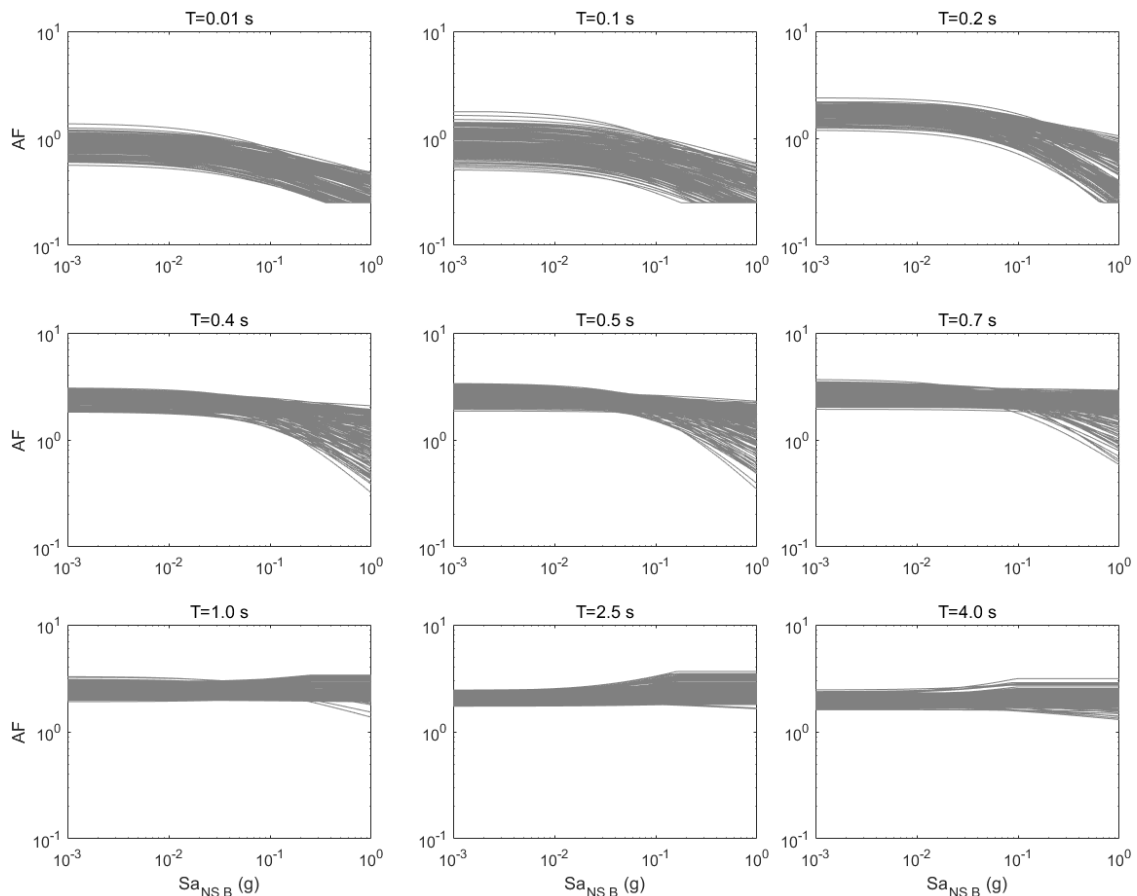


Figure 4.7. Fitted AF functions for all zones for select periods (for M=4.5 and R=5 km). Note that lower and upper limits are imposed for short- and long-periods, respectively.

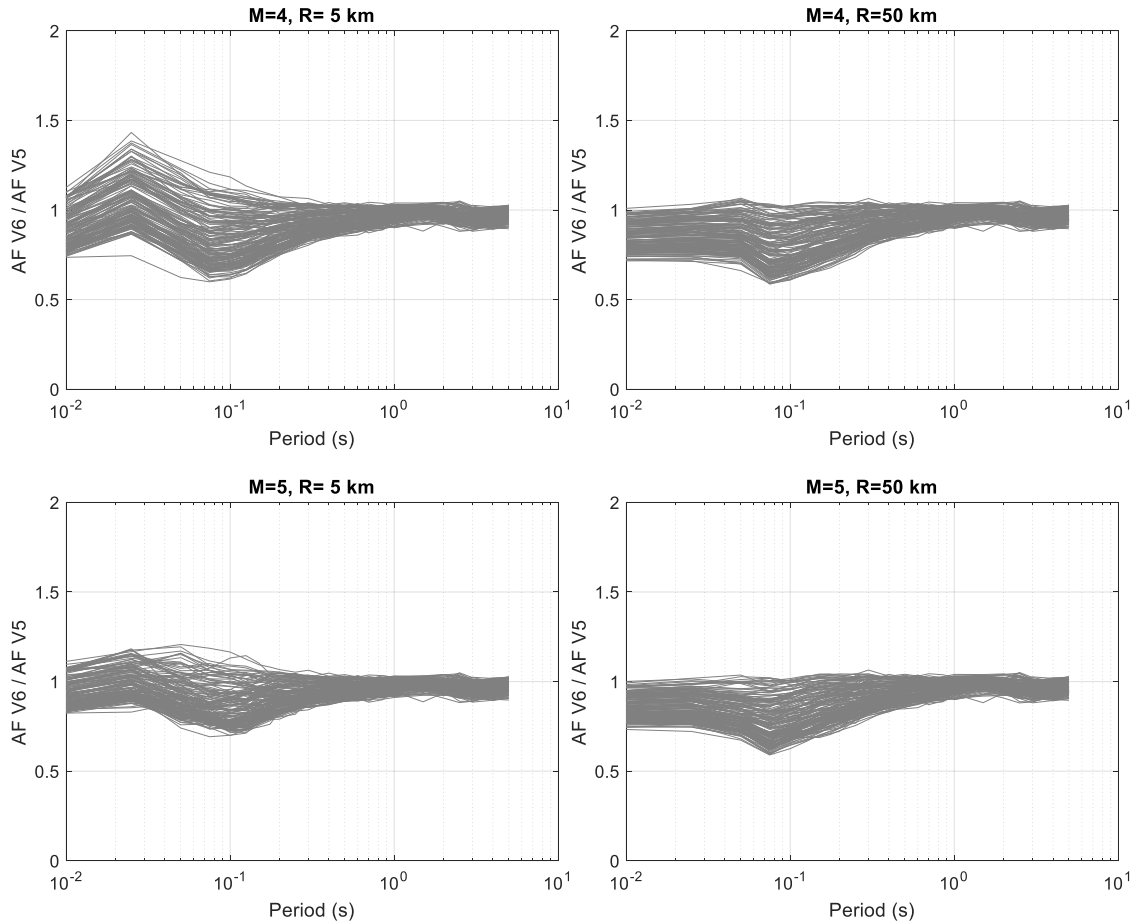


Figure 4.8. Ratios of AFs of V6 GMM over V5 GMM for all the zones. Each plot corresponds to a selected magnitude/distance combination. Spectral accelerations at rock were selected using the V5 GMM rock model.

Figure 4.9 shows the AFs for all the zones in the Groningen field for a fixed scenario ($M = 4.5$ and $R = 5$ km) and selected periods. While the values of the AFs are slightly lower than in the GMM V5 model (see Section 6.1), the spatial distribution of AFs is similar to that observed in previous versions of the model (e.g., Figure 9.18 in Bommer *et al.*, 2017b and Figure 4.10 in Bommer *et al.*, 2018).

An additional check for the model validity is that the AFs computed for a station should fall within the range of variability of the AFs computed for the zone where the station lies. This check is shown in Figure 4.10, which plots the difference between zone and station AFs for a selected set of magnitude and distance combinations that fall within the range of the recordings at the Groningen field. The AFs computed for the stations have in general stronger magnitude and distance dependence, which is seen as a wider spread of the difference in AFs for shorter periods for different scenarios. For the two stations shown in Figure 4.10, the differences are in general within two standard deviation of the zone AFs. In general, the AFs for the zones are slightly lower than the AFs for the station at shorter periods, and are similar for longer periods ($T > 0.1$ s).

The values for site-to-site variability for GMM V6 are nearly the same as those for the GMM V5. A comparison of these values is shown in Figure 4.11. The spatial distribution of these values is shown in Figure 4.12. The spatial distribution of these values is similar to the distribution in the V5 GMM (see Figure 4.13 in Bommer *et al.*, 2018).

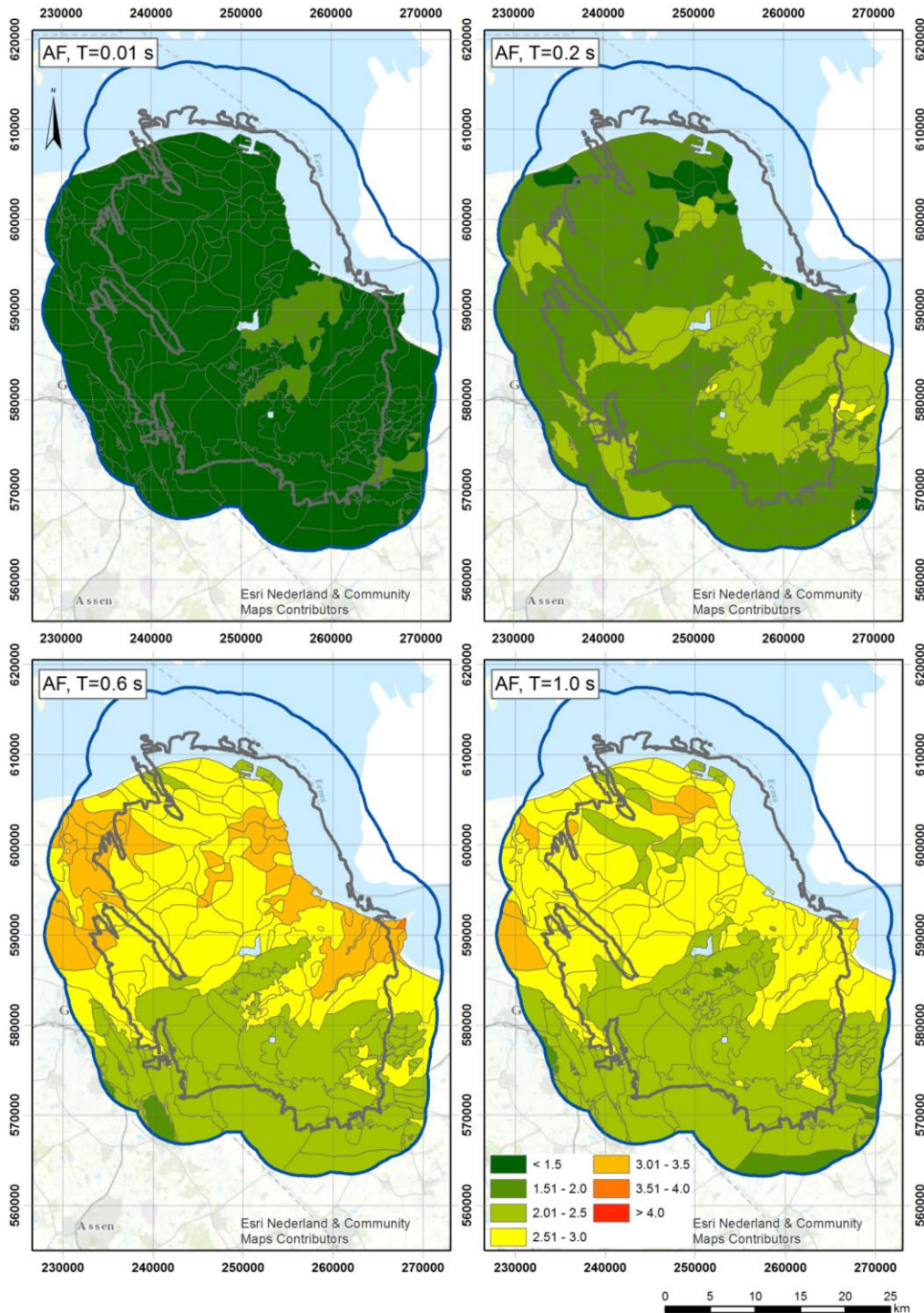


Figure 4.9. Weak motion AFs (e^{f1^*}) for the zones in the Groningen region. The AFs are shown for an M 4.5, R 5 km scenario and selected periods.

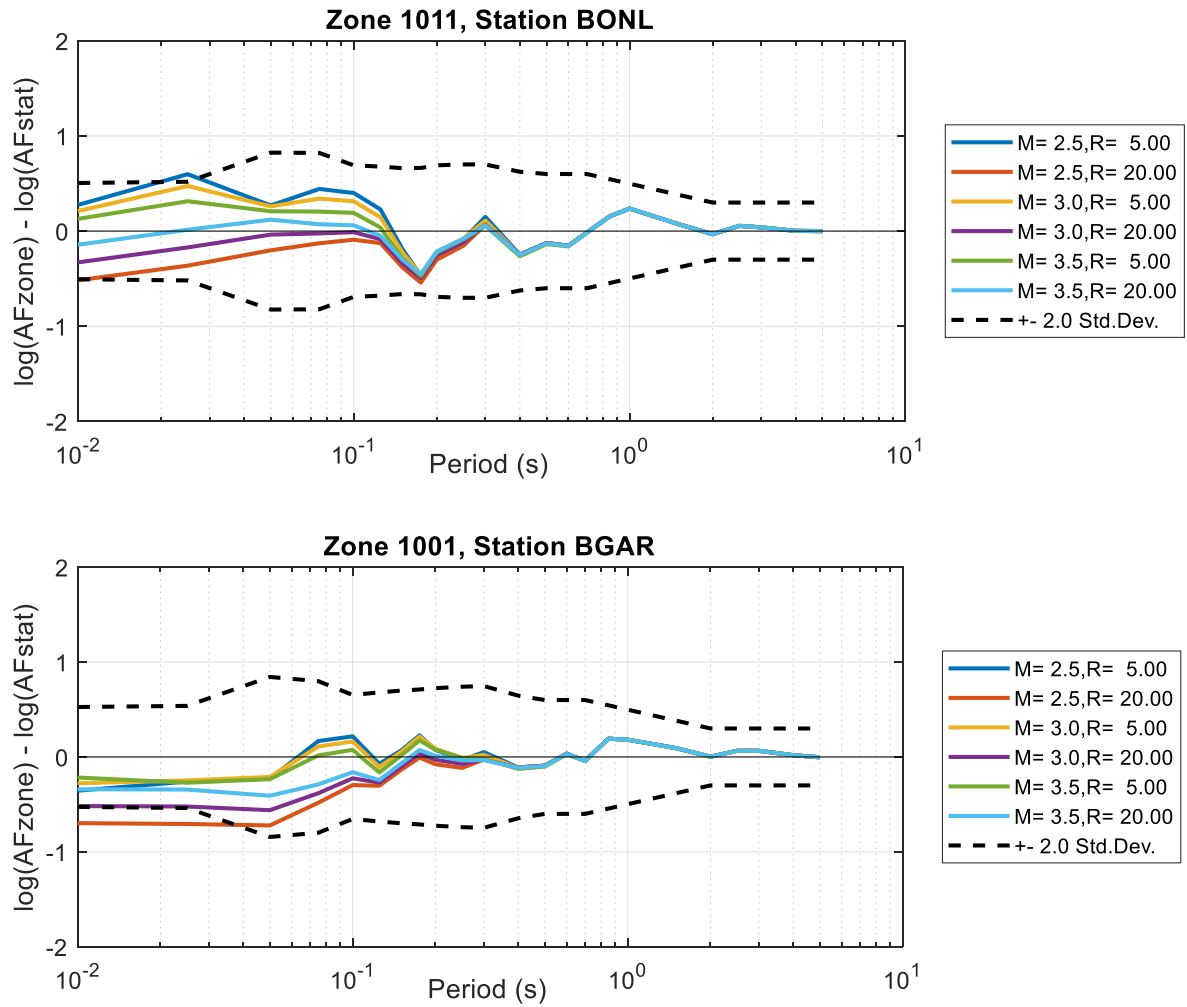


Figure 4.10. Comparison of linear AF for selected stations and the corresponding zone where the station is located. AFs are shown for selected magnitude and distance pairs that correspond to the range of recorded motions in the Groningen field. Similar plots for all other B-station recordings are given in Appendix III.

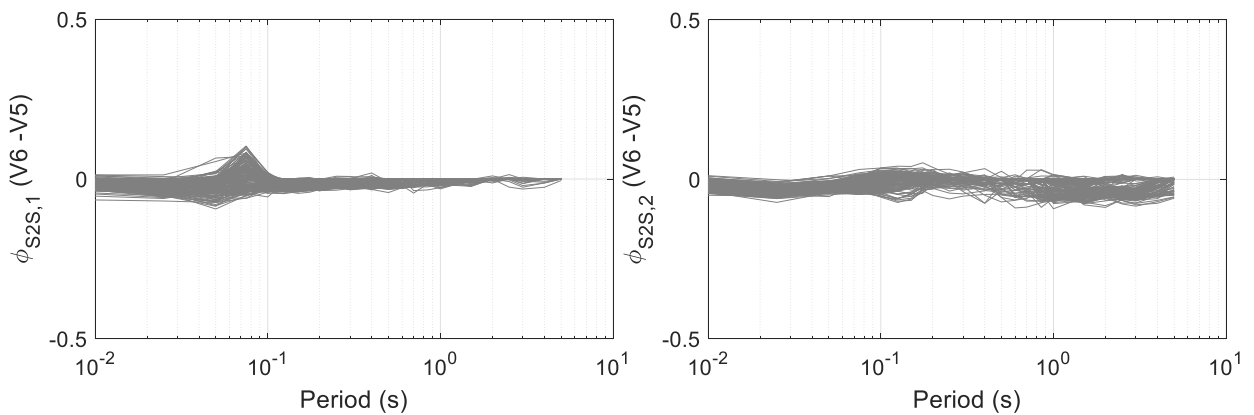


Figure 4.11. Difference in ϕ_{S2S} values between the V6 GMM and the V5 GMM. The plot on the left is for low intensity values ($\phi_{S2S,1}$), and the plot on the right is for high intensity values ($\phi_{S2S,2}$).

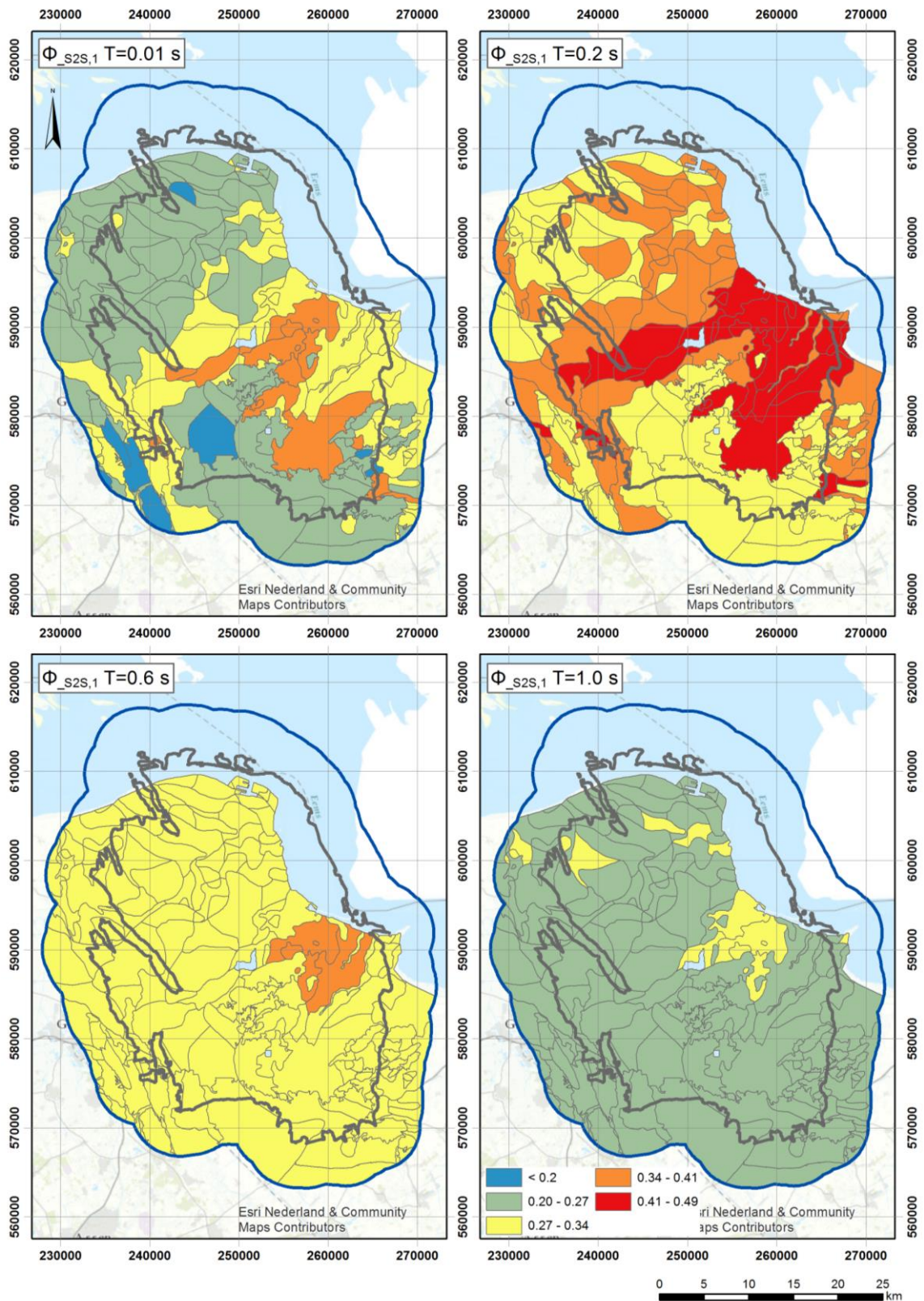


Figure 4.12. $\phi_{s2s,1}$ values for selected periods and for all zones in the Groningen region.

5. MODEL SUMMARY and IMPLEMENTATION

As noted in Chapter 1, this chapter provides a concise summary of the complete model for those interested in its implementation. This means that some information is repeated from previous chapters but for the convenience of the user, the complete model is presented here in its entirety. Section 5.1 presents the basic model elements, including the equations and their coefficients, as well as identifying all of the electronic supplements where the model parameters are listed; in previous GMM reports, similar information was included as an Executive Summary. Section 5.2 provides instructions for the sampling of the variance components.

5.1. Complete GMM logic-tree

The V6 Groningen GMM has the same basic structure as the V5 model: equations for the prediction of accelerations at the NS_B rock horizon combined with frequency-dependent non-linear site AFs assigned to zones defined throughout the study area (onshore gas field plus 5 km buffer). As for the V5 model, the V6 GMM provides predictions of 5%-damped spectral accelerations [Sa(T)], at 23 periods and peak ground velocity (PGV); in all cases, the geometric mean of the horizontal components is predicted. As in V5, the predictions at the NS_B horizon are a function of local magnitude (M_L) and rupture distance (R_{rup}).

The functional form of the predictive equations is essentially the same as in V5 and the logic-tree structure is also the same, with four branches for the median predictions and two branches for the within-event variability. There has been a small change in the field zonation, with the division in two parts of two out of the 160 zones of the V4 and V5 models, resulting in 162 zones, as defined by the RD X-Y coordinates of the voxels included within each zone.

This section summarises the basic elements of the V6 model as required for its implementation in hazard and risk calculations. The coefficients and additional values (such as the site amplification zonation) are included in supplementary CSV files identified in the text.

Equations for Median Motions at NS_B Rock Horizon

The equations for predicting the median ground-motion parameters at the NS_B rock horizon are a function of only magnitude (M_L) and distance (R_{rup}); hereafter, these are specified simply as M and R , the latter measured in km. The model has exactly the same functional form as the V4 and V5 models for motions at the NS_B horizon and can be represented as comprising a source component and a path component, the latter being a function of magnitude and distance:

$$\ln(Y) = g_{source}(M) + g_{path}(R, M) \quad (5.1)$$

where Y is either $Sa(T)$ in cm/s^2 or PGV in cm/s . The source-related terms are segmented into three ranges of magnitude:

$$g_{source}(M) = m_0 + m_1(M - 4.7) + m_2(M - 4.7)^2 \quad M \leq 4.7 \quad (5.2a)$$

$$g_{source}(M) = m_0 + m_3(M - 4.7) \quad 4.7 < M \leq 5.45 \quad (5.2b)$$

$$g_{source}(M) = m_0 + m_3(5.45 - 4.7) + m_4(M - 5.45) + m_5(M - 5.45)^2 \quad M > 5.45 \quad (5.2c)$$

Similarly, the path terms are also segmented into ranges of rupture distance:

$$g_{path}(R, M) = (r_0 + r_1M) \ln\left(\frac{R}{3}\right) \quad R < 7 \quad (5.3a)$$

$$g_{path}(R, M) = (r_0 + r_1M) \ln\left(\frac{7}{3}\right) + (r_2 + r_3M) \ln\left(\frac{R}{7}\right) \quad 7 \leq R < 12 \quad (5.3b)$$

$$g_{path}(R, M) = (r_0 + r_1M) \ln\left(\frac{7}{3}\right) + (r_2 + r_3M) \ln\left(\frac{12}{7}\right) + (r_4 + r_5M) \ln\left(\frac{R}{12}\right) \quad R \geq 12 \quad (5.3c)$$

There are four versions of the median equations for Y at the NS_B horizon, as summarised in Table 5.1; these models correspond to different values of the stress parameter, $\Delta\sigma$. There are two central models, both having the same value of the stress parameter in the magnitude range of the existing Groningen data; at larger magnitudes, the stress parameters rise to lower (Ca) and higher (Cb) values.

Table 5.1. Weights on the four branches for median predictions at NS_B.

Branch	Model	Code	Weight
1	Lower	L	0.1
2	Central – lower	Ca	0.3
3	Central – upper	Cb	0.3
4	Upper	U	0.3

The coefficients of equations (5.2) and (5.3) for the four individual models are presented in the file [gmpe_medians_NS_B_20190314_v6.csv](#).

Sigma Model for NS_B Rock Horizon GMPEs

The sigma model representing the aleatory variability in the values of $\ln(Y)$ from Eq.(5.1) includes a between-earthquake component, τ , and a within-earthquake component, ϕ_{SS} . If Y_μ is the median value obtained from Eqs.(5.1) to (5.3), then two different quantities may be predicted by sampling from the components of variability: Y_{GM} , the geometric mean component (to be used for hazard mapping), and Y_{arb} , the arbitrary component (to be used in risk calculations):

$$\ln(Y_{GM}) = \ln(Y_\mu) + \varepsilon_E \tau + \varepsilon_S \phi_{SS} \quad (5.4a)$$

$$\ln(Y_{arb}) = \ln(Y_\mu) + \varepsilon_E \tau + \varepsilon_S \phi_{SS} + \varepsilon_C \sigma_{C2C} \quad (5.4b)$$

The ε values are standard normal variates that represent the numbers of standard deviations from the each of the normal distributions; σ_{C2C} is the component-to-component variability. The component-to-component variability model has not changed from the V5 model and includes dependence on both magnitude and distance. The component-to-component variance is defined by the following equations for the value at different periods, T:

$$\sigma_{c2c}^2(M, R) = 0.026 + 1.03[5.6 - \min(5.6, \max[M, 3.6])]R^{-2.22} \quad T \leq 0.1s \quad (5.5a)$$

$$\sigma_{c2c}^2(M, R) = 0.045 + 5.315[5.6 - \min(5.6, \max[M, 3.6])]R^{-2.92} \quad T \geq 0.85s \quad (5.5b)$$

For periods in between 0.1 and 0.85 seconds, the following interpolation is used:

$$\sigma_{c2c}^2(T, M, R) = \sigma_{c2c}^2(0.1, R) + \left[\frac{\log(T) - \log(0.1)}{\log(0.85) - \log(0.1)} \right] [\sigma_{c2c}^2(0.85, R) - \sigma_{c2c}^2(0.1, R)] \quad (5.6)$$

A unique value of between-earthquake variability is associated with each period (and PGV) and there are two equally-weighted branches for the within-event variability. The between-earthquake variability values are modified from V5 but the values of the within-event variability are identical to those used in the V4 and V5 models. The complete logic-tree for motions at the NS_B horizon is illustrated in Figure 5.1. The values of the sigma components are presented in the file [gmpe_sigmas_NS_B_20190325_v6.csv](#).

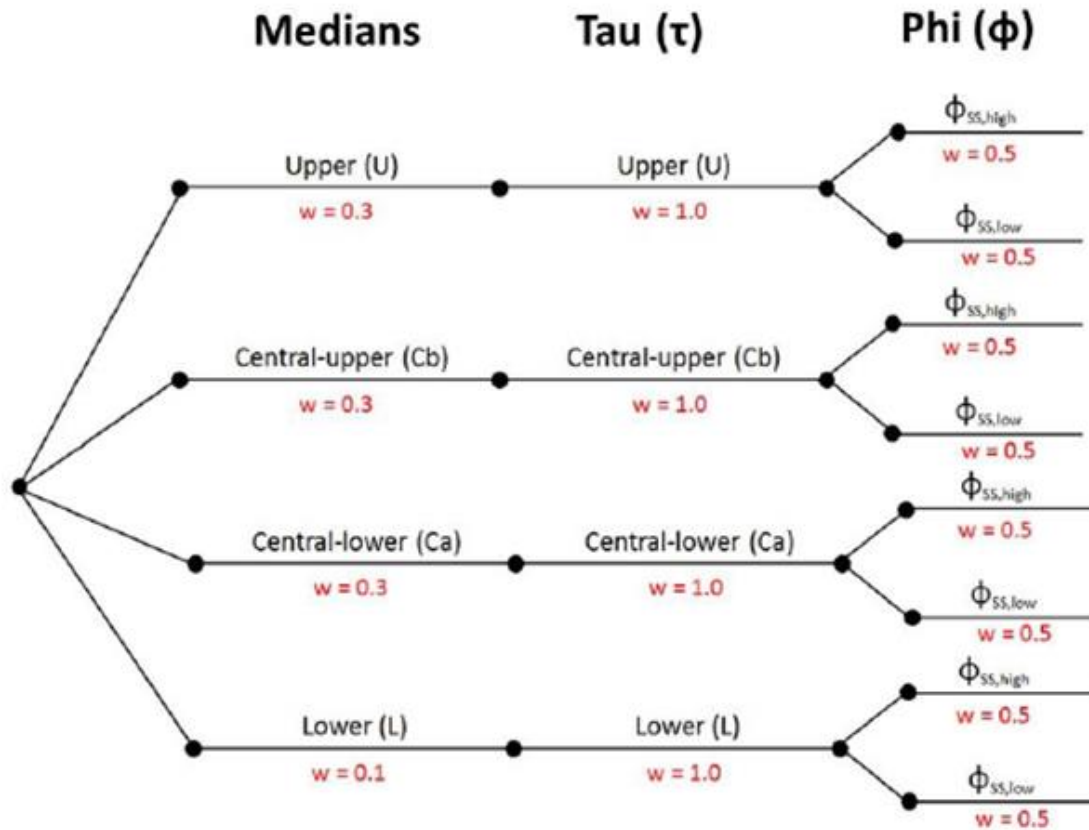


Figure 5.1. Logic-tree structure for model for motions at the NS_B horizon

Field Zonation

The study area is divided into **162** zones having a common set of AFs for both Sa(T) and PGV (Figure 5.2). The zones are defined by a numerical code; the zones and their geographical limits are identical to those defined for the V4 and V5 models, except four zones which have resulted from the division of two previous zones. A list of 140,862 voxel squares of 100 x 100 m—each identified by the RD coordinates of their centre—and the zone to which each voxel is identified is provided in the following file: [gmpeSurfaceZonation_20190319_v6.csv](#).

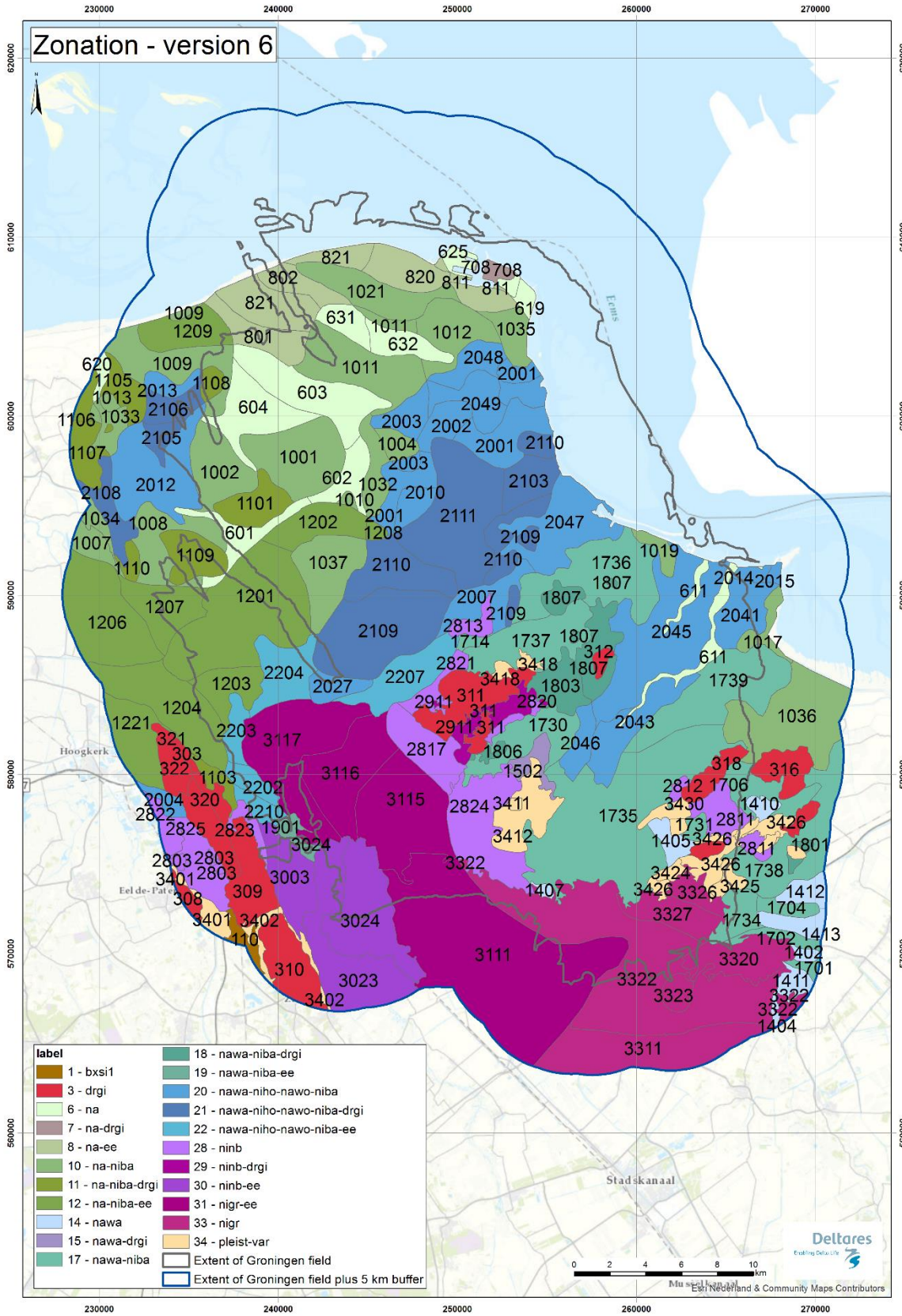


Figure 5.2. V6 zonation of the Groningen field for site AFs

Median Non-Linear Soil Amplification Factors

For each of the 162 zones and each ground-motion parameter [spectral acceleration, Sa(T), at 23 periods and PGV], the amplification factors, AF, are defined as follows:

$$\ln[AF(Sa)] = f_1^* + f_2 \ln\left(\frac{Sa_{NS_B,g} + f_3}{f_3}\right) \quad (5.7a)$$

$$\ln[AF(PGV)] = f_1^* + f_2 \ln\left(\frac{PGV_{NS_B} + f_3}{f_3}\right) \quad (5.7b)$$

In Eq.(5.7a), $Sa_{NS_B,g}$ is Sa(T) at the NS_B horizon, expressed in units of g (981 cm/s²); in Eq.(5.7b), PGV_{NS_B} is the PGV value at the same reference rock horizon, in units of cm/s. This general formulation is unchanged from the V5 model.

The first term on the right-hand side of Eq.(5.7), f_1^* , is the exponent of the linear part of the AFs. The term is magnitude- and distance-dependent and for Sa(T) this dependence is defined by the following equation:

$$f_1^* = [a_0 + a_1 \ln(R)] + [b_0 + b_1 \ln(R)] [\min(M, M_{ref}) - M_{ref}] \quad (5.8)$$

where M_{ref} is given by:

$$M_{ref} = M_1 - \left[\frac{\ln(R) - \ln(3)}{\ln(60) - \ln(3)} \right] (M_1 - M_2) \quad (5.9)$$

where M_1 and M_2 are model parameters.

For PGV, f_1^* , is given by:

$$f_1^* = [a_0 + a_1 \ln(R)] + [b_0 + b_1 \ln(R)] (M - M_1) \quad M \leq M_1 \quad (5.10a)$$

$$f_1^* = [a_0 + a_1 \ln(R)] + d(M - M_1) \quad M > M_1 \quad (5.10b)$$

The model parameters a_0 , a_1 , b_0 , b_1 , M_1 and M_2 are all given for all periods and all zones (except zones 2813 and 3411 which are entirely covered by water) in the file [gmpeSurfaceAmplificationModel_20190326_v6.csv](#). For PGV, the same parameters are given but M_2 is given as -99 since this coefficient is not used for this ground-motion parameter. The coefficient d used in Eq.(5.10b) is also included in the file, and is entered as 0 for Sa(T). The values of $\ln(AF)$ in Eqs.(5.7a) and (5.7b) are subject to upper and lower limits of AF_{max} and AF_{min} , which are also included in the

same file. It should be noted that the model for AF is only applicable for magnitudes greater than or equal to $M_L 2$.

Site-to-Site Variability Model

The variability in the site AFs is given by the standard deviation ϕ_{S2S} , which is defined as a tri-linear function as defined in the following equations (and illustrated in Figure 5.3):

$$\phi_{S2S} = \phi_{S2S,1} \quad Sa_{NS_B,g} < Sa_{Low} \quad (5.11a)$$

$$\phi_{S2S} = \phi_{S2S,1} + (\phi_{S2S,2} - \phi_{S2S,1}) \left[\frac{\ln(Sa_{NS_B,g}) - \ln(Sa_{low})}{\ln(Sa_{high}) - \ln(Sa_{low})} \right] \quad Sa_{Low} \leq Sa_{NS_B,g} \leq Sa_{High} \quad (5.11b)$$

$$\phi_{S2S} = \phi_{S2S,2} \quad Sa_{NS_B,g} > Sa_{High} \quad (5.11c)$$

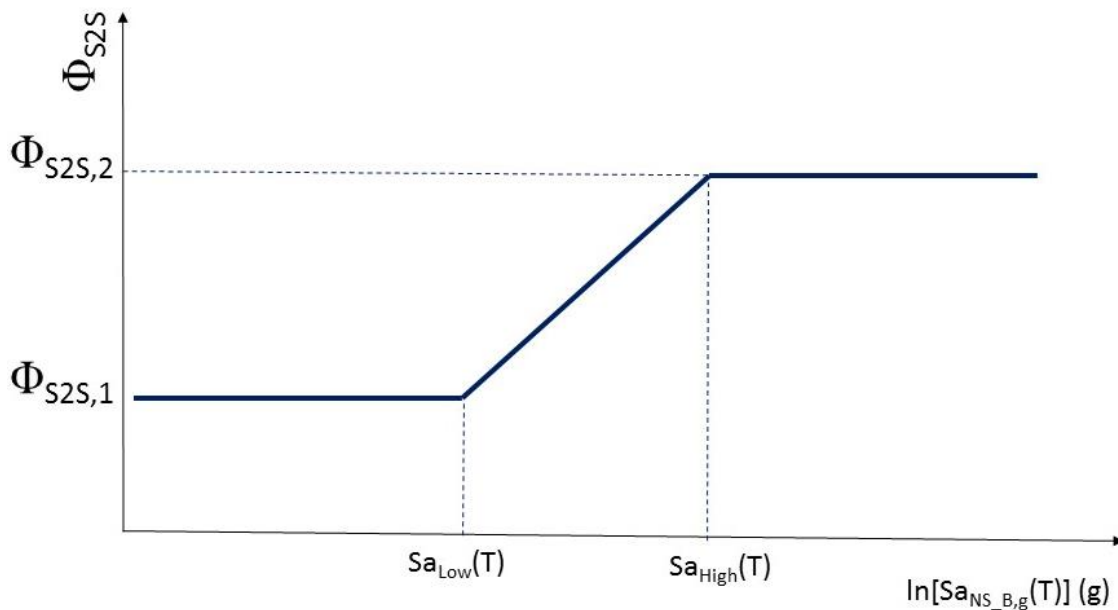


Figure 5.3. Schematic illustration of the site-to-site variability model. The values on the x-axis is the $Sa(T)$ at the NS_B , expressed in units of g , or the PGV value in cm/s . In either case, the value is obtained by application of Eqs.(5.1) to (5.4)

The four parameters defining the site-to-site variability model for $Sa(T)$ at all 23 periods and also for PGV in each of the 162 site amplification zones are listed in the file [gmpeSurfaceAmplificationModel_20190326_v6.csv](#).

Period-to-Period Correlation of Residuals of Sa(T)

For the risk calculations, values of Sa(T) calculated at a given location for different periods, T, must account for the period-to-period correlations of the residuals. The correlation coefficients, to be applied to all components of variability, for Sa(T) at all 23 periods are exactly the same as those used in the V4 model and these are provided in the CSV file: **gmpe_period2period_correlations_20190325_v6.csv**. The content of this file is identical to the file provided with the V4 model (**gmpe_period2period_correlations_20170131_v4.csv**) and the V5 model (**gmpe_period2period_correlations_20170824_v5.csv**) but a new file has been created to create a consistent suite of input files for the V6 model.

Summary List of Electronic Supplements

1. gmpe_medians_NS_B_20190314_v6.csv
2. gmpe_sigmas_NS_B_20190325_v6.csv
3. gmpeSurfaceZonation_20190319_v6.csv
4. gmpeSurfaceAmplificationModel_20190326_v6.csv
5. gmpe_period2period_correlations_20190325_v6.csv

These files are all contained in the folder “V6 GMM electronic supplements”, which is made available as a zipped file of the same name.

5.2. Sampling of variance components

The prediction of the median values of SA and PGV is relatively straightforward, simply applying the relevant values of M and R for each earthquake-site combination, and then applying the relevant AF depending on the zone within which the site is located. However, the models predict distributions of values rather than unique estimates of SA and PGV. In all cases, the intensity measures (SA and PGV) are log-normally distributed and their joint distribution is assumed to be multivariate log-normal. For both model development and sampling it is convenient to work with the log-transformed intensity measures such that variation about the median motion for a given scenario is defined by a symmetric normal distribution (or multivariate normal). The scale of the variation in this transformed space is defined by a standard deviation. The total standard deviation in ground-motion prediction models is usually represented by the symbol sigma (σ) and the total residuals are then defined by the product of σ and epsilon (ϵ) the number of standard deviations sampled (and a standard normal variate).

The purpose of this section is to define the procedures for sampling the aleatory variability in the prediction of the ground-motion parameters. The hazard and risk model for the Groningen field uses Monte Carlo simulations and therefore the focus is on the random sampling of ϵ values in each ground-motion realisation. The process is schematically illustrated in Figure 5.3, which depicts the estimation of SA

for a single value of T at three locations (over two zones) as a result of a single earthquake. In practice, however, the implementation is somewhat more complicated because the sampling of variance components must also respect correlations between parameters and spatial correlation as well. In the following, the first subsection defines the different components of variability and then the issue of spatial correlation is discussed. After that, the sampling is discussed for different applications of increasing complexity with regards to the variability.

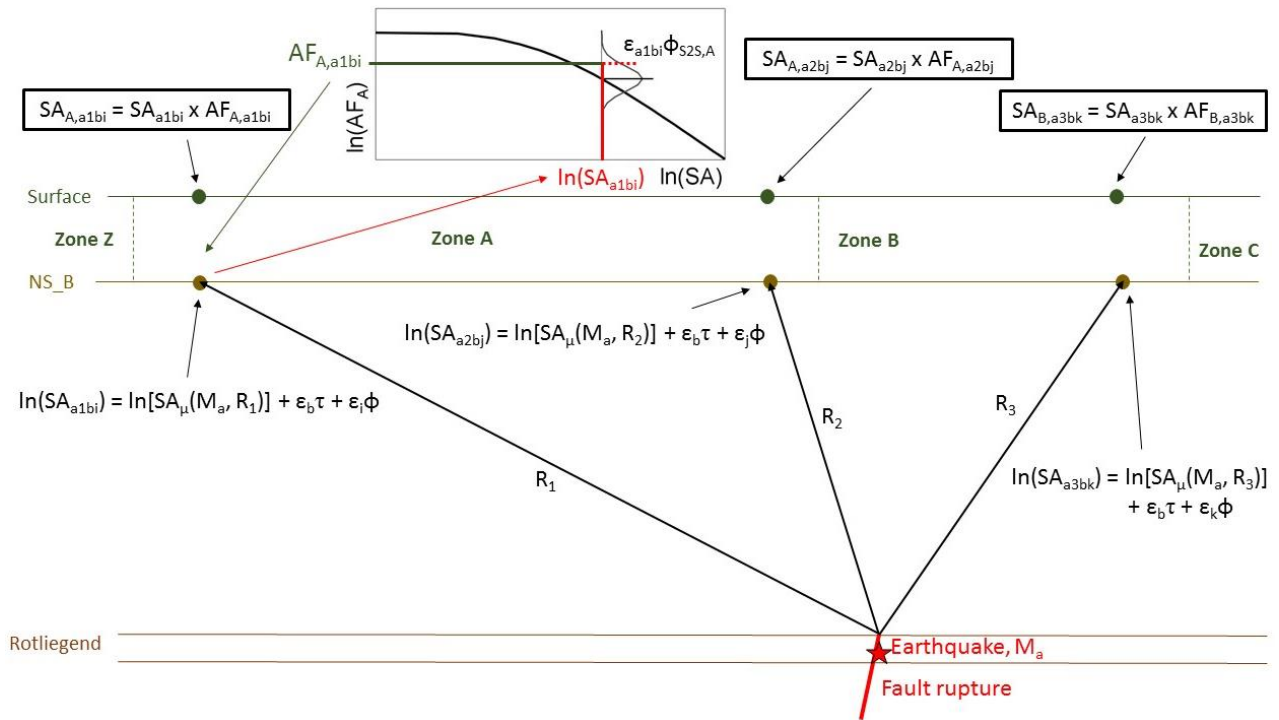


Figure 5.3. Schematic illustration of the calculation of SA at three surface points, in two zones, for an earthquake of magnitude M_a and an event-term of $\epsilon_b\tau$; in this simple example, the within-event variability is sampled without considering spatial correlation (Bommer *et al.*, 2017c).

Components of Variability in the Groningen GMM

The components of variability defined in the Groningen GMM are listed in Table 5.2, indicating also which ground-motion parameters they are related to and where they are applied both in terms of a reference horizon and in the calculation of hazard or risk.

The total variability on the geometric mean ground-motion amplitudes is given by:

$$\sigma_{GM} = \sqrt{\tau^2 + \phi_{SS}^2 + \phi_{S2S}^2} \quad (5.12)$$

whereas the total variability of the arbitrary component of motion is given by:

$$\sigma_{arb} = \sqrt{\tau^2 + \phi_{SS}^2 + \phi_{S2S}^2 + \sigma_{c2c}^2} \quad (5.13)$$

Table 5.2. Elements of ground-motion variability in the Groningen GMM

Symbol	Description	GM Parameter ¹	Horizon ²	H or R ³	Epsilon ⁴
σ_{GM}	Standard deviation of geometric mean of ground-motion parameters	Sa(T), PGV	NS_B	Hazard	ε_{GM}
σ_{arb}	Standard deviation of arbitrary component of ground-motion parameters	Sa(T), PGV	NS_B	Risk ⁵	ε_{arb}
τ	Between-event variability of ground-motion parameters	Sa(T), PGV	NS_B	H & R ⁵	ε_E
ϕ_{SS}	Within-event non-ergodic variability of amplitude-based parameters	Sa(T), PGV	NS_B	H & R ⁵	ε_S
σ_{c2c}	Component-to-component variability of spectral accelerations	Sa(T)	NS_B	Risk	ε_c
ϕ_{S2S}	Site-to-site variability associated with AFs	Sa(T)	Surface	H & R	ε_Z

Notes: 1 – The ground-motion parameters to which it applies; 2 – Reference elevation at which applied; 3 – Whether used in hazard or risk calculations; 4 – Symbol for normalised residual used to sample distribution; 5 – PGV is not currently employed in probabilistic risk calculations.

One correlation model is defined for inter-period correlations, and its characteristics are summarised in Table 5.3. This correlation model is used to construct the full correlation matrix that is required for the sampling process within the risk calculations.

Table 5.3. Correlations of residuals in the Groningen GMM

Symbol	Description	GM Parameter ¹	Horizon ²
ρ_{T2T}	Period-to-period correlation of spectral accelerations	Sa at multiple T	NS_B

Notes: 1 – The ground-motion parameters to which it applies; 2 – Reference elevation at which employed.

Spatial Correlation of Ground Motions

Another correlation of ground-motion residuals is that which occurs spatially since observations from dense recording networks have revealed that epsilon values at closely-spaced locations tend to be correlated rather than being entirely random.

For the calculation of Group Risk or any other aggregate measure of the seismic risk, the spatial correlation of ground motions is important since it leads to pockets of higher-than-average and lower-than-average ground motions rather than simply random spatial variation of the amplitudes. The coincidence of a pocket of higher-than-average ground motions with a group of seismically vulnerable structures will result in higher estimates of Group Risk than when spatial correlation of the ground motions is ignored. Although the primary focus of the risk modelling is Individual Local Personal Risk (ILPR, which is a location-specific measure), Group Risk estimates may be needed and for this reason, spatial correlation does need to be considered.

For the current (V6) risk modelling purposes, the spatial correlation is reasonably approximated (Stafford *et al.*, 2019) with a simpler model that assumes perfect correlation within each of the 162 site amplification zones and no within-event correlation between one zone and another. In practice, this correlation of ground-amplitude amplitudes is not perfect because the NS_B motions, the AFs and σ_{c2c} all depend on M and R, and the value of R will vary for different grid points within a zone. Consequently, while the correlation of the within-event residuals is perfect, the actual ground-motion amplitudes over the zone will vary spatially.

Sampling Variability in Hazard Calculations for PGV and SA(T)

When hazard maps are generated in terms of these 24 parameters [*i.e.*, Sa(T) at 23 response periods plus PGV], they are treated completely independently. The uniform hazard response spectra (UHRS) at specified location are obtained from individual hazard curves for Sa at the 23 response periods. The hazard is calculated at grid points defined across the field, usually with several grid points located within each site response zone.

The sequence of sampling of variability to be followed in generating the hazard estimates is therefore as follows:

1. For each earthquake and ground-motion parameter, a value of ϵ_E is randomly sampled.
2. For each grid point, the NS_B motion is calculated randomly sampling ϵ_S ; this means that spatial correlation is ignored at the reference rock horizon.
3. For each grid point, the median surface motion is estimated by applying the AF value conditioned on the realisation of the NS_B motion (including the two components of variability sampled in steps #1 and #2).
4. The final surface motion at each location is then calculated by randomly sampling ϵ_Z ; here again, spatial correlation is ignored and the site-to-site variability is therefore interpreted as being due to spatial variability of the soil profiles and dynamic soil properties within the zone.

Sampling Variability in Ground-motion Values for Risk Calculations

When ground motions at the surface are predicted for the purpose of providing inputs to risk calculations, a number of differences arise when compared to the same predictions within the hazard calculations. One of these is that the component-to-component variability needs to be added in order to obtain estimates of the arbitrary component of motion rather than the geometric mean. Secondly, spatial correlation needs to be approximated as was described earlier. And finally, since the risk calculations are made for several building types at a given location—which have different vibration periods and some of which have different vibration periods along their two axes—the period-to-period correlations of $Sa(T)$ also need to be sampled. The sampling sequence now becomes as follows:

1. For each earthquake, the covariance matrix for between-event residuals is sampled in order to obtain a vector $\boldsymbol{\varepsilon}_E$ that contains between-event residuals for all 23 spectral ordinates. This vector can be expressed mathematically as $\boldsymbol{\varepsilon}_E = [\varepsilon_E(T_1) \quad \dots \quad \varepsilon_E(T_{23})]^T$. The correlation matrix can be defined as:

$$\boldsymbol{\rho} = [\boldsymbol{\rho}_{Sa(T),Sa(T)}] = \begin{bmatrix} \rho_{Sa(T_1),Sa(T_1)} & \rho_{Sa(T_1),Sa(T_2)} & \dots & \rho_{Sa(T_1),Sa(T_{23})} \\ \rho_{Sa(T_2),Sa(T_1)} & \rho_{Sa(T_2),Sa(T_2)} & \dots & \rho_{Sa(T_2),Sa(T_{23})} \\ & \vdots & \ddots & \vdots \\ \rho_{Sa(T_{23}),Sa(T_1)} & \rho_{Sa(T_{23}),Sa(T_2)} & \dots & \rho_{Sa(T_{23}),Sa(T_{23})} \end{bmatrix} \quad (5.14)$$

2. For each zone, the NS_B motion for the arbitrary component needs to reflect both the variability suggested by ϕ_{SS} as well as the component-to-component variability associated with σ_{c2c} . Rather than sample separate sets of epsilon values for each of these components individually, a vector of epsilon values $\boldsymbol{\varepsilon}_A = [\varepsilon_A(T_1) \quad \dots \quad \varepsilon_A(T_{23})]^T$ is generated. For each ground-motion measure, the residual of the arbitrary component is given by $\varepsilon_A \sqrt{\phi_{SS}^2 + \sigma_{c2c}^2} \equiv \varepsilon_S \phi_{SS} + \varepsilon_C \sigma_{c2c}$. That is, the covariance matrix from which $\boldsymbol{\varepsilon}_A$ is sampled has diagonal elements that are defined by $\phi_{SS}^2 + \sigma_{c2c}^2$ (for all spectral ordinates). The off-diagonal elements of the covariance matrix make use of the same correlation matrix elements as used for the sampling of the between-event residuals. The sampled values of $\boldsymbol{\varepsilon}_A$ are used at all grid points within a zone to approximate spatial correlation.
3. For each grid point, the median surface motion is estimated by applying the AF value conditioned on the realisation of the NS_B motion (including the two components of variability $\boldsymbol{\varepsilon}_E$ and $\boldsymbol{\varepsilon}_A$ sampled in steps #1 and #2).
4. The final surface motion at each location is then calculated by randomly sampling ε_Z ; for a given period, the same value of ε_Z should be invoked at every grid point within a zone in order to represent perfect spatial correlation.

6. CONCLUDING REMARKS

This report has presented the latest stage of development in the evolution of the Groningen ground-motion model, once again generated to a very tight schedule (notwithstanding the elapsed time since the issue of the V5 GMM because a V6 model was not originally envisaged). In this closing chapter, we compare the predictions from the V6 GMM to those from the previous version, and also discuss issues that would warrant refinement if there were to be another iteration.

6.1. Comparison between V5 and V6 GMM

Inevitably, the first question posed each time a new version of the GMM is issued is how it compares with the previous version. Some differences between the V5 and V6 models are to be expected in view of the use of an expanded database and the updated site response model with appreciably larger damping values.

Median Surface Predictions

Appendix V shows comparisons of median response spectral ordinates in selected zones for various combinations of magnitude and distance. In each case, the plots compare the predictions from the V6 model with those from both the V5 and V4 models. The most important general observation that can be made is that the V6 predictions are generally higher than those from the V5 model, and often comparable to those from the V4 model (although it is probably not helpful to over-emphasise the V4 model given that its derivation was affected by an erroneous relationship between M_L and M). The V6 predictions generally exceed those of the V5 model at shorter periods, especially for periods below 0.1 seconds, although the exceedance occurs in many cases across the full period range at larger magnitudes. For scenarios that have a strong influence on hazard and risk estimates—such as M_L 5 at 3 km distance (*i.e.*, epicentral locations)—the differences are most pronounced at shorter periods but also vary very significantly from zone to zone. In some cases, such as zone 1206, the two models yield very similar predictions except at periods of 0.1 second and lower.

Another feature that is worthy of note is the degree of period-to-period fluctuation in the spectral ordinates of the V6 predictions, especially in the shorter period range. Such fluctuations are also visible in the spectra from the V5 model. These fluctuations in the spectral shapes are related to the amplification factors and most likely are the result of the scenario-dependence in the linear amplification factors (Stafford *et al.*, 2017). This feature was not present in the V4 model, which yields smoother spectral shapes at the ground surface.

Rock Motions and Amplification Factors

The differences observed between V5 and V6 spectra at the surface are, to some extent, reflected in the comparisons between the model predictions at the NS_B horizon, which are shown in Appendix II. The general pattern is that the V6 model predicts higher ordinates at shorter periods and the difference increases with increasing distance but at short distances is more pronounced at small magnitudes. All of these observations are broadly consistent with the source, path and site parameters obtained from the V6 inversions, which lead to higher values of the stress parameter in the small magnitude range, lower site kappa for the NS_B, and a higher estimate of Q.

These differences reflect higher motions at the NS_B obtained by deconvolution of the recordings compared to those obtained in the V5 model-building process. While this could be explained simply by the increased levels of low-strain damping in the site response model (Section 2.3)—thus requiring higher amplitudes of motion at the NS_B horizon to explain the observed surface motions—it would also appear to be a consequence of switching from the use of 200-m geophone (G4-station) records to the surface accelerograph (G0-station) recordings, as discussed below.

Figures 6.1 and 6.2 compare the amplification factors, AF, from the V4, V5 and V6 models for two zones. The pattern in both cases is similar, namely that the V6 AFs are markedly lower, particular for lower levels of acceleration. Under higher levels of excitation, the V6 AFs become more similar to those of the V5 model, except at long periods (5 s) where they are slightly larger. These patterns are consistent with the higher soil damping values in the V6 site response profiles. These observations suggest that the higher median amplitudes of surface motions obtained with the V6 model are more related to increases in the NS_B levels of motion than to changes in the AFs.

Surface vs. Borehole Instruments

As noted above, the most obvious explanation for the appreciable differences between the V5 and V6 predictions at the ground surface—apart from the expanded database, which in itself would not be expected to result in such larger changes—is the change in the site response model and in particular the higher values now adopted for low-strain damping. However, the differences between the V5 and V6 models may also be related in large part from the decision to move from using G4-station recordings to using the accelerograms from the G0-stations. If the site response models constructed for the field are broadly correct and reliable, then the motions at NS_B obtained from deconvolution of the G0 and G4 recordings should be very similar. Figure 6.3 shows the ratios of FAS obtained from deconvolving G0-station records to the NS_B to those obtained from deconvolution of the G4-station

geophone recordings, and it can be immediately appreciated that there is considerable scatter but the general trend is a ratio appreciably larger than unity (apart from a dip at around 0.5-0.6 Hz).

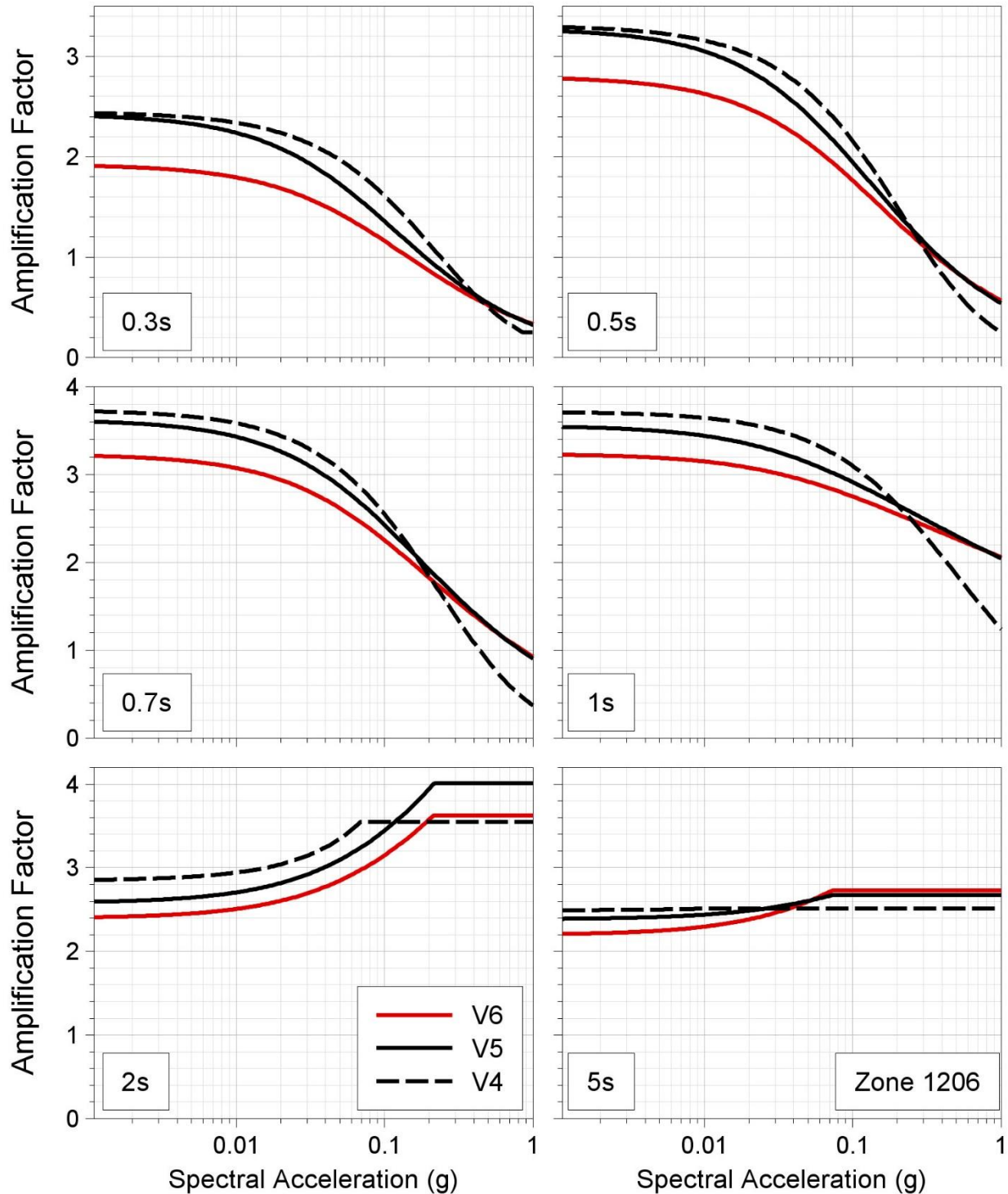


Figure 6.1. Comparison of V4, V5 and V6 AFs at selected periods for zone 1206 plotted as a function of $Sa(T)$ in the NS_B rock horizon

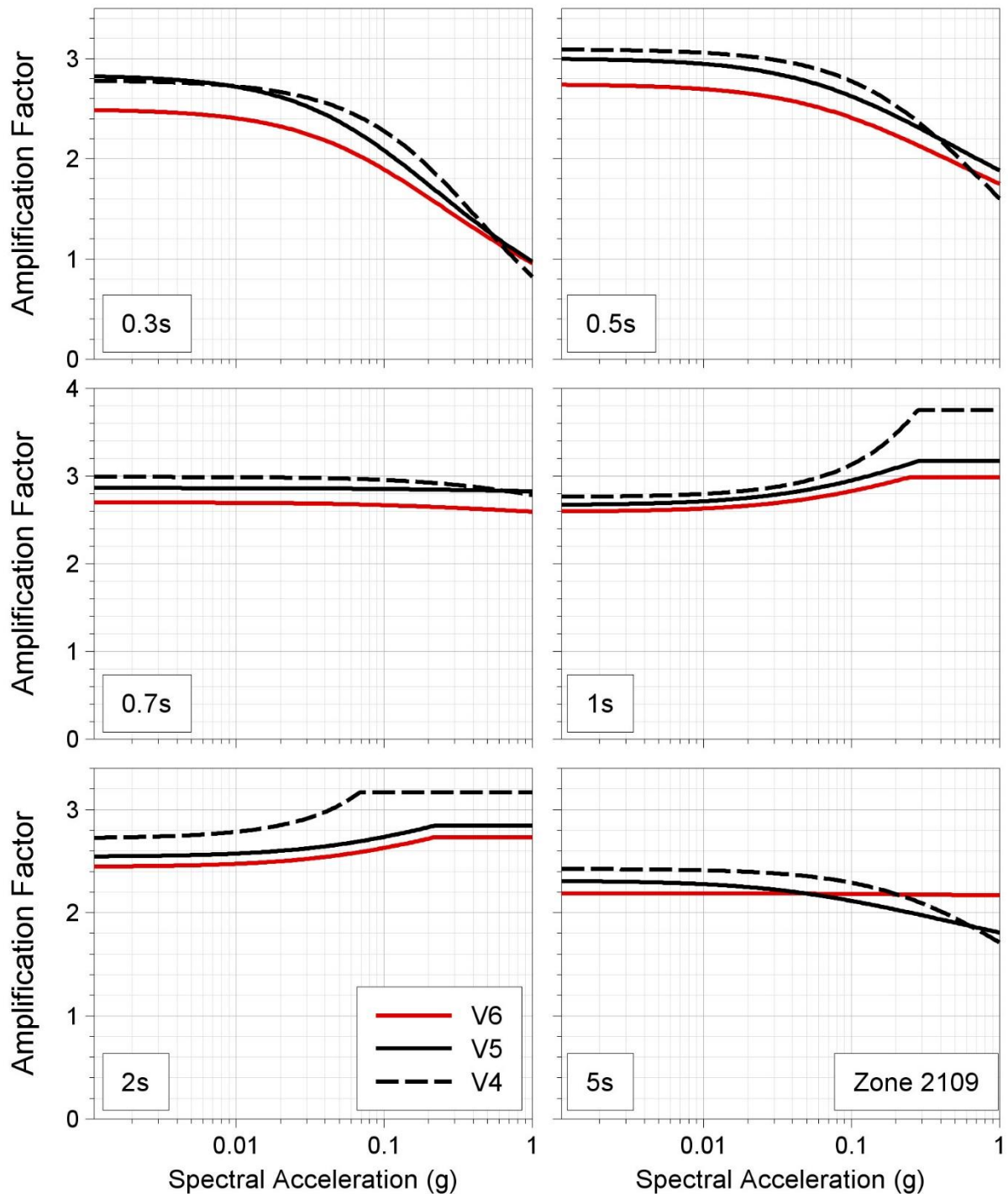


Figure 6.2. Comparison of V4, V5 and V6 AFs at selected periods for zone 2109 plotted as a function of $Sa(T)$ in the NS_B rock horizon

The ratios are on the order of about 1.5 across most of the frequency range, apart from the previously noted dip, which may be due to a resonance effect associated with the free surface reflection or simply to the poor signal-to-noise ratios at low frequencies. For frequencies above 10 Hz, the ratio increases exponentially, which would be consistent with the higher damping in the uppermost part of the soil profiles. Figure 6.4 shows a similar plot but for the response spectral ordinates at the

NS_B horizon, which show an average ratio close to 2 across the period range. Figures 6.5 and 6.6 show similar plots from the V5 and V6 models, which show remarkably similar patterns.

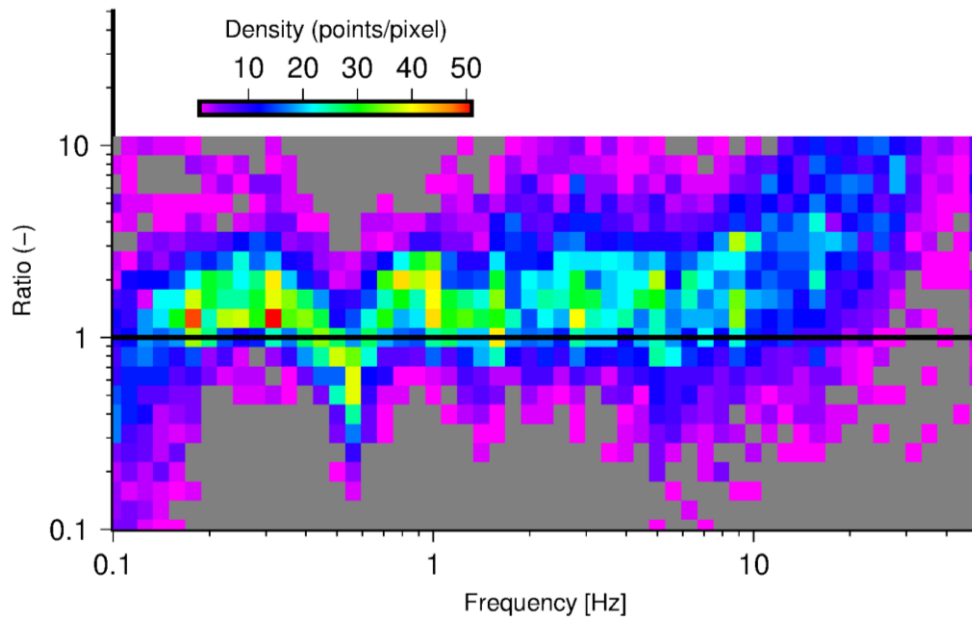


Figure 6.3. Ratios of FAS at NS_B obtained from deconvolution of the G0-station records to those from deconvolution of the G4-station recordings

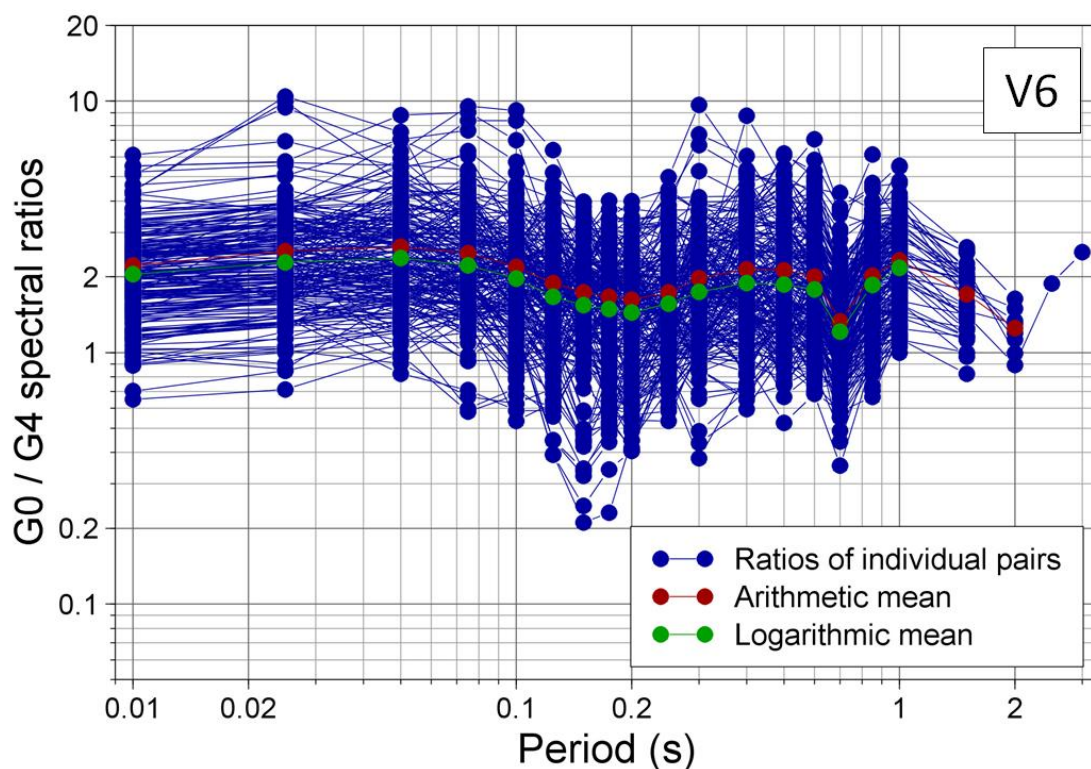


Figure 6.4. Ratios of Sa(T) at NS_B from G0 recordings to those from G4 records

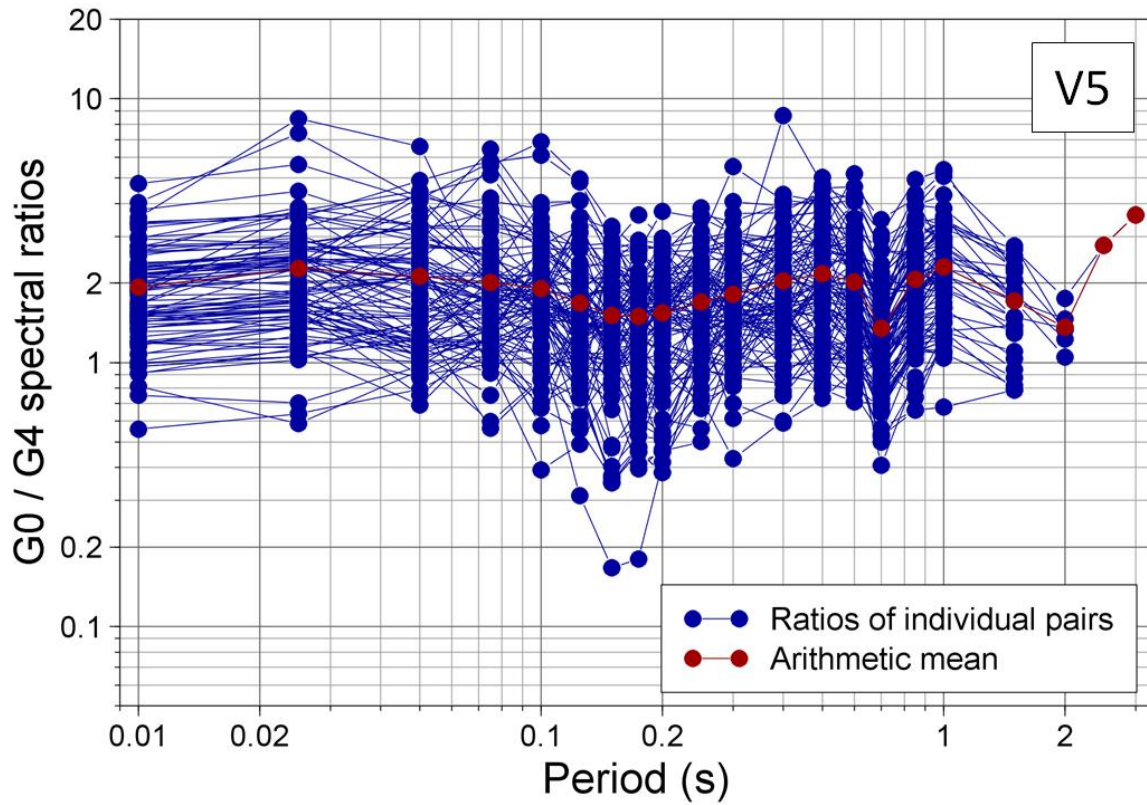


Figure 6.5. Ratios of Sa(T) at NS_B from G0 recordings to those from G4 records using the V5 database and site response model

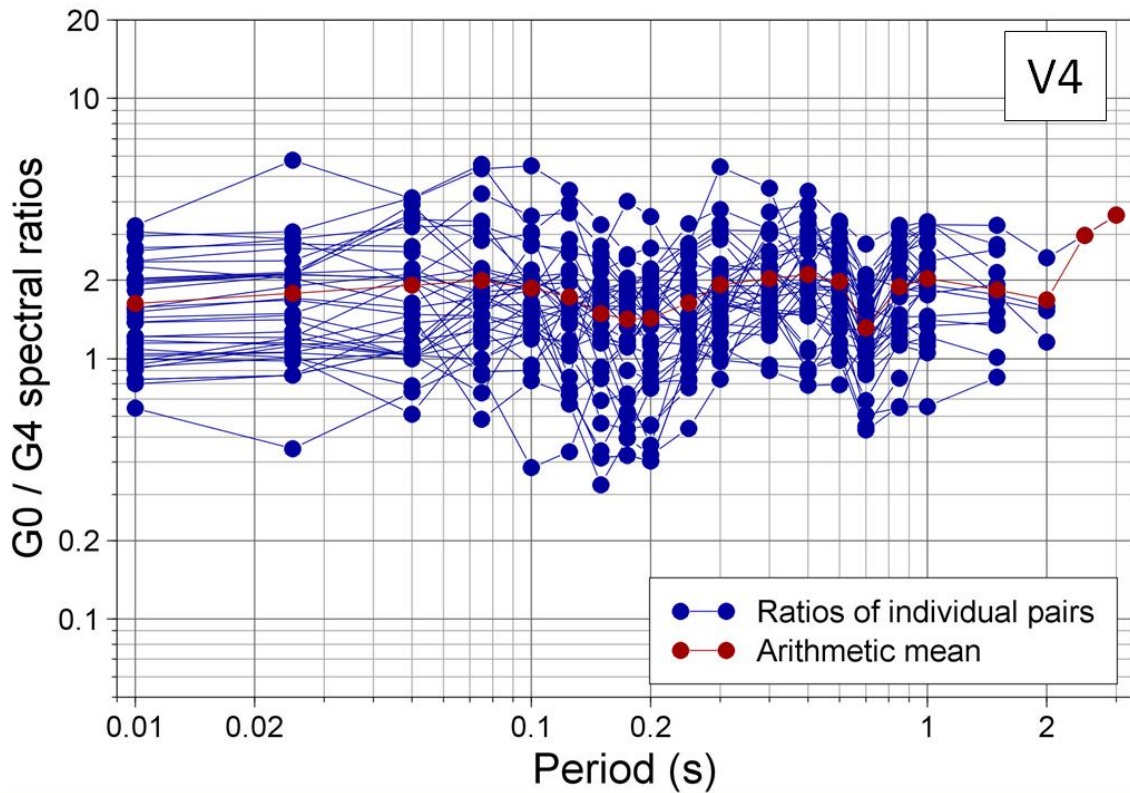


Figure 6.6. Ratios of Sa(T) at NS_B from G0 recordings to those from G4 records using the V4 database and site response model

The consistency of this pattern across three models with different soil damping models would suggest that the difference in the resulting NS_B motions is not due to this factor. The explanation would then have to reside either in vagaries of the calculation of within-column AFs (noted in Section 2.1 as one of the motivations for moving to the use of surface recordings) or else in some systematic differences between the behaviour of borehole geophones and the surface accelerographs.

In terms of the question of whether the geophone are recording the correct amplitudes of motion, Appendix VI summarises work conducted by KNMI to explore this issue, which includes comparison of recordings from the G2-station geophones with recordings from co-located broadband seismographs installed in 100 m boreholes. The conclusion from these investigations is that the instruments are operating correctly and hence another explanation needs to be sought for the differences in the NS_B motions obtained from inversions of the two sets of recordings. As noted below, this will be a subject of ongoing investigation beyond the delivery of the V6 model.

In closing this discussion, however, it can be stated very clearly in view of the ratios shown in Figures 6.3 and 6.4, the decision to move to the use of surface accelerographs rather than borehole geophones has clearly been vindicated. It is also very important to clarify that such checks between the ratios of the two sets of motions deconvolved to the reference rock horizon were made during earlier stages of the Groningen GMM work but at the time they indicated that there was broad consistency between the two suites of motions. This conclusion was reached because, as is now known, the G0-station recordings used previously had one-half of the correct amplitude, hence leading to ratios close to unity at the NS_B horizon—and in effect concealing the differences now observed.

Aleatory Variability

The figures in Appendices II and V only compare median predictions from the V5 and V6 GMMs. Inferences regarding the impact of the change from the V5 GMM to the V6 model on hazard and risk estimates also need to consider the aleatory variability terms, which are randomly sampled in the calculations.

As previously discussed in Section 3.4, there are four elements of aleatory variability in the V6 model: calculations combine between-event variability (τ), within-event variability (ϕ_{SS}), component-to-component variability (σ_{c2c}) and between-site variability (ϕ_{S2S} , which includes the variability in site response). The ϕ_{SS} and σ_{c2c} models are unchanged from the V5 GMM, but there are differences in the other two variances. As shown in Figure 3.12, the inter-event (between-earthquake) variability yields slightly lower values at short periods (< 0.5 s), which to some extent can be

expected to counteract the effect the increased median predictions in this period range.

In terms of ϕ_{S2S} , the values for the V6 model are generally found to be somewhat lower than those of the V5 model, particularly for stronger NS_B motions, as illustrated in Figures 6.7 and 6.8 for the same zones for which the AFs were shown in Figures 6.1 and 6.2.

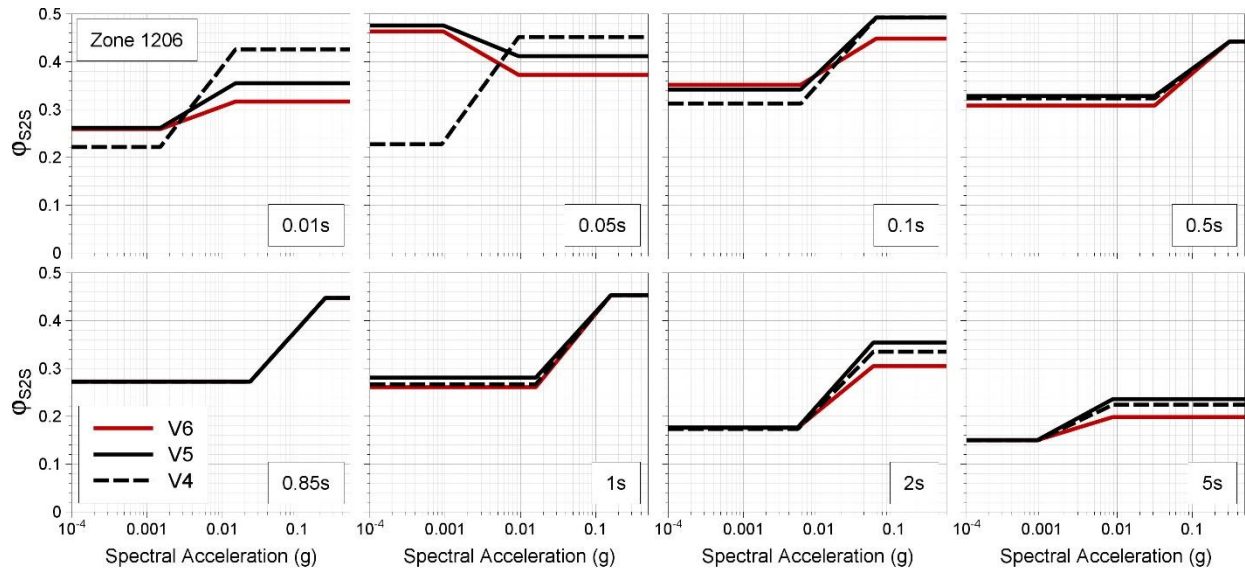


Figure 6.7. Site-to-site variability in zone 1206 from the V4, V5 and V6 models

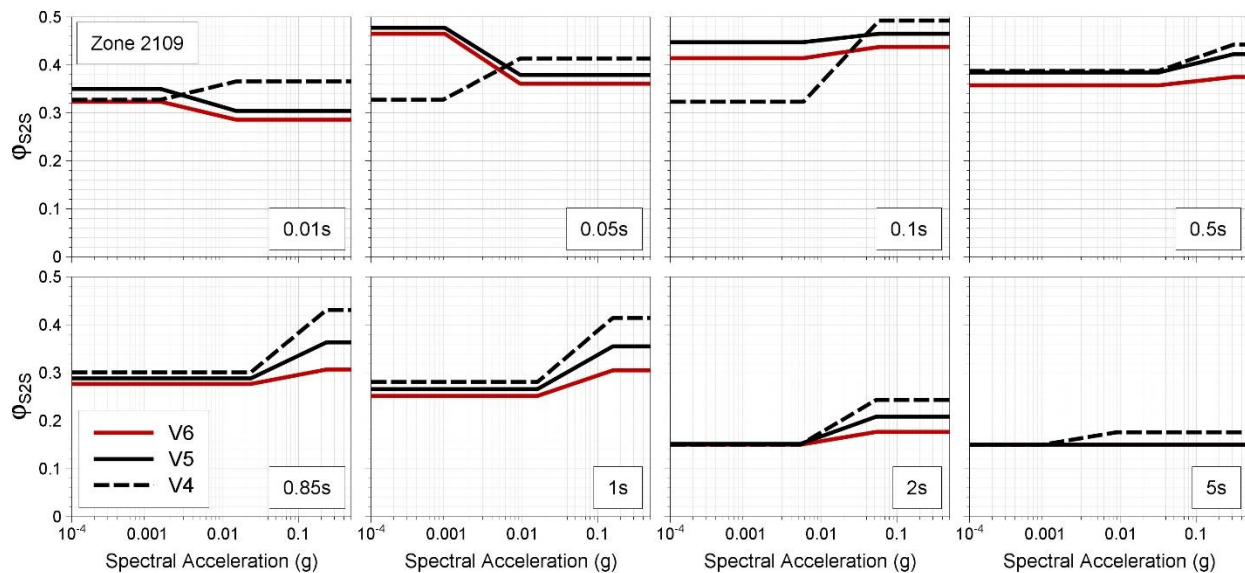


Figure 6.8. Site-to-site variability in zone 2109 from the V4, V5 and V6 models

6.2. Possible future refinements of the GMM

The V6 model has been produced on an accelerated schedule, as noted earlier, and at the same included a number of changes with respect to the previous V5 model. In closing this report, we therefore briefly consider how the model may be refined in the next stage of development. Before looking ahead, however, we briefly look at the model performance with respect to the recorded motions.

V6 Model Performance

Appendix IV shows residuals of the surface motions with respect to the V6 model. These are calculated by first finding the event-term and within-event residuals at the NS_B horizon, and then subtracting these from the total residuals at the surface. The interpretation of these final value residuals at the surface is that they represent spatial variability associated with the uppermost 800 m in the field, whereas the within-event residuals at the NS_B horizon are interpreted as representing the spatial variability related to source radiation and deeper path effects.

The main conclusion that can be drawn from these plots is that the model is generally a good fit to the data, despite the fact that the analysis begins with deconvolving the motions to the NS_B using location-specific amplification factors but predicts the surface motions using zone-specific AFs. Appendix III shows plots of the ratios of station-specific AFs (which are scenario-specific as well) to the AF for the zone in which each station is located. The plots show that there is generally reasonable agreement between the two, the clear exception to this being the BHAR station, where for periods of less than 0.5 second, the zone (3117) AF is between 5 and 10 times larger than the station-specific AF. This is particularly surprising given that the station-specific profile at BHAR gives a V_{S30} of 184 m/s whereas the median V_{S30} value for zone 3117 is 230 m/s.

The mismatch between the station-specific and zone-specific AFs is reflected in the large negative residuals in the lower frame of the plots for the short oscillator periods in Appendix IV, where the BHAR stations stands out as an unusual case. On re-examination, such a pattern was also present in the V5 model but was to somehow less apparent amid the generally poorer fit of the surface residuals. The discrepancy at this station will be a key topic for investigation as the GMM work goes forward.

Another interesting observation that can be made concerning the performance of the V6 GMM. Figure 2.3 showed the ratios of linear AFs calculated using the measured V_s profiles at the B-network stations to those obtained with the modelled V_s profiles, based on GeoTop, for the same locations (the differences corresponding only to the near-surface portion of the profiles). The figure shows considerable scatter but a mean trend that points to a small negative bias at short periods and modest positive

bias at longer oscillator periods. Figure 6.9 shows this average trend plotted together with curves showing the relative bias in the four models (logic-tree branches) with respect to the NS_B motions, separated into those coming from B-station recordings and those from G0-station recordings. The similarity in the form and, at periods greater than 0.1 s, the amplitude of the curves is remarkable; for the central branches, which should most closely reproduce the data, the average relative bias matches the and strongly suggests that the grey curves at short periods as well. This strongly suggests that the bias can be explained to a large degree by systematic differences between the AFs calculated using the measured and modelled V_s profiles.

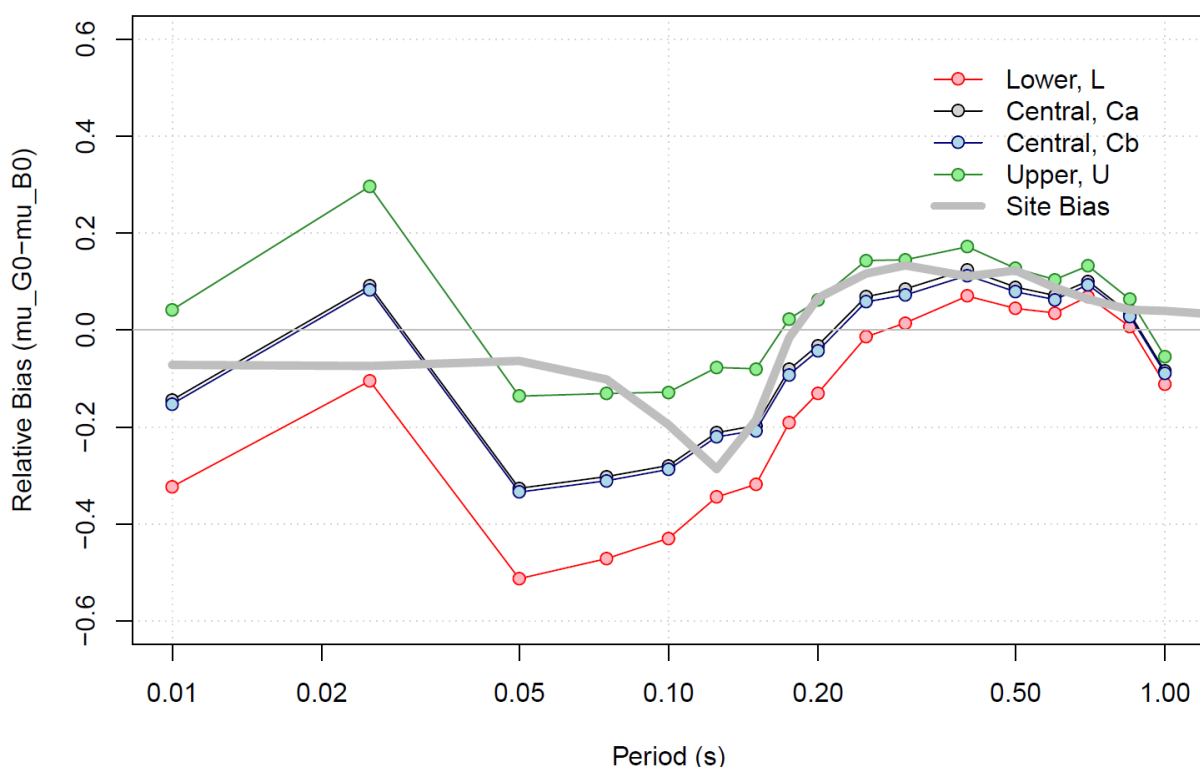


Figure 6.9. Comparison of the average trend of the ratios of AFs calculated using measured and modelled profiles at the B-stations (grey curve) with the relative bias of the model for NS_B motions computed with recordings from B-stations and G0-stations

The V7 GMM

In the first issue of this report, dated 30 March 2019, the following statements were made regarding the development of a seventh version of the GMM:

“In every stage of the GMM development, multiple changes—including new ground-motion recordings, new information regarding velocity and soil properties, and different modelling approaches—have been made with respect to

the previous model version. Moreover, the derivation process (see Figure 1.9) is long and not easily iterated, so issues that have arisen at each stage are addressed in the following version development in tandem with the kind of changes noted above. It is now considered imperative to go through a development stage that is less rushed and also is only a refinement of a model without introducing any major changes. In view of this, the commitment is to produce a V7 GMM for delivery at the beginning of 2020, which in effect allows for a 9-month development period. it has been decided that the database and general framework for the model derivation will remain unchanged from the V6 GMM. This means that the model will also make use of the existing database of B-station and G0-station accelerograph recordings. If new events in the relevant magnitude range ($ML \geq 2.5$) occur in the coming weeks and months, the recordings will be used to check the V7 model but not incorporated into the derivation of the model (unless there is something exceptional about the event, such as being of magnitude equal to or larger than the 2012 Huizinge event)..... In view of the decision to phase out gas production from the Groningen field in the coming years, it is likely that the V7 GMM will be the final version of the model. In view of this, serious consideration will be given to reconvening the international review panel for this final stage in order to elicit constructive feedback from a team of highly knowledgeable individuals with extensive experience in ground-motion modelling. The focused and informed feedback from this esteemed group, provided with the clear aim of assisting the overall development of an excellent model, was of great value in earlier stages of development and such helpful input would be of great value now as the model undergoes its final iteration.”

At the workshop convened with the Review Panel in September 2019, the GMM development team presented the V6 model derivation and the initial analyses that had been undertaken towards refining some elements, particularly the damping model. There was also extensive discussion of the usability of the B-station recordings following the conclusion of the KEM researchers to reject all of the records from this network in their own work. When the plan to complete the V7 GMM in the remaining period from the end of the workshop (held on 9-10 September) until the scheduled delivery in the first days of 2020, the review panel classified this plan as “irresponsible” given that such an accelerated process would not allow for their feedback to be taken into account and would be very unlikely to produce a significantly improved GMM. In the formal report issued by the panel following the Workshop (the complete report is include as Appendix VII), the following statement was made:

“While the development of a Version 7 model had been envisioned, with a delivery date in December 2019, we recommend against proceeding to Version 7 model development at this time. Instead, we recommend that the ground-motion team work through technical issues that were raised in the workshop

(and are discussed below), which are likely to affect the ground motion model. Following panel review of the findings, the next phase of model development can commence. Attempting to complete all of this before the end of 2019 would likely lead to rushed work products without adequate review, and as such, a Version 7 model developed under such conditions would not necessarily improve upon the existing Version 6 model. We believe that Version 6 is a significant advance on the Version 5 model that we have previously endorsed and is suitable for use in hazard and risk assessments.”

In view of this feedback, the eminently sensible decision was taken to abandon the planned sprint to generate the V7 GMM by the end of 2019; any hazard and risk calculations to be performed in the meantime can make use of the V6 summarised herein. The V7 GMM will be completed in the second half of 2020, following a different developmental approach. A new three-day Workshop with the review panel has been scheduled for the end of May 2020, at which the GMM development team will present the outcomes from exploratory studies on numerous aspects of the model building (Table 7.1).

Table 7.1. Exploratory analyses and investigations towards the development of the V7 GMM

Area	Task
Epistemic Uncertainty	Explore ranges of uncertainty in V1 to V6 GMMs (cf. other projects)
	Calibration of upper branch of medians to match tectonic GMPEs
	Logic-tree branches for sigma components (esp. Tau)
	Logic-tree structure for site response uncertainty
	Simulations with more degrees of freedom and compare to logic-tree
	Proposed new logic-tree structure for V7 GMM
Site Response Model	Resolution of G0 vs G4 inconsistency at NS_B horizon
	Final low-strain damping model, incl. unmodified geotechnical models
	Explore the impact of adding logic-tree branches for Dmin
	Incorporation of new Vs profiles and CPTs at G-stations from Fugro
	Lateral variability of Vs and AFs in view of flexible array measurements
	Calibration of AFs using borehole recordings
	Fitting of non-linear response factors
Wierden analyses	Assess how wierde are taken into account in GeoTOP
	Assess how well they are represented in the Site response model
	Compare site response with and without the wierde Vs profile
Record Selection	Analysis of V6 GMM residuals at B- and G-stations
	Inventory (incl. visual inspection) of B-network stations
	Installation of geophones at B-stations and analysis of recordings
	Modelling of SSI effects at B-stations and influence on in-building motions
	Finalisation of V7 GMM database including record processing
Model Performance	Calculation of residuals from V6 model using all network recordings
Modelling Choices	Source modelling choices and transition from induced to triggered events
	Discontinue modelling of spectral ordinates at periods < 0.1 s?
	Direct and indirect prediction of average spectral ordinates 0.01-1.0 s?

The intention is to be unconstrained in terms of the size of the logic-tree, for example, which has been limited to very few nodes and branches until now, which was originally a response to the run times required for the hazard and risk computations. The codes used for these calculations are now significantly more efficient and it is the view of both the development team and the review panel that the logic-tree should be constructed to capture the centre, the body and the range of technically-defensible interpretations of the available data and models, independent of any practical limitations. Table 7.1 lists very brief descriptions of the exploratory tasks that are currently underway towards the development of the V7 GMM, the outcomes of which will be presented and discussed at the Workshop in late May. At an appropriate point between the date of issue of this report and the Workshop, a closed working meeting of the full GMM development team will be convened to review and discuss the progress with these tasks.

Based on the feedback from the review panel in late May, which may prompt a few additional exploratory analyses, a plan will be finalised to initiate the sequence of steps that will be involved to generate the V7 GMM. This final model and its detailed documentation will be issued in late Q3 or Q4 2020, hopefully allowing for review of the draft report by the panel.

8. References

- Abrahamson, N.A. & R.R. Youngs (1992). A stable algorithm for regression-analyses using the random effects model. *Bulletin of the Seismological Society of America* **82**, 505-510.
- Akkar, S., M.A. Sandikkaya & J.J. Bommer (2014). Empirical ground-motion models for point- and extended-source crustal earthquake scenarios in Europe and the Middle East. *Bulletin of Earthquake Engineering* **12**(1), 359-387. *Erratum: 12*(1), 389-390.
- Bindi, D., M. Massa, L. Luzi, G. Ameri, E. Pacor, R. Puglia & P. Augliera (2014). Pan-European ground-motion prediction equations for the average horizontal component of PGA, PGV, and 5%-damped PSA at spectral periods up to 3.0 s using the RESORCE dataset. *Bulletin of Earthquake Engineering* **12**(1), 391-430.
- Bommer, J.J., B. Dost, B. Edwards, P.P. Kruiver, P. Meijer, M. Ntinalexis, A. Rodriguez-Marek, E. Ruigrok, J. Spetzler & P.J. Stafford (2017b). *V4 Ground-Motion Model (GMM) for Response Spectral Accelerations, Peak Ground Velocity, and Significant Durations in the Groningen Field*. Version 2.1, 23 June 2017, 541 pp.
- Bommer, J.J., B. Dost, B. Edwards, P.P. Kruiver, P. Meijer, M. Ntinalexis, A. Rodriguez-Marek, E. Ruigrok, J. Spetzler & P.J. Stafford (2018). *V5 Ground-Motion Model for the Groningen Field*. Revision 1, 14 March 2018, 299 pp.
- Bommer, J.J., B. Dost, B. Edwards, P.P. Kruiver, M. Ntinalexis, A. Rodriguez-Marek, P.J. Stafford & J. van Elk (2017c). Developing a model for the prediction of ground motions due to earthquakes in the Groningen gas field. *Netherlands Journal of Geoscience* **96**(5), s203-s213.
- Bommer, J.J., B. Dost, B. Edwards, P.J. Stafford, J. van Elk, D. Doornhof & M. Ntinalexis (2016). Developing an application-specific ground-motion model for induced seismicity. *Bulletin of the Seismological Society of America* **106**(1), 158-173.
- Bommer, J.J., P.J. Stafford, B. Edwards, B. Dost, E. van Dedem, A. Rodriguez-Marek, P. Kruiver, J. van Elk, D. Doornhof & M. Ntinalexis (2017a). Framework for a ground-motion model for induced seismic hazard and risk analysis in the Groningen gas field, The Netherlands. *Earthquake Spectra* **33**(2), 481-498.
- Boore, D.M. (2005). *SMSIM – Fortran programs for simulating ground motions from earthquakes: Version 2.3—A revision of OFR 96-80*. US Geological Survey Open-File Report 00-509, 55 pp.
- Boore, D.M. (2009). Comparing stochastic point-source and finite-source ground-motion simulations: SMSIM and EXSIM. *Bulletin of the Seismological Society of America* **99**, 3202-3216.
- Boore, D.M., J.P. Stewart, E. Seyhan & G.M. Atkinson (2014). NGA-West2 equations for predicting PGA, PGV, and 5% damped PSA for shallow crustal earthquakes. *Earthquake Spectra* **30**(3).
- Brune, J.N. (1970). Tectonic stress and spectra of seismic shear waves from earthquakes. *Journal of Geophysical Research* **75**, 4997-5009.
- Brune, J.N. (1971). Correction. *Journal of Geophysical Research* **76**, 5002.

Campbell, K.W. & Y. Bozorgnia (2014). NGA-West2 ground motion model for the average horizontal components of PGA, PGV, and 5%-damped elastic pseudo-acceleration response spectra. *Earthquake Spectra* **30**(3), 1087-1115.

Chiou, B.S.J. & R.R. Youngs (2014). Update of the Chiou and Youngs NGA model for the average horizontal component of peak ground motion and response spectra. *Earthquake Spectra* **30**(3), 1117-1153.

Darendeli, M. (2001). *Development of a new family of normalized modulus reduction and material damping curves. Ph.D. Thesis, Dept. of Civil Eng., University of Texas, Austin, TX.*

De Crook, T. & B. Wassing (1996). Opslingering van trillingen bij aardbevingen in Noord-Nederland, *KNMI-RGD interim report*, 14pp.

De Crook, T. & B. Wassing (2001). Voorspelling van de opslingering van trillingen bij aardbevingen, *Geotechniek*, 47-53.

Dost, B., B. Edwards & J.J. Bommer (2018). The relationship between M and M_L – a review and application to induced seismicity in the Groningen gas field, the Netherlands. *Seismological Research Letters* **89**(3), 1062-1074.

Dost, B., E. Ruigrok & J. Spetzler (2017). Development of probabilistic seismic hazard assessment for the Groningen gas field. *Netherlands Journal of Geoscience* **96**(5), s235-s245.

Edwards, B., B. Zurek, E. van Dedem, P.J. Stafford, S. Oates, J. van Elk, B. deMartin & J.J. Bommer (2019). Simulations for the development of a ground motion model for induced seismicity in the Groningen gas field, The Netherlands. *Bulletin of Earthquake Engineering*, **17**, 4441-4456.

Hofman, L. J., Ruigrok, E., Dost, B. & Paulssen, H. (2017). A shallow seismic velocity model for the Groningen area in the Netherlands. *Journal of Geophysical Research: Solid Earth*, **122**(10), 8035-8050.

Kottke, A.R. & E.M. Rathje (2008). *Technical Manual for STRATA*. PEER Report 2008/10, Pacific Earthquake Engineering Research Center, University of California at Berkeley, February, 84 pp.

Kruiver, P.P., A. Wiersma, F.H. Kloosterman, G. de Lange, M. Korff, J. Stafleu, F. Busscher, R. Harting, J.L. Gunnink, R.A. Green, J. van Elk & D. Doornhof (2017b). Characterisation of the Groningen subsurface for seismic hazard and risk modelling. *Netherlands Journal of Geosciences* **96**(5), s215-s233.

Kruiver, P.P., G. de Lange, A. Wiersma, P. Meijers, M. Korff, J. Peeters, J. Stafleu, R. Harting, R. Dambrink, F. Busschers, J. Gunnink (2015). *Geological schematisation of the shallow subsurface of Groningen - For site response to earthquakes for the Groningen gas field*. Deltares Report No. 1209862-005-GEO-0004-v5-r, 16 March 2015.

Kruiver, P. P., E. van Dedem, E. Romijn, G. de Lange, M. Korff, J. Stafleu, J.L. Gunnink., A. Rodriguez-Marek, J.J. Bommer, J. van Elk & D. Doornhof (2017a). An integrated shear-wave velocity model for the Groningen gas field, The Netherlands. *Bulletin of Earthquake Engineering* **15**(9), 3555-3580.

Meng, F.Y. (2003). *Dynamic Properties of Sandy and Gravelly Soils*, PhD Thesis, Department of Civil Engineering, University of Texas, Austin, TX.

Motazedian, D. & G.M. Atkinson (2005). Stochastic finite-fault modelling based on a dynamic corner frequency. *Bulletin of the Seismological Society of America* **95**, 995-1010.

Noorlandt, R.P., P.P. Kruiver, M.P.E. de Kleine, M. Karaoulis, G. de Lange, A. Di Matteo, J. von Ketelhodt, E. Ruigrok, B. Edwards, A. Rodriguez-Marek, J.J. Bommer, J. van Elk & D. Doornhof (2018). Characterisation of ground-motion recording stations in the Groningen gas field. *Journal of Seismology* **22**(3), 605-623.

Rathje, E.M., A.R. Kottke & M.C. Ozbey (2005). Using inverse random vibration theory to develop input Fourier amplitude spectra for use in site response. *Proceedings of 16th International Conference on Soil Mechanics and Geotechnical Engineering: TC4 Earthquake Geotechnical Engineering Satellite Conference*, September 2005, Osaka, Japan, 160-166, DOI: 10.13140/2.1.3695.3920.

Rodriguez-Marek, A., F. Cotton, N.A. Abrahamson, S. Akkar, L. Al Atik, B. Edwards, G.A. Montalva & H.M. Dawood (2013). A model for single-station standard deviation using data from various tectonic regions. *Bulletin of the Seismological Society of America* **103**(6), 3149-3163.

Rodriguez-Marek, A., P.P. Kruiver, P. Meijers, J.J. Bommer, B. Dost, J. van Elk & D. Doornhof (2017). A regional site-response model for the Groningen gas field. *Bulletin of the Seismological Society of America* **107**(5), 2067-2077.

Romijn., R. (2017) *Groningen Velocity Model 2017 – Groningen full elastic velocity model September 2017*. NAM report.

Schneider, R. & E. Safak (2006). Extracting the building response using seismic interferometry: Theory and application to the Millikan Library in Pasadena, California. *Bulletin of the Seismological Society of America* **96**(2), 586-598.

Stafford, P.J., Rodriguez-Marek, A., B. Edwards, P.P. Kruiver & J.J. Bommer (2017). Scenario dependence of linear site effect factors for short-period response spectral ordinates. *Bulletin of the Seismological Society of America* **107**(6), 2859-2872.

Stafford, P.J., B.D. Zurek, M. Ntinalexis & J.J. Bommer (2019). Extensions to the Groningen ground-motion model for seismic risk calculations: component-to-component variability and spatial correlation. *Bulletin of Earthquake Engineering* **17**, 4417-4439.

Tonn, R. (1991). The determination of the seismic quality factor Q from VSP data: A comparison of different computational methods. *Geophysical Prospecting* **39**(1), 1-27.

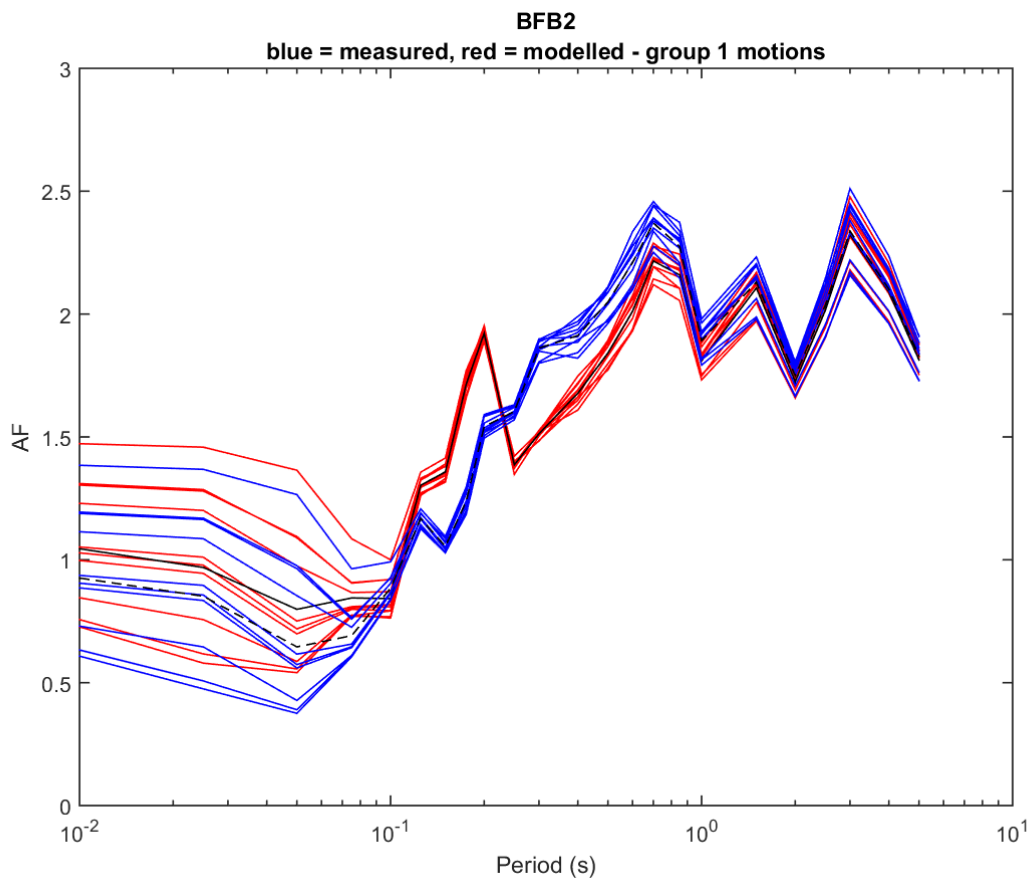
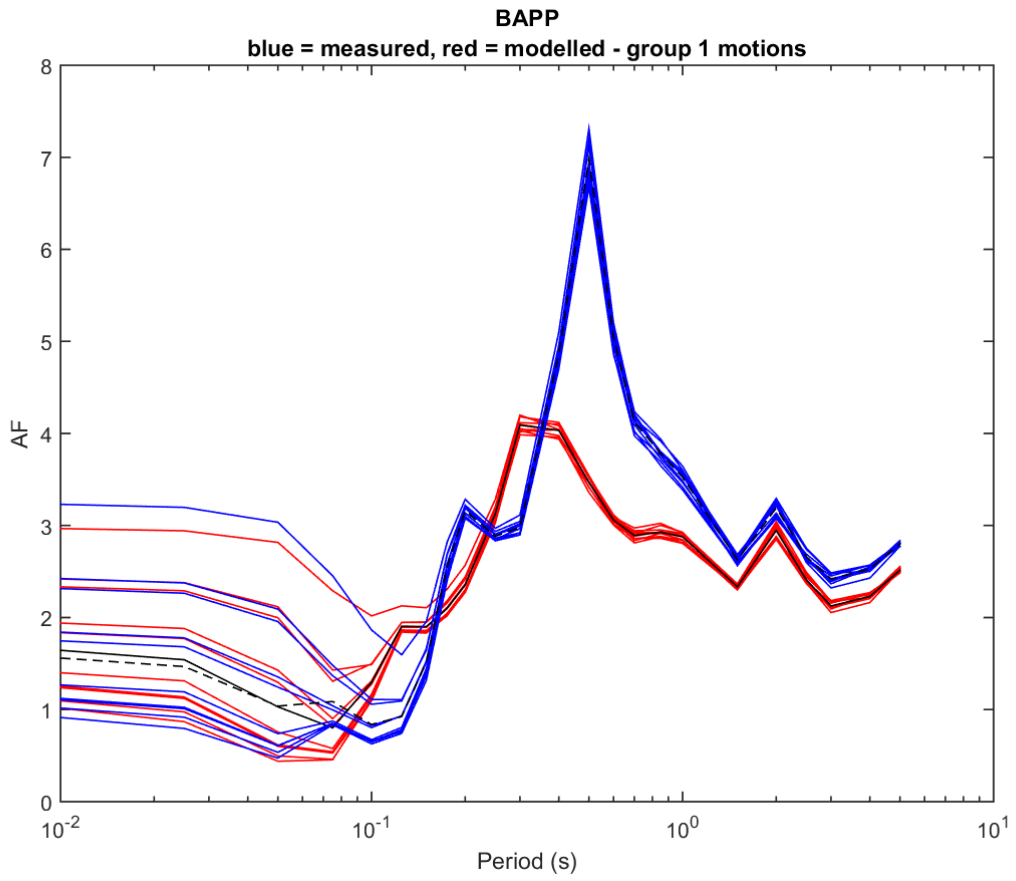
van Elk, J., S.J. Bourne, S.J. Oates, J.J. Bommer, R. Pinho & H. Crowley (2019). A probabilistic model to evaluate options for mitigating induced seismic risk. *Earthquake Spectra*, <https://doi.org/10.1193/050918EQS118M>

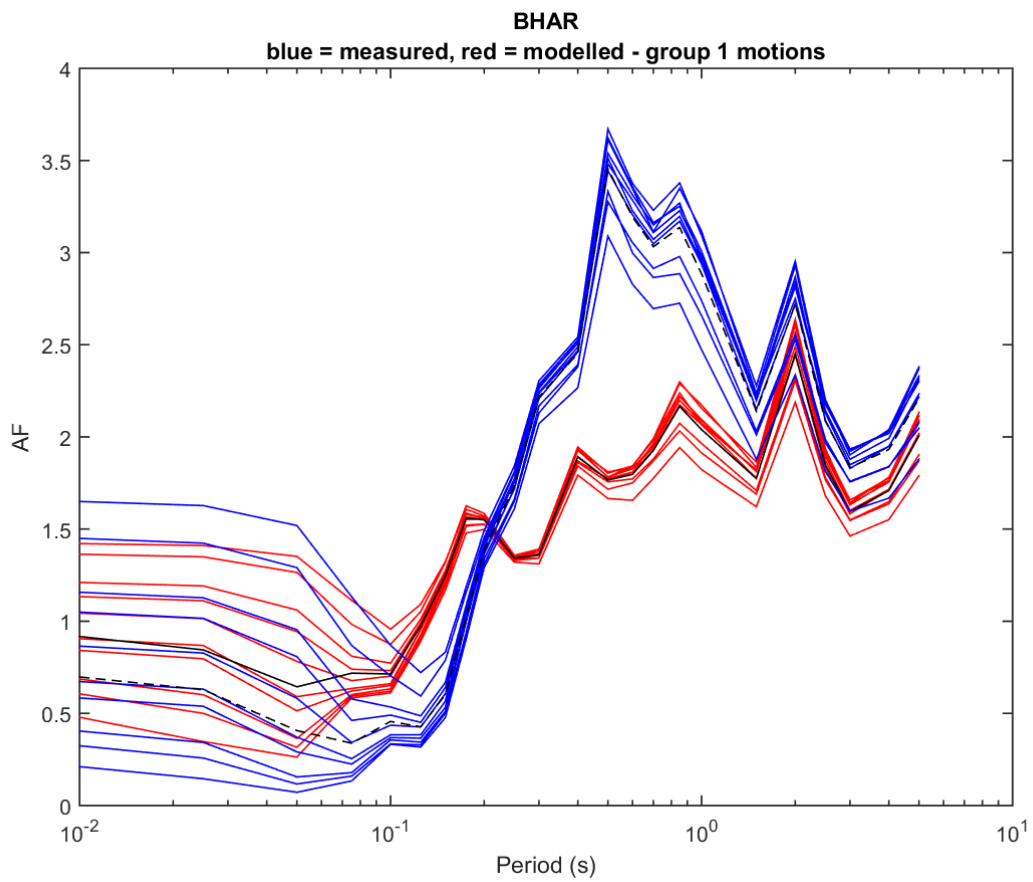
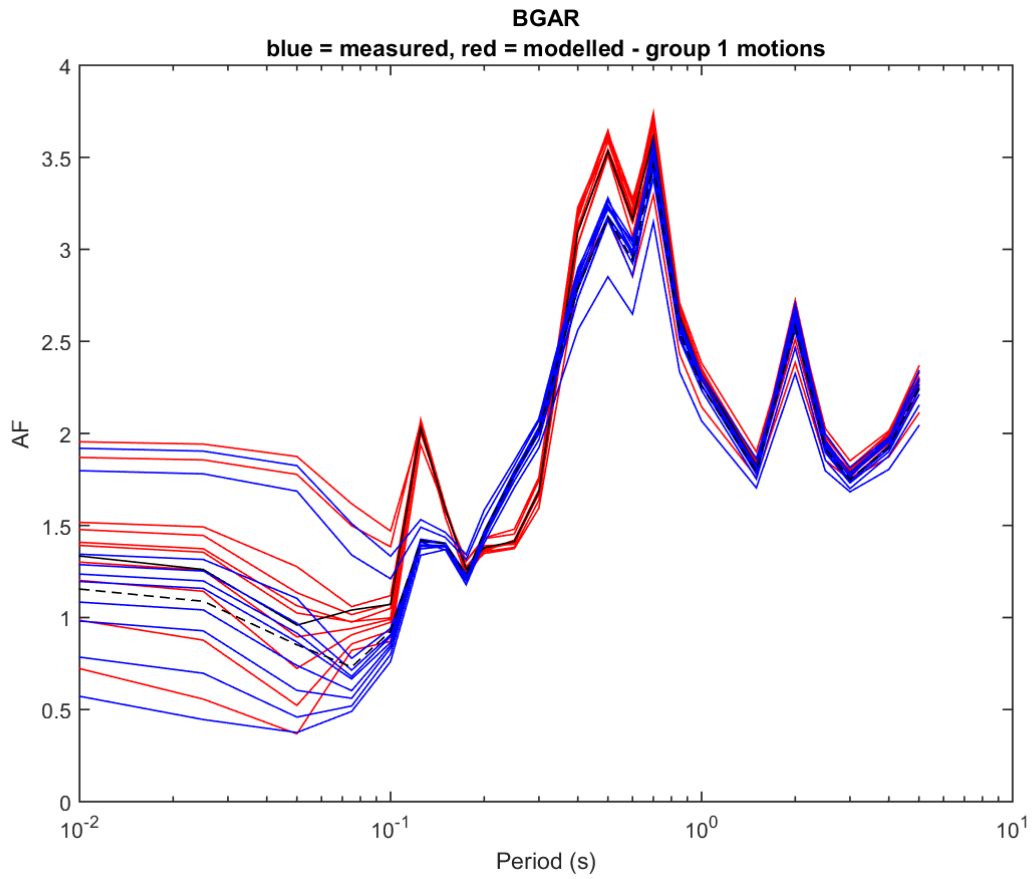
Yenier, E. & G.M. Atkinson (2015). Regionally adjustable generic ground-motion prediction equation based on equivalent point-source simulations: Application to central and eastern North America. *Bulletin of the Seismological Society of America* **105**, 1989-2009.

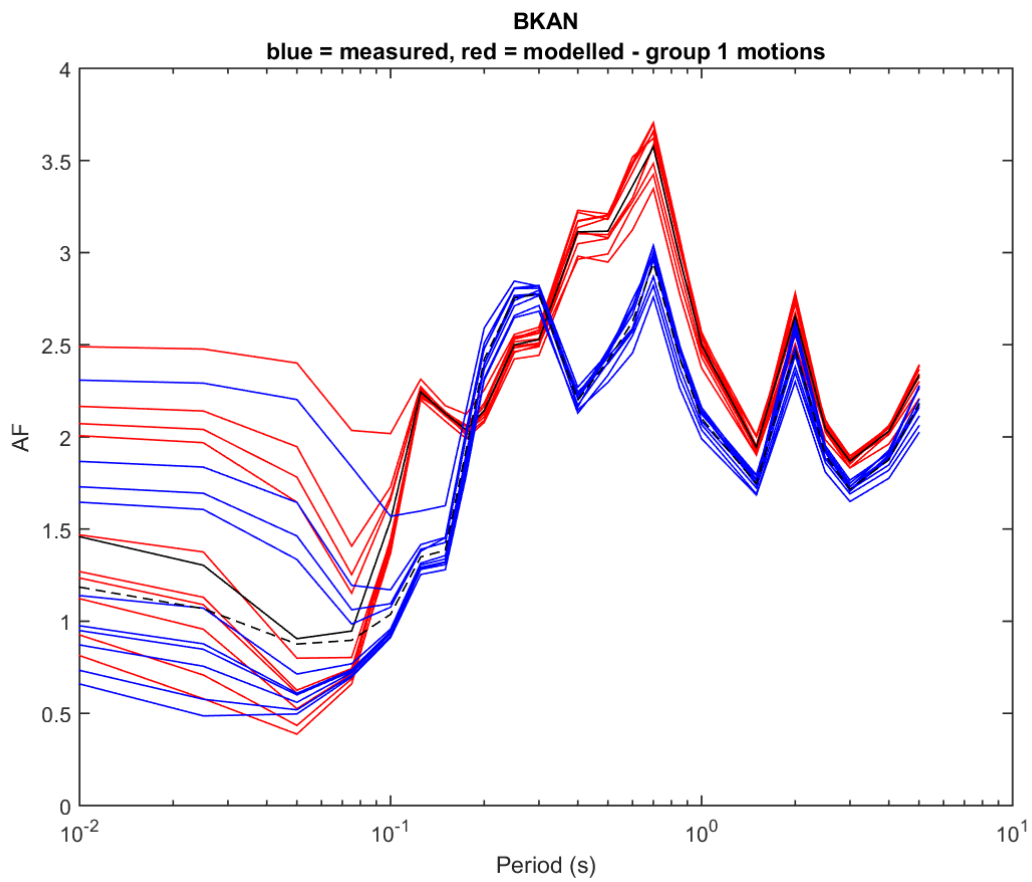
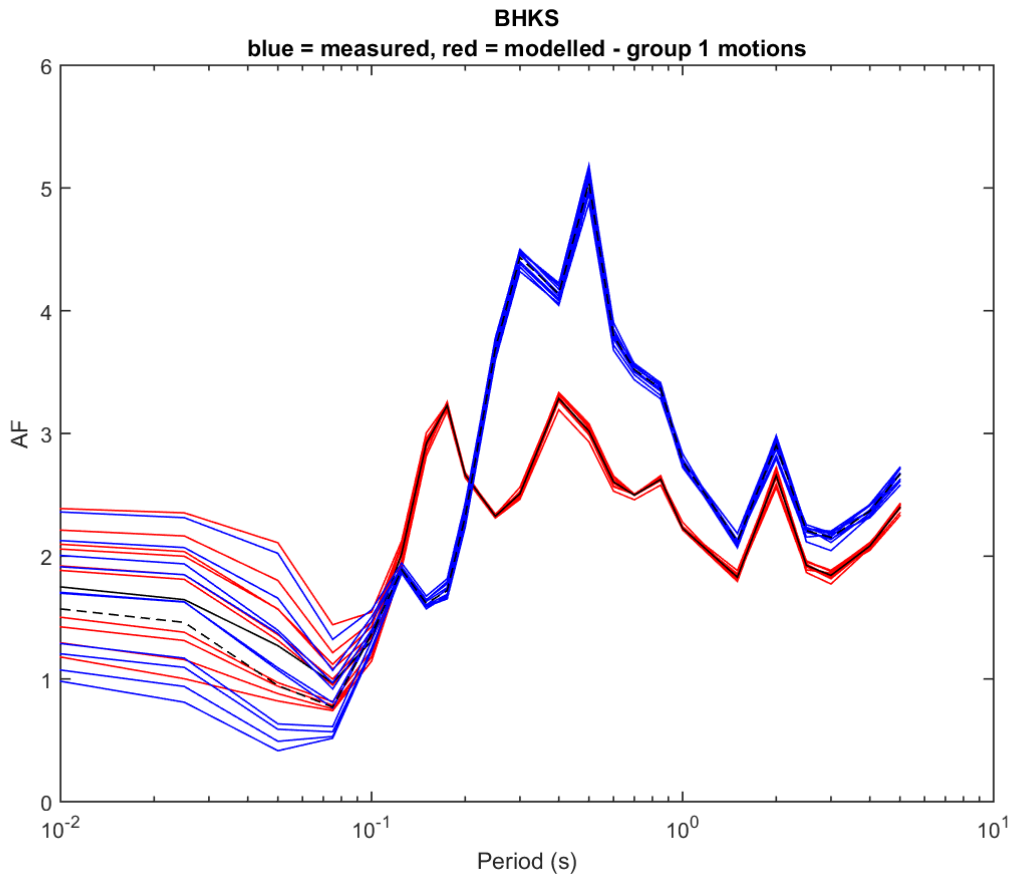
APPENDIX I

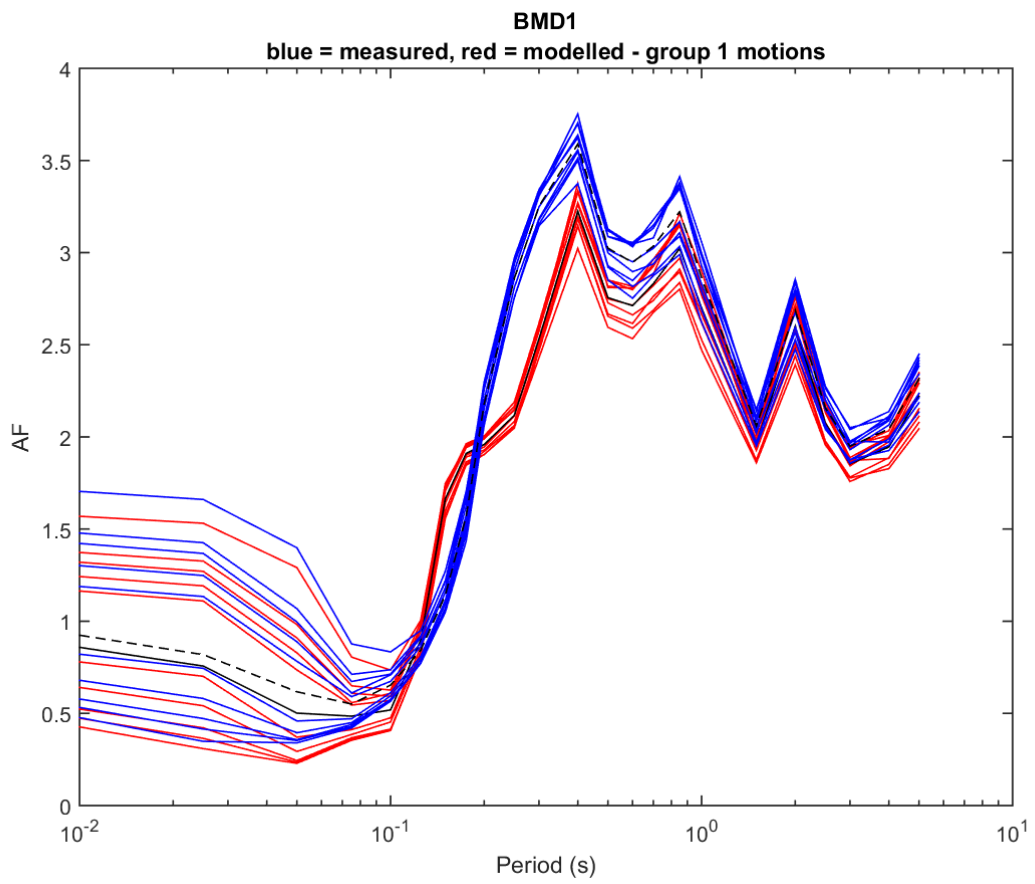
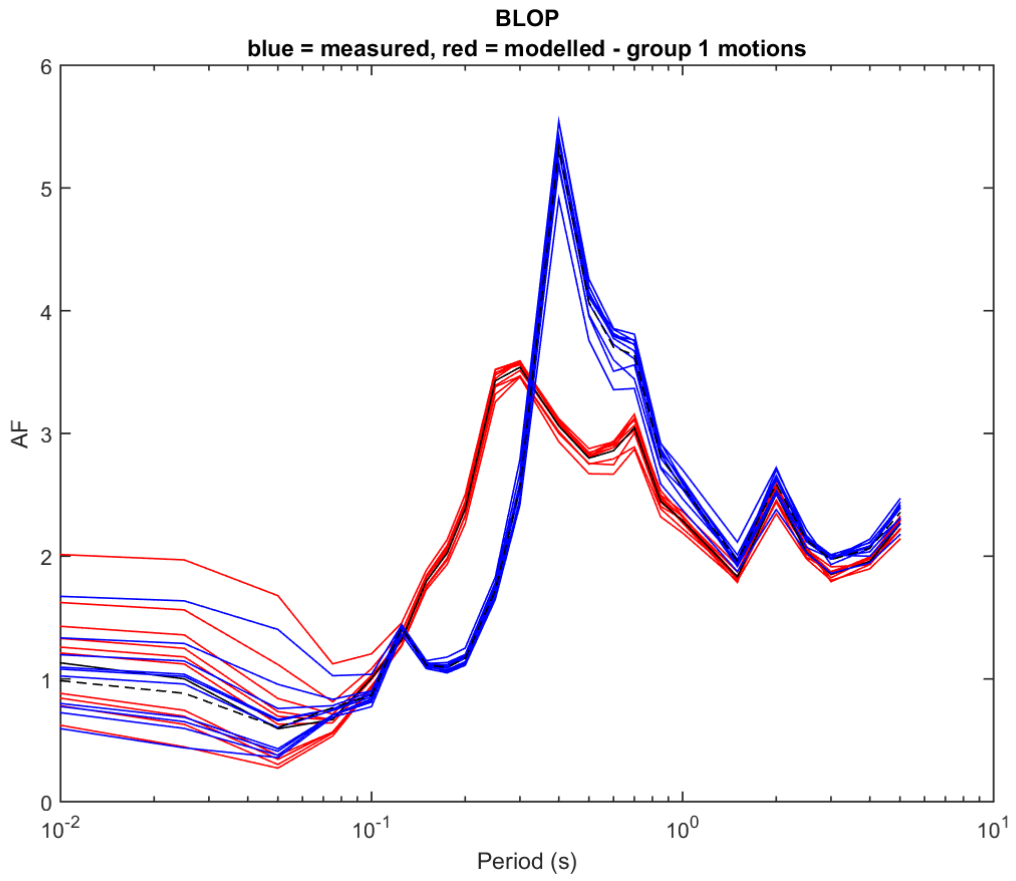
Amplification Factors at B-station Accelerograph Sites Calculated with Measured and Modelled Shear-wave Velocity Profiles

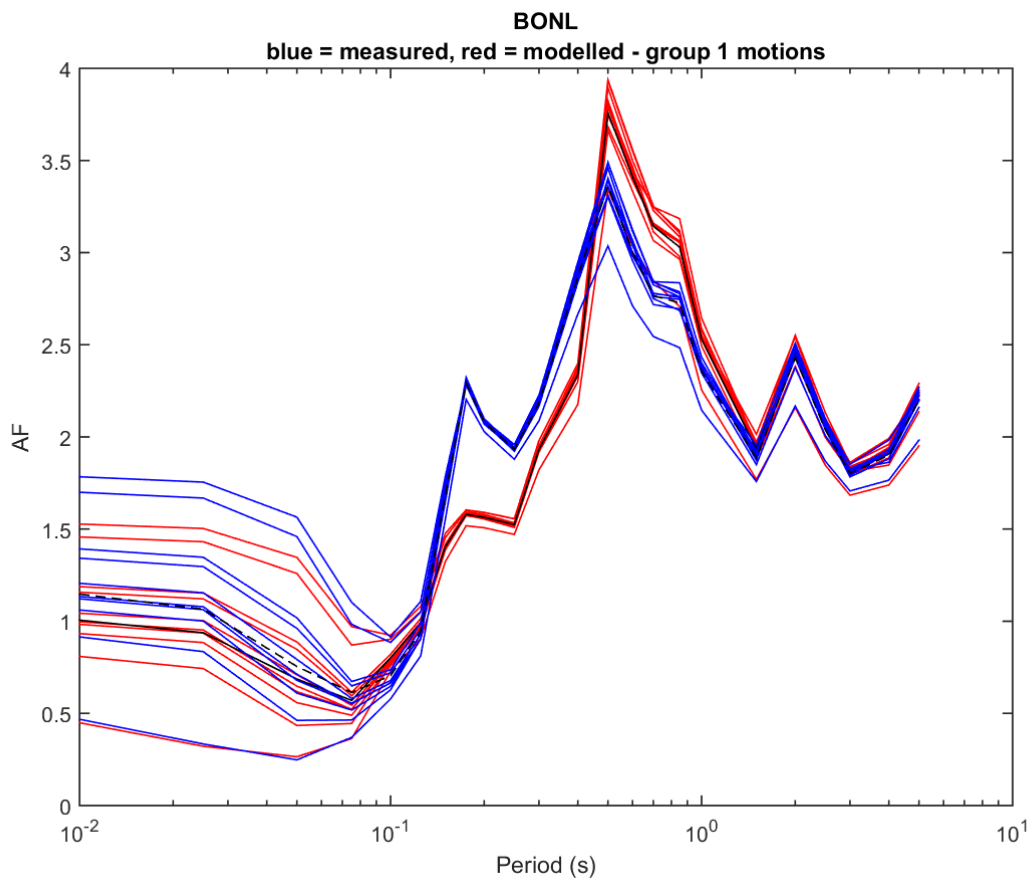
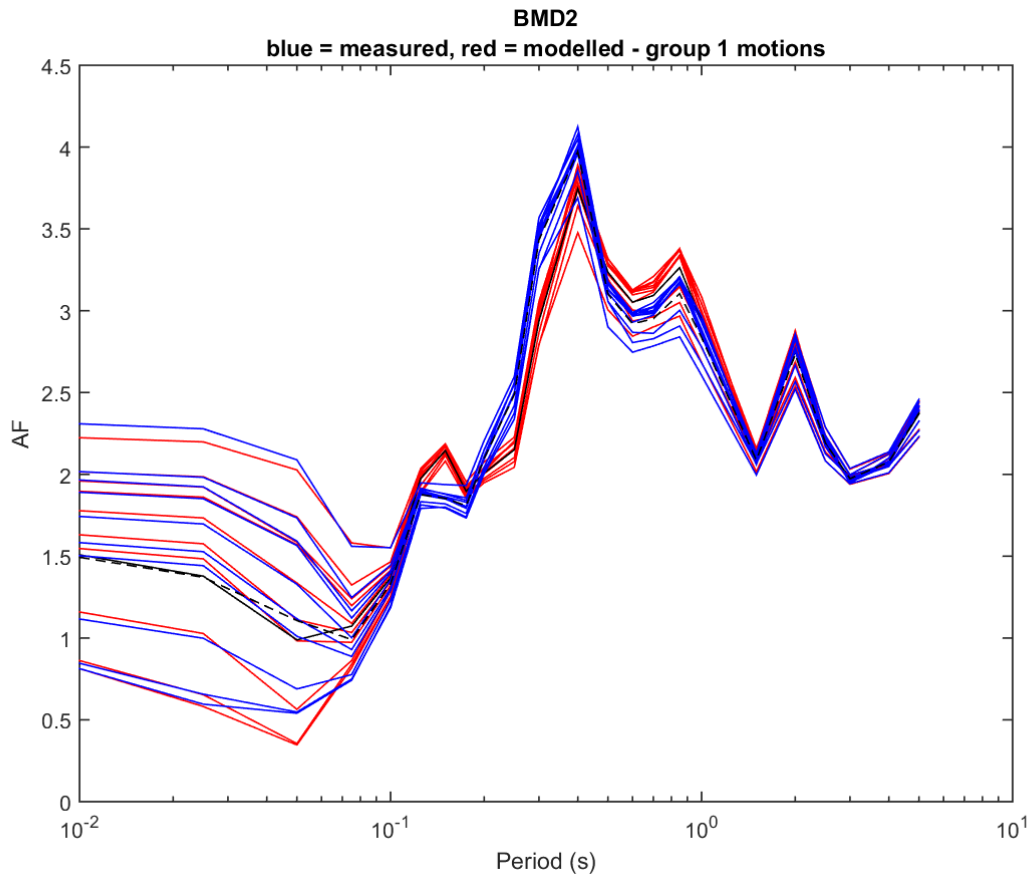
Each plot shows the AFs at an individual station calculated using STRATA and the Group 1 input FAS at NS_B (see Section 4.1), as a function of oscillator period. In each plot, the AFs obtained using the measured near-surface V_s profiles are plotted in blue, and those from the modelled profiles, based on the GeoTop model, are shown in red. For completeness, these plots are followed by the full set of comparisons between the measured (blue) and modelled (red) V_s profiles.

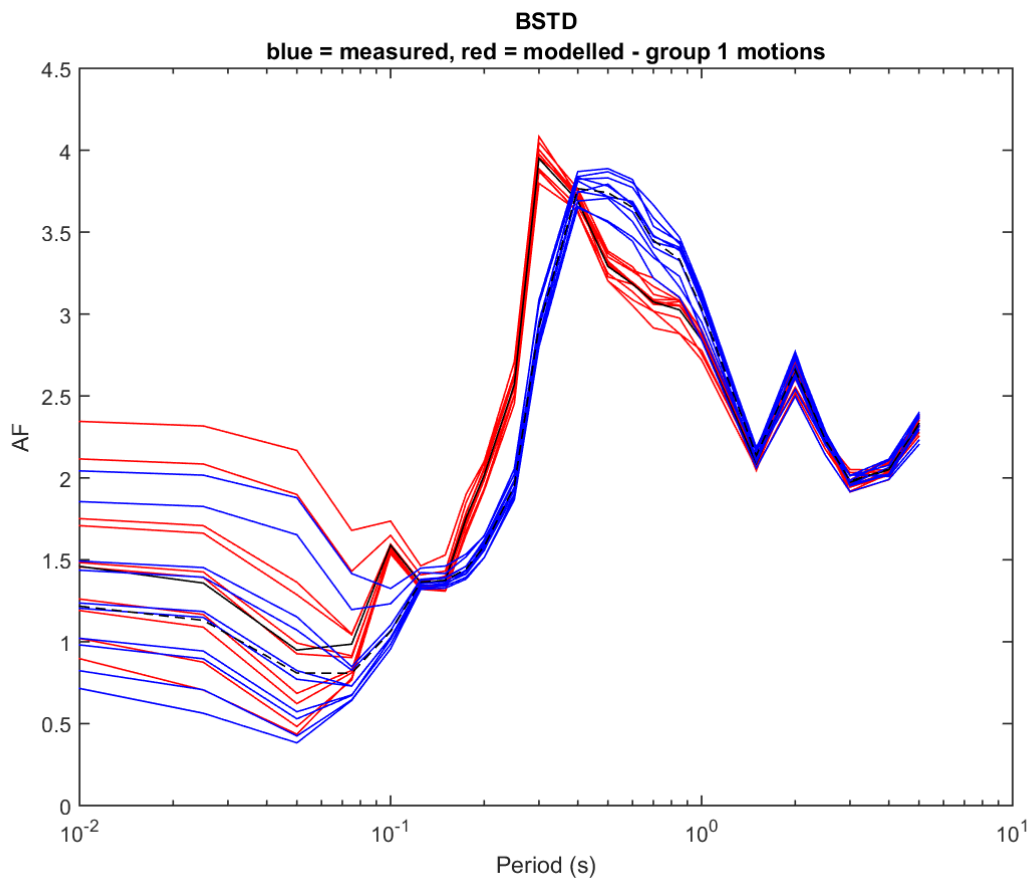
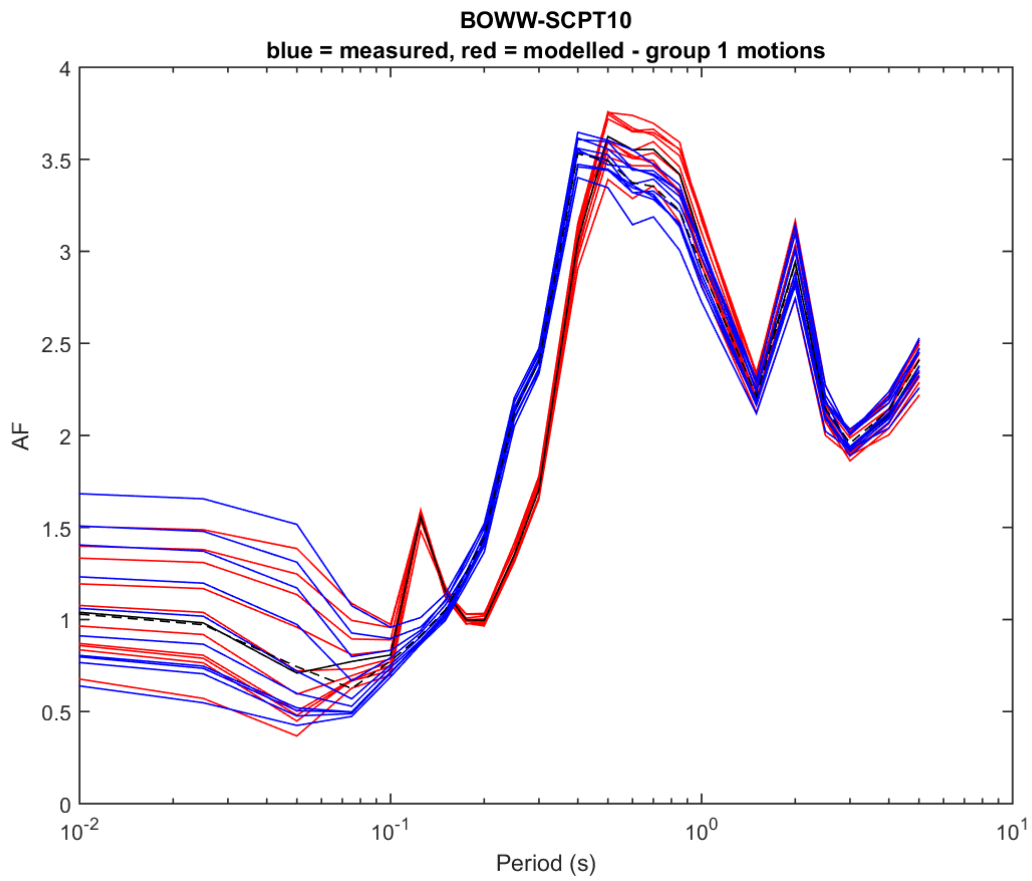


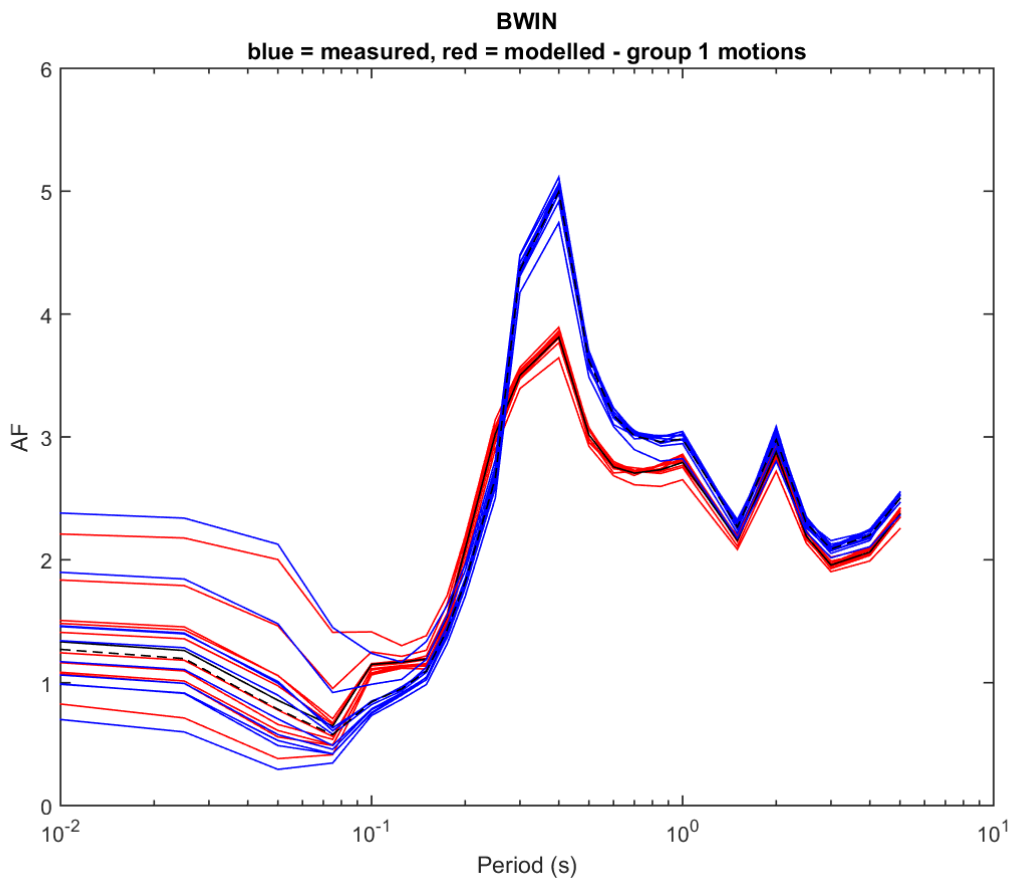
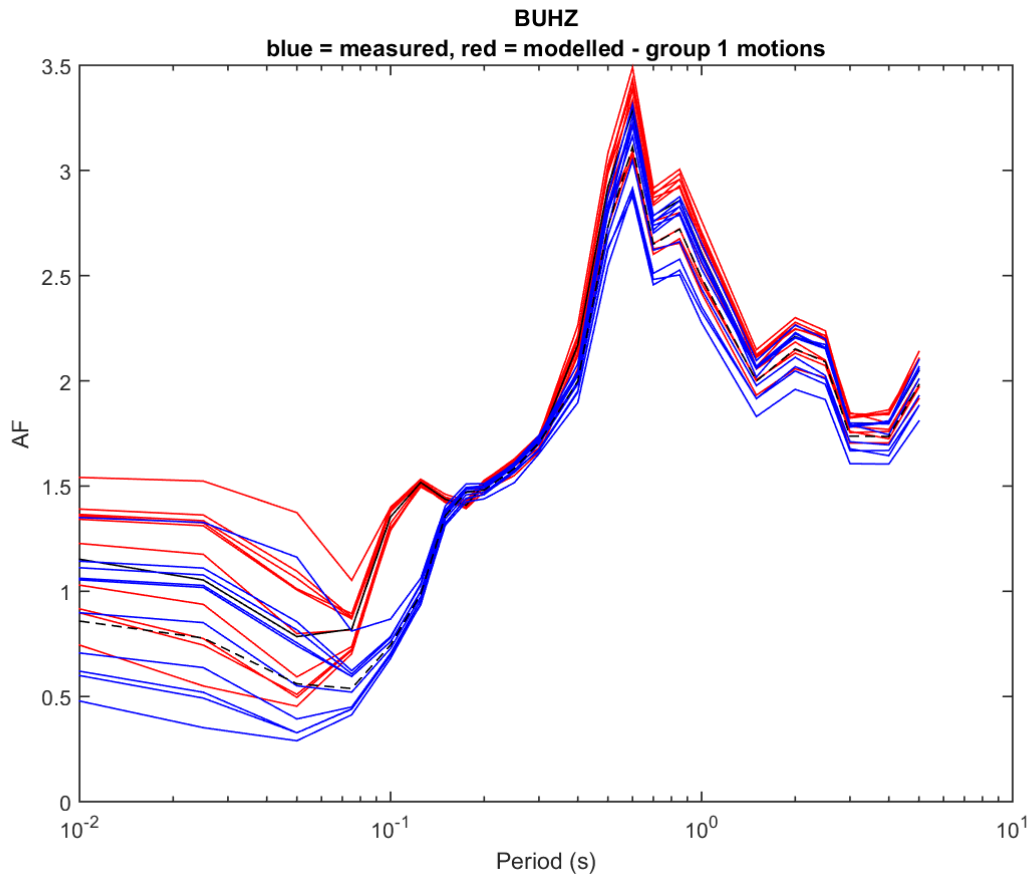


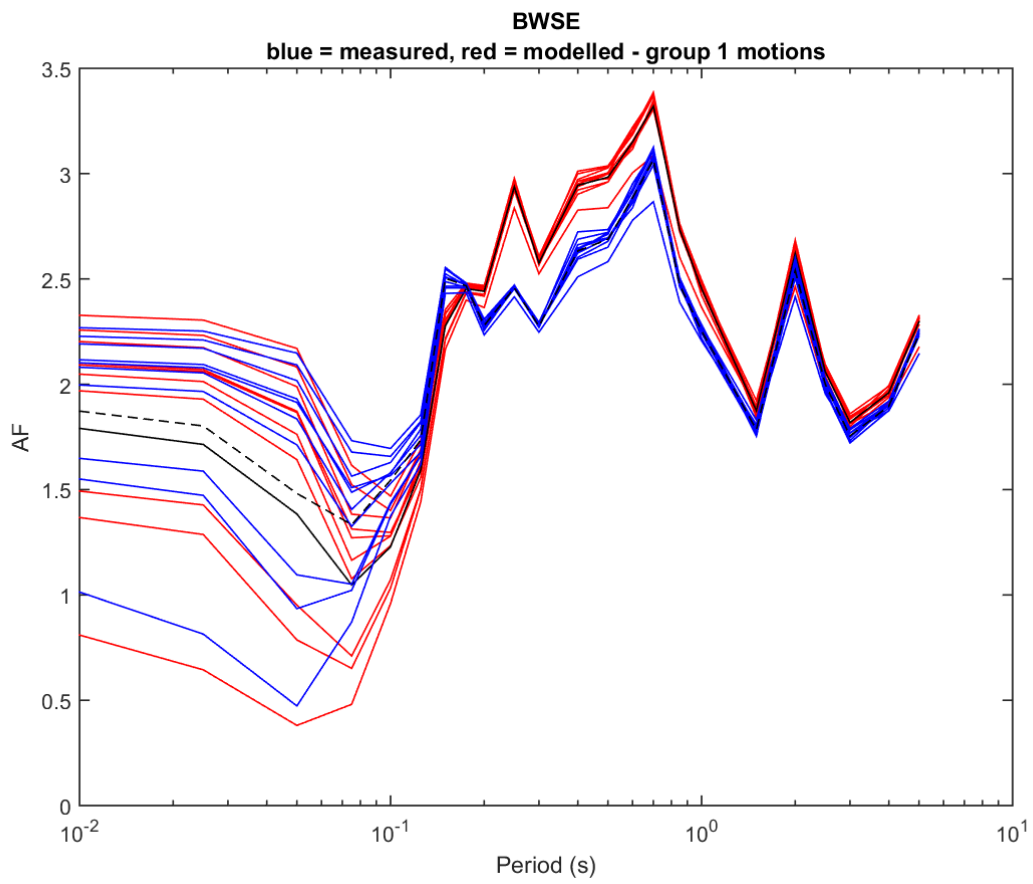
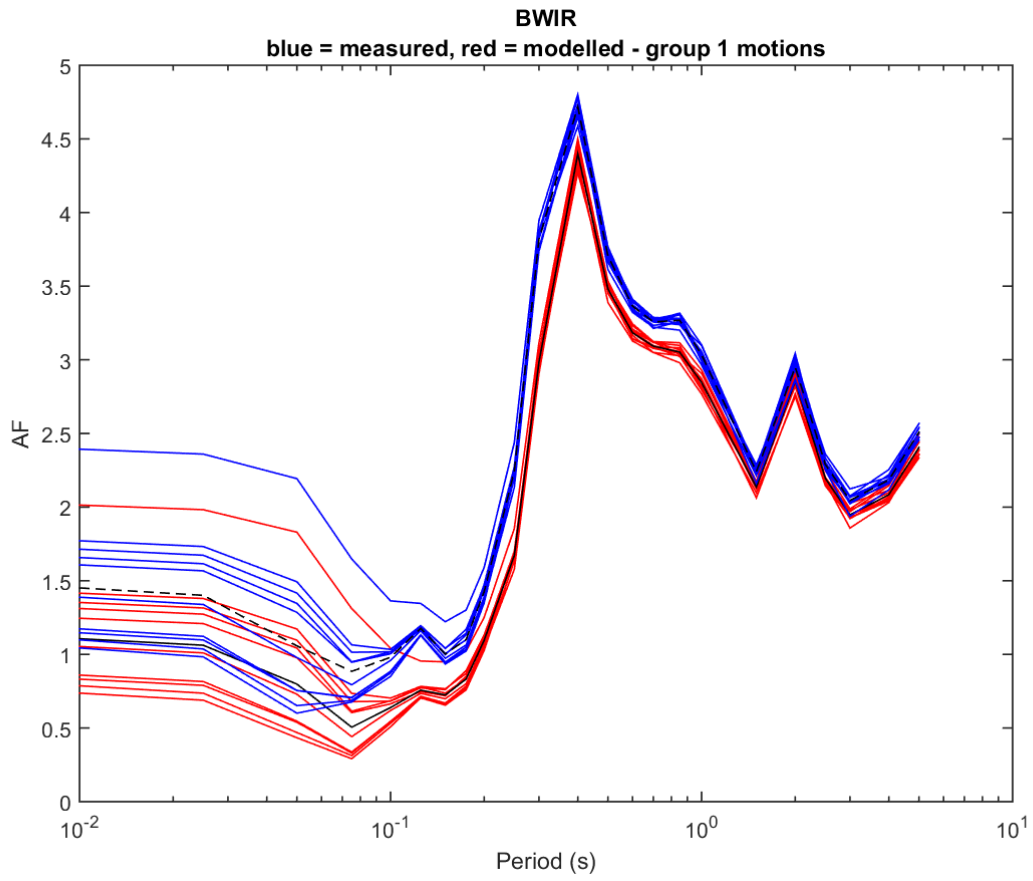


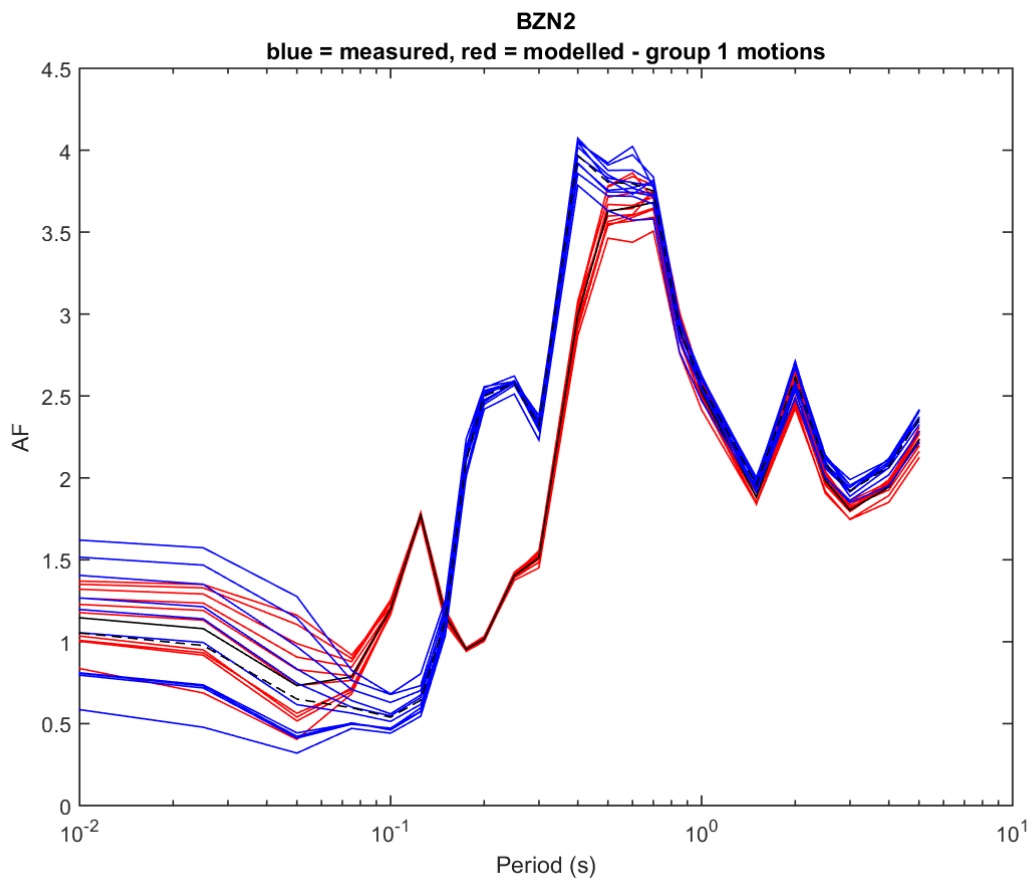
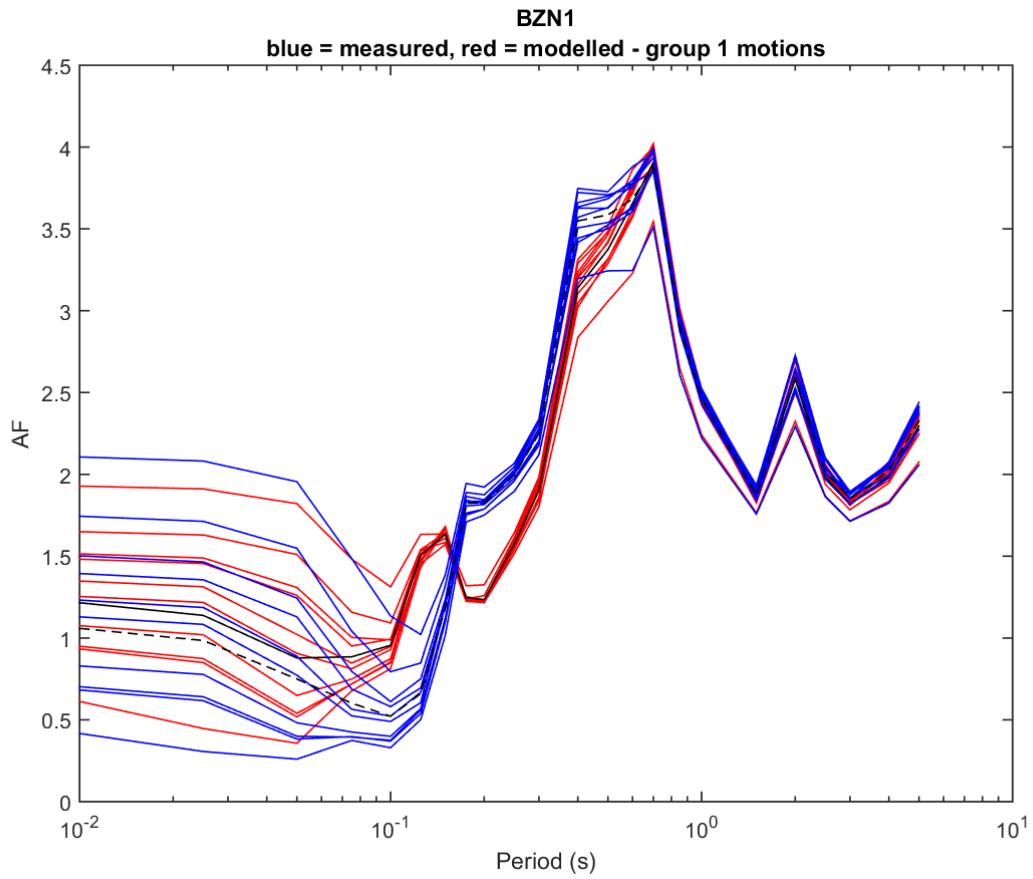


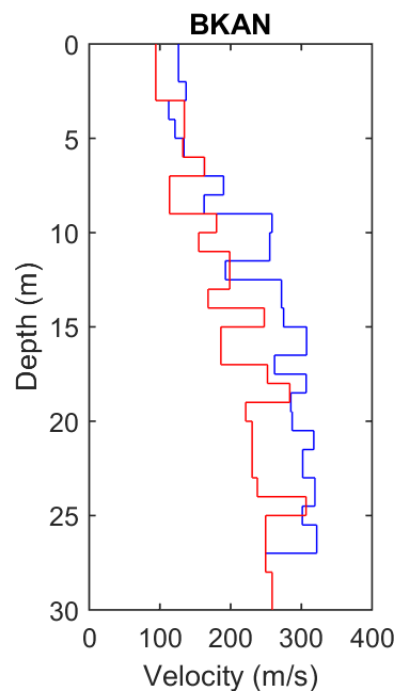
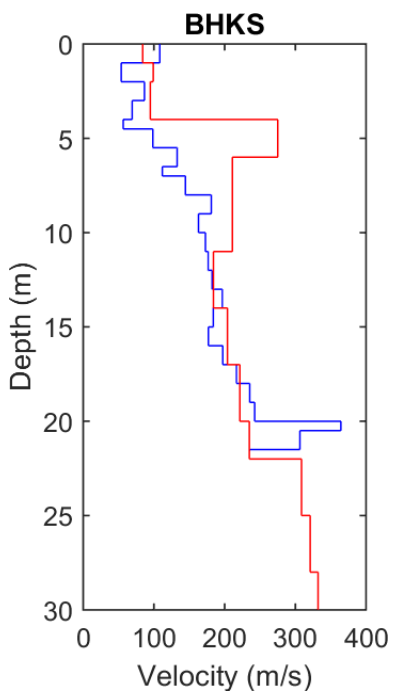
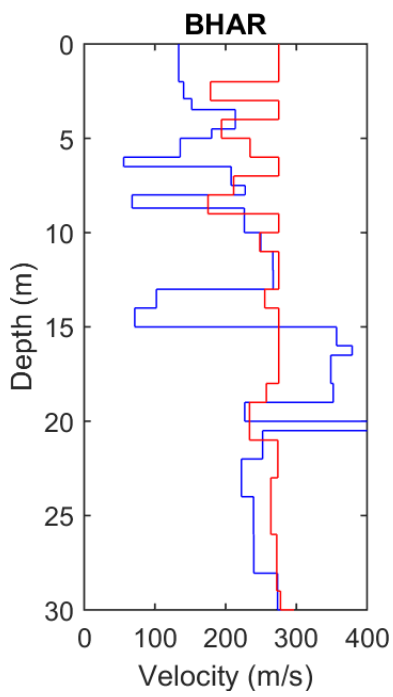
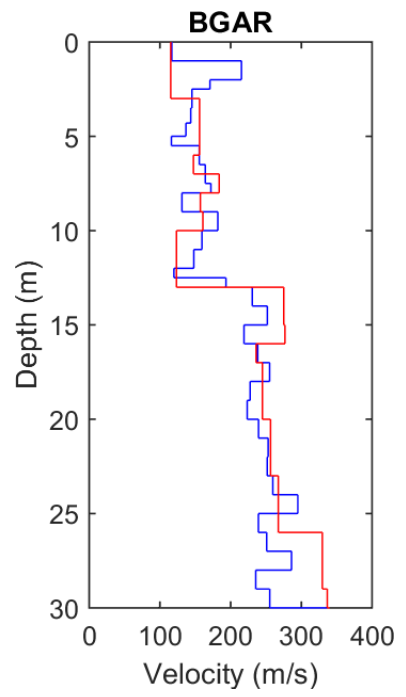
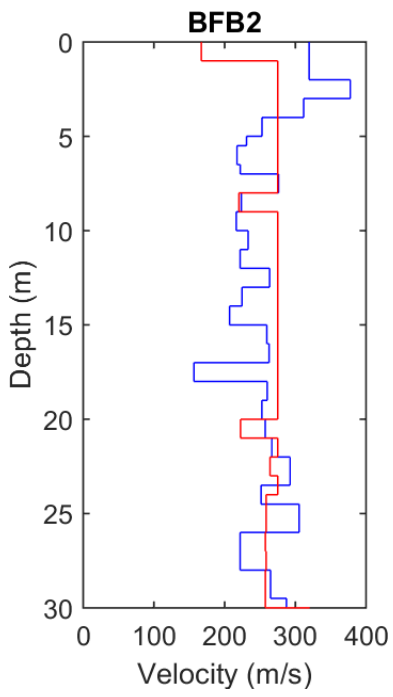
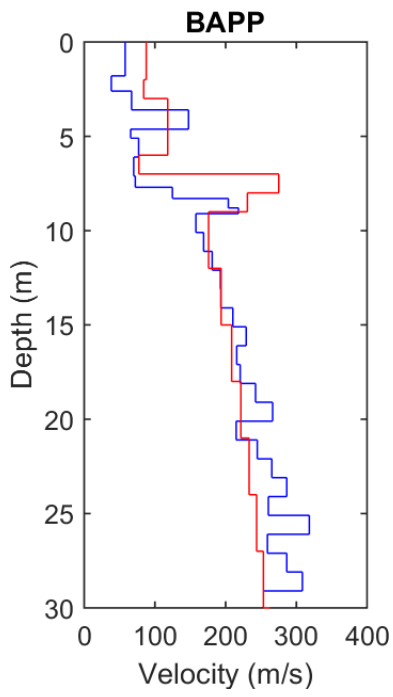


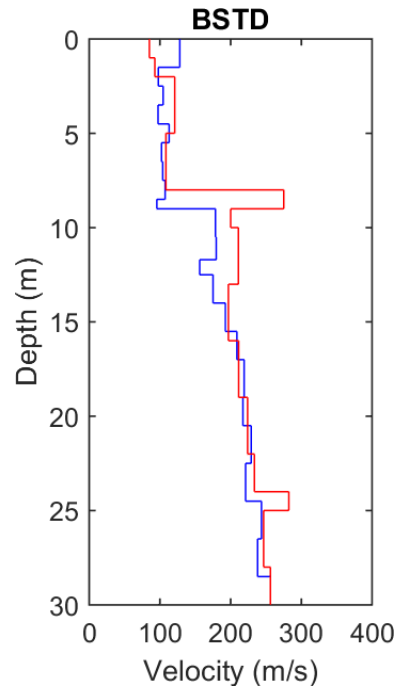
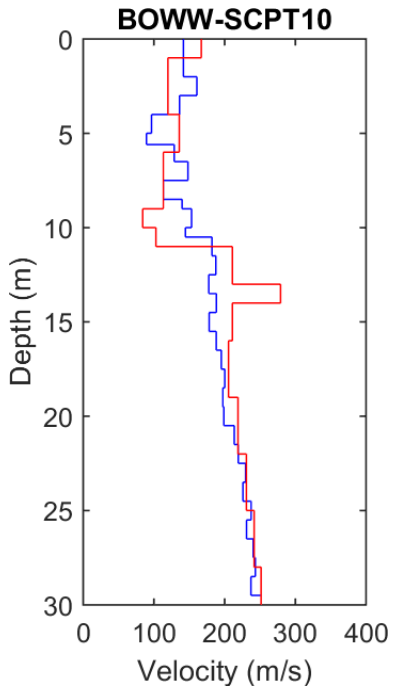
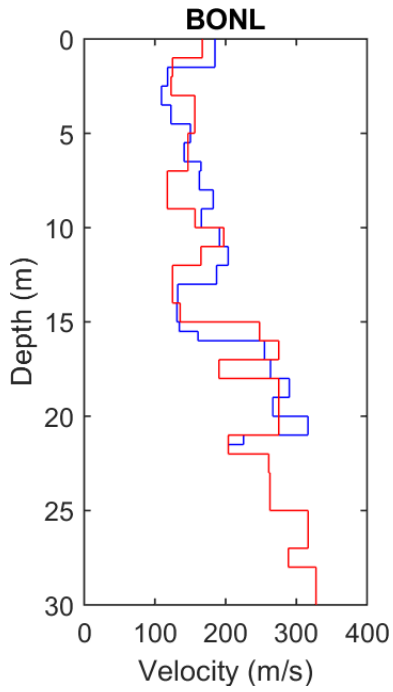
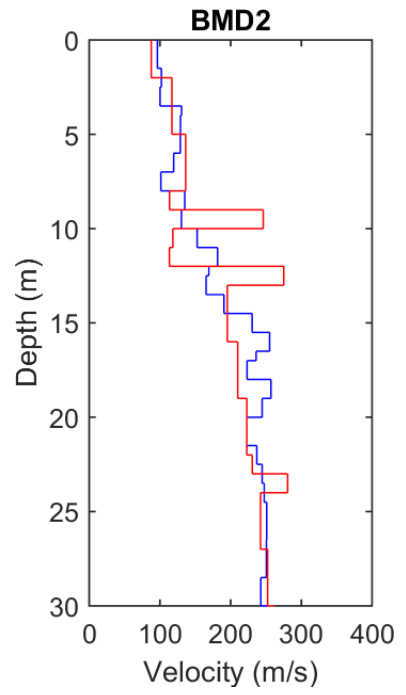
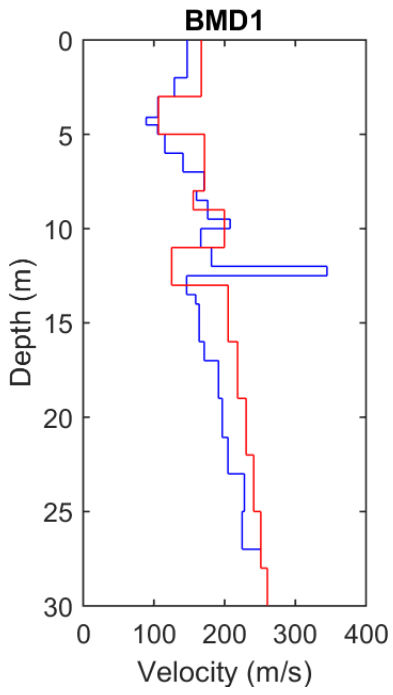
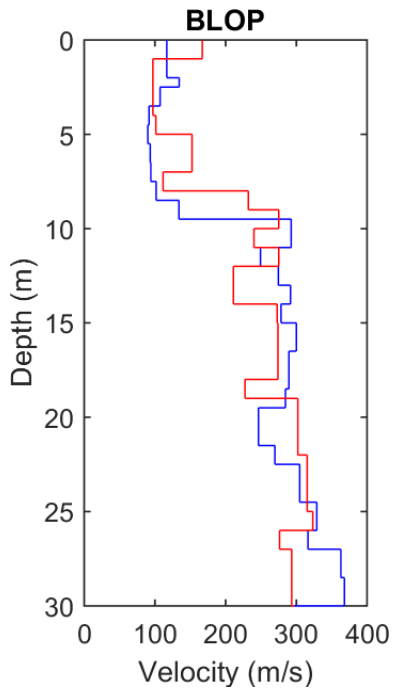


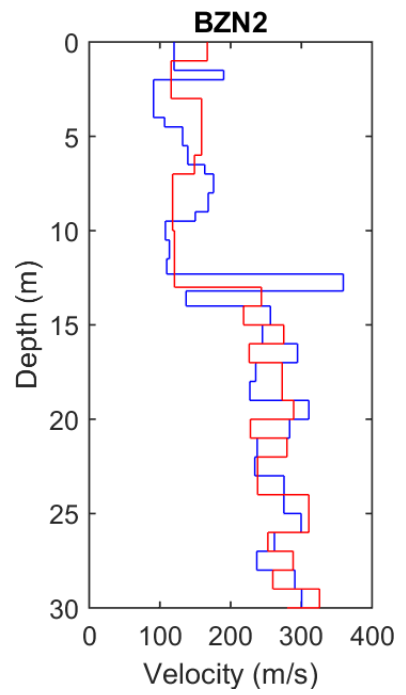
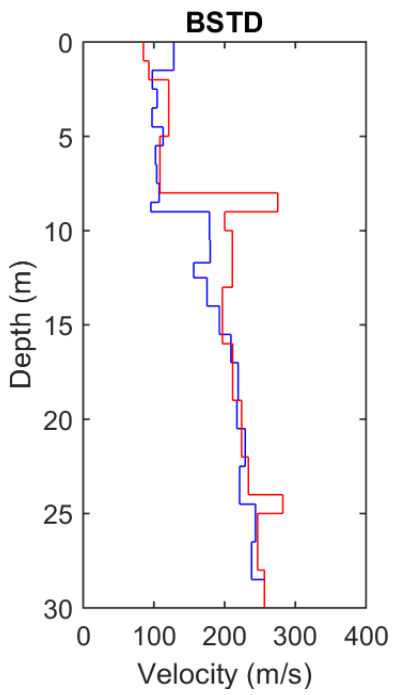
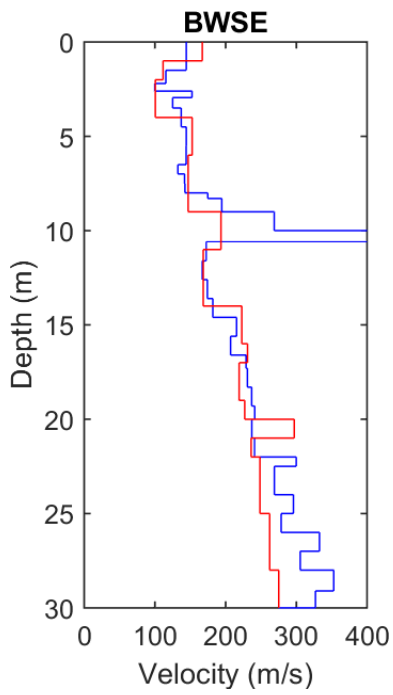
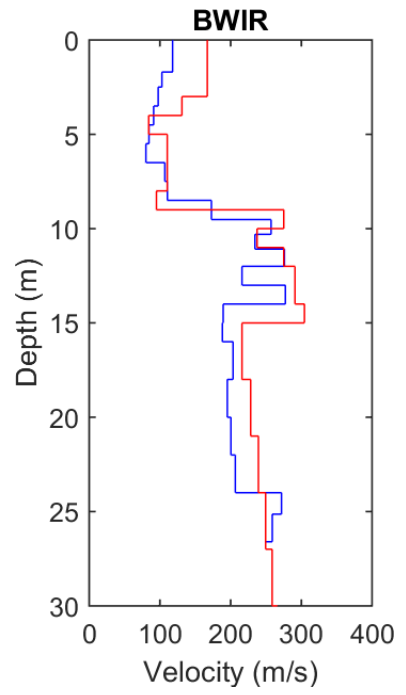
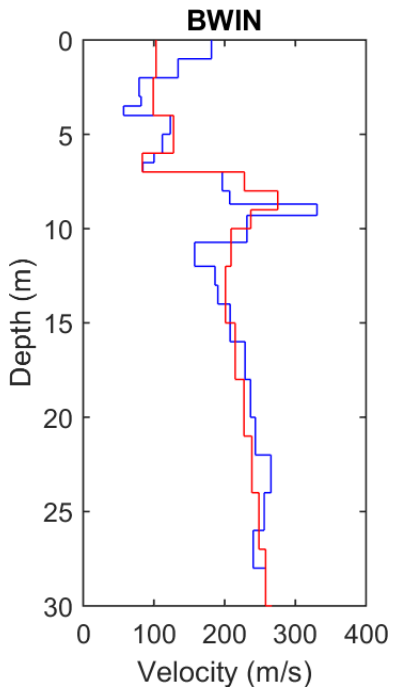
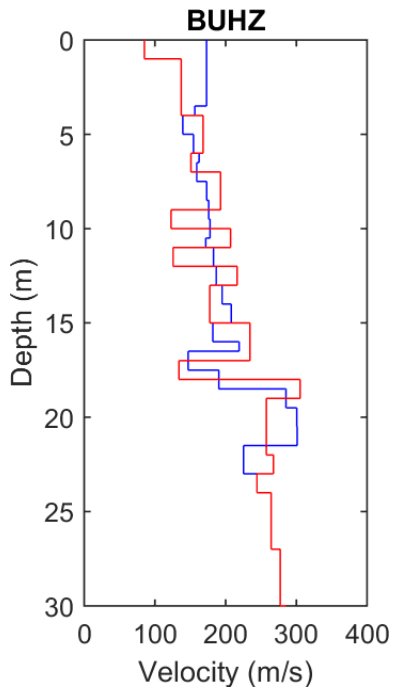










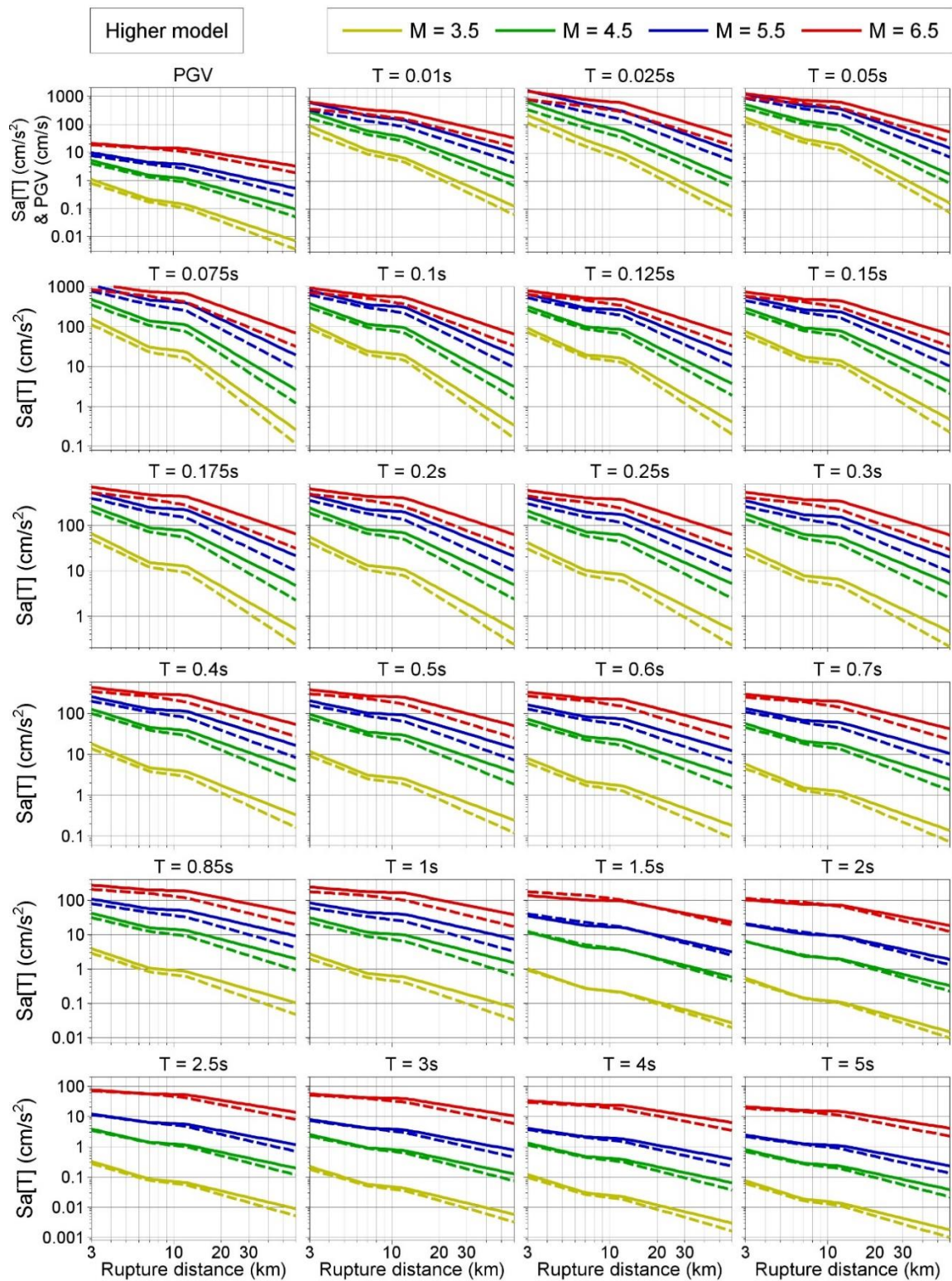


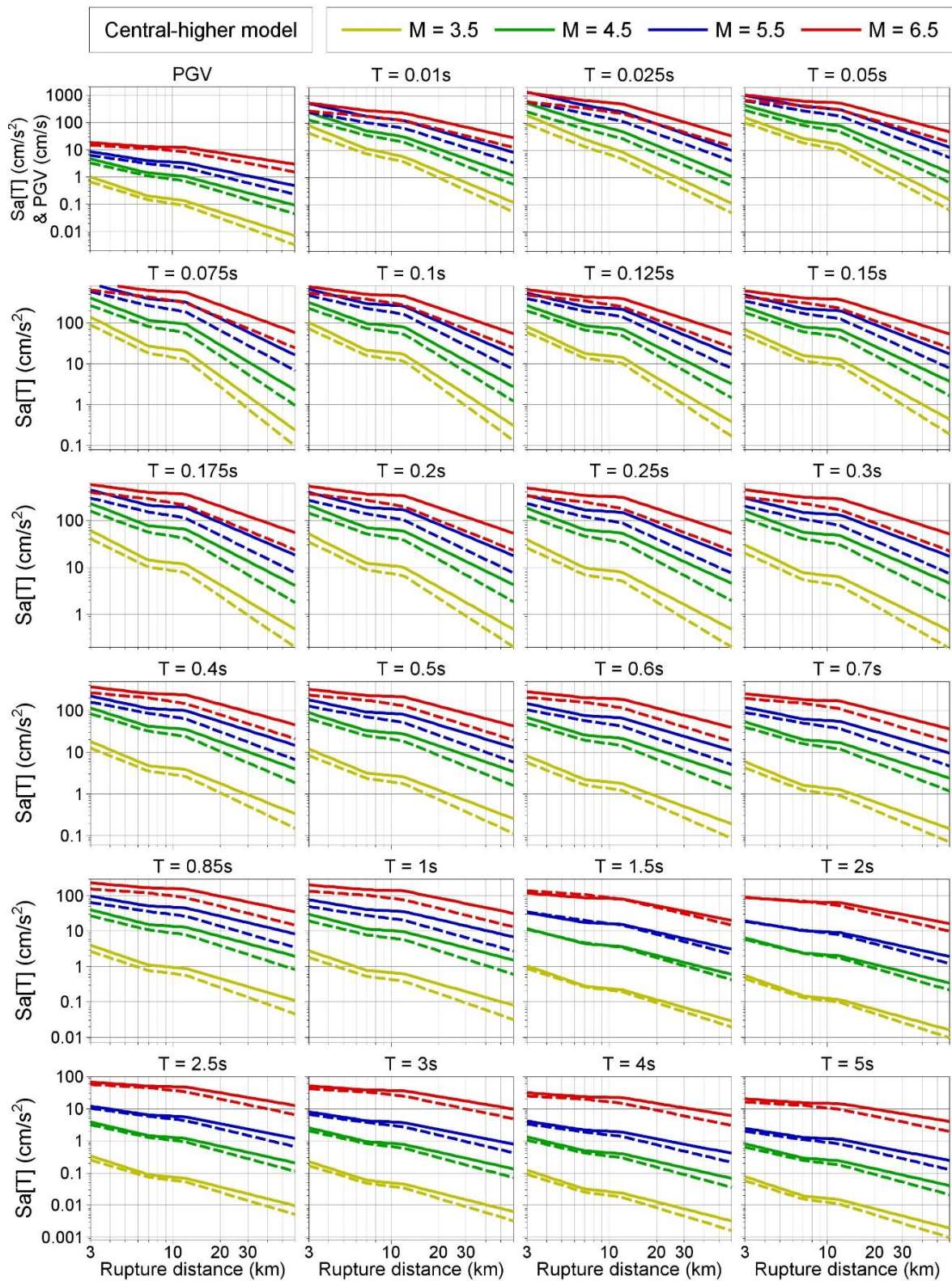
APPENDIX II

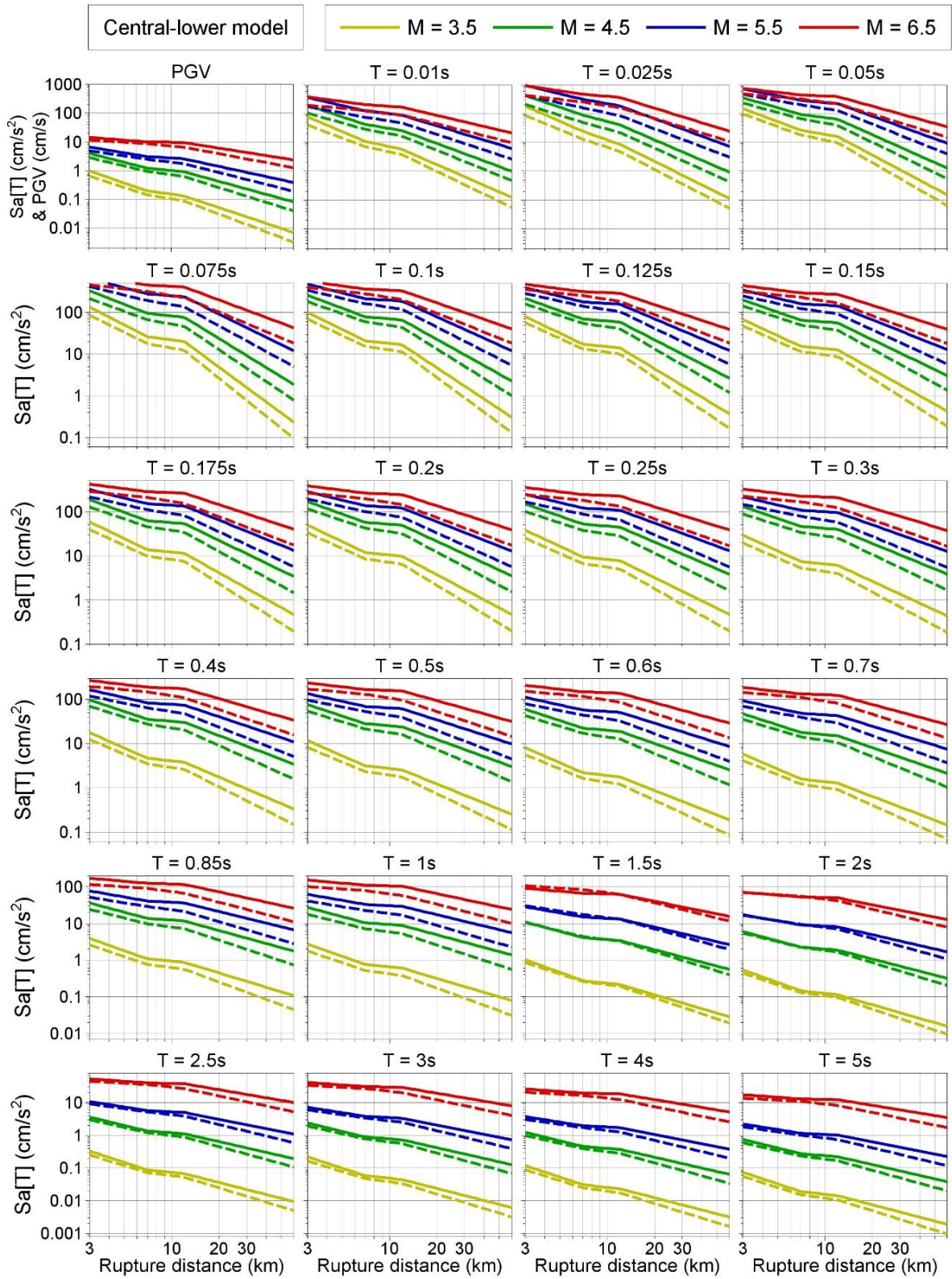
Median Predictions of Motions at NS_B

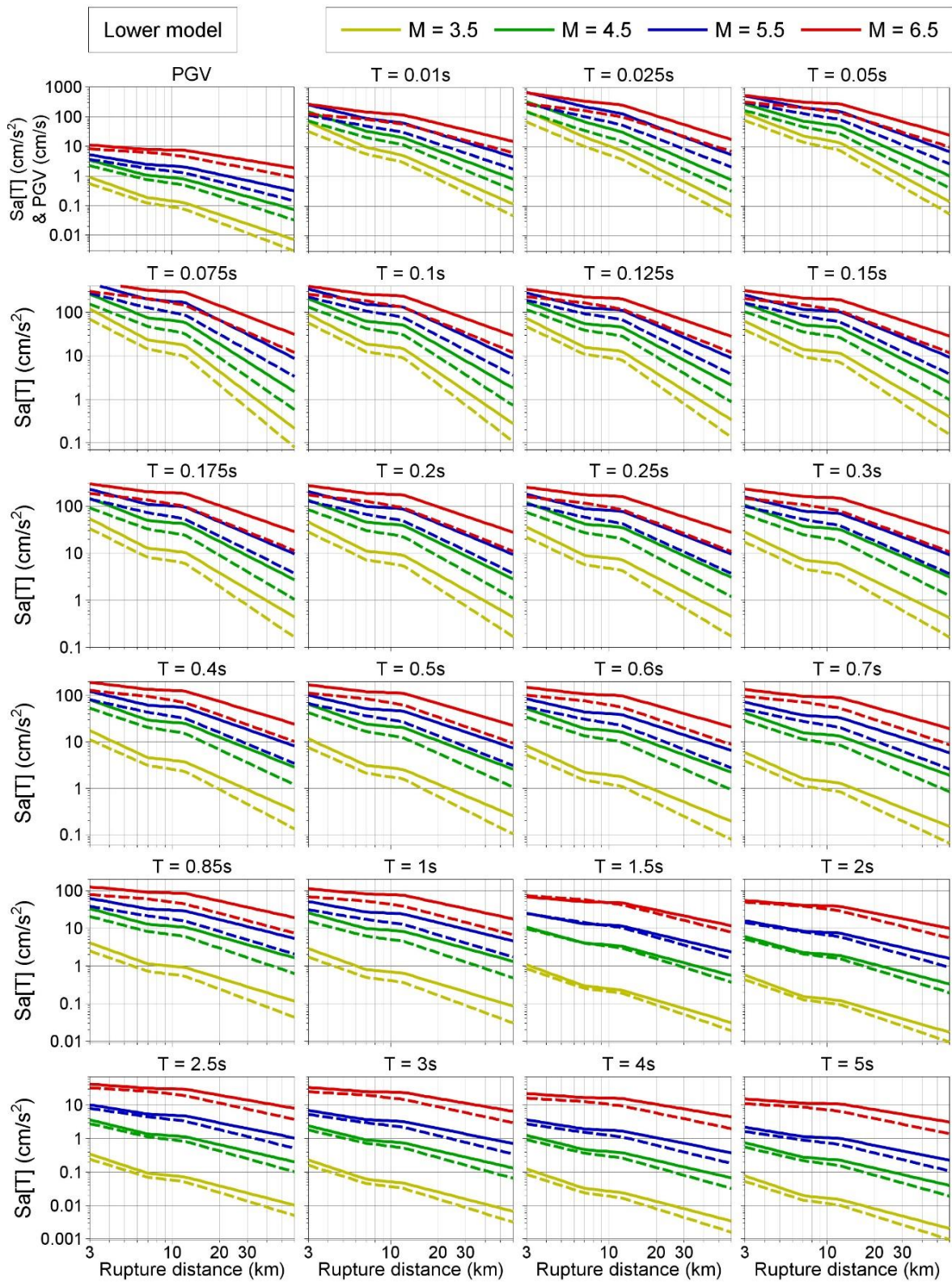
The V6 model medians are shown in *full* while the V5 model medians in *dashed* lines.

A2.1 Plots of median predictions at NS_B shown with respect to distance

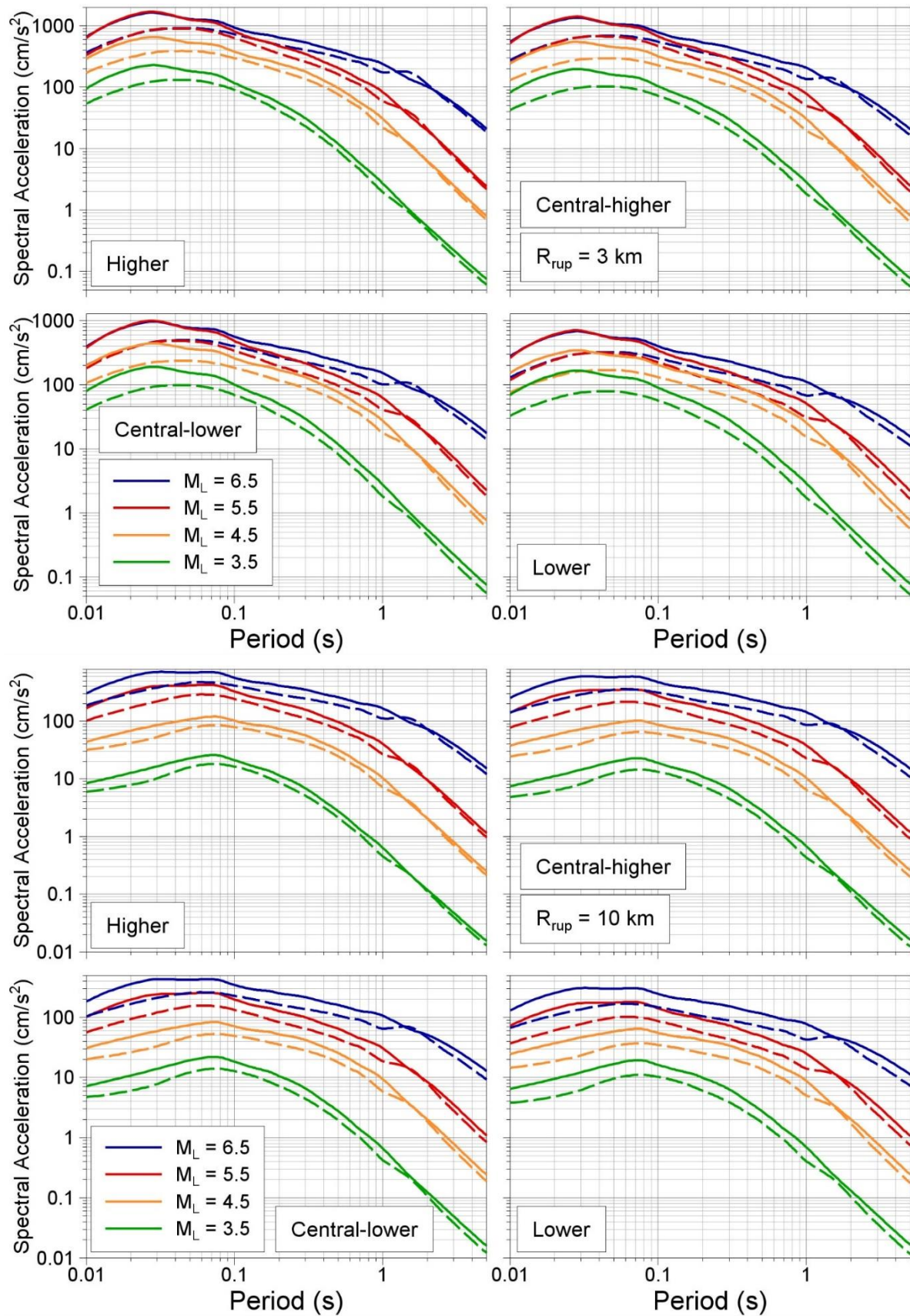


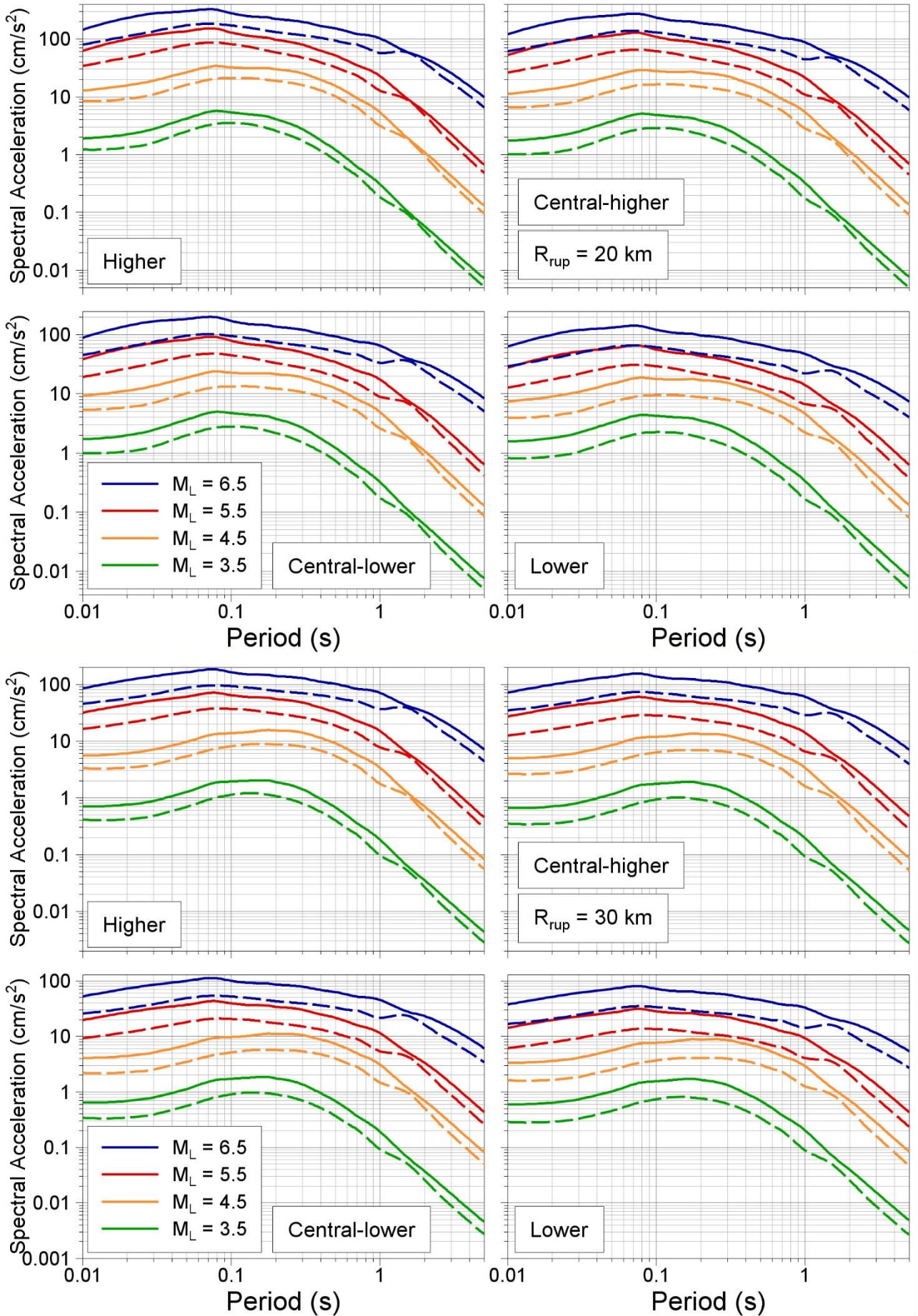


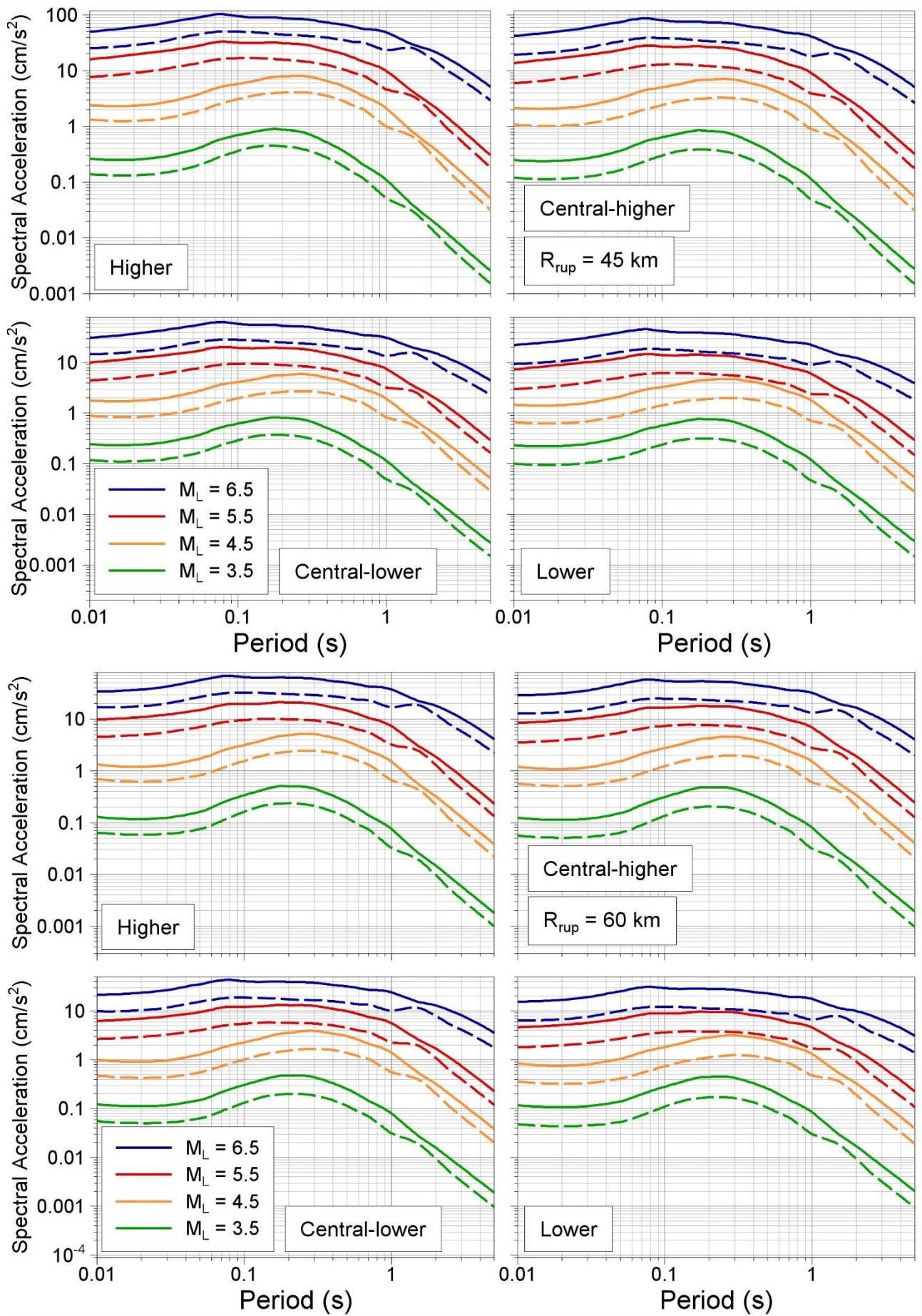




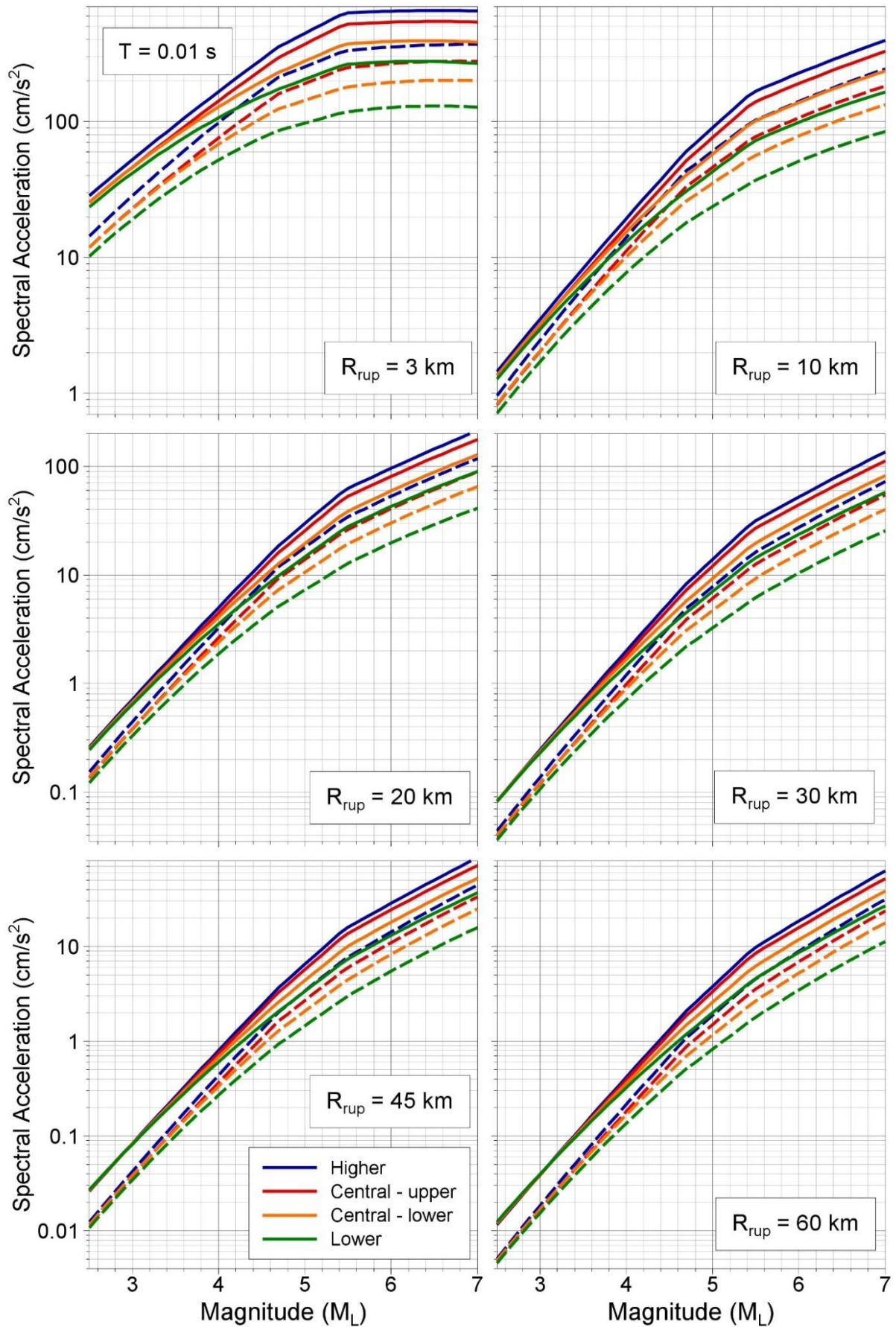
A2.2 Response Spectra

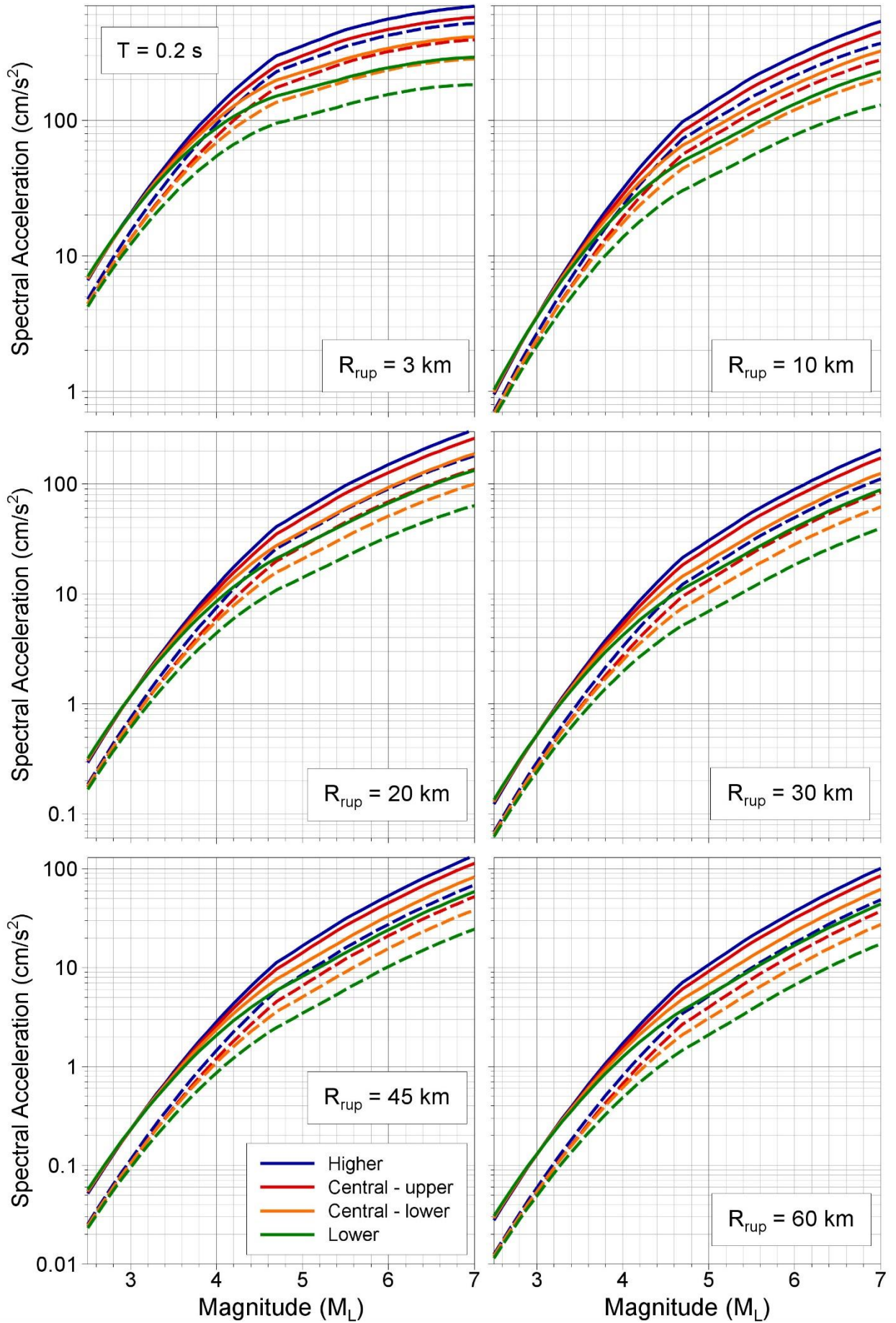


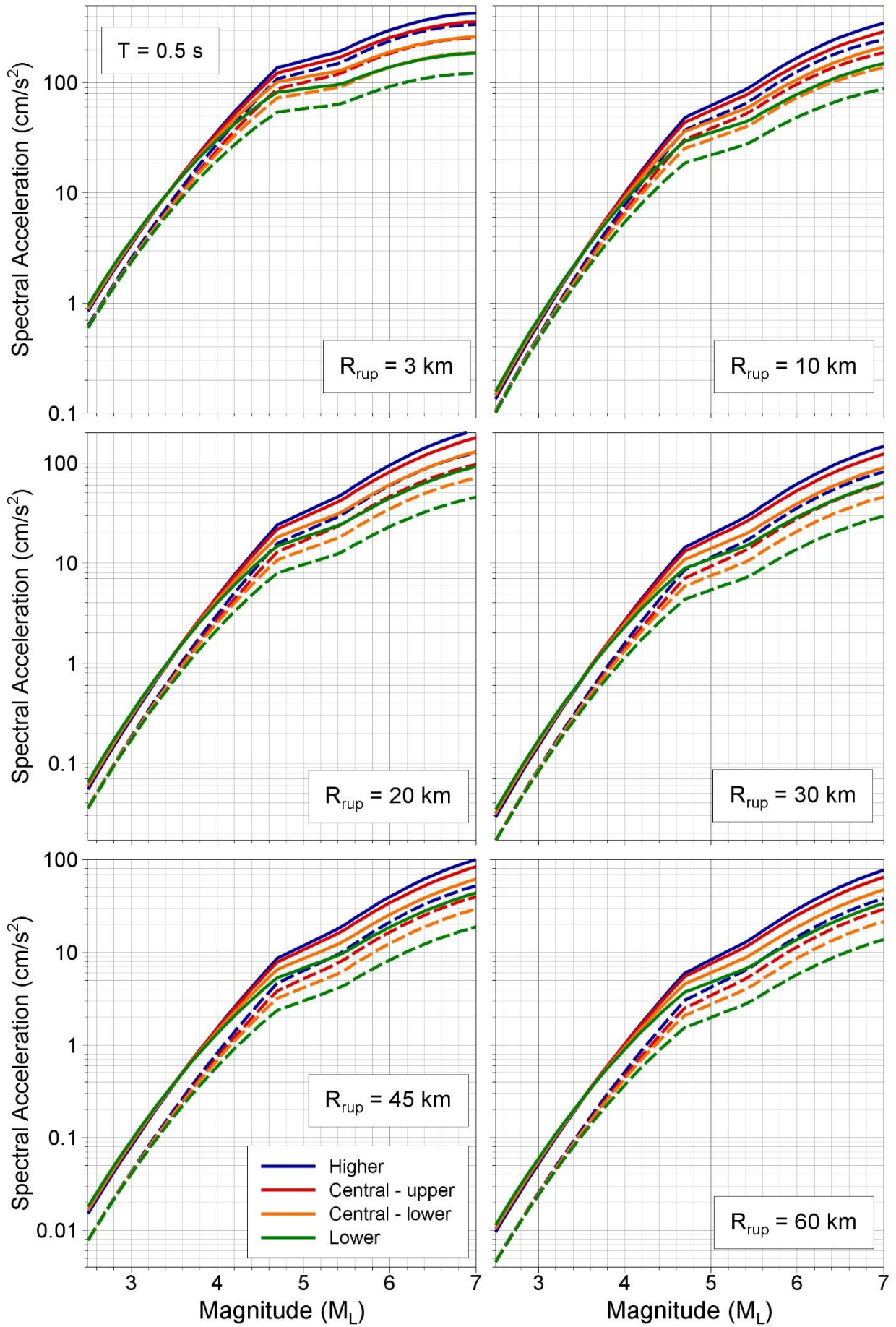


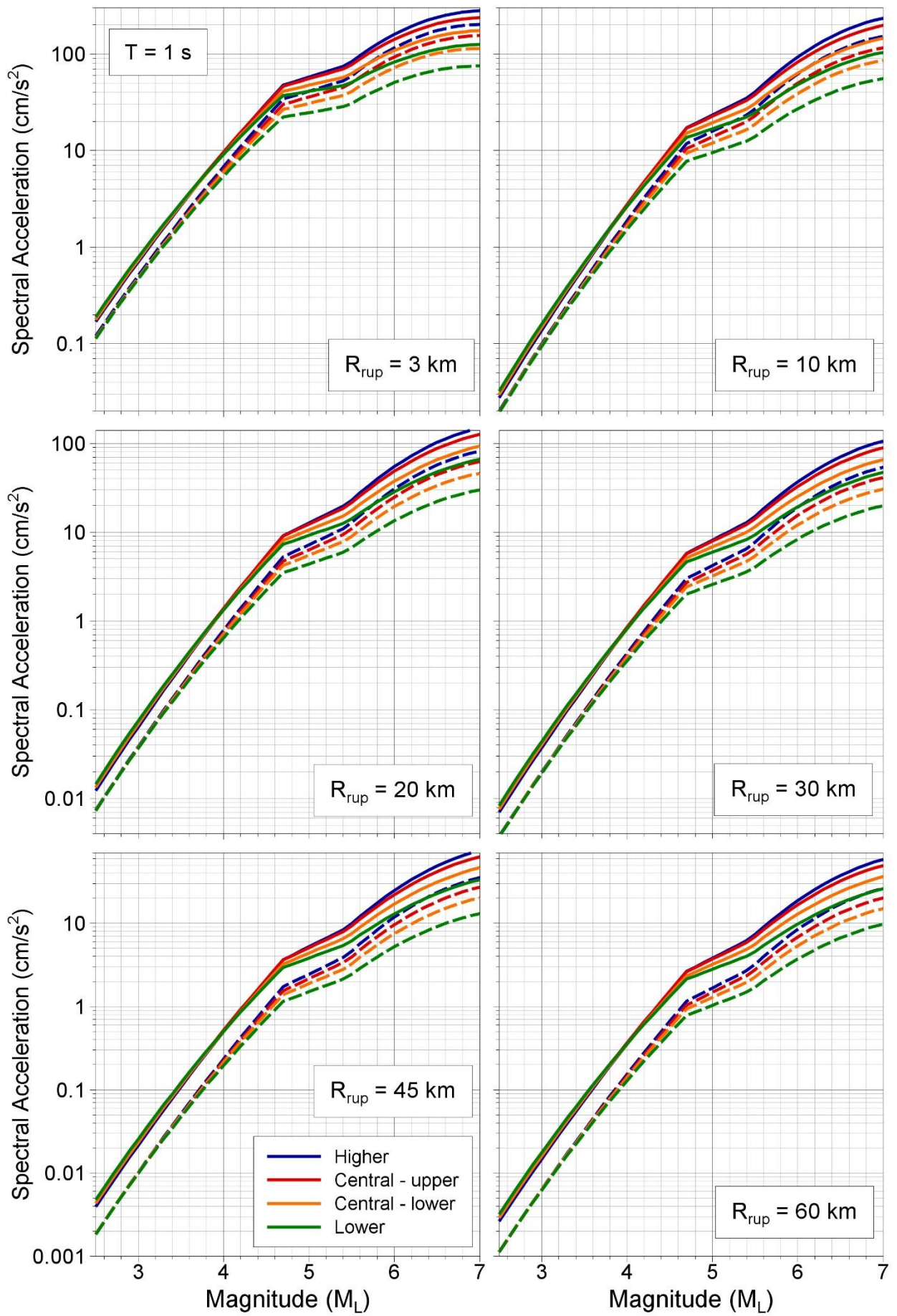


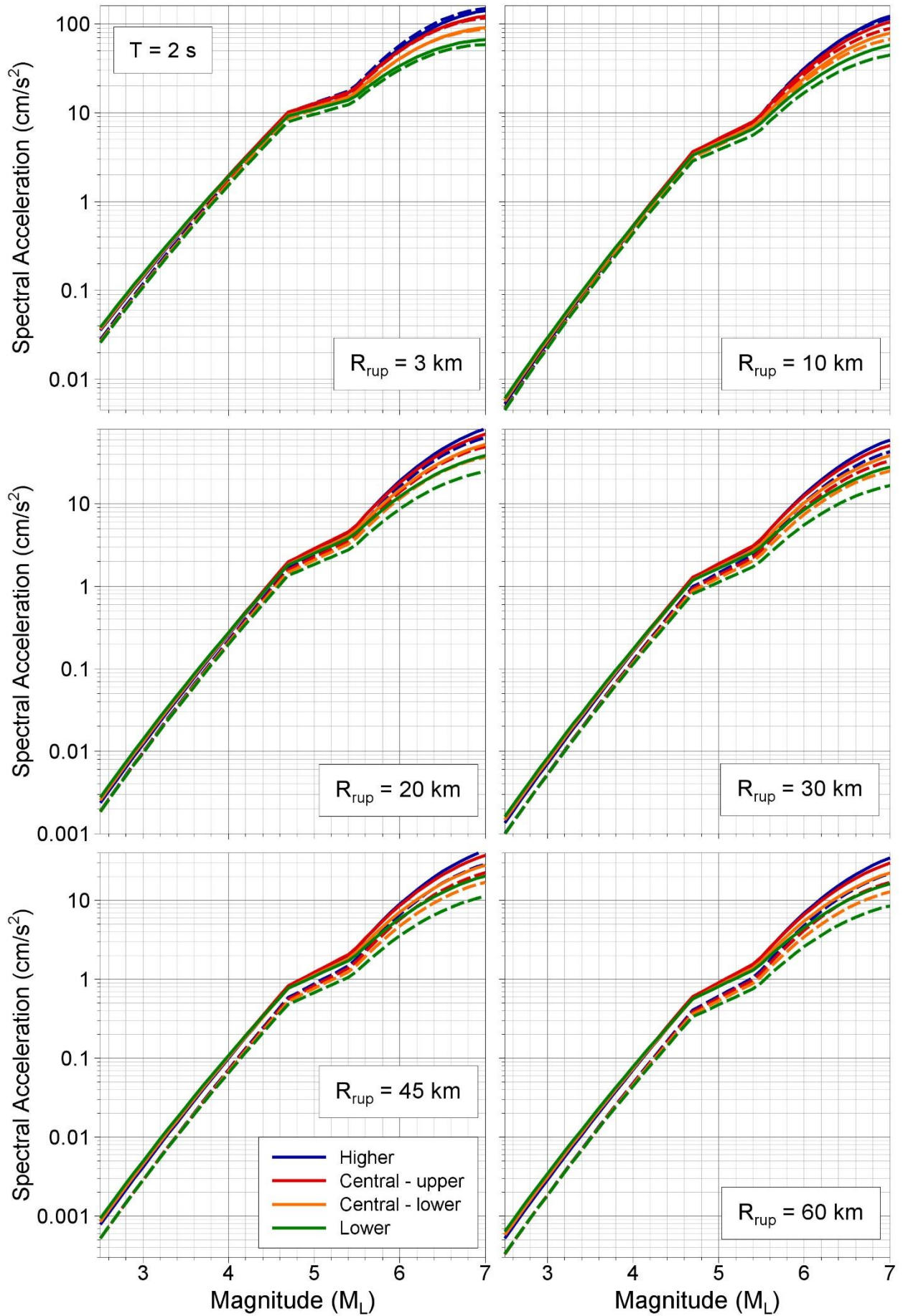
A1.3 Plots of median predictions at NS_B shown with respect to magnitude

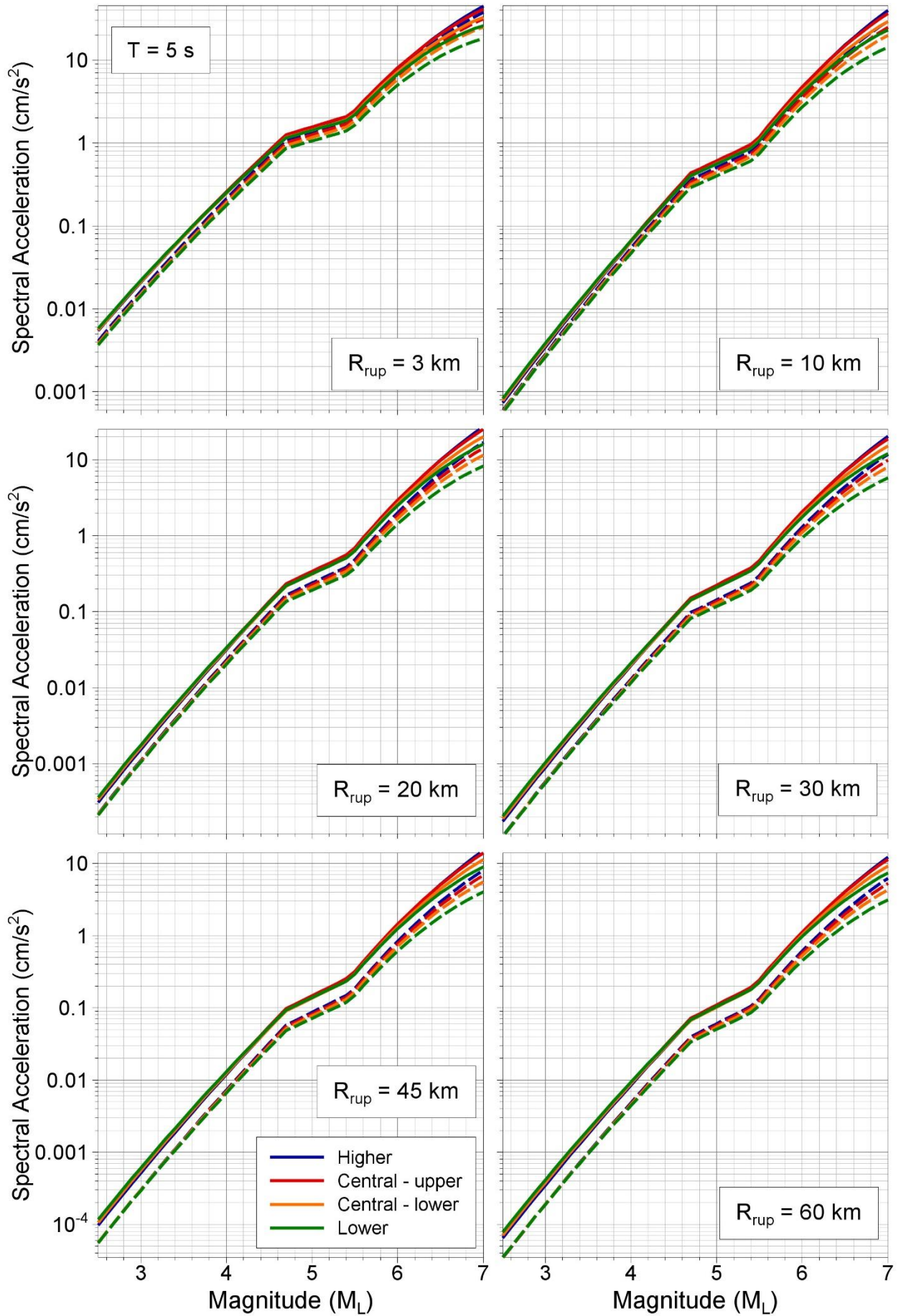






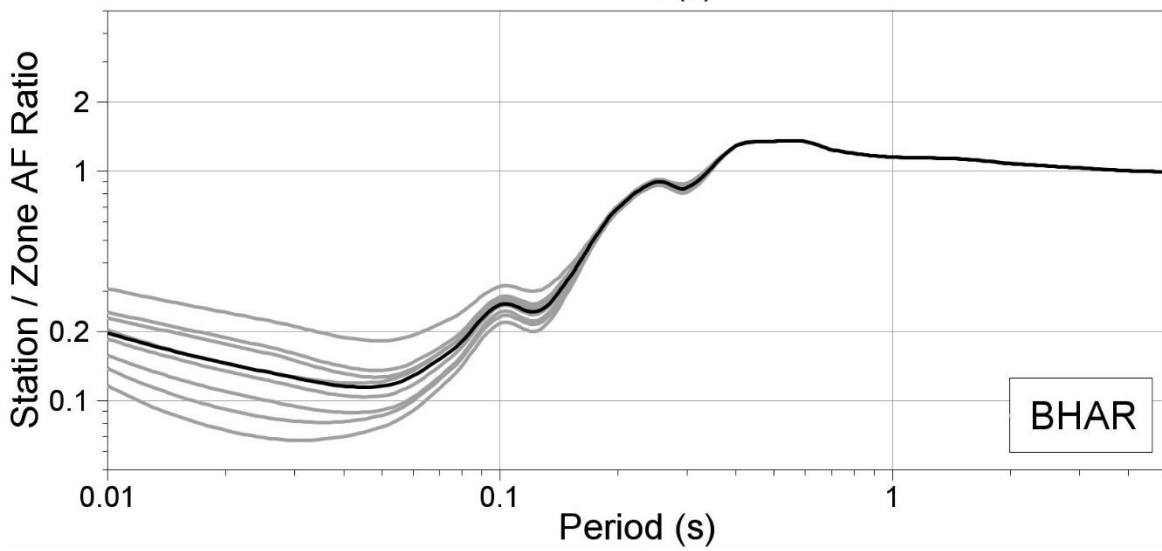
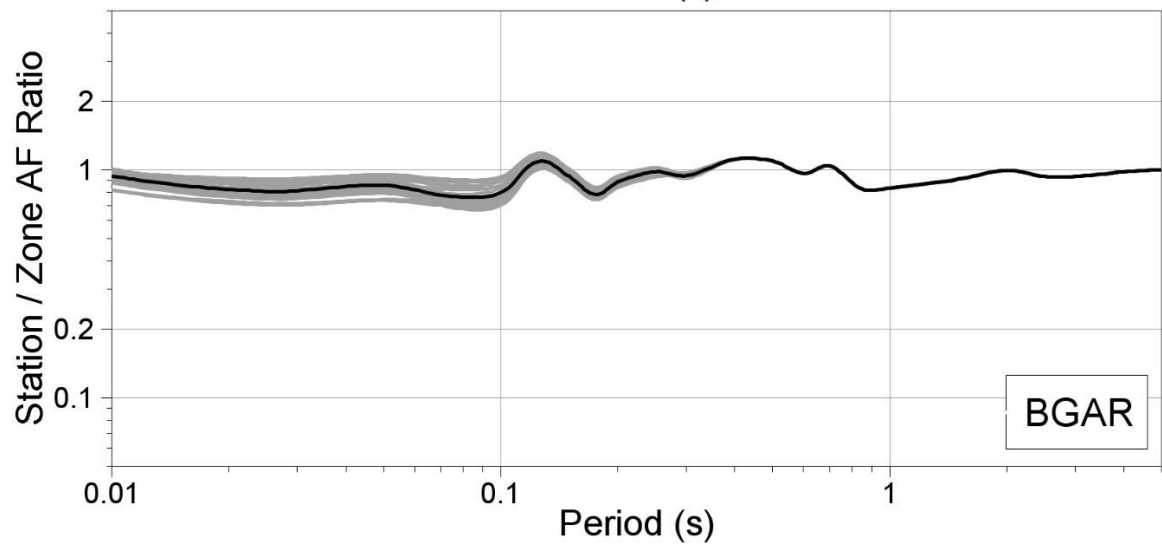
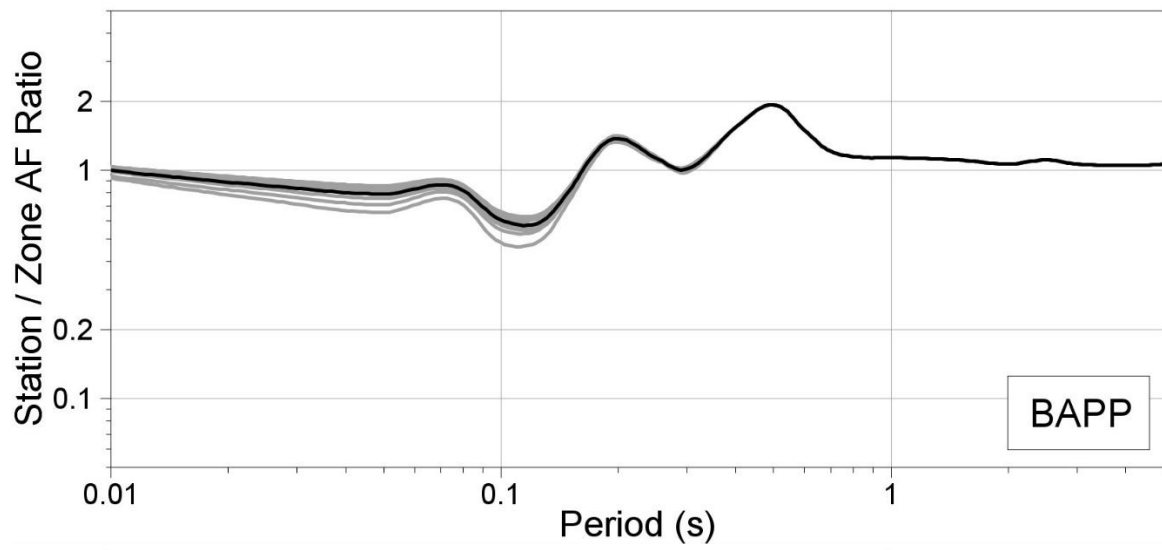


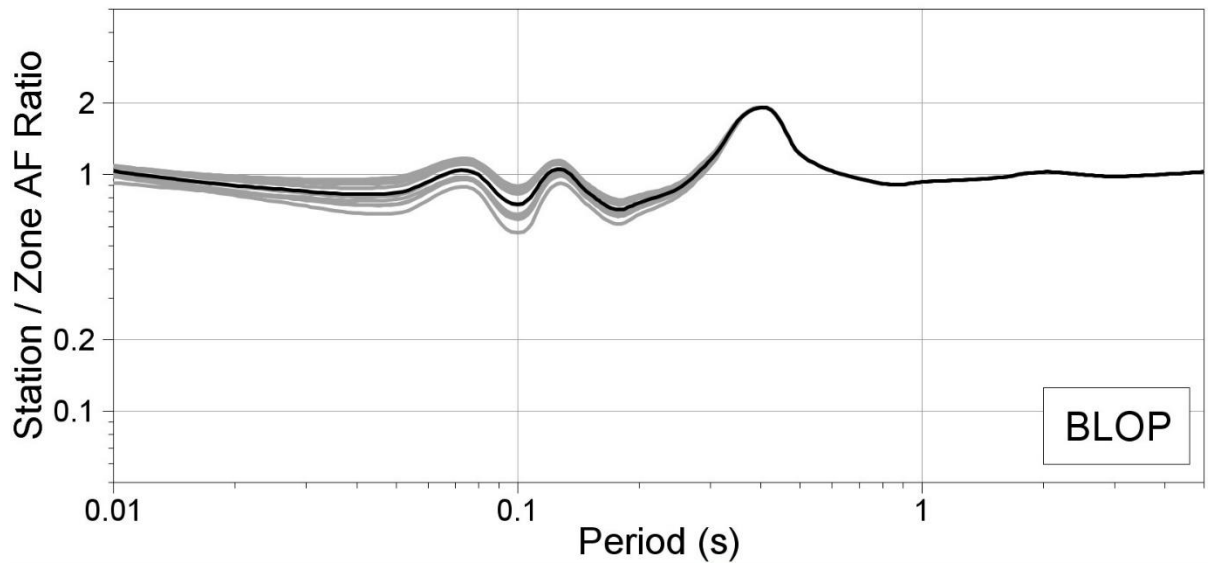
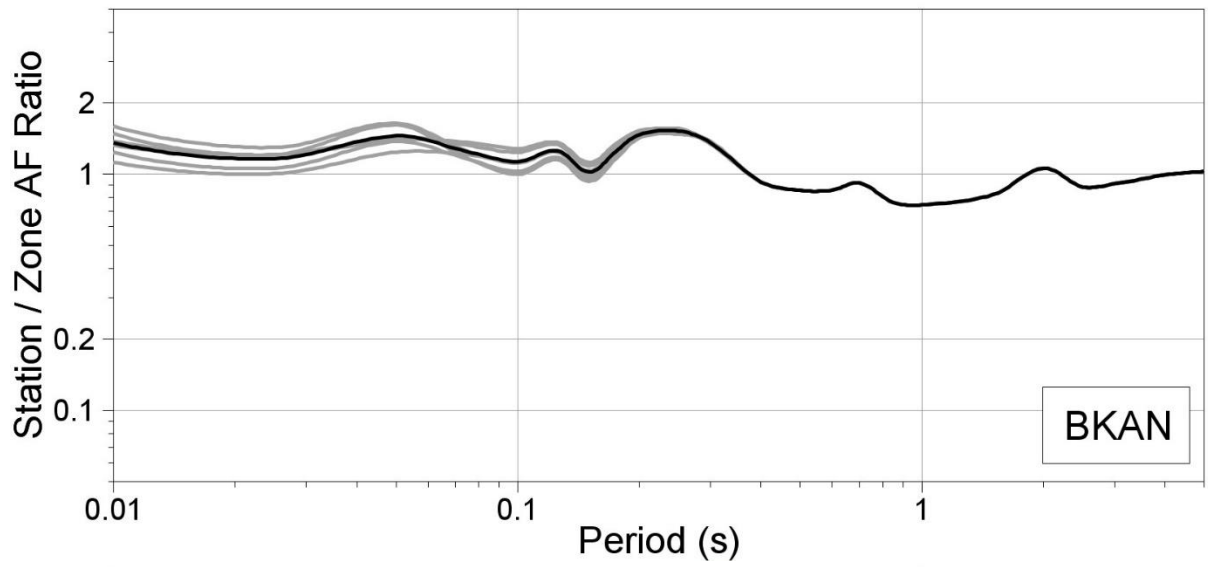
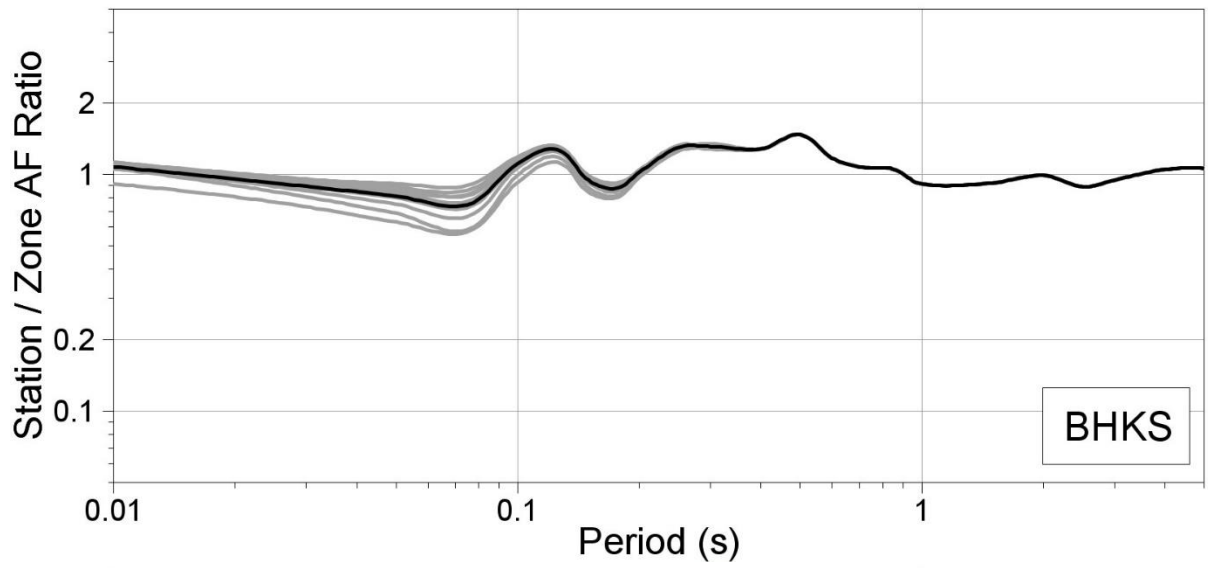


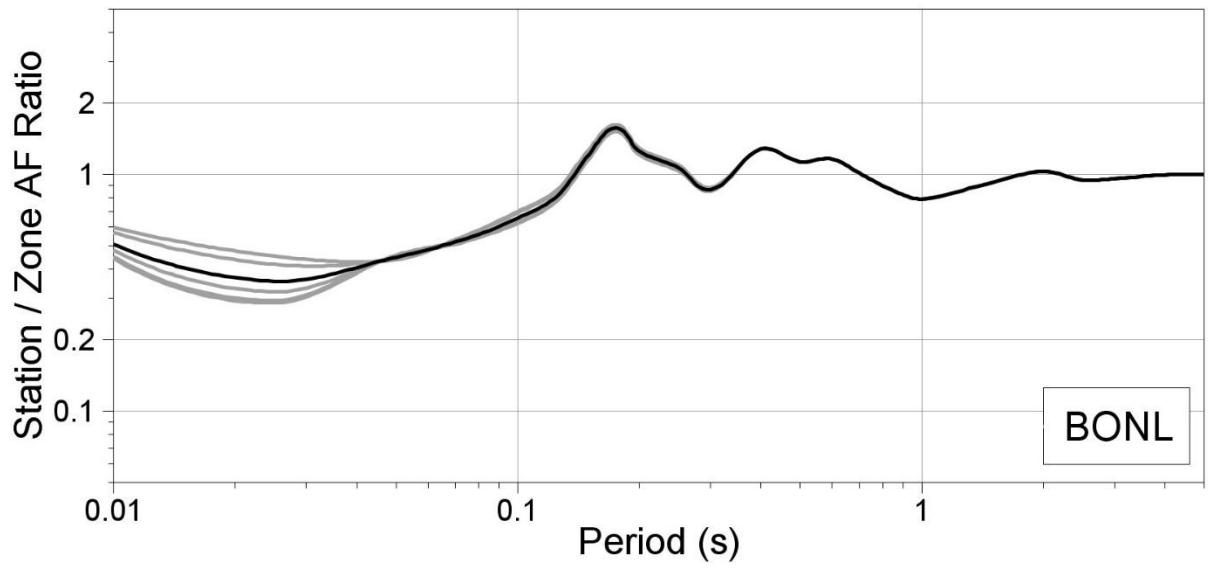
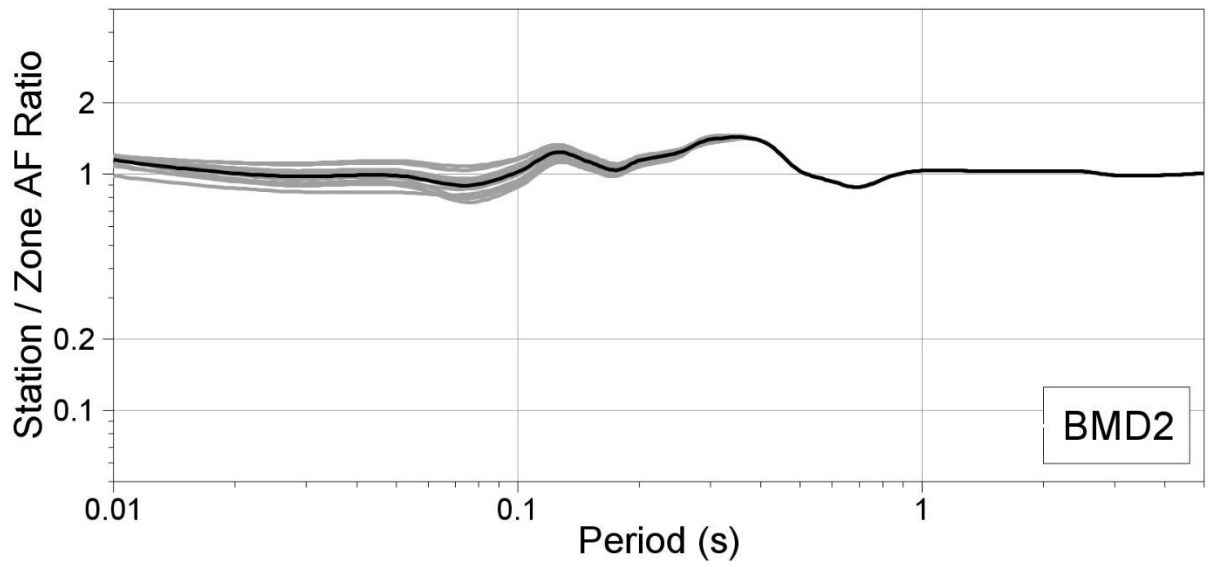
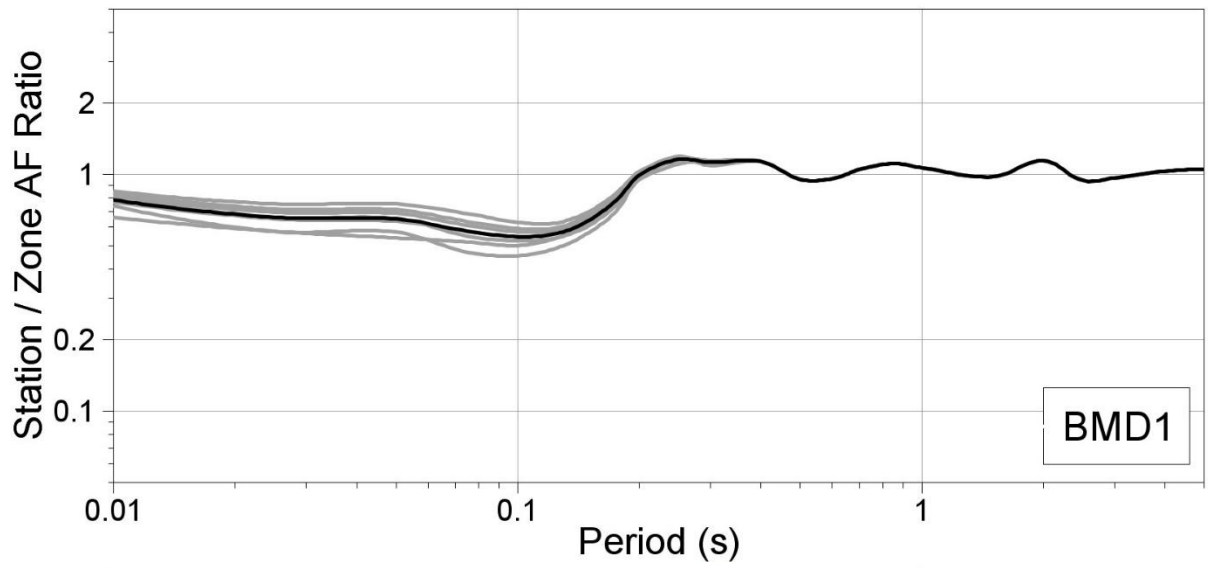


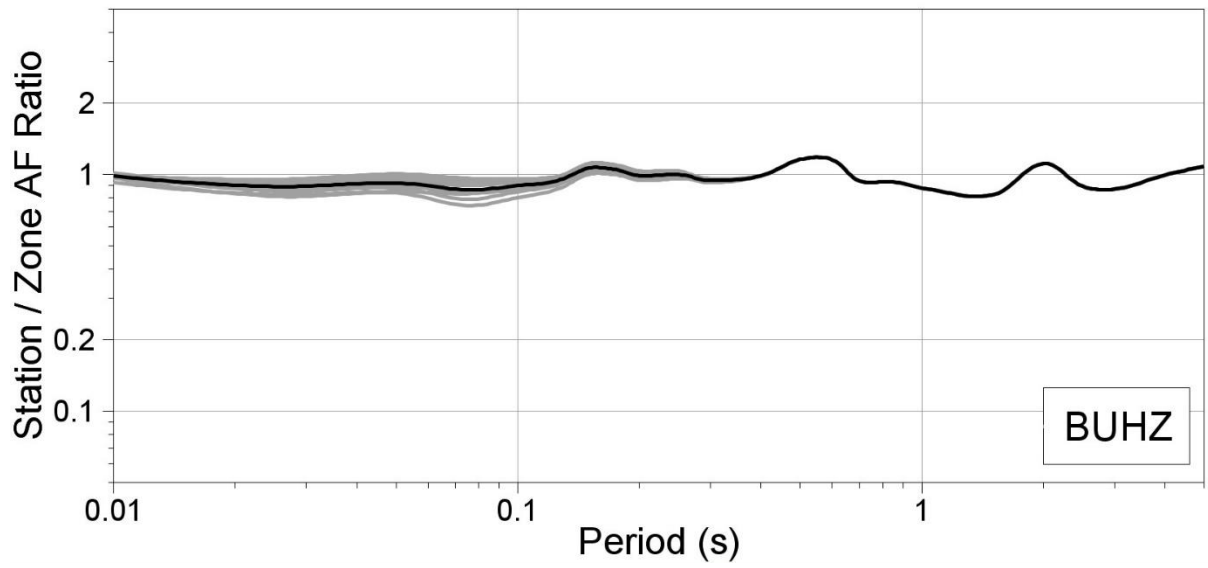
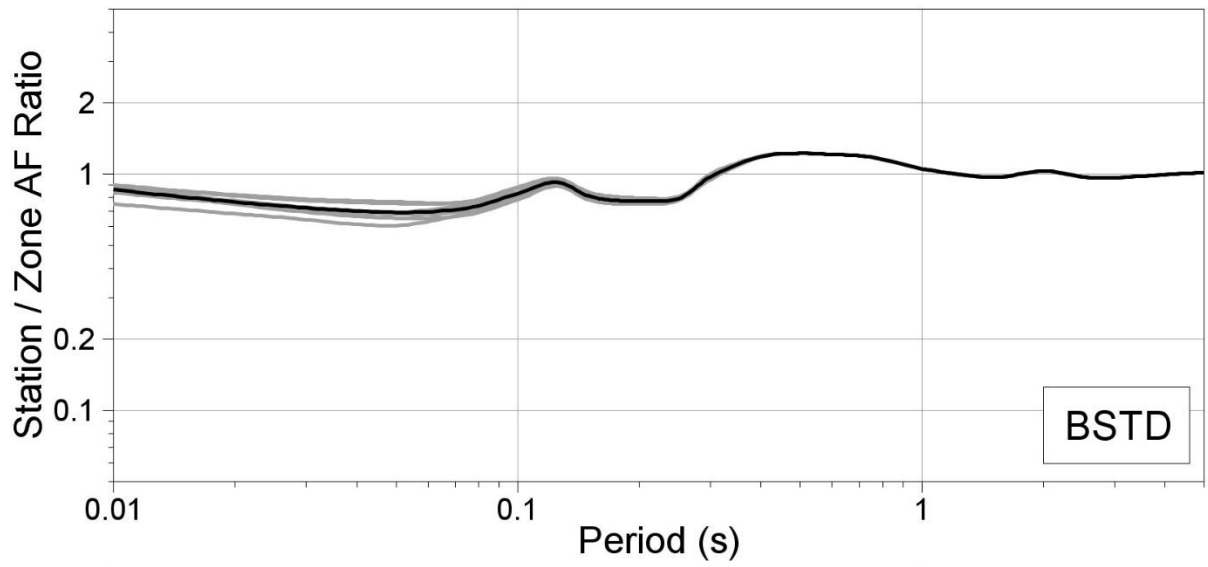
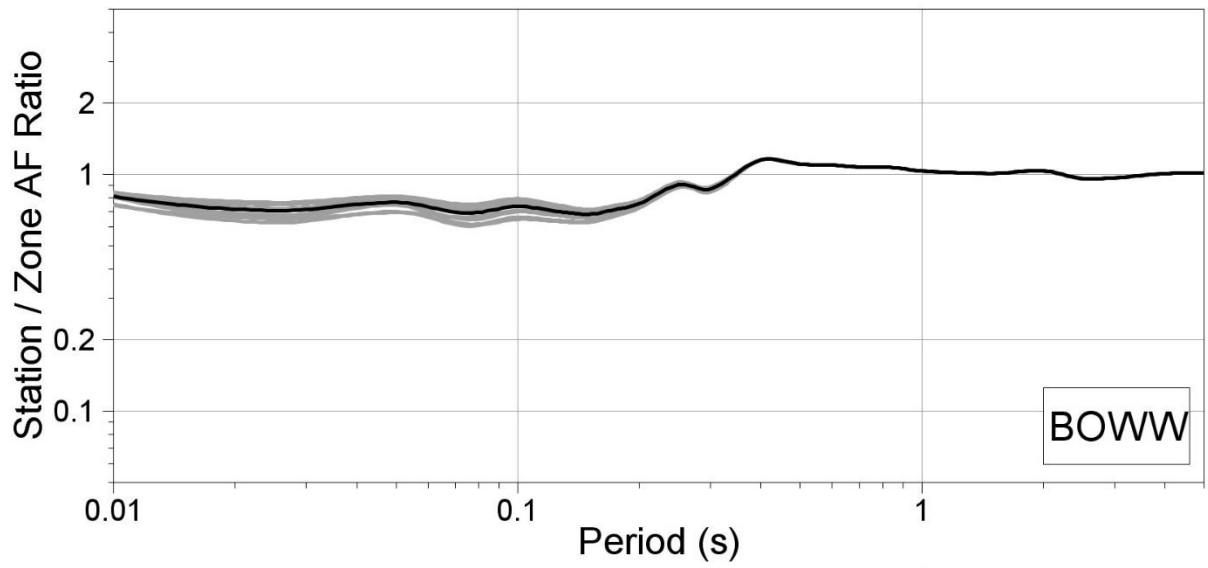
APPENDIX III

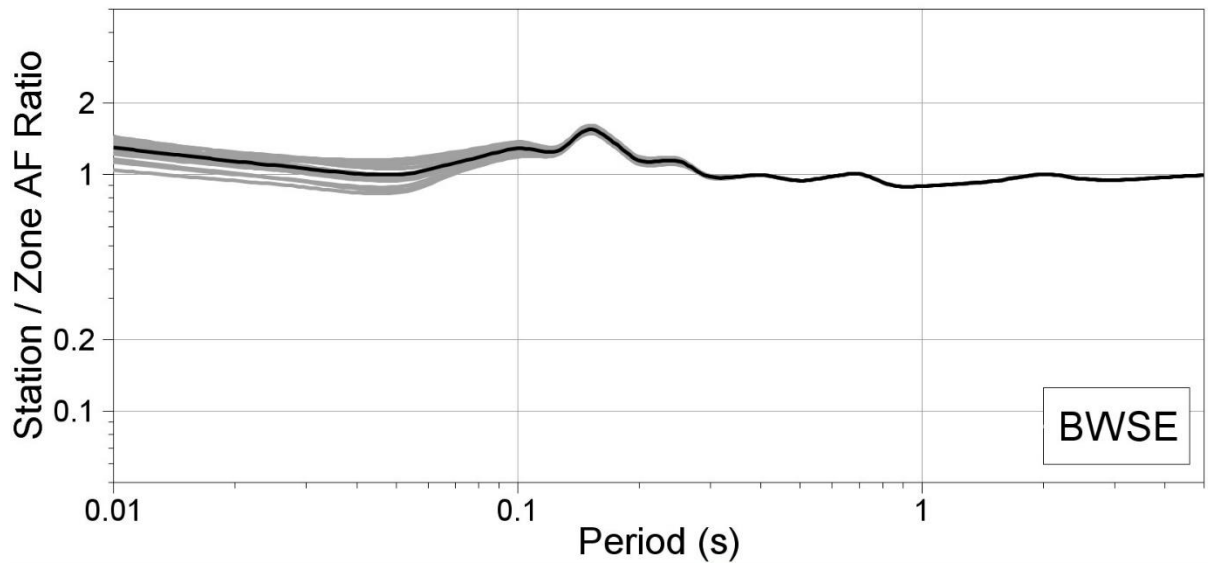
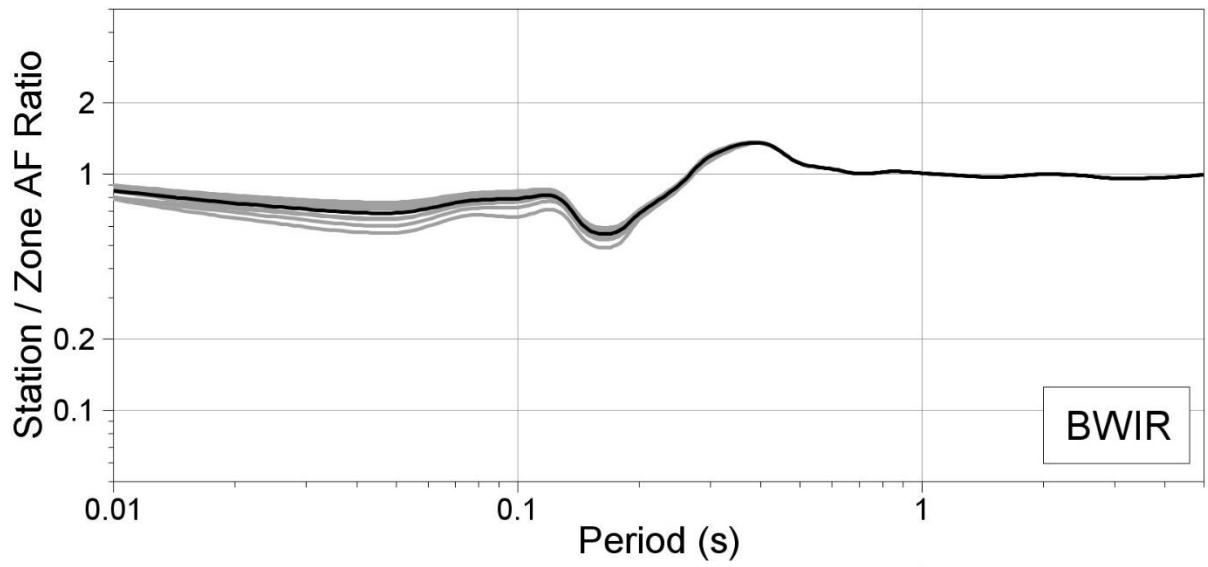
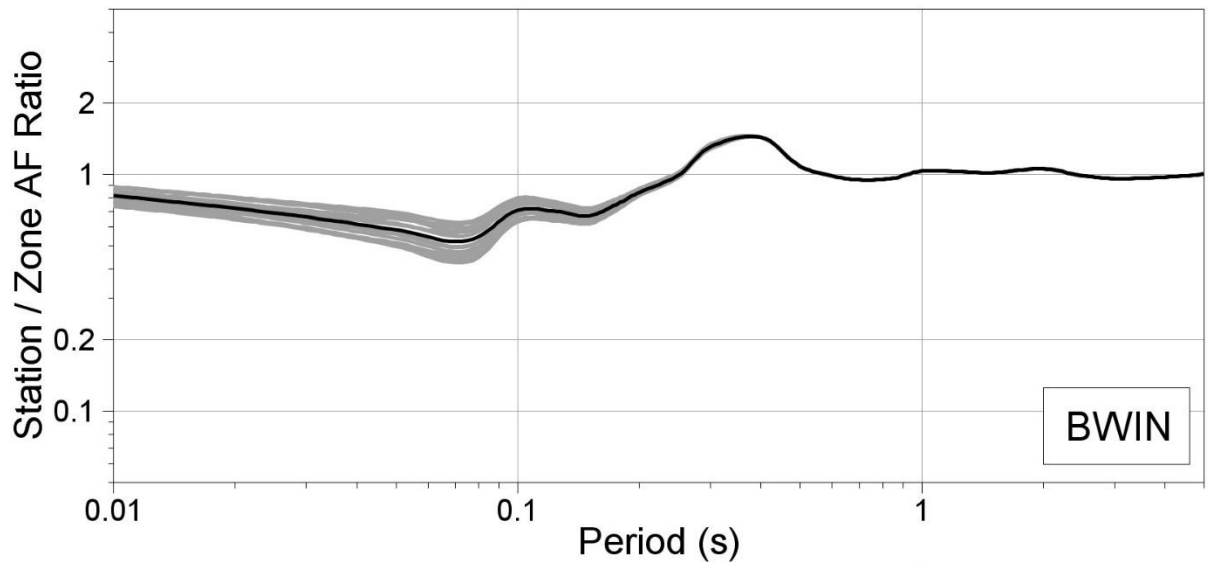
Stations vs Zone Linear AFs

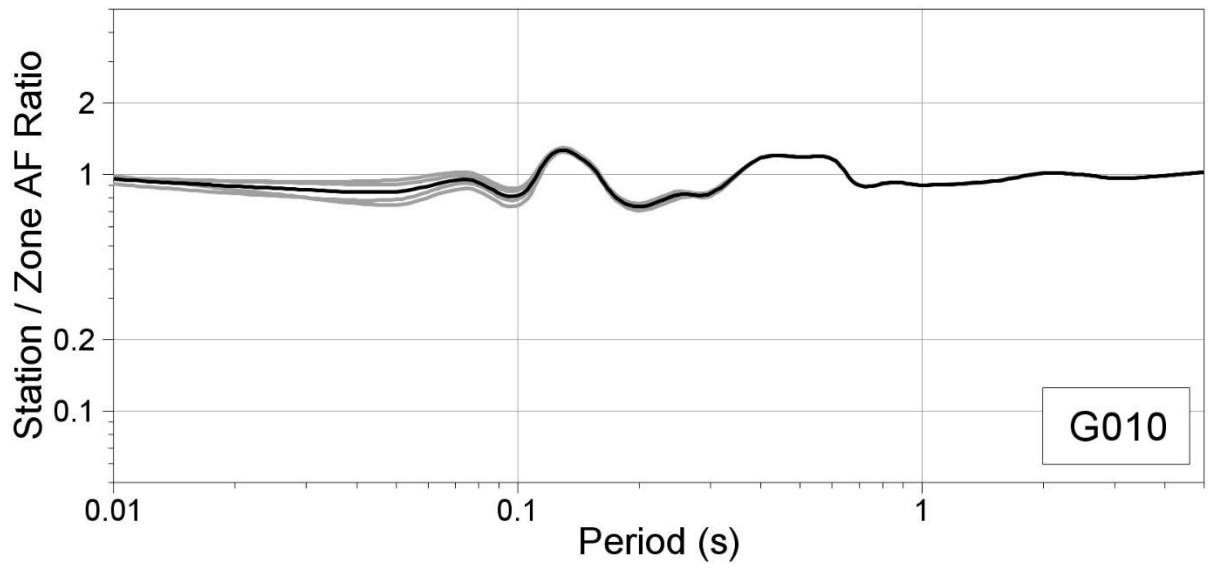
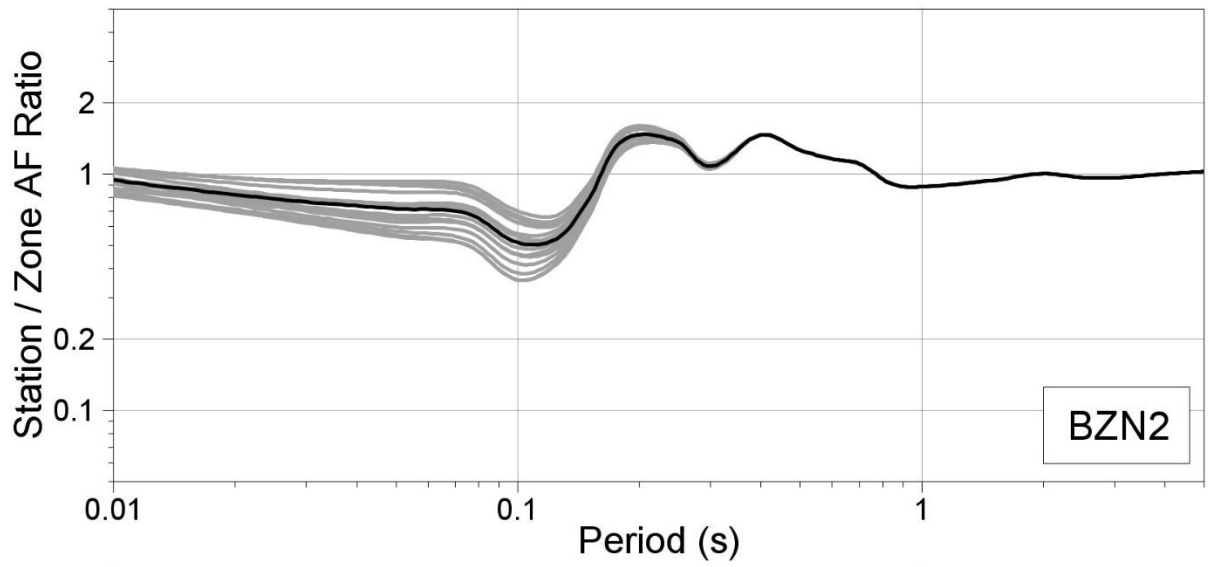
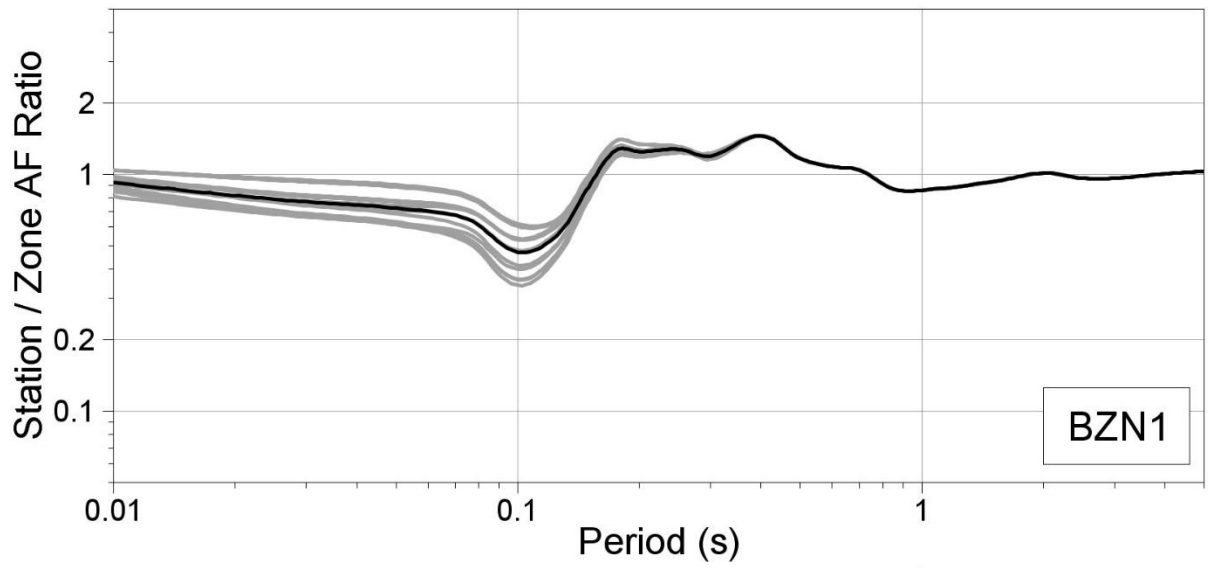


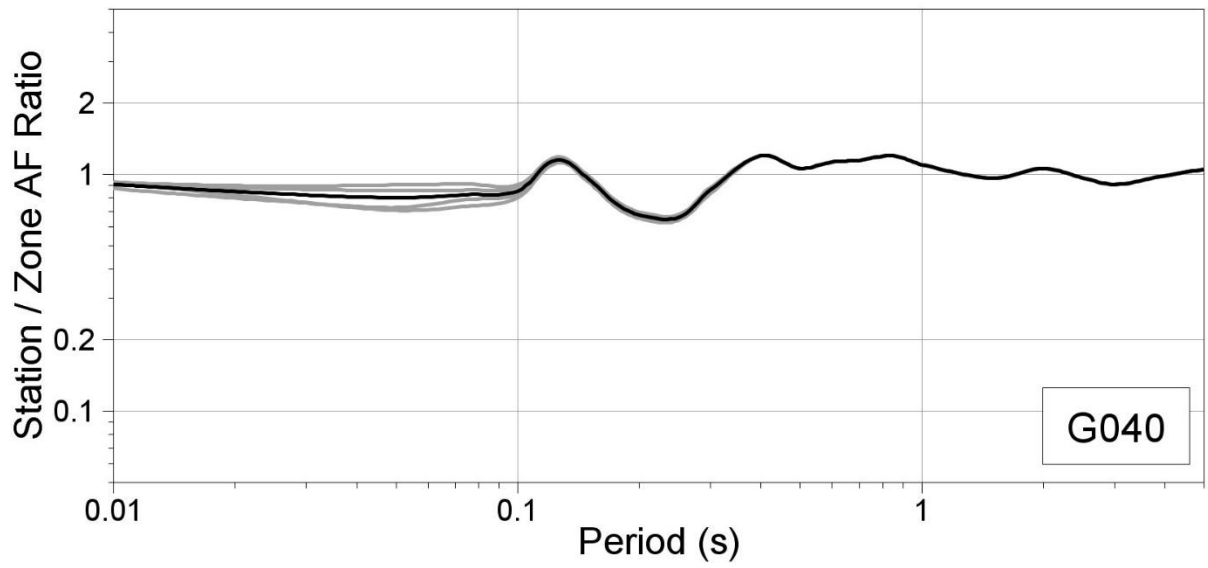
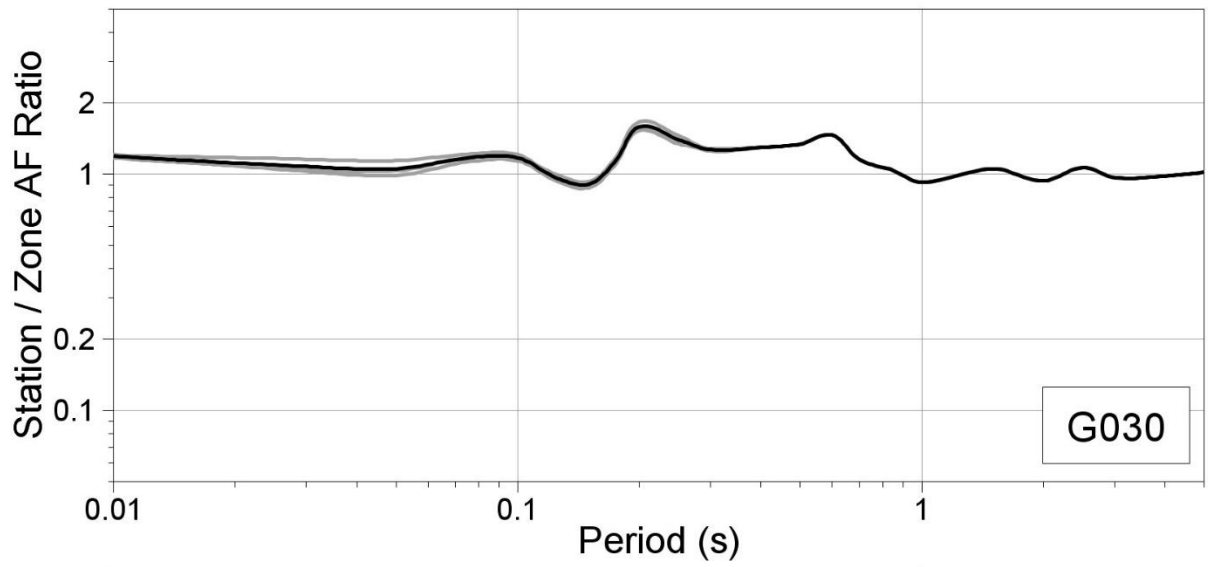
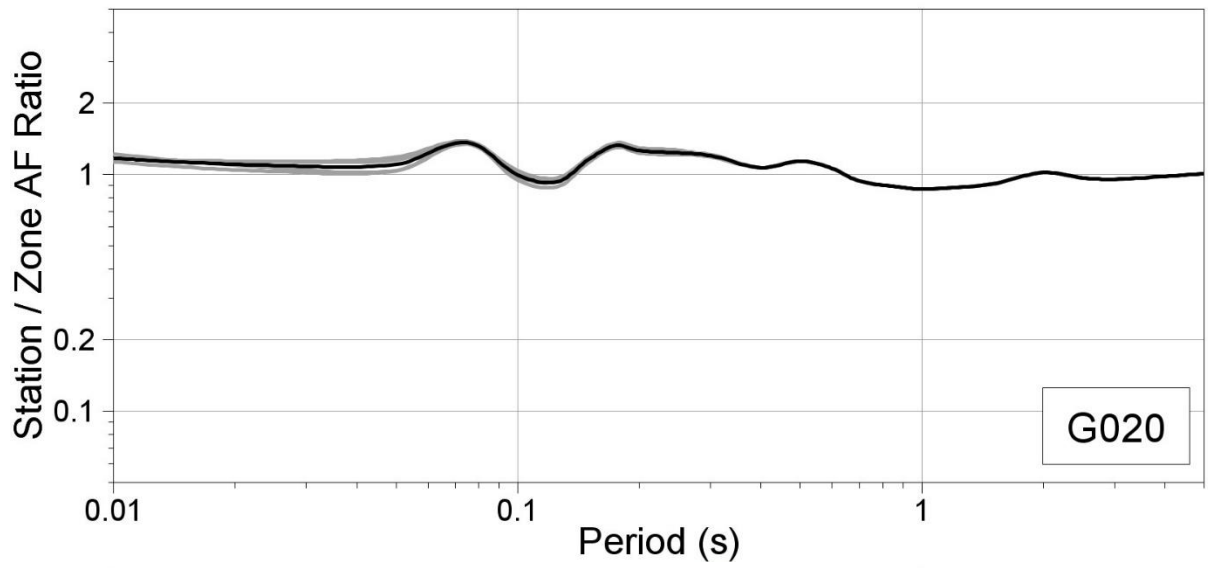


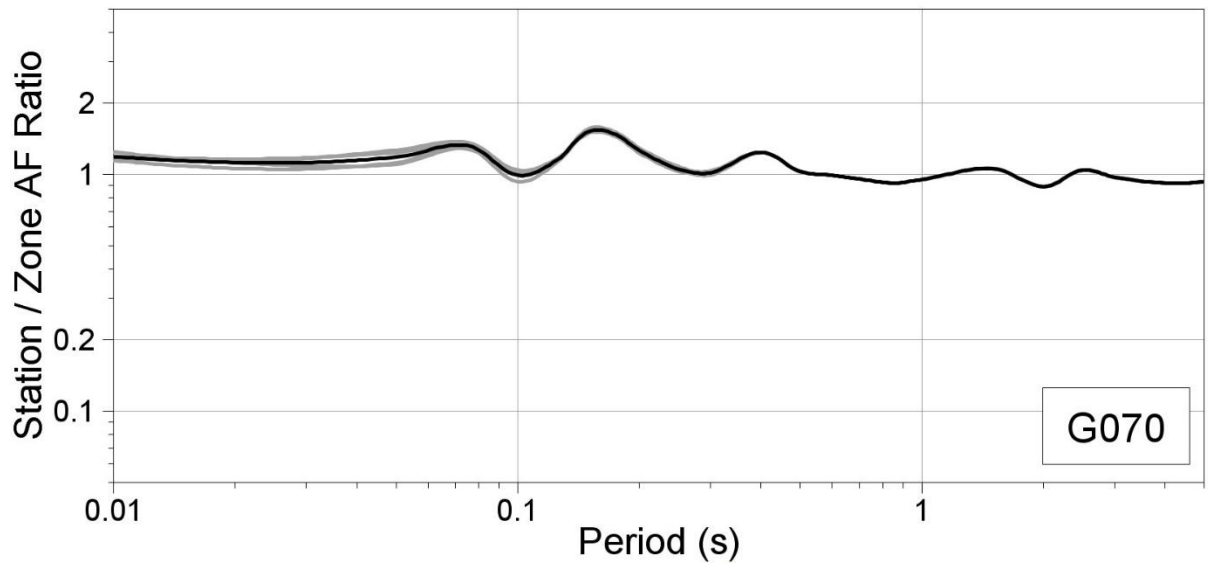
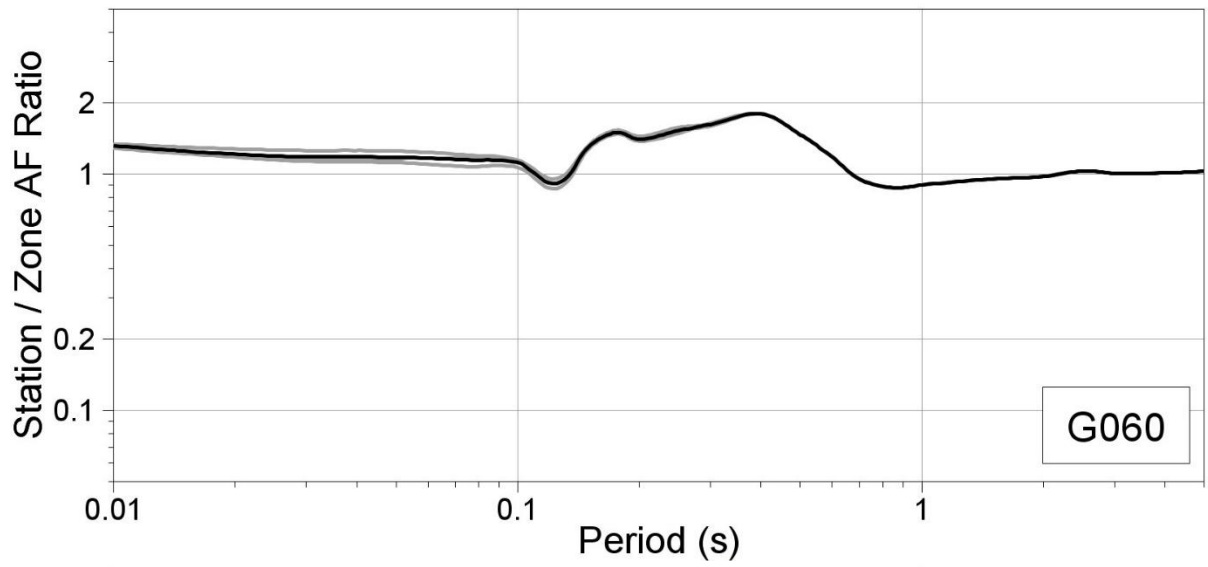
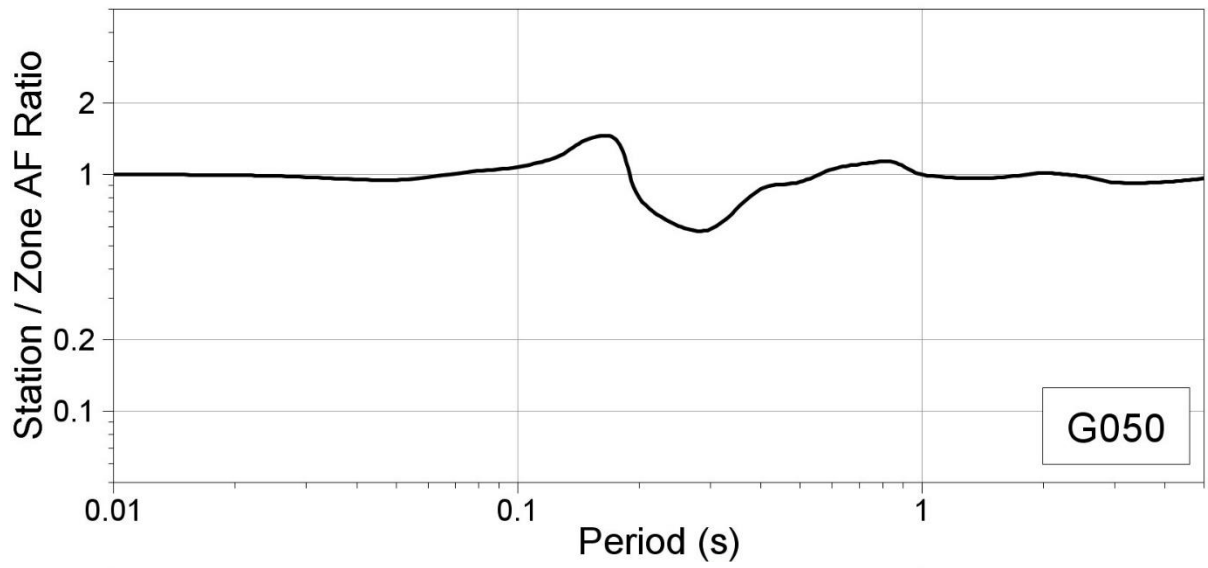


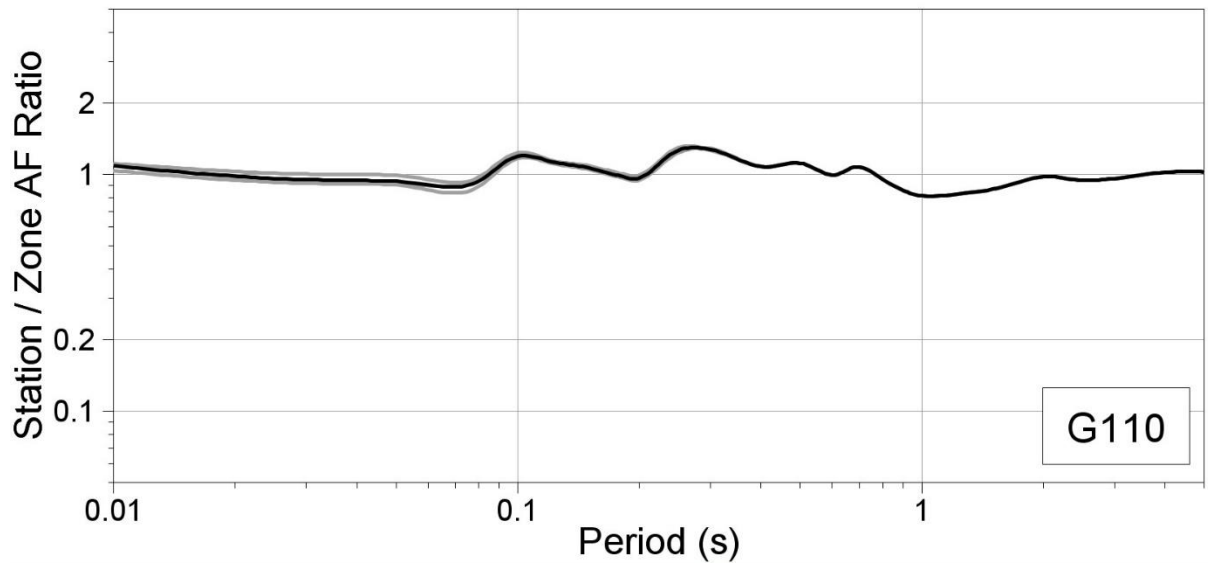
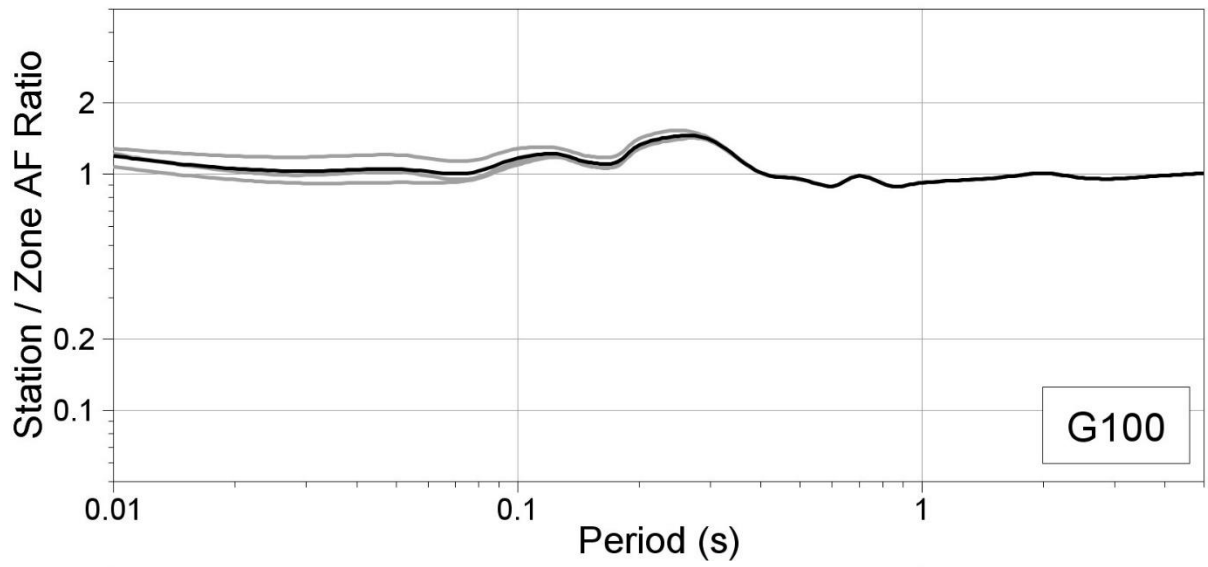
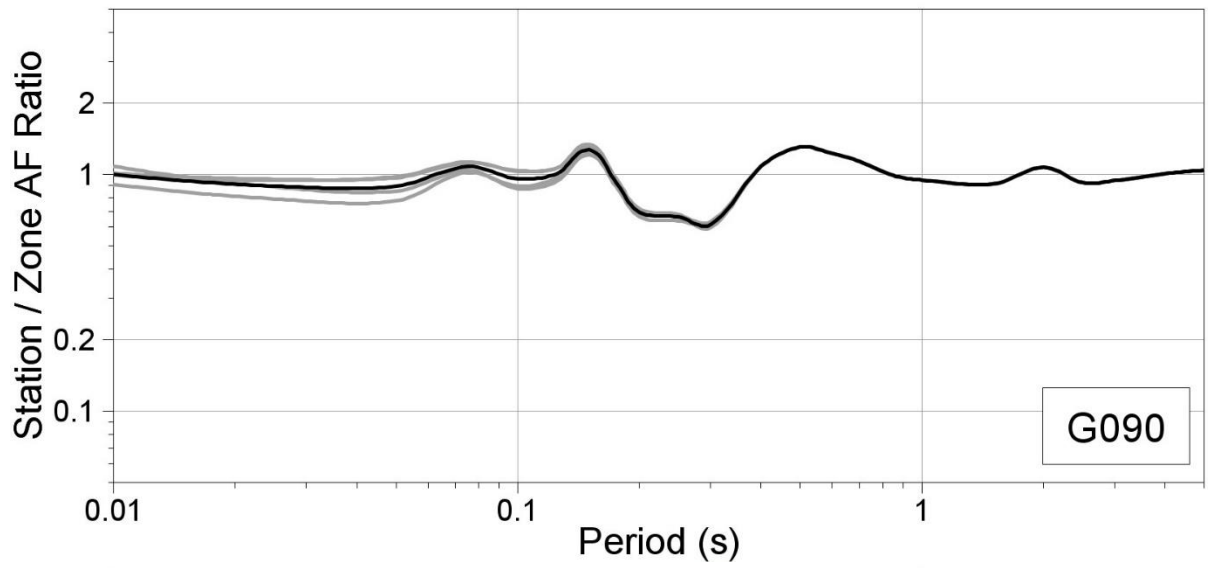


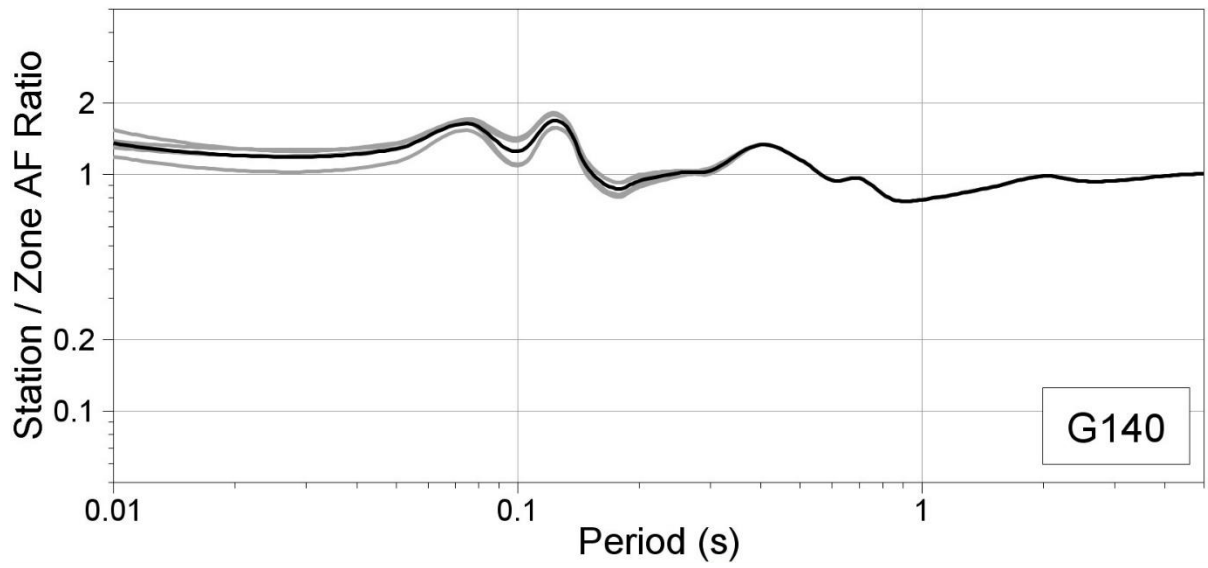
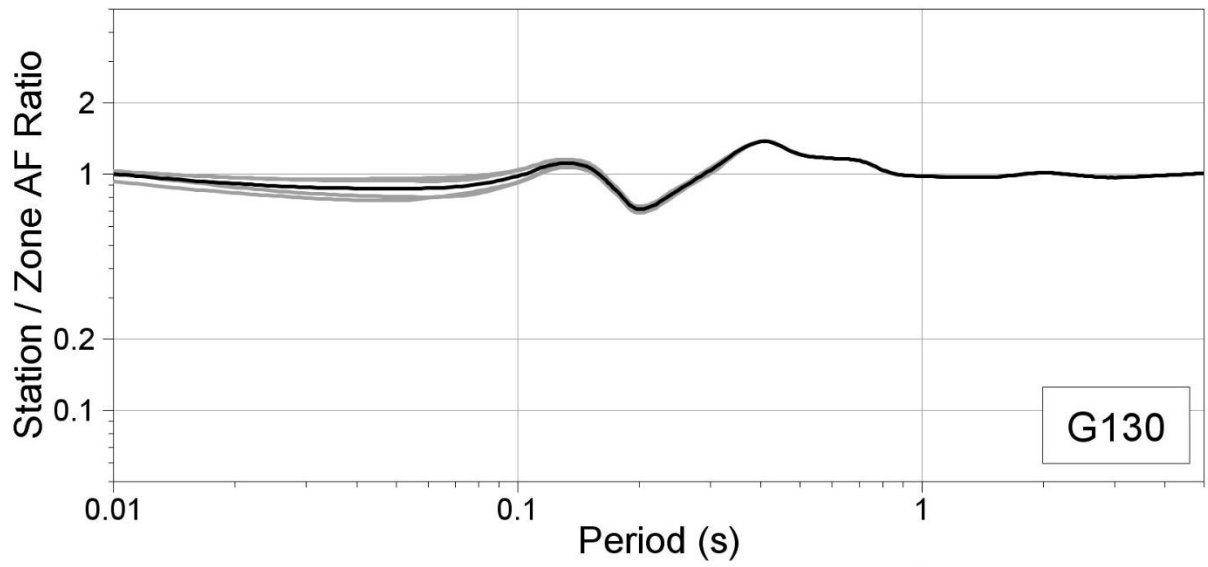
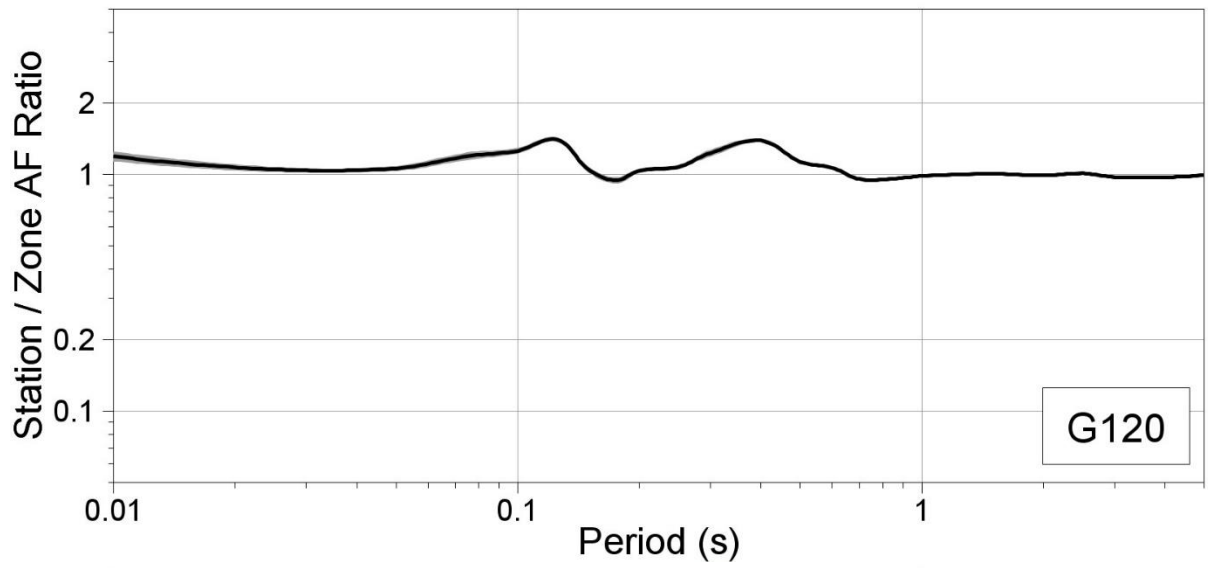


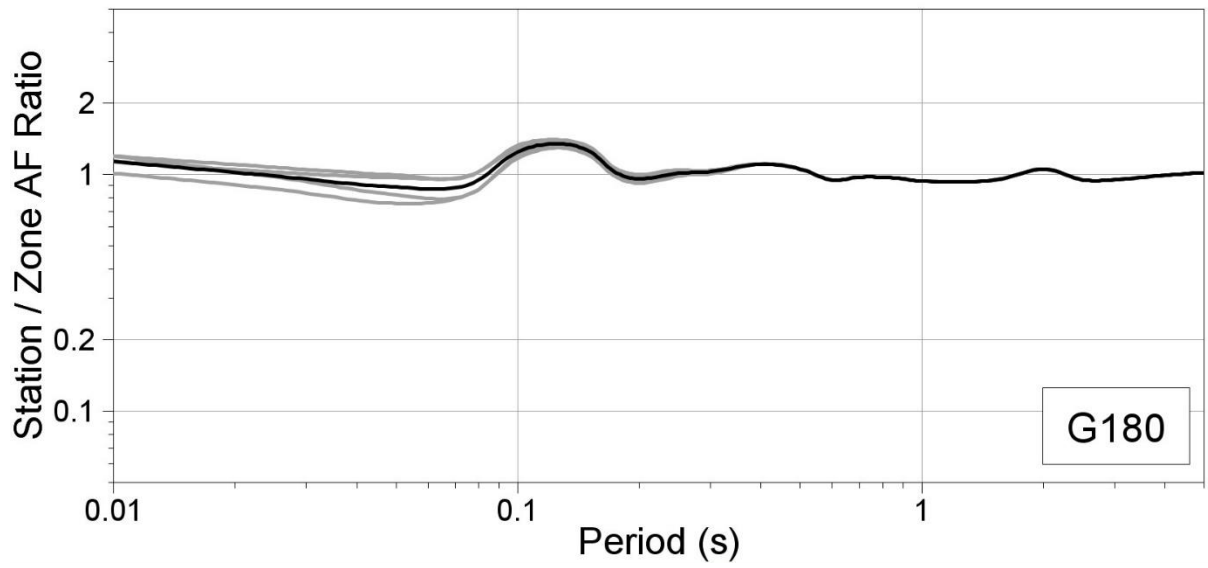
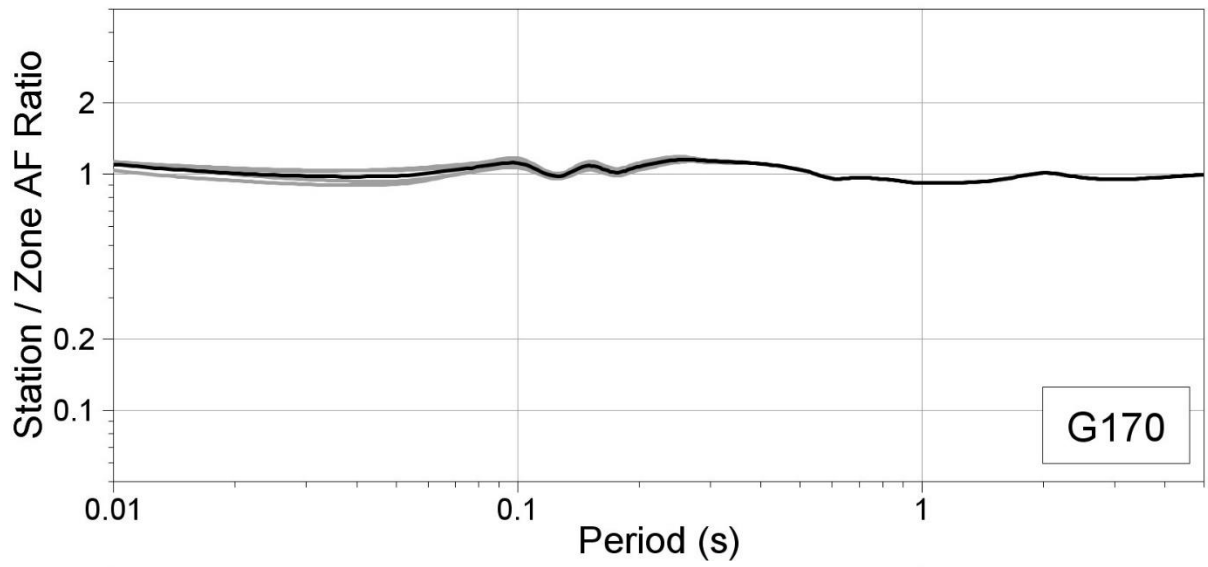
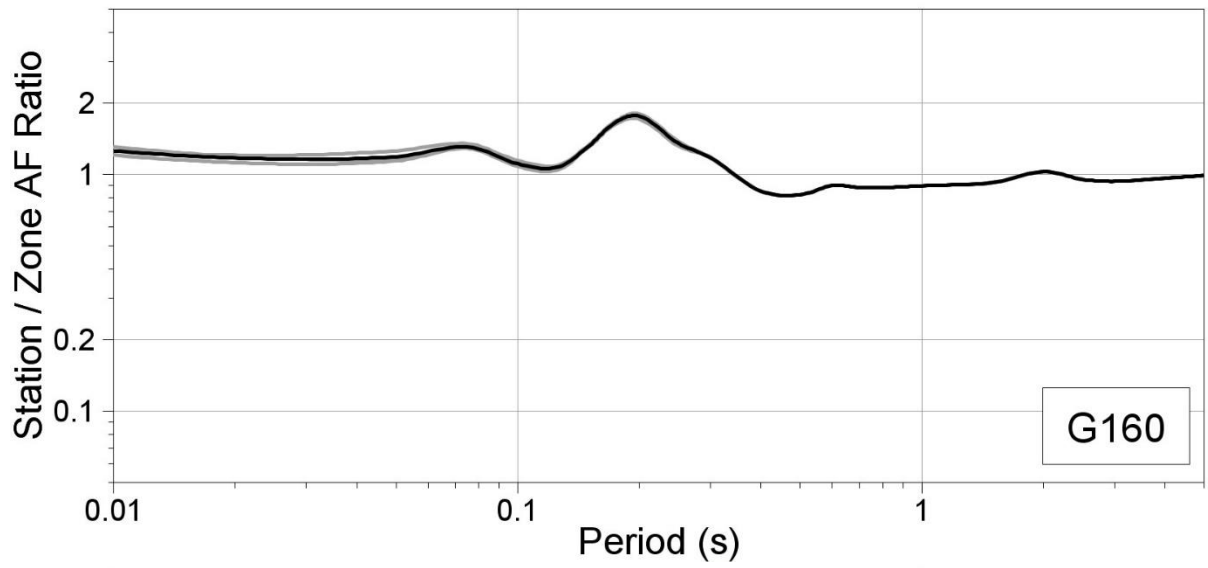


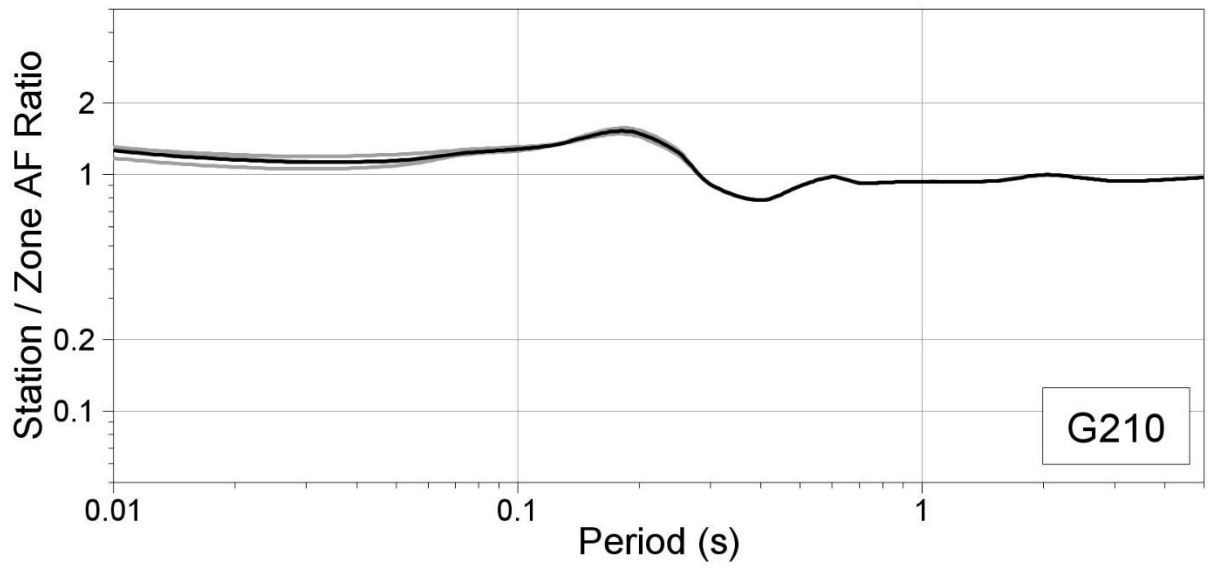
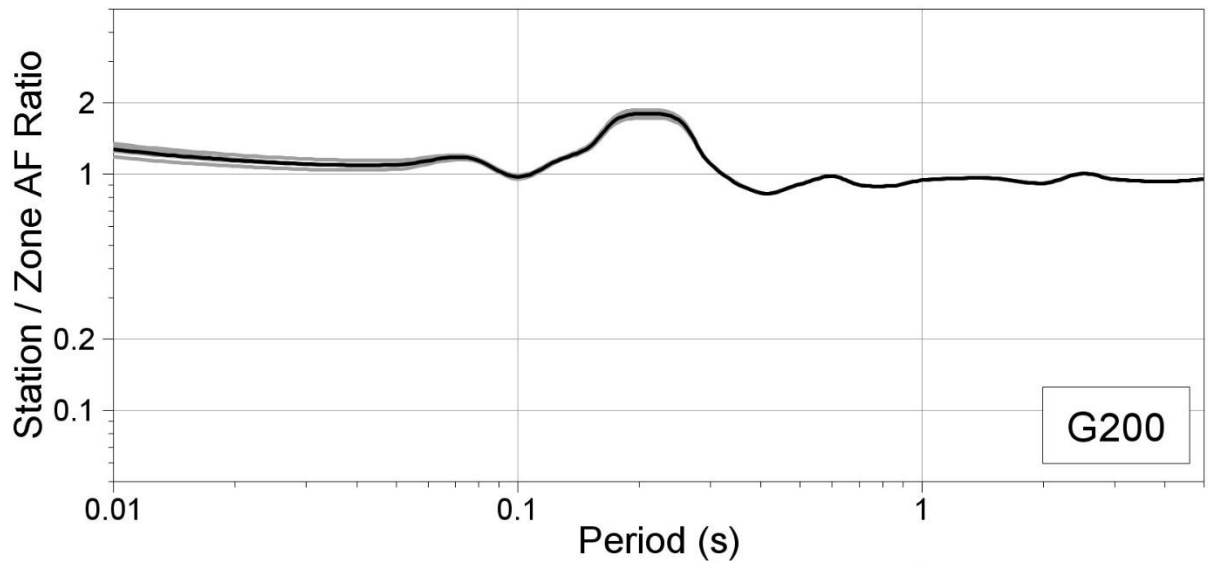
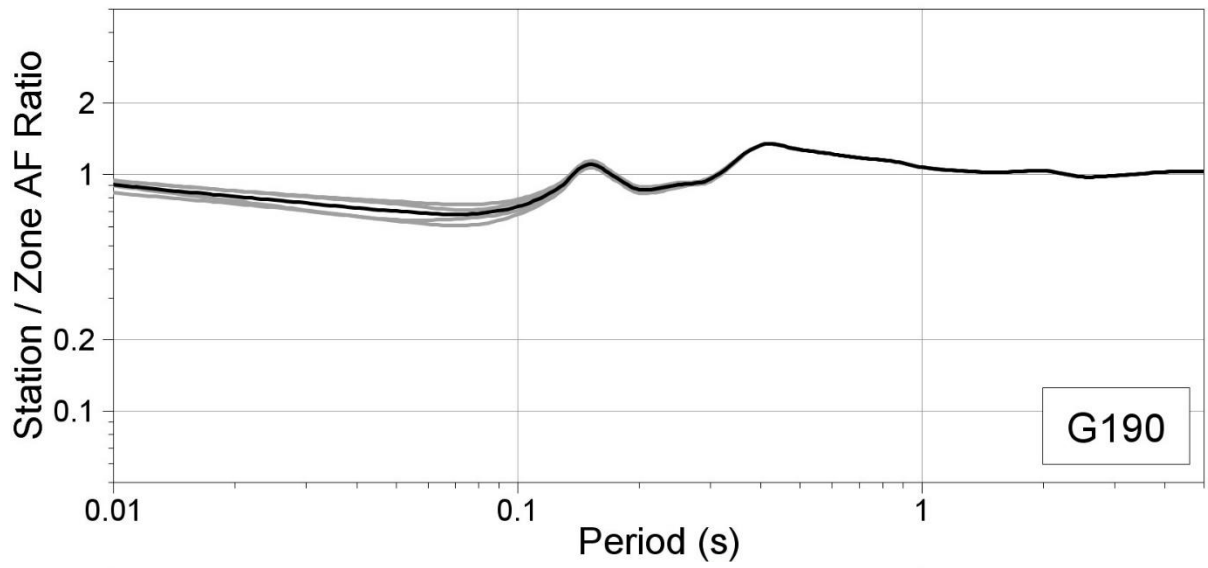


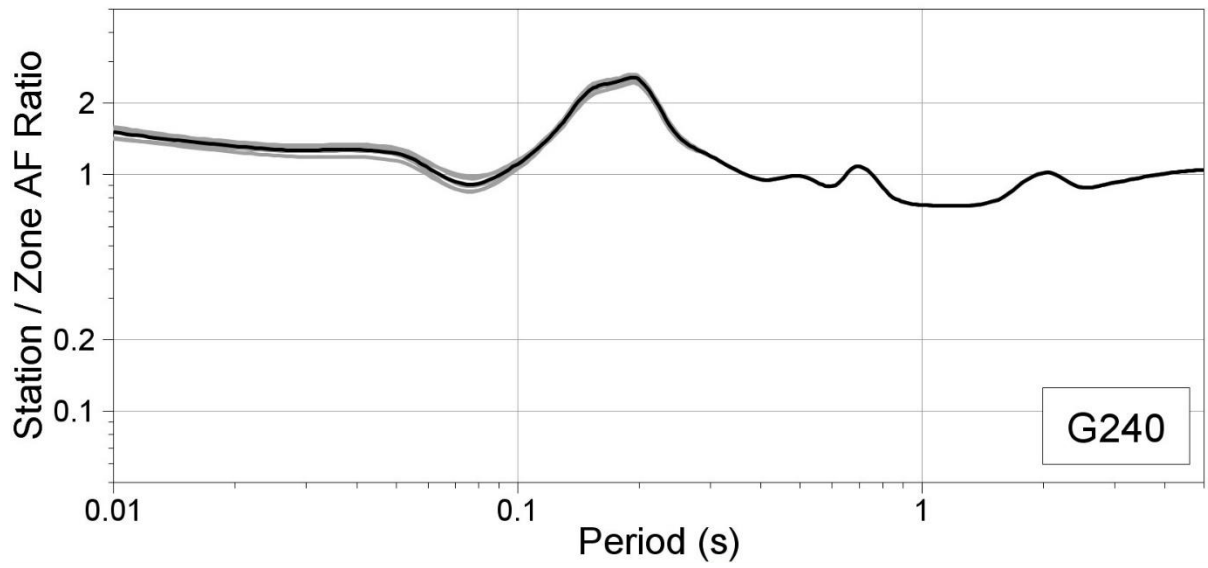
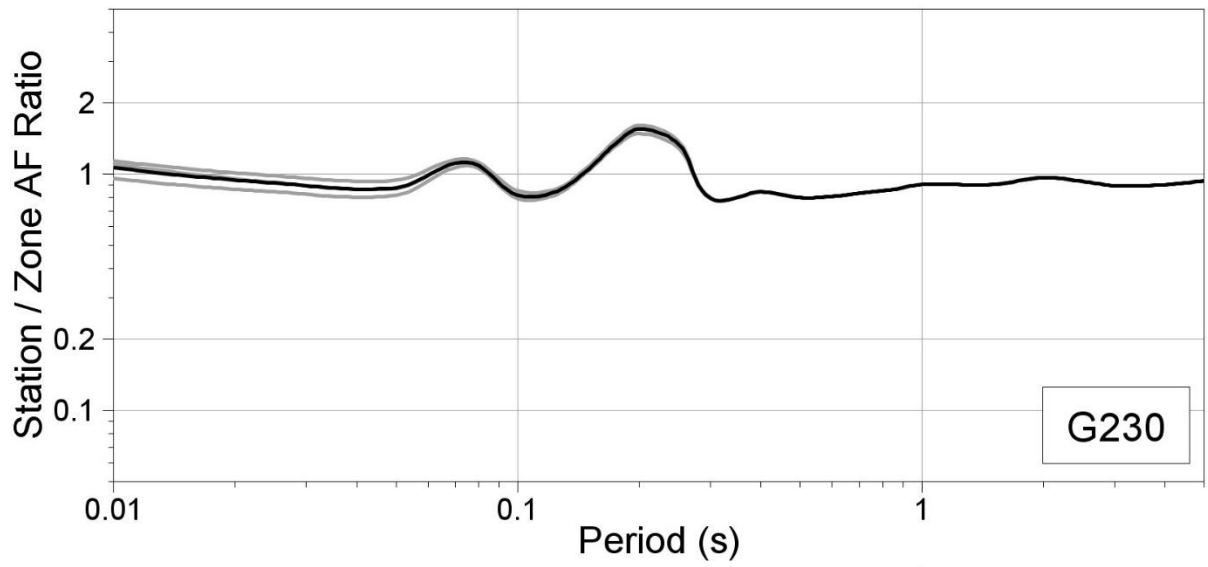
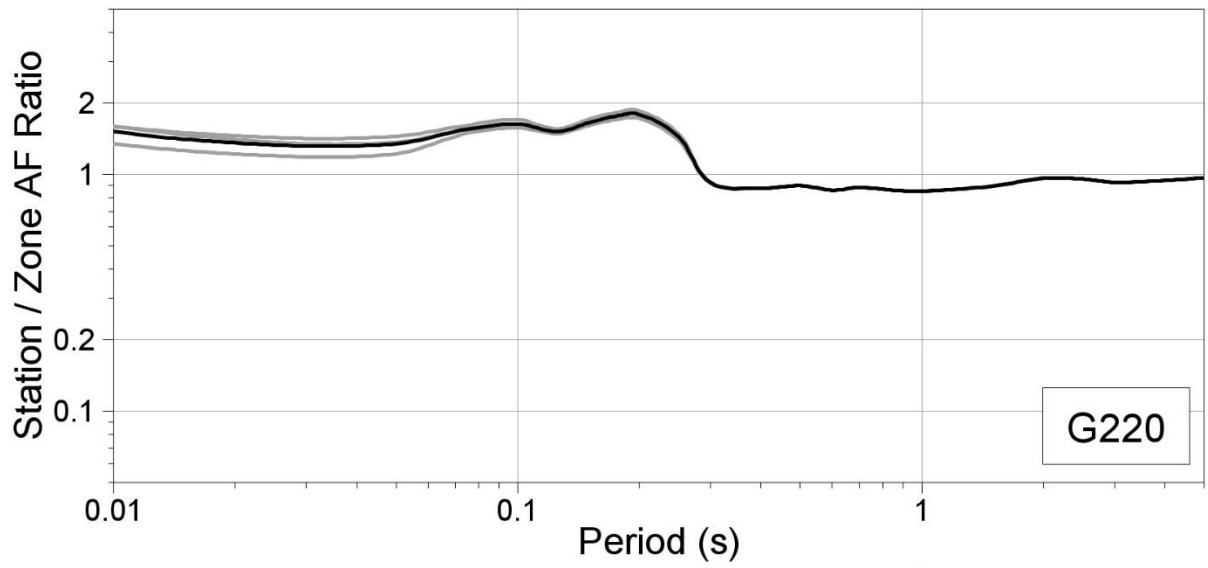


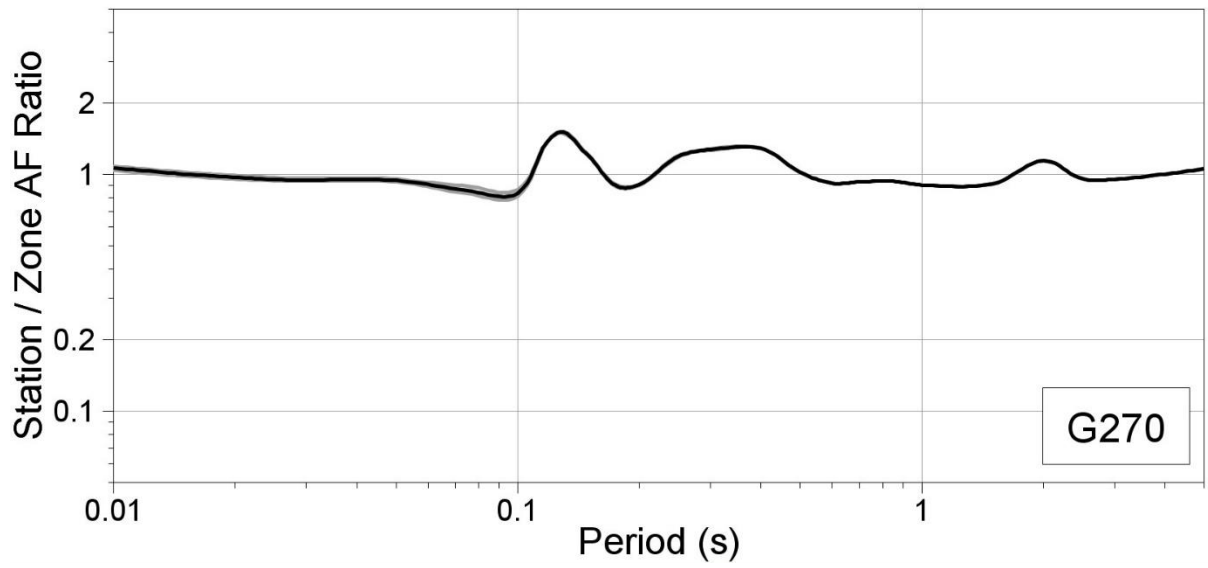
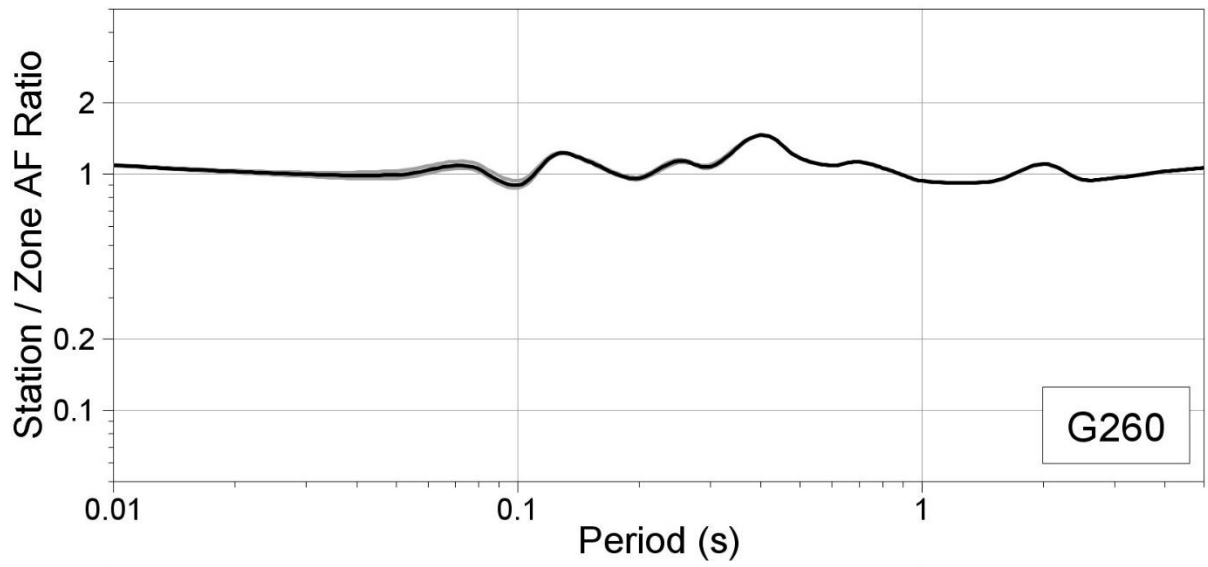
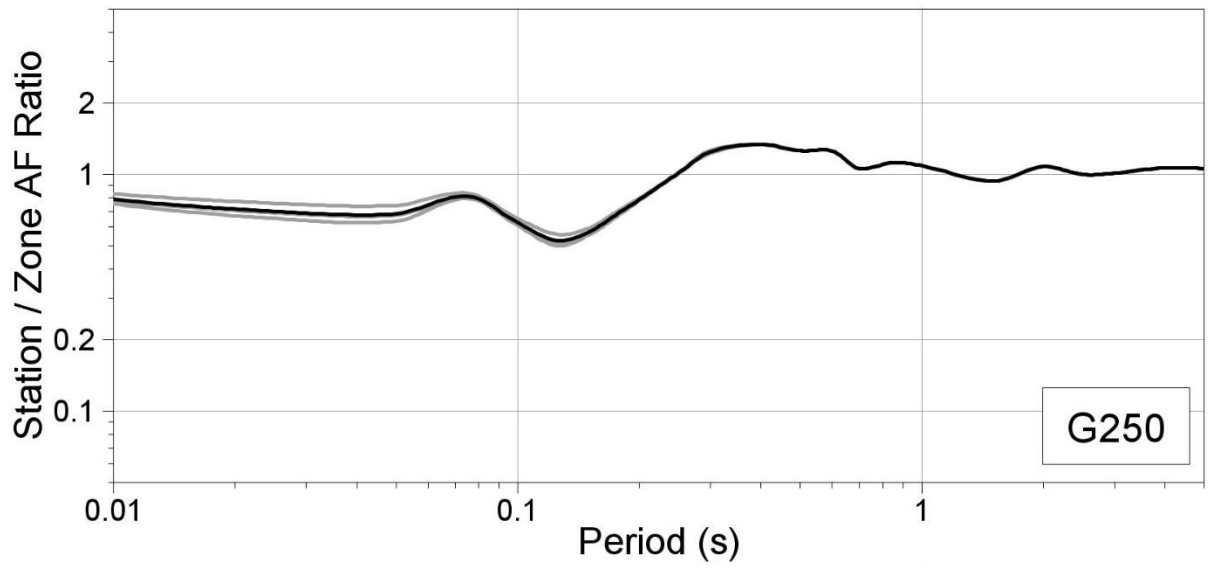


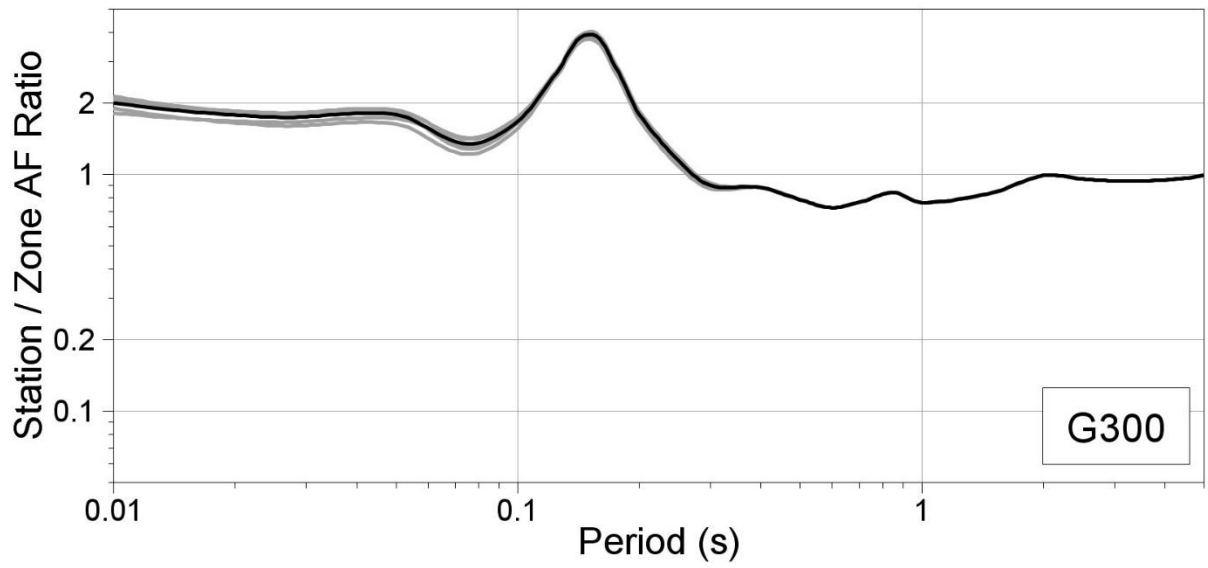
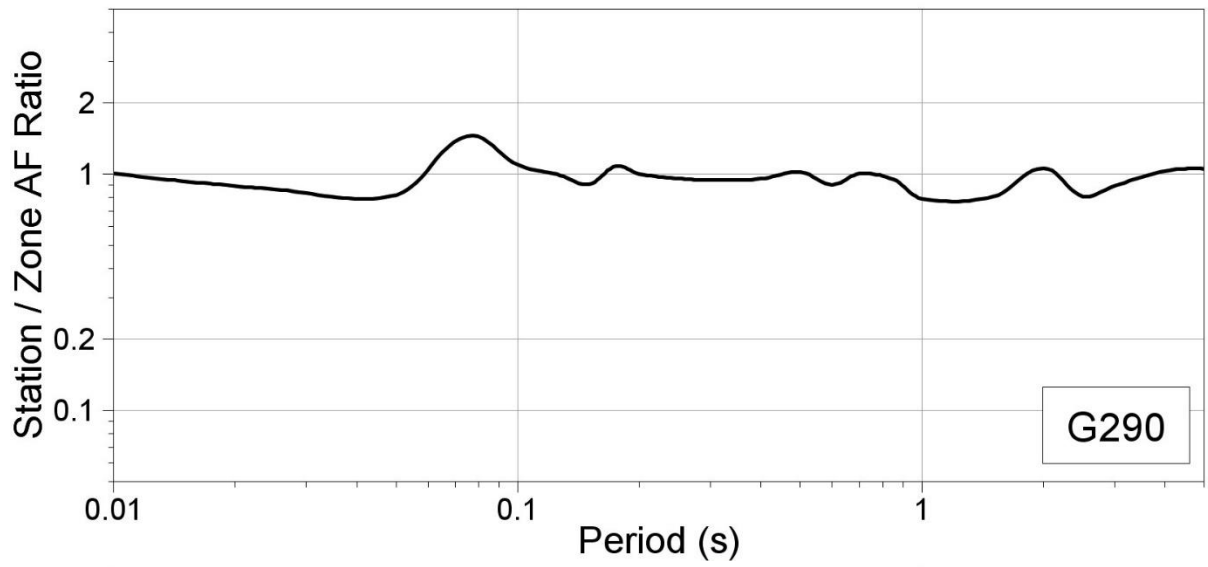
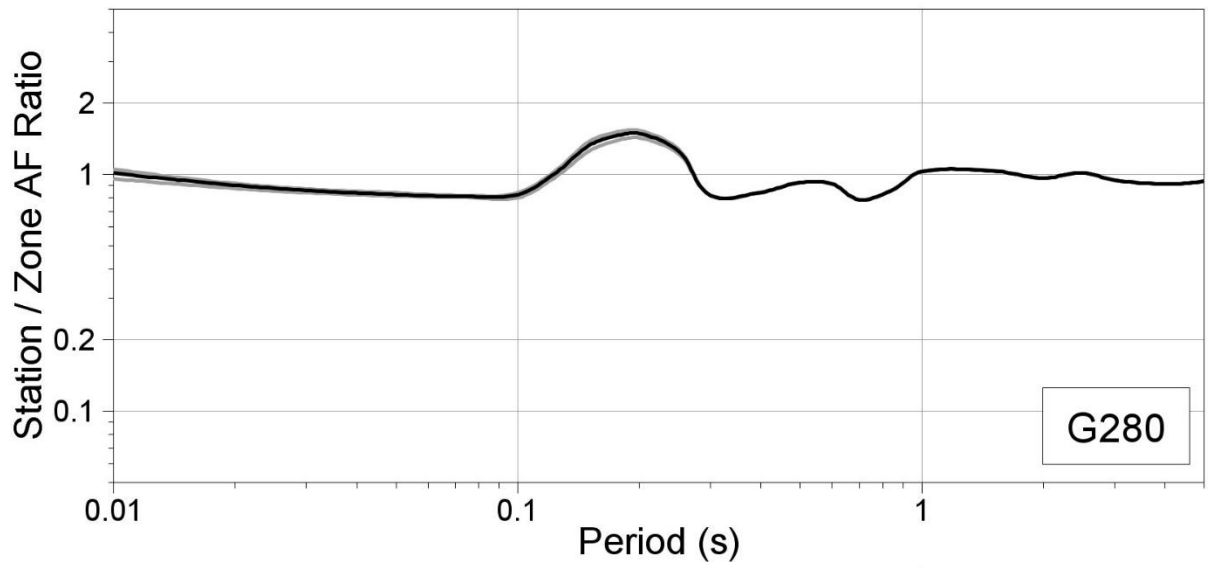


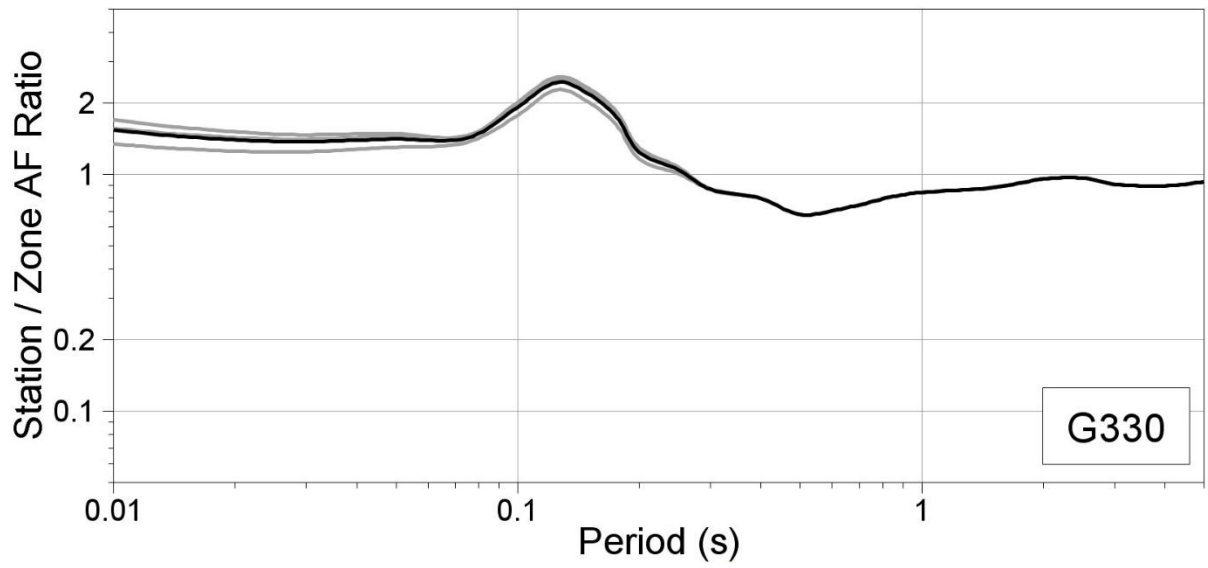
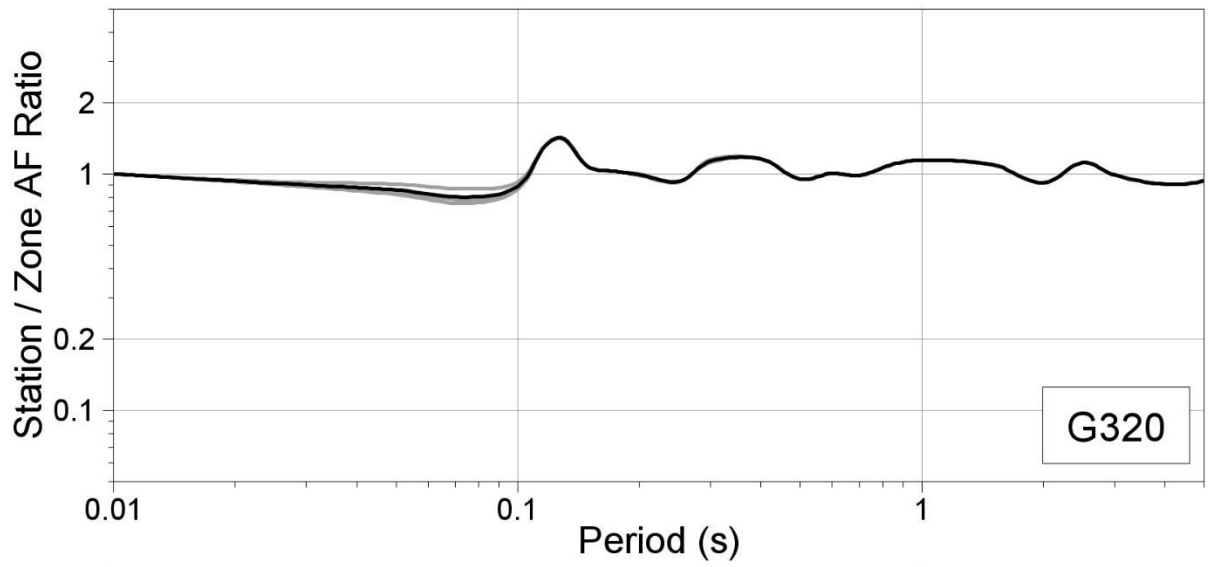
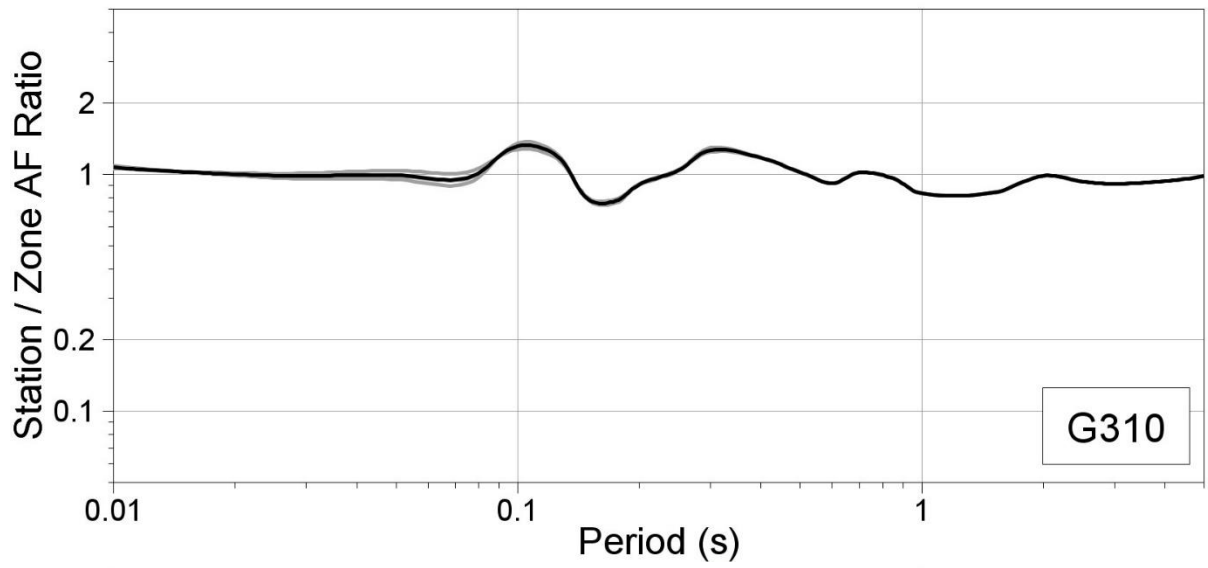


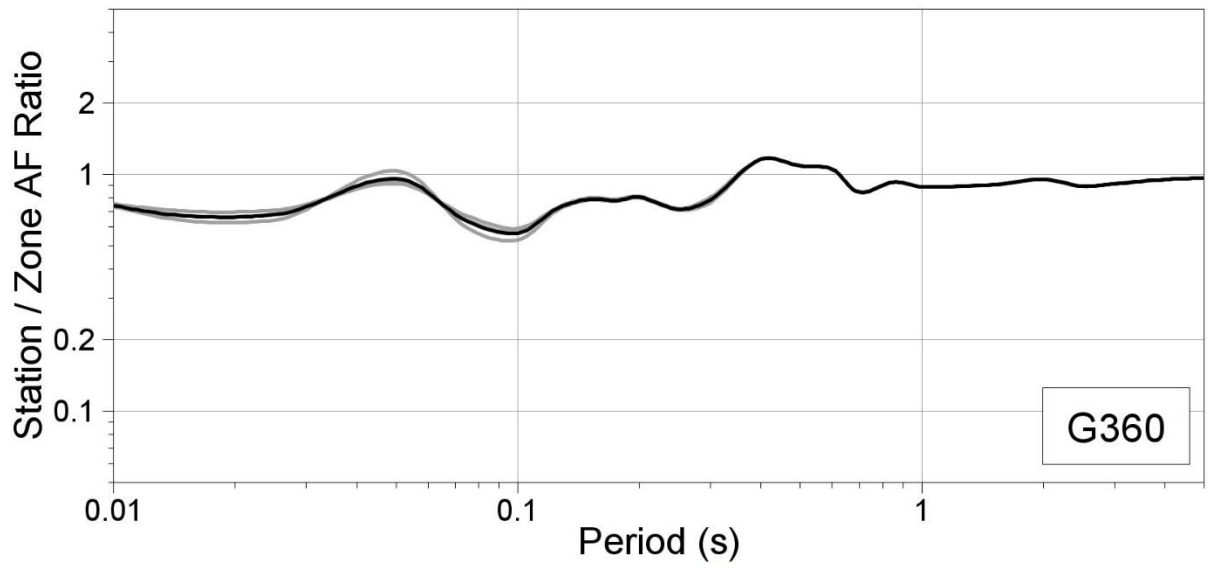
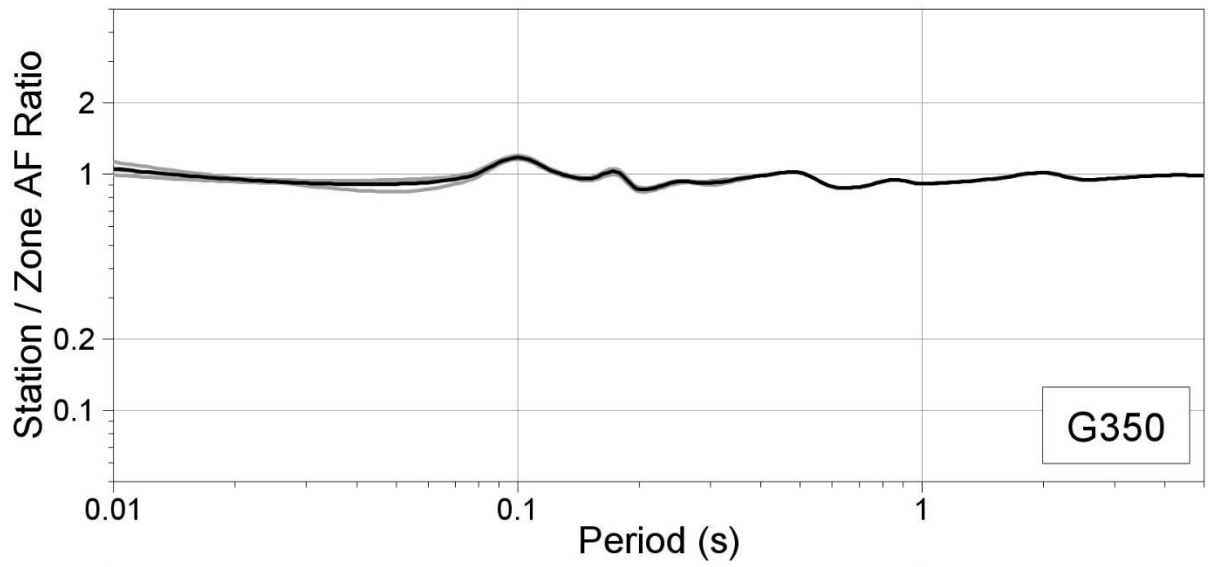
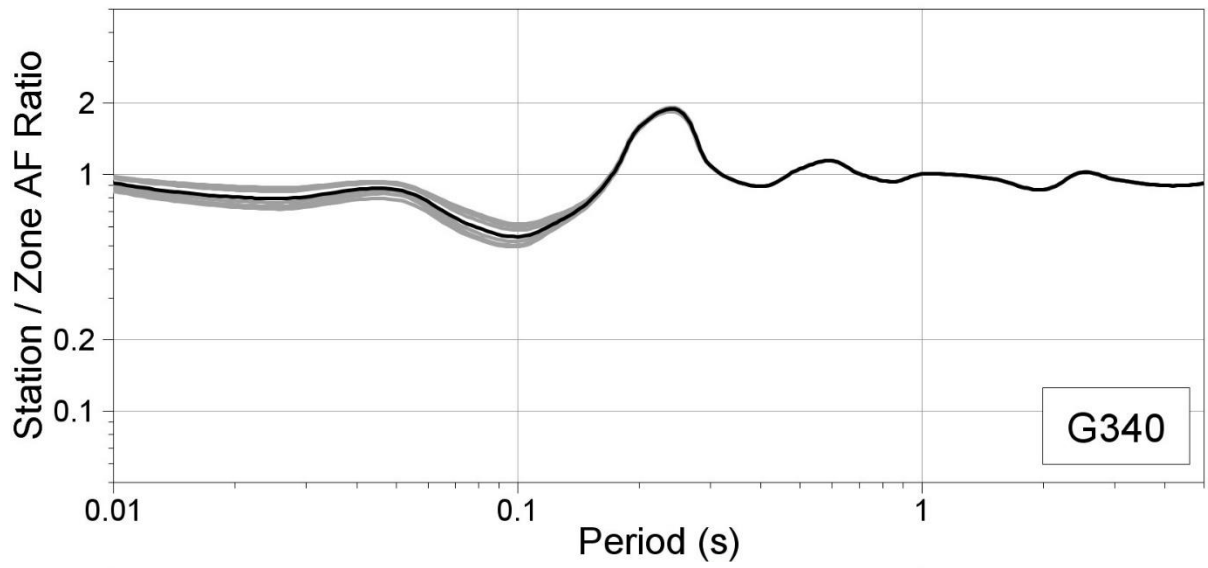


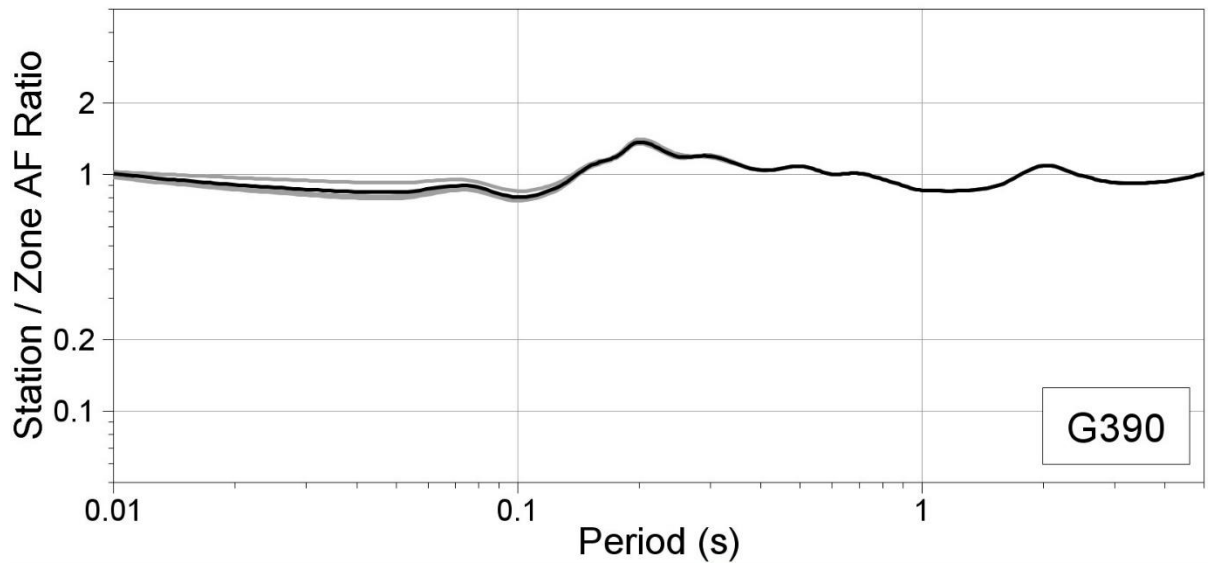
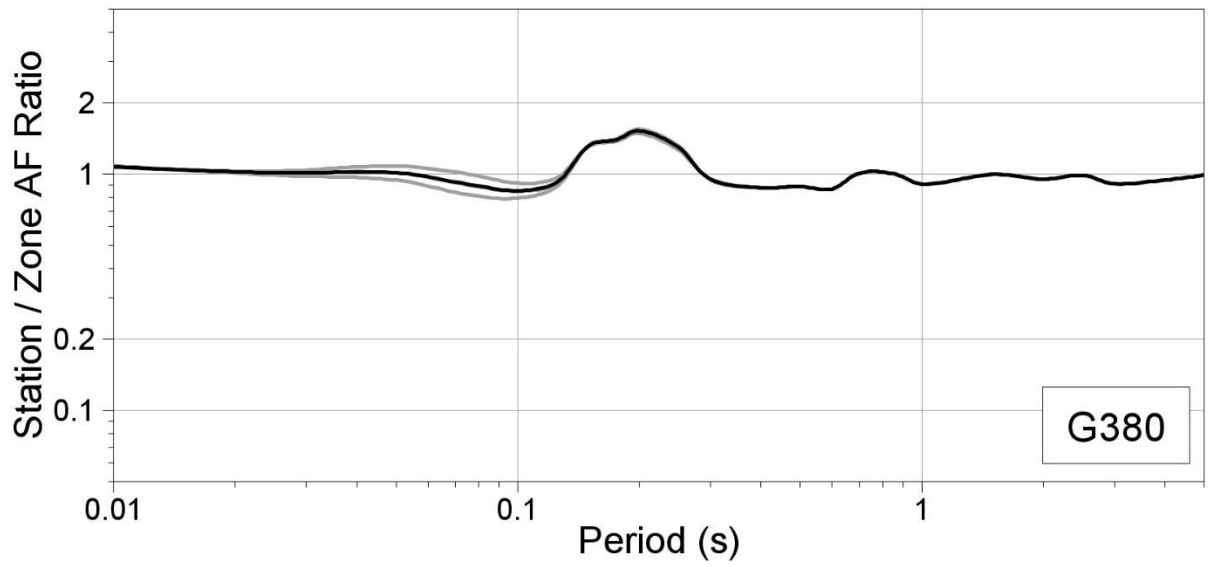
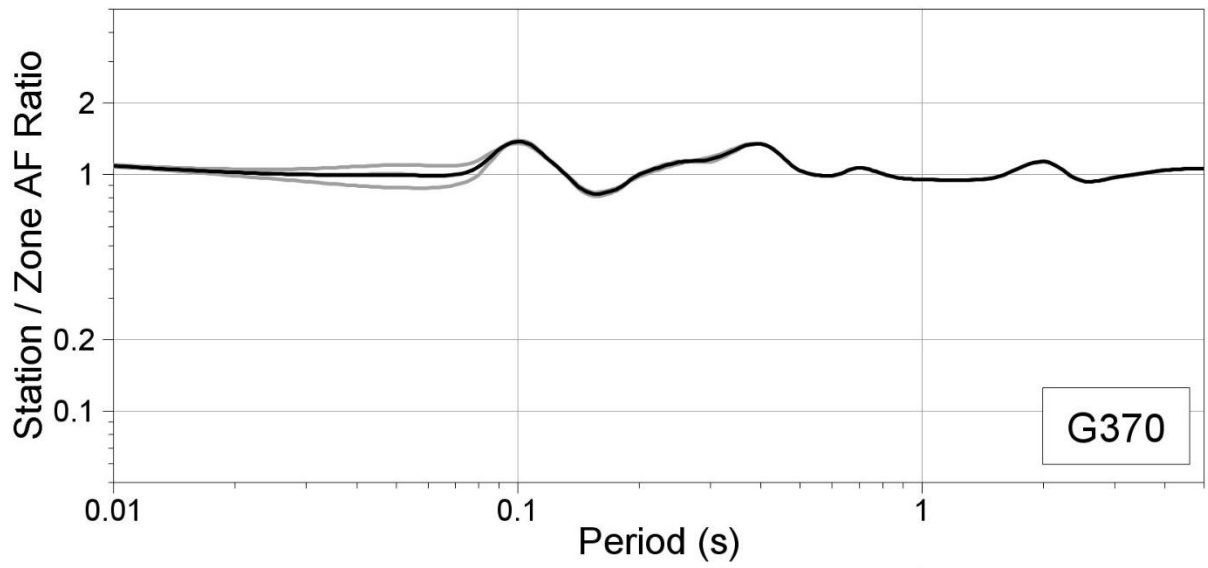


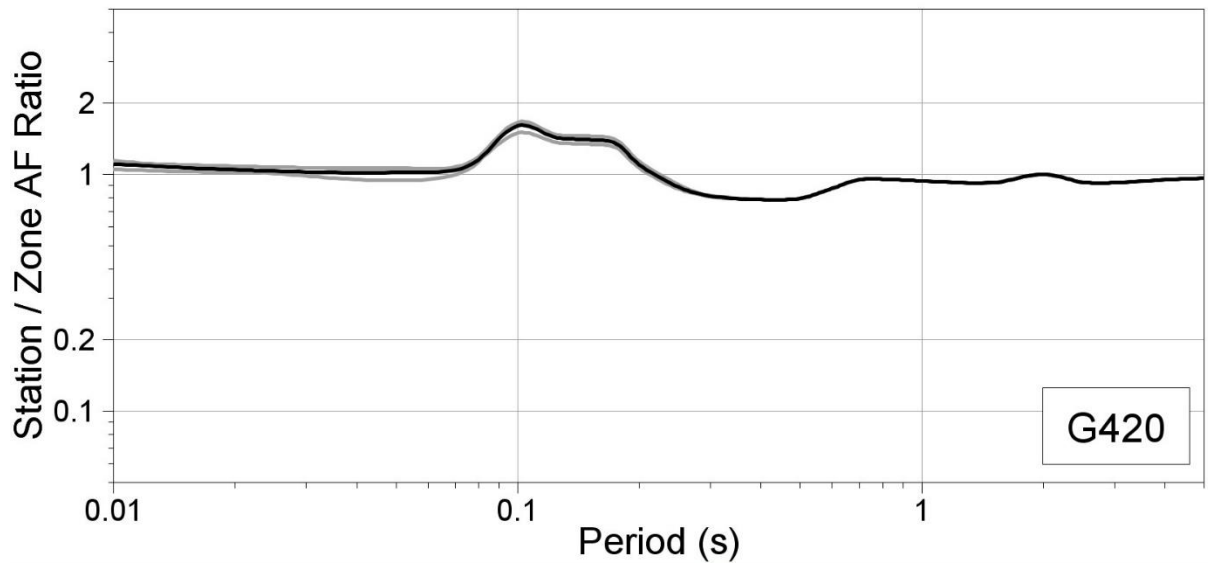
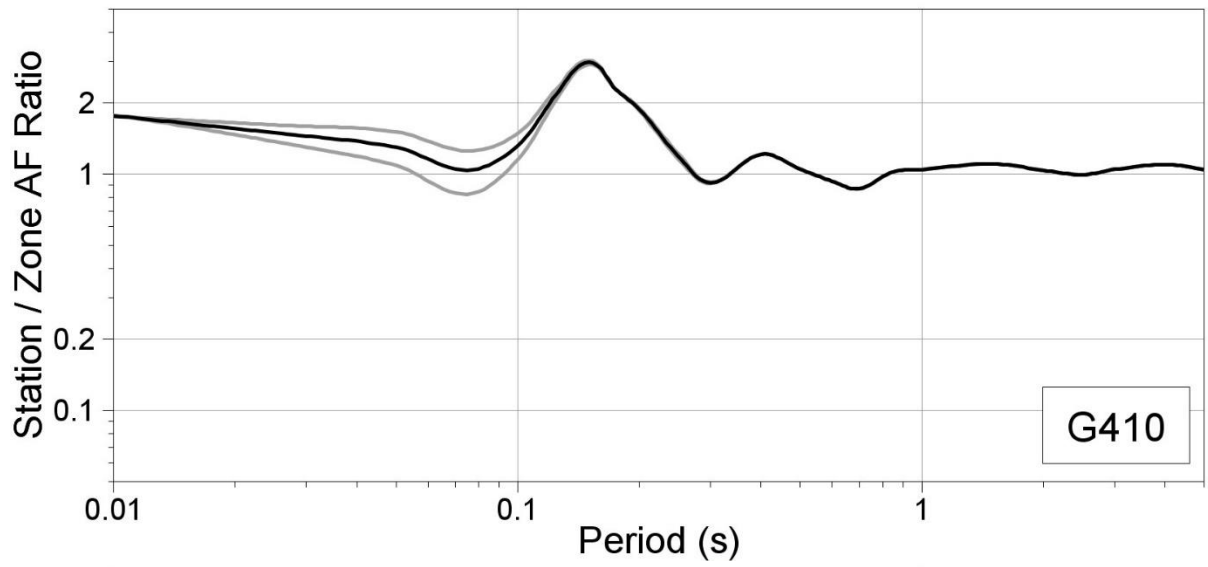
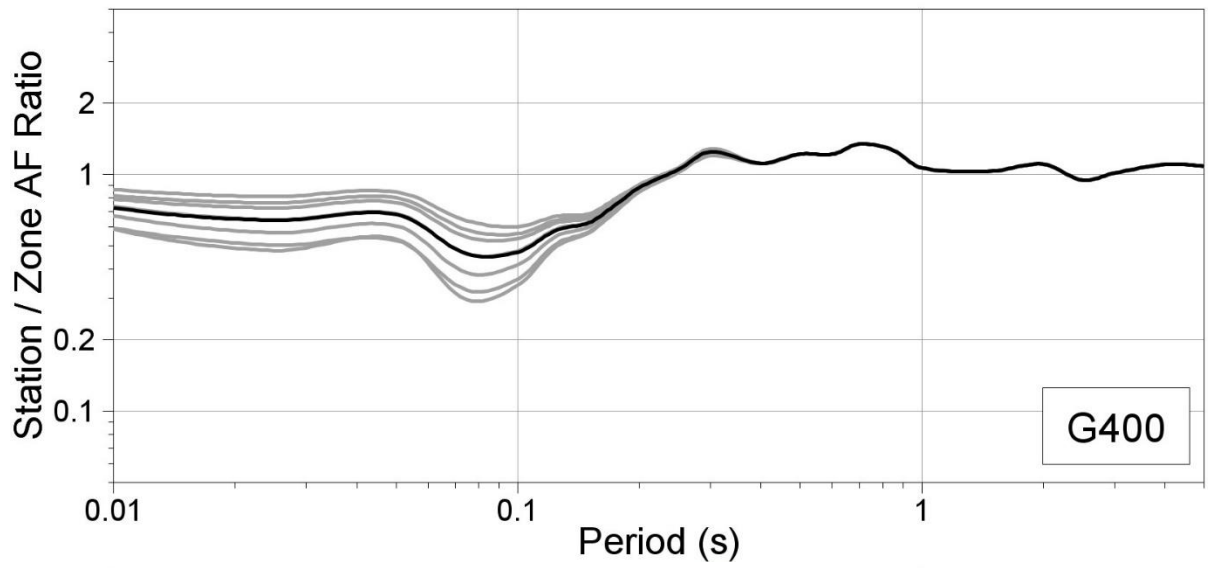


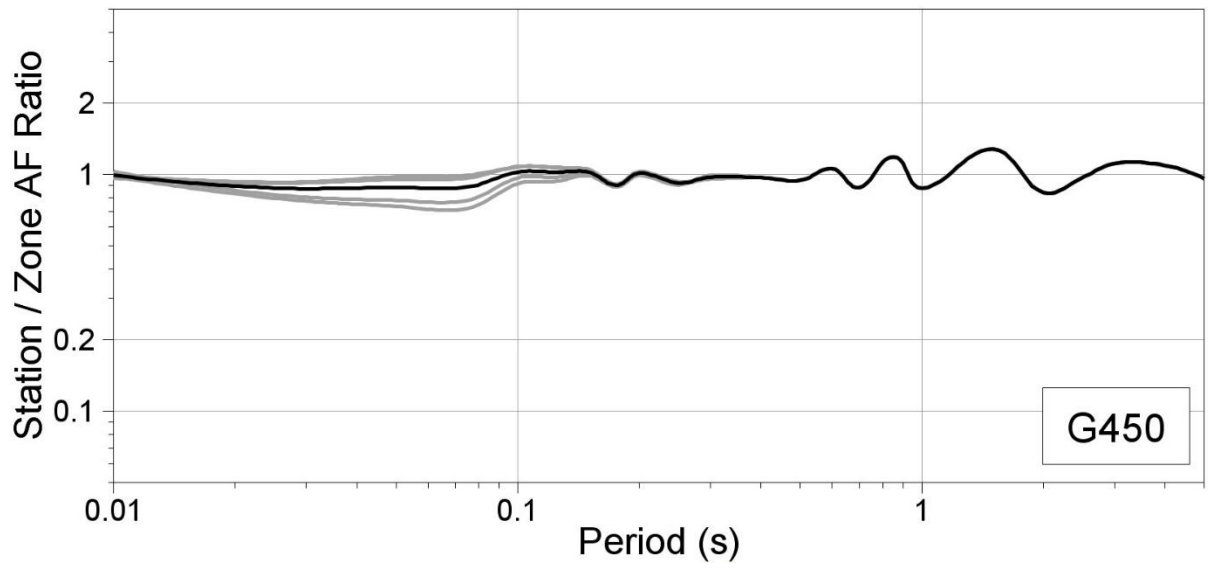
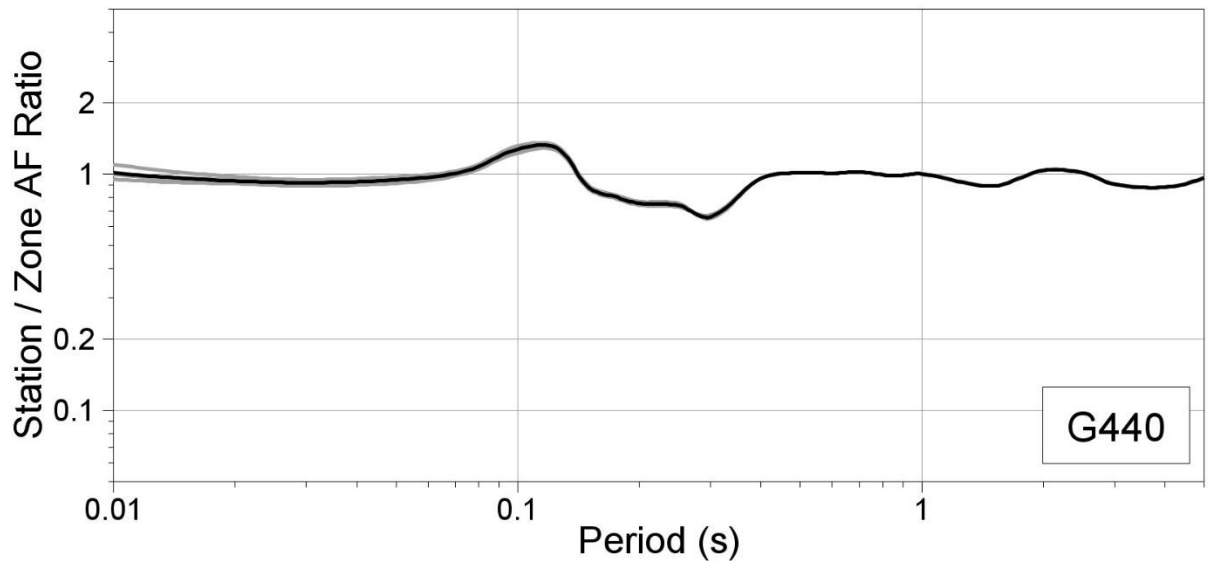
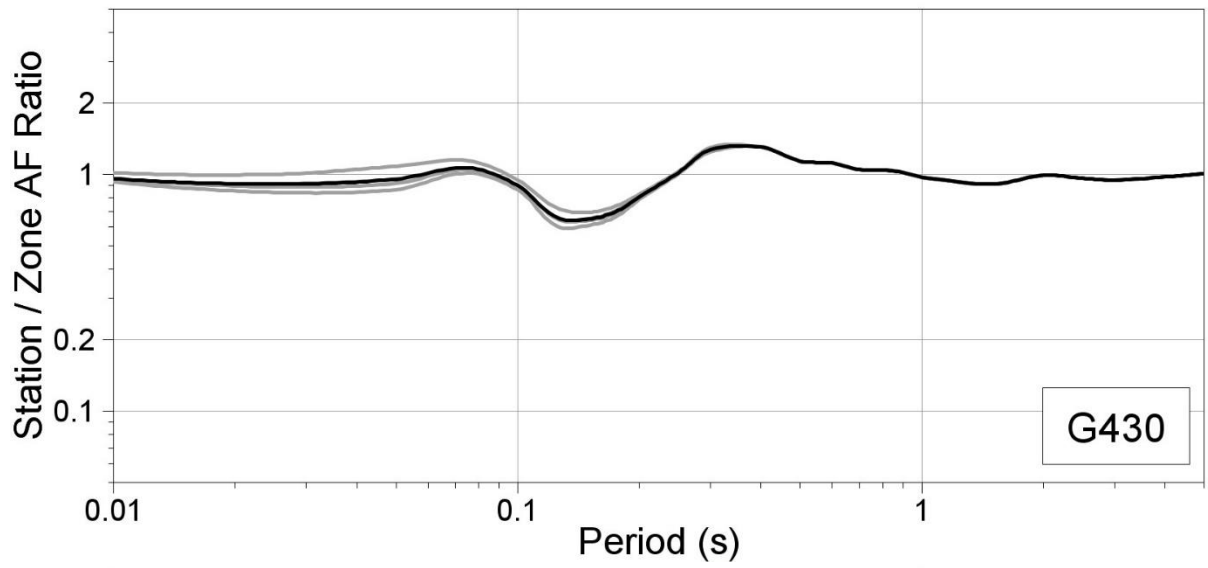


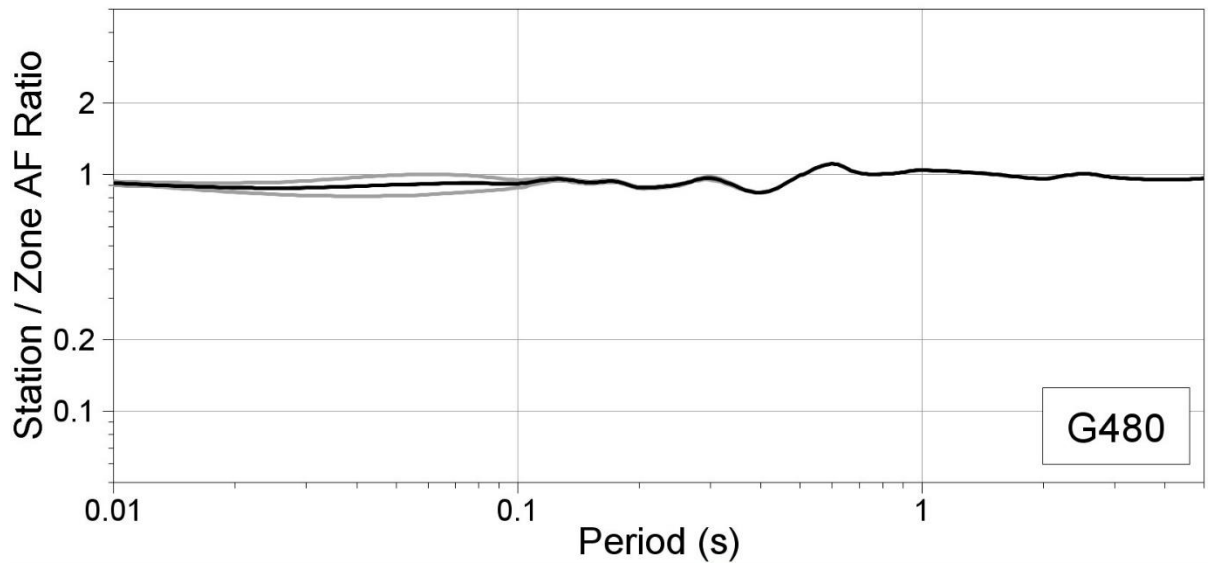
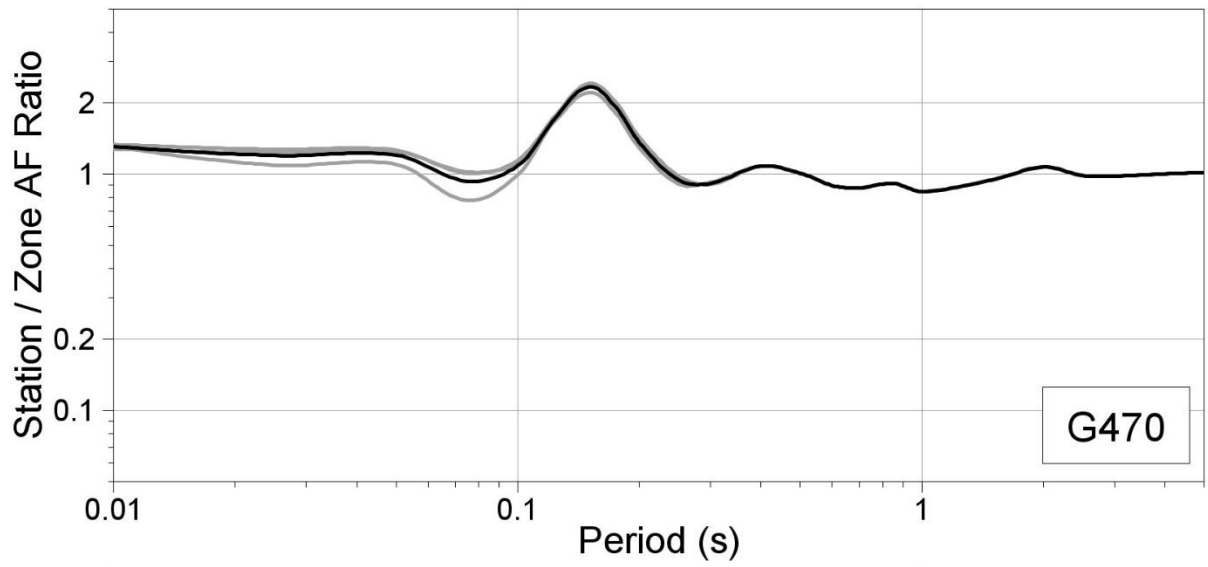
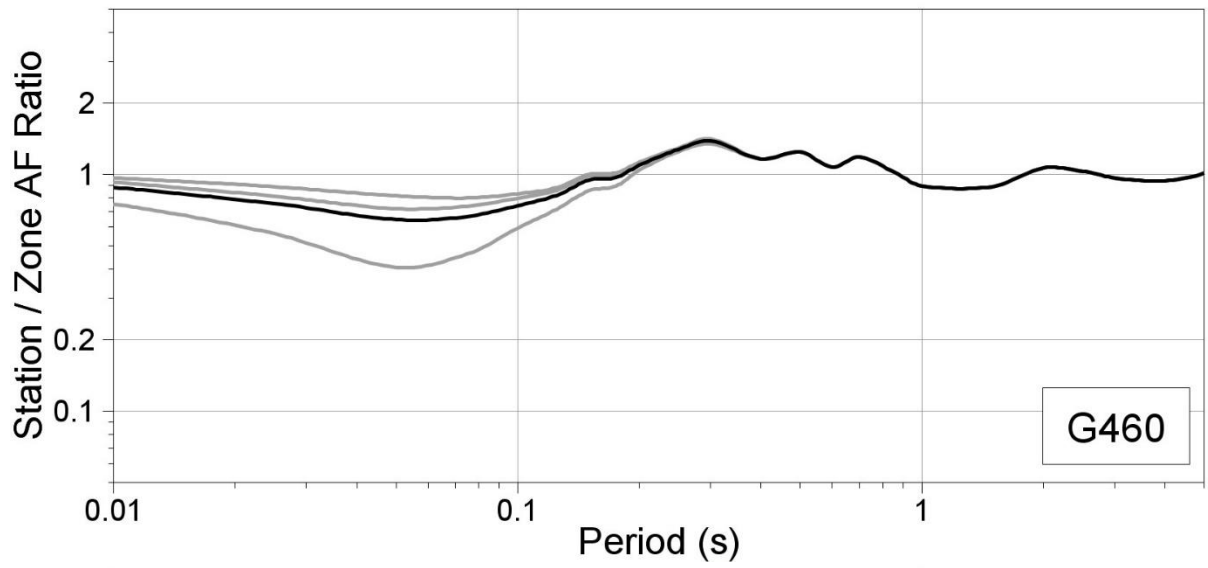


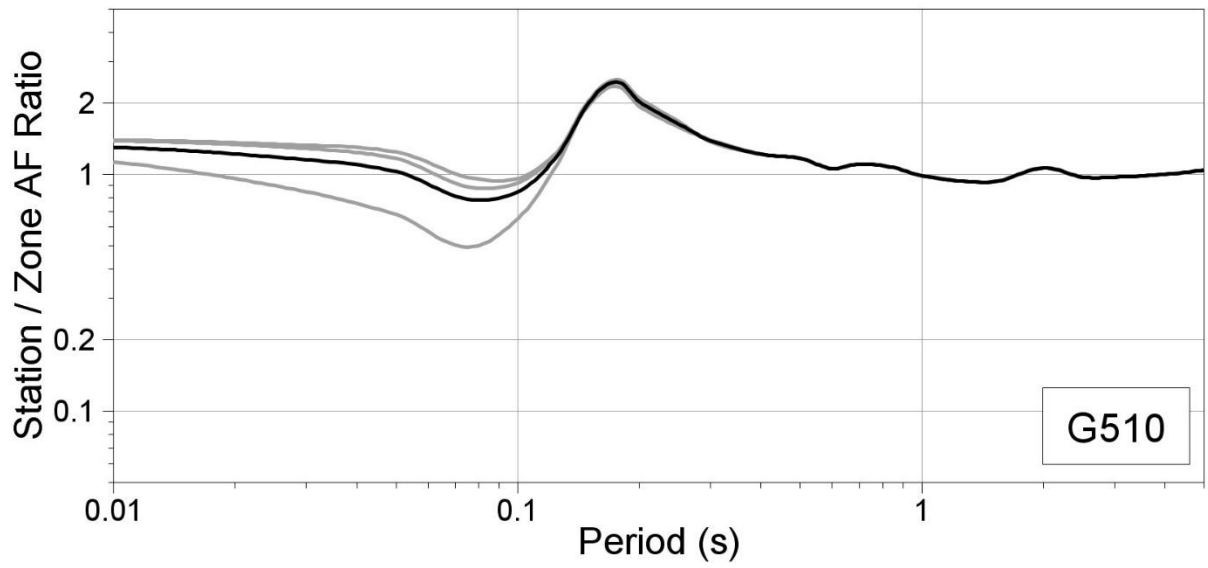
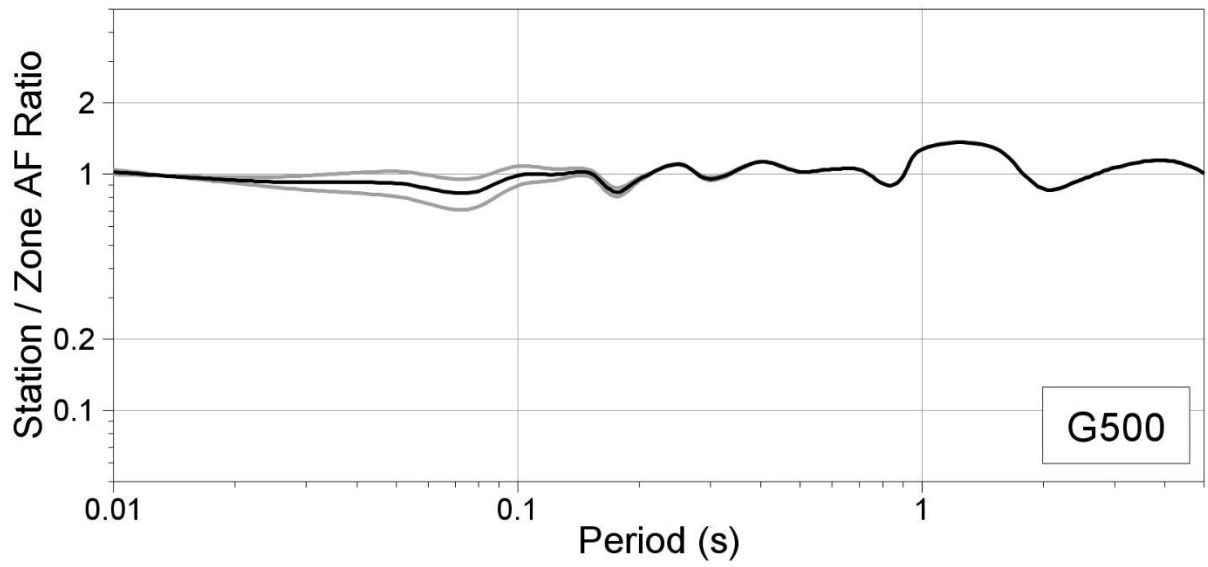
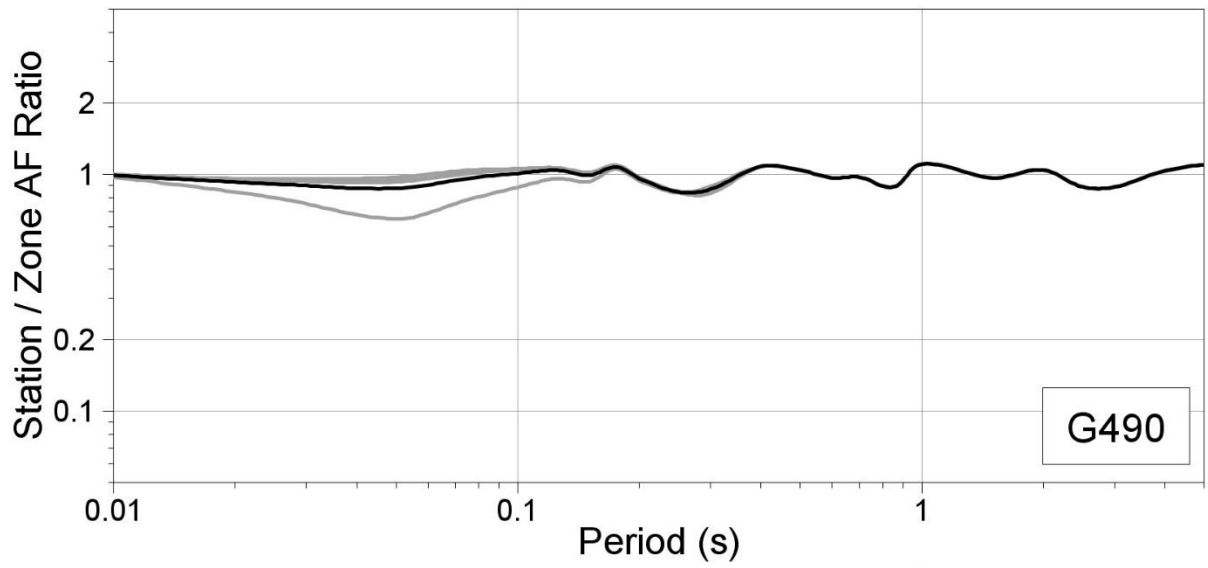


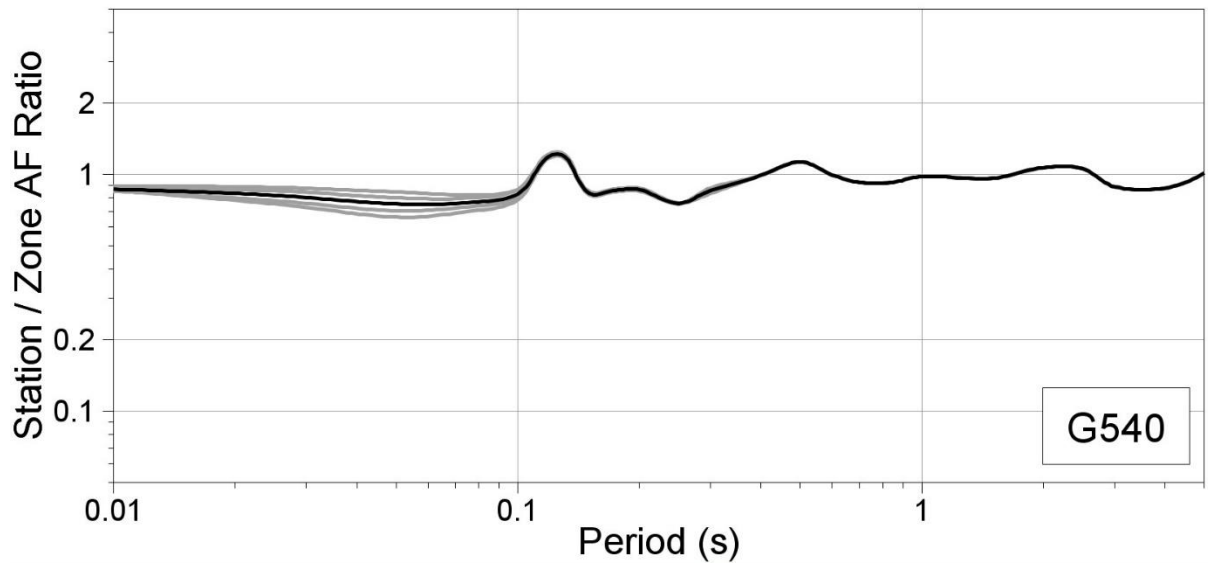
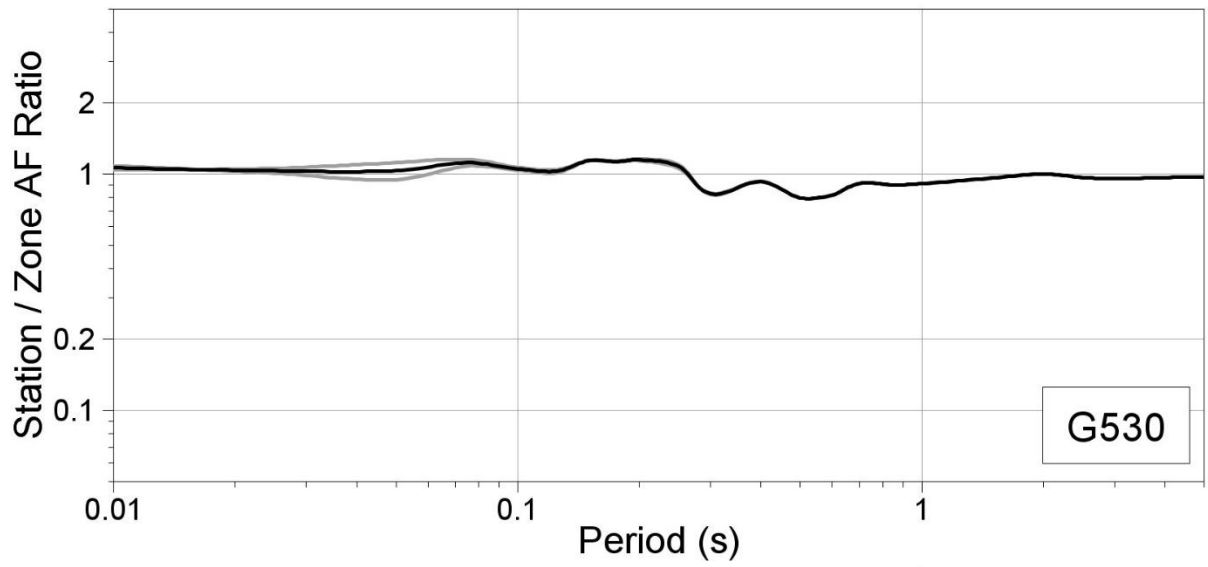
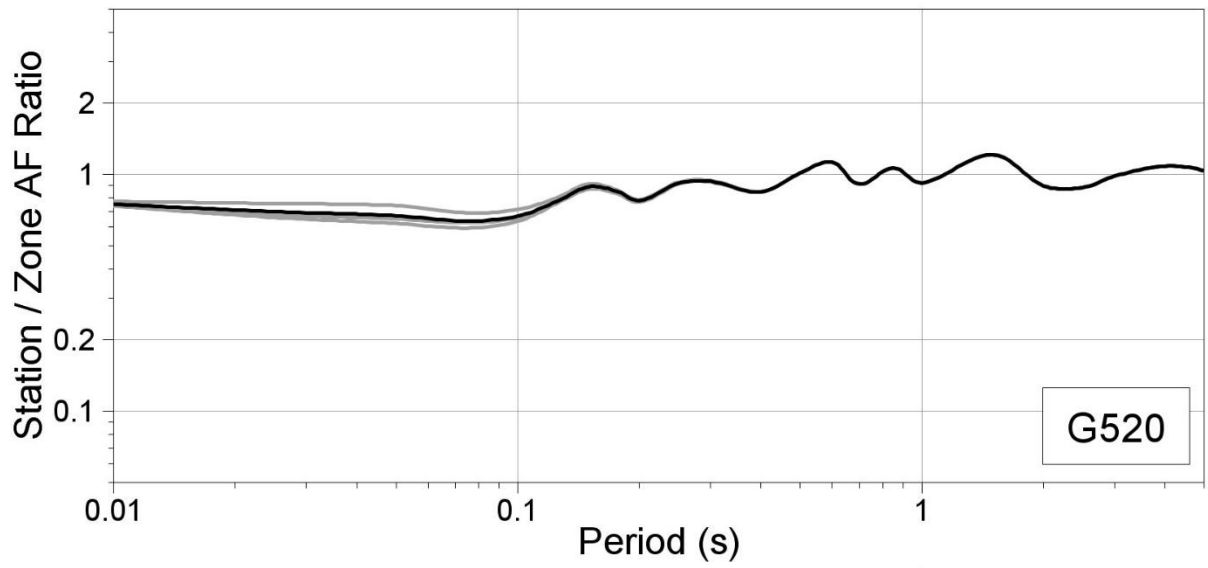


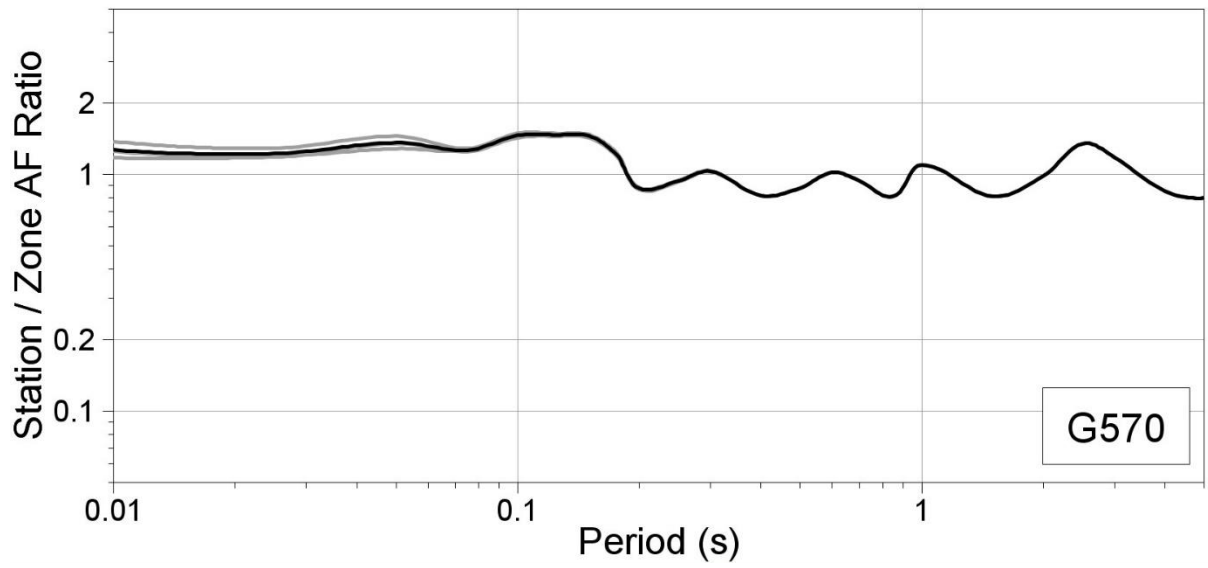
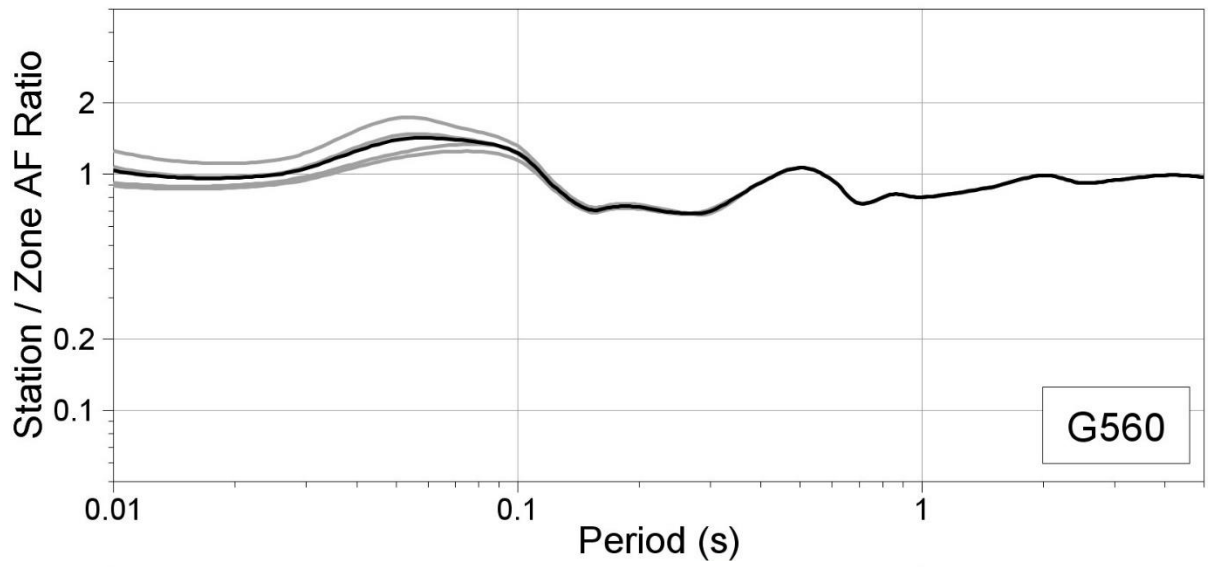
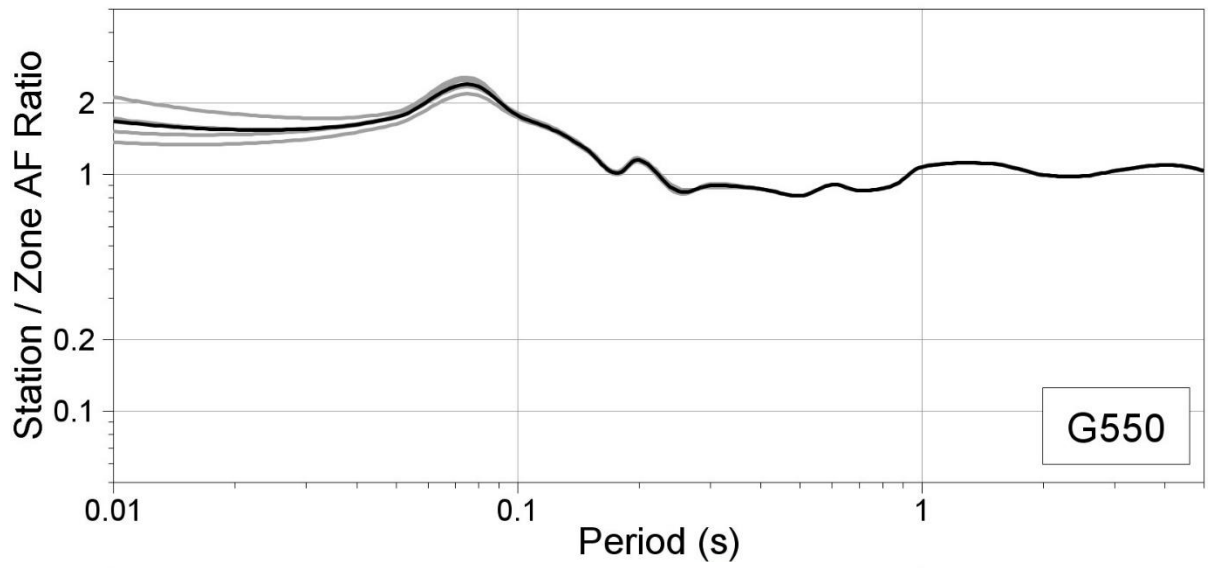


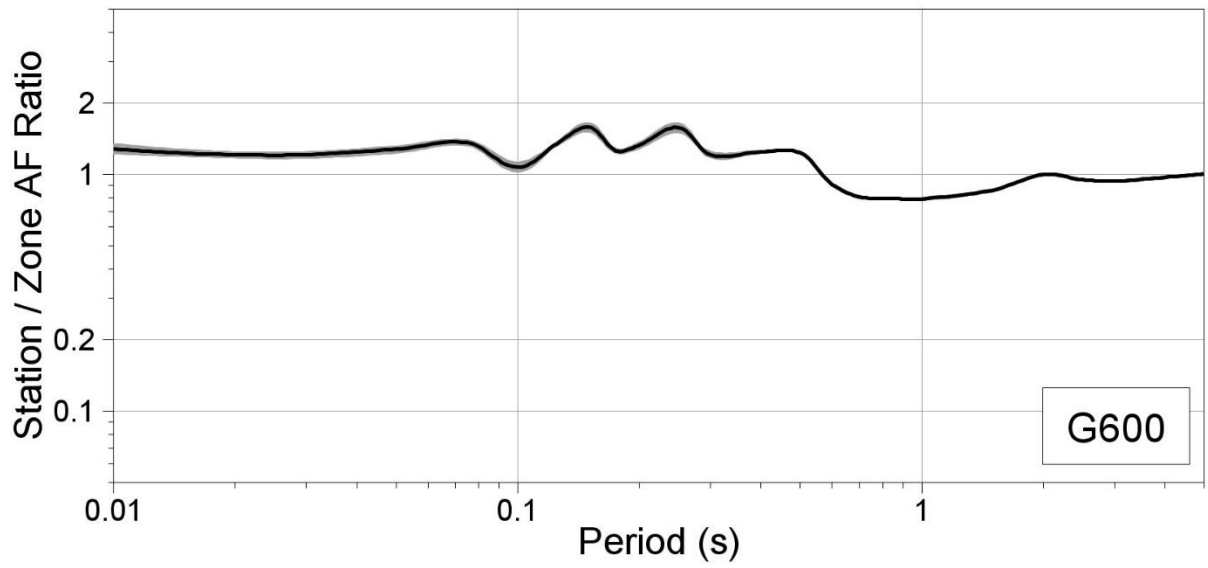
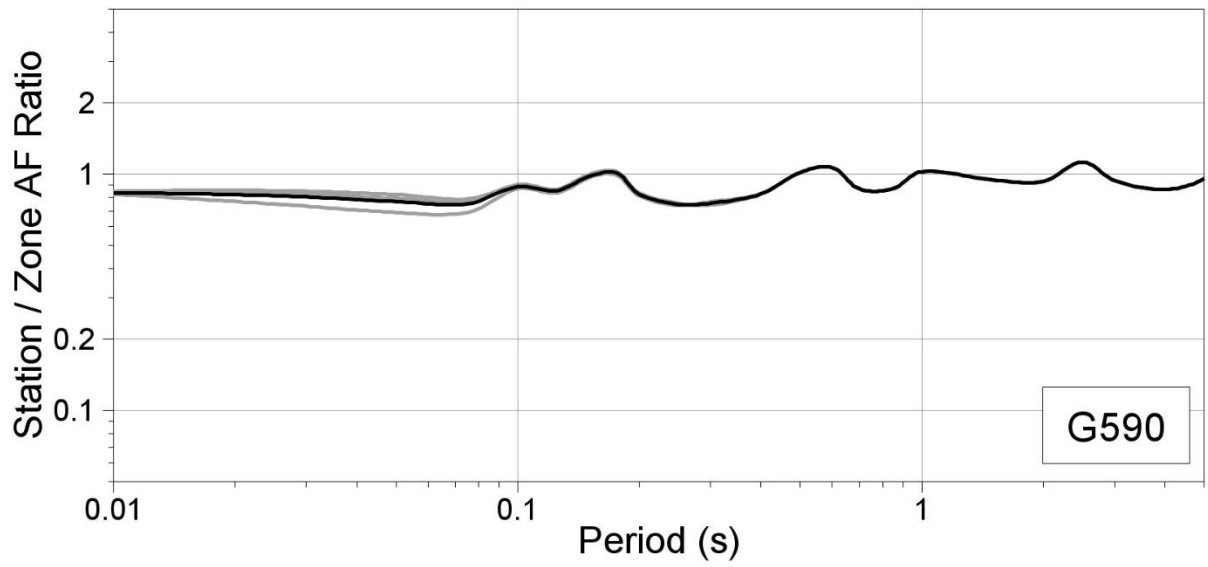
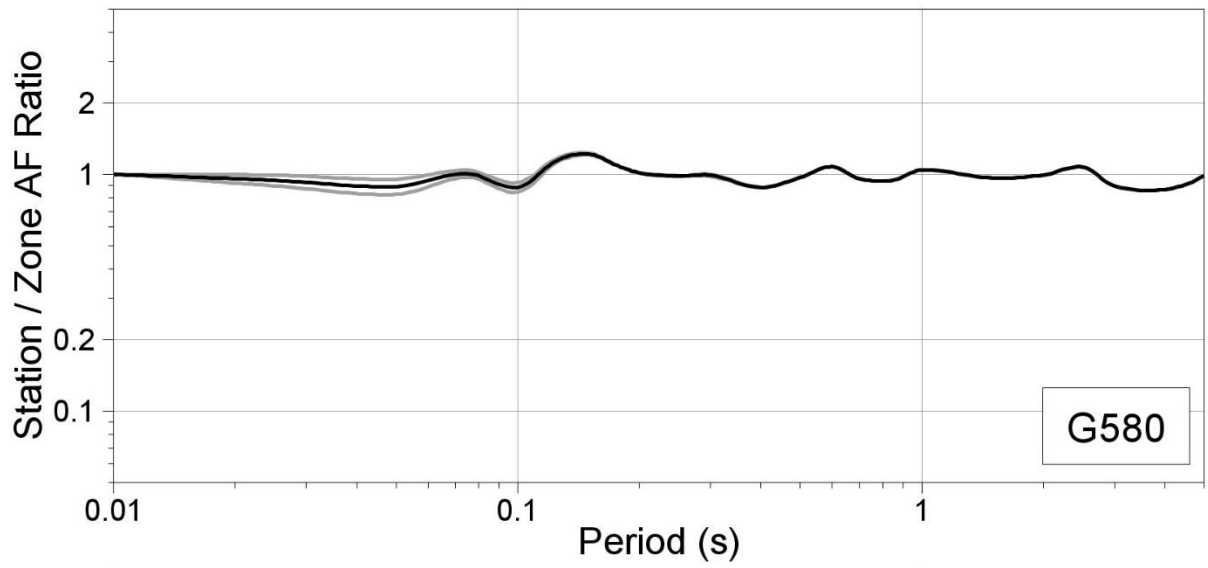


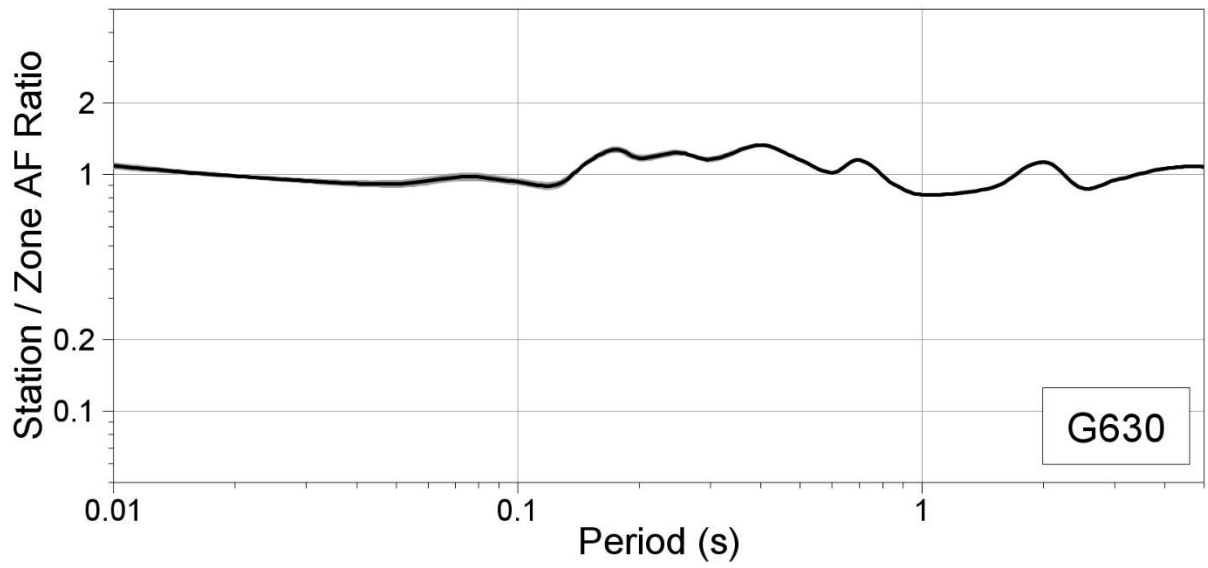
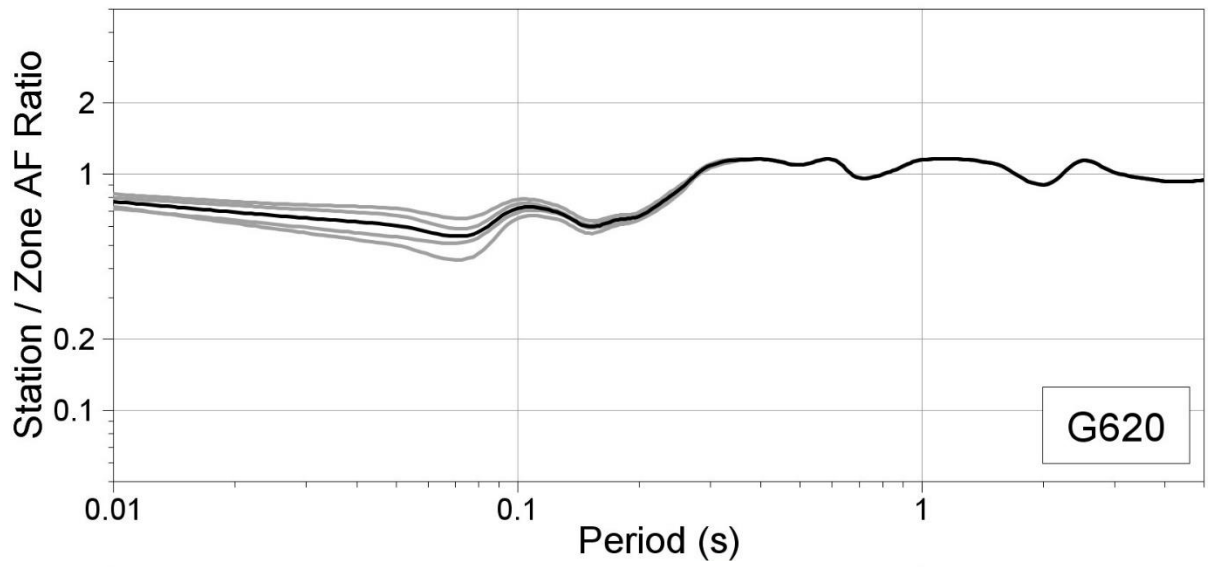
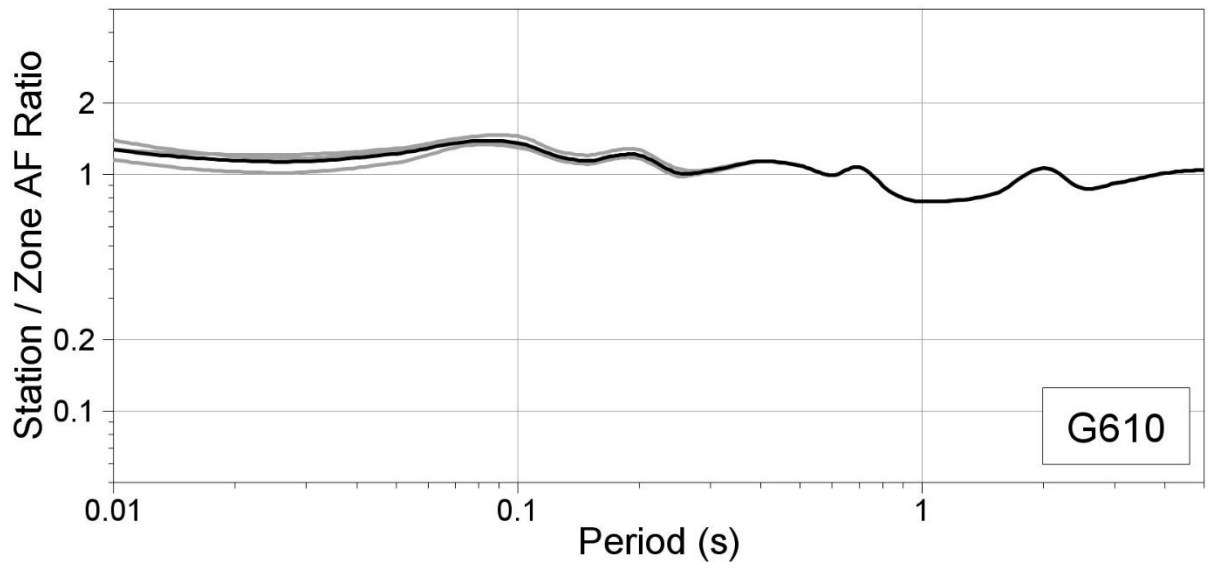


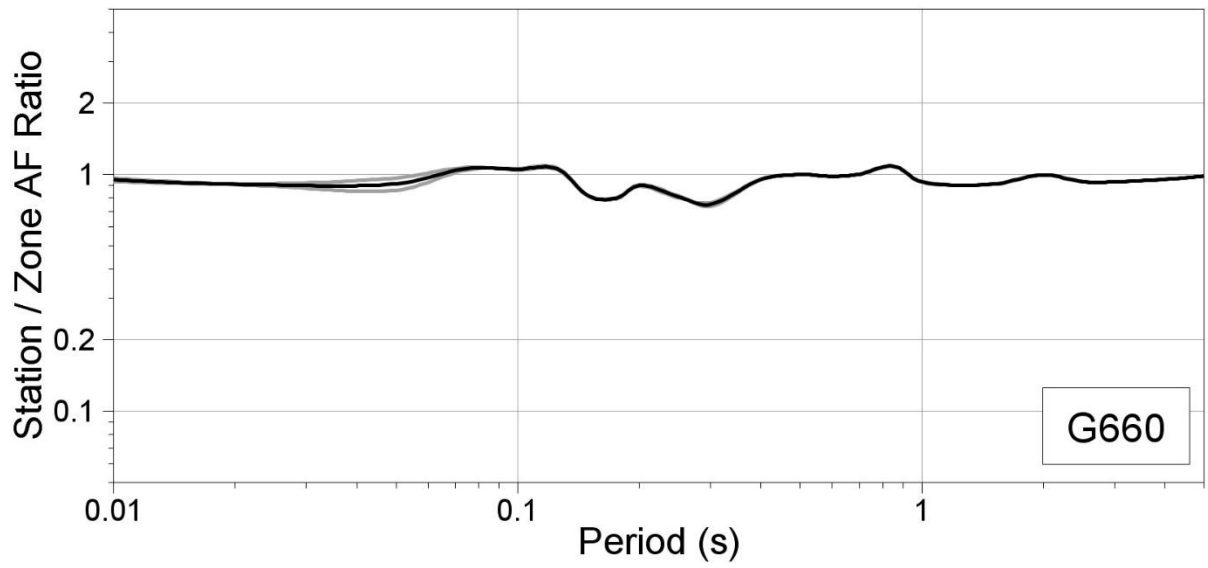
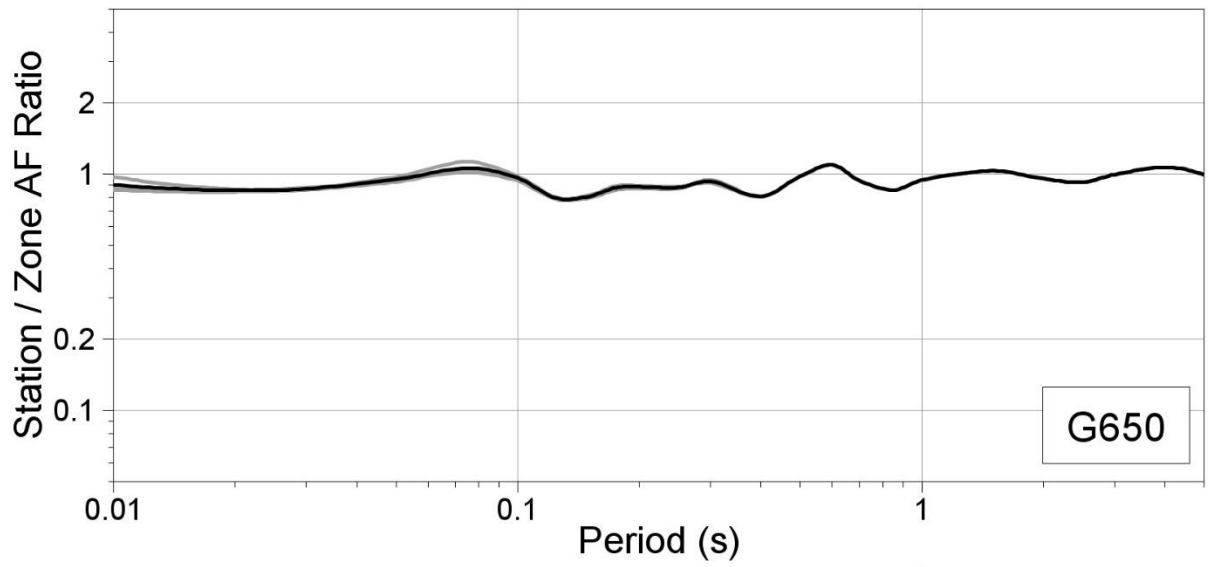
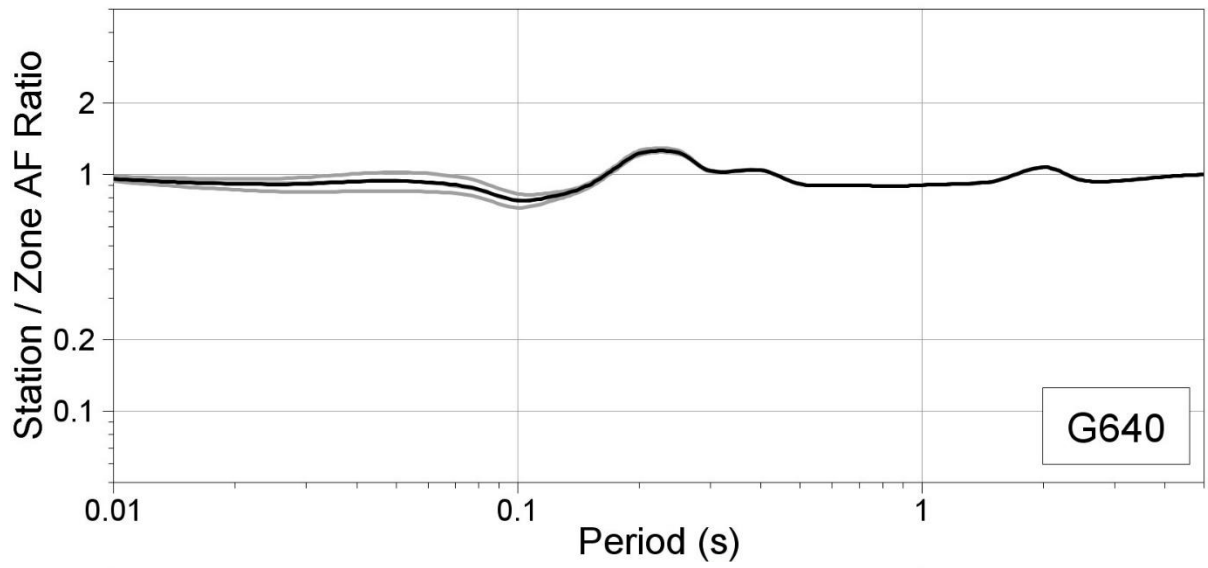


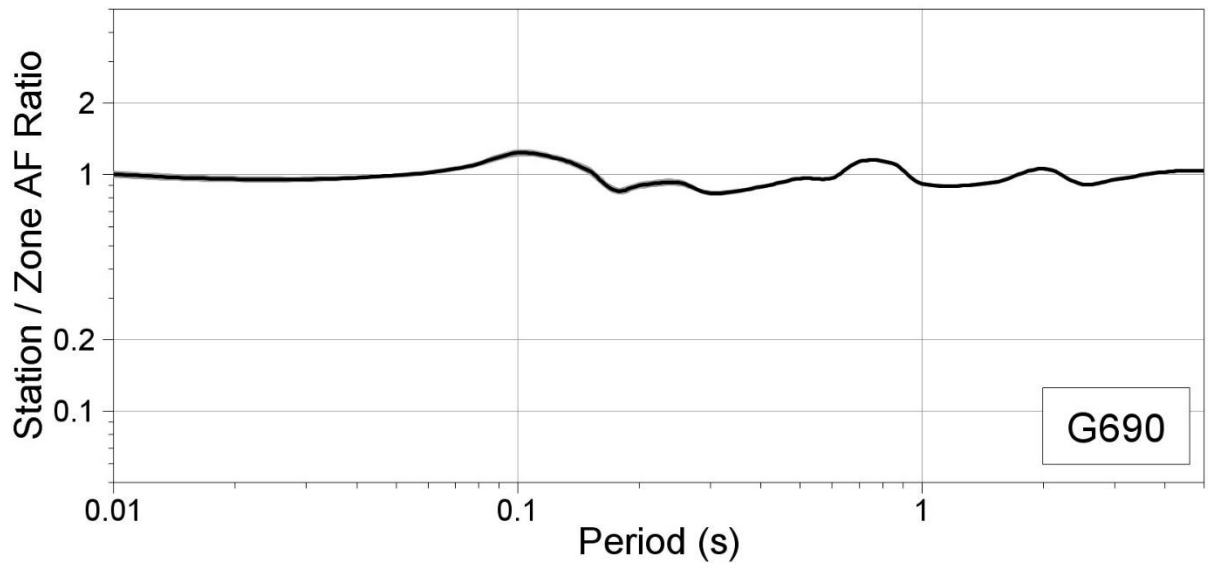
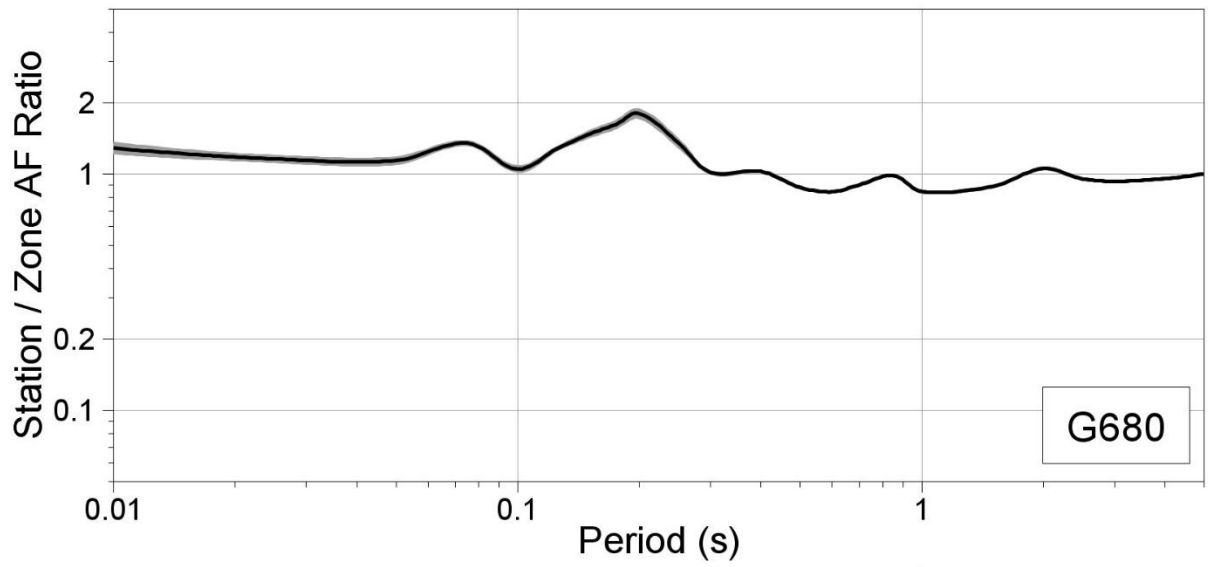
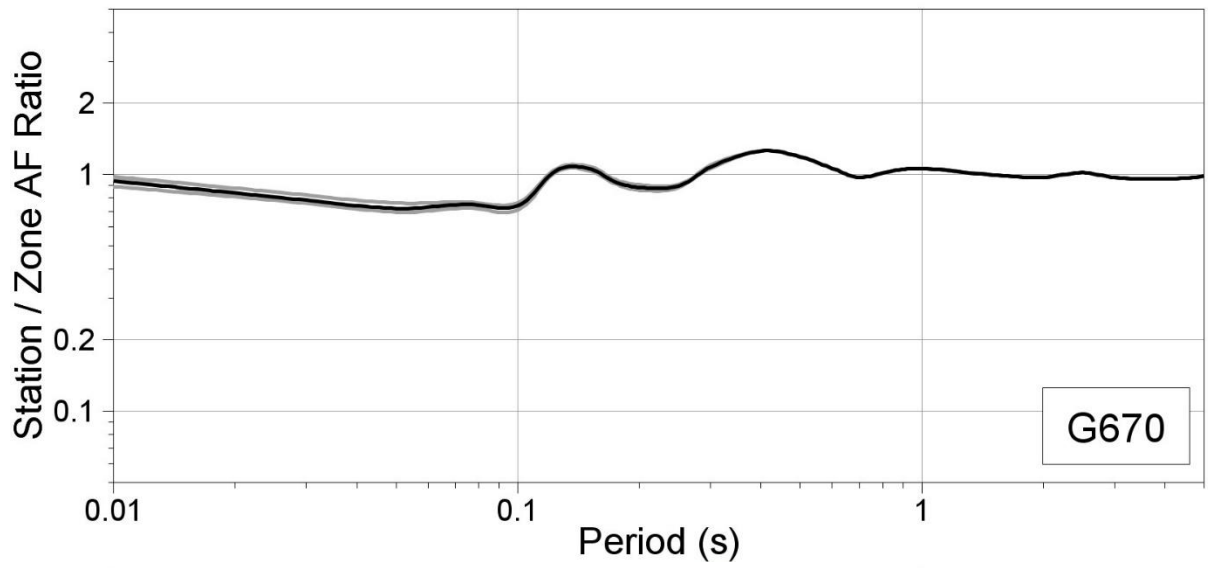


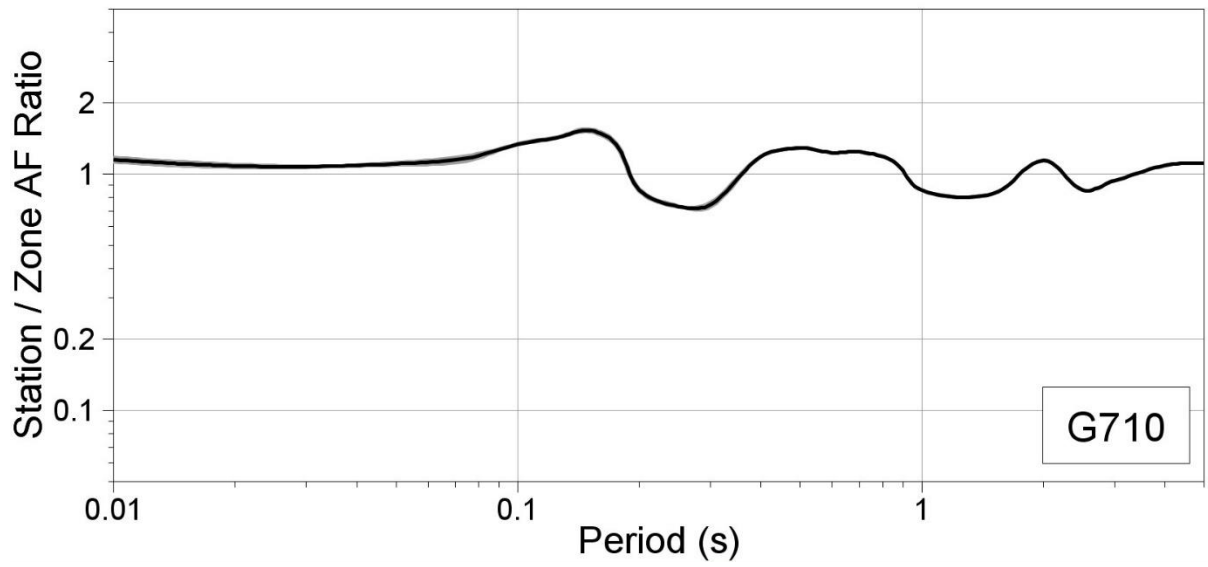
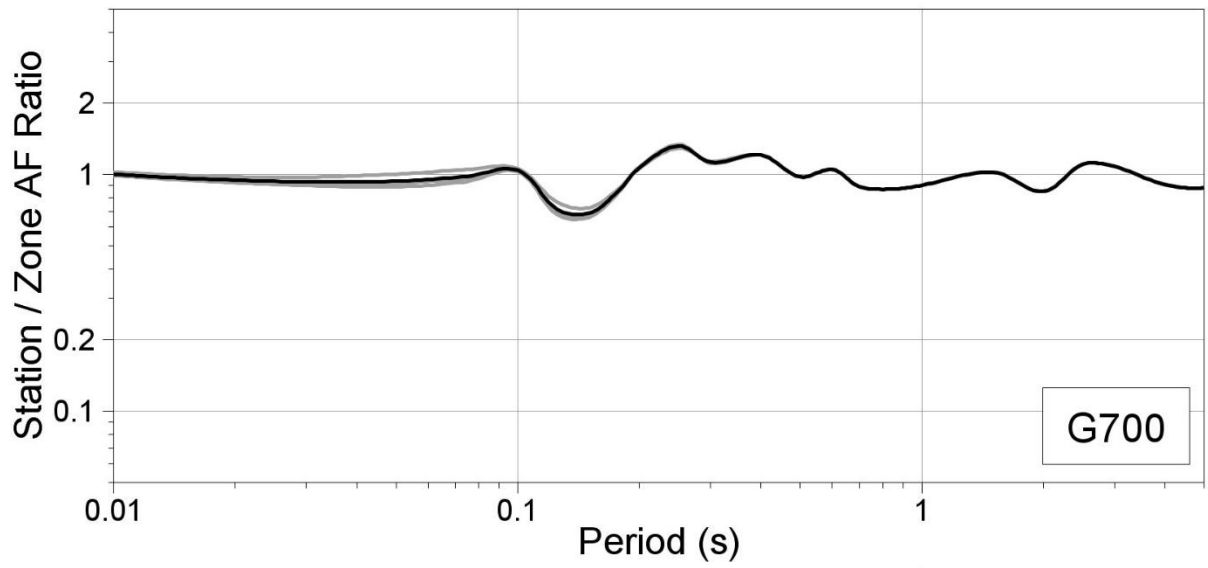


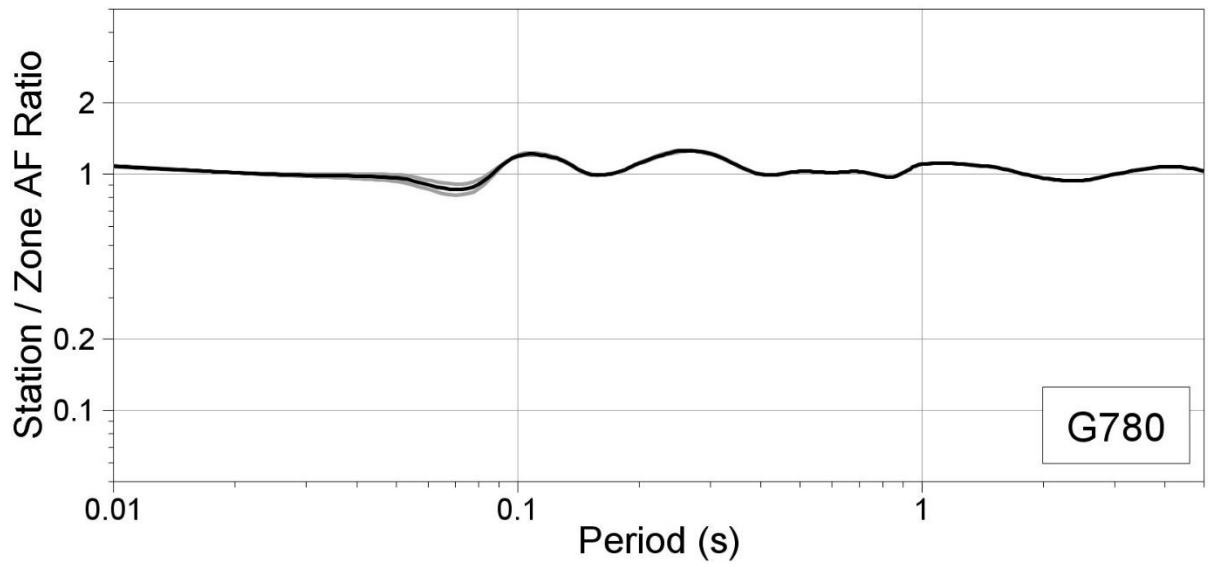
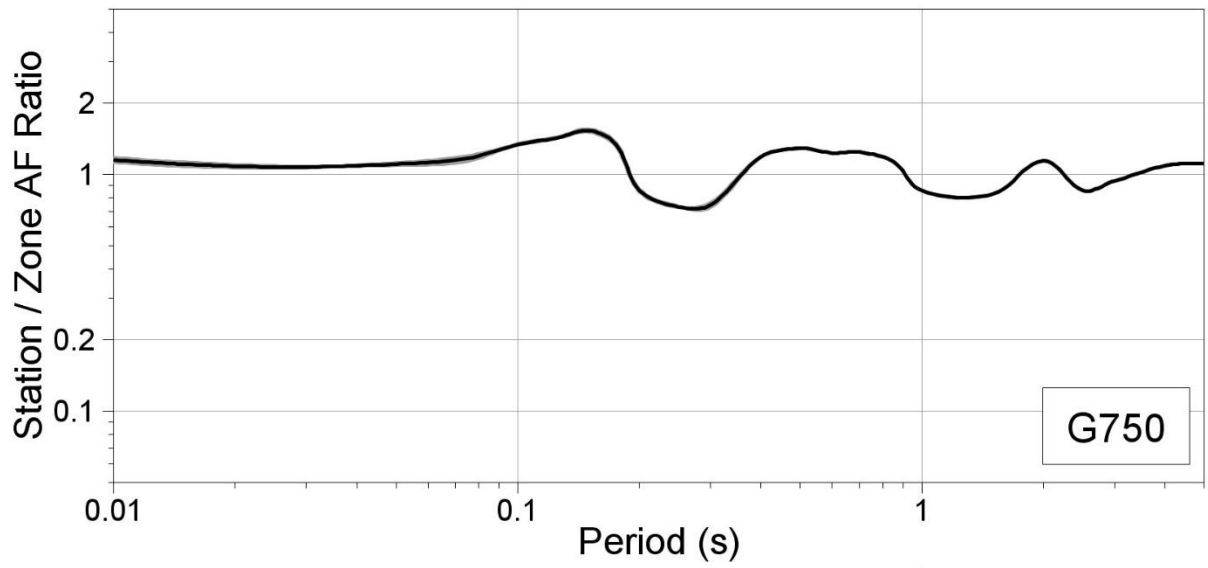








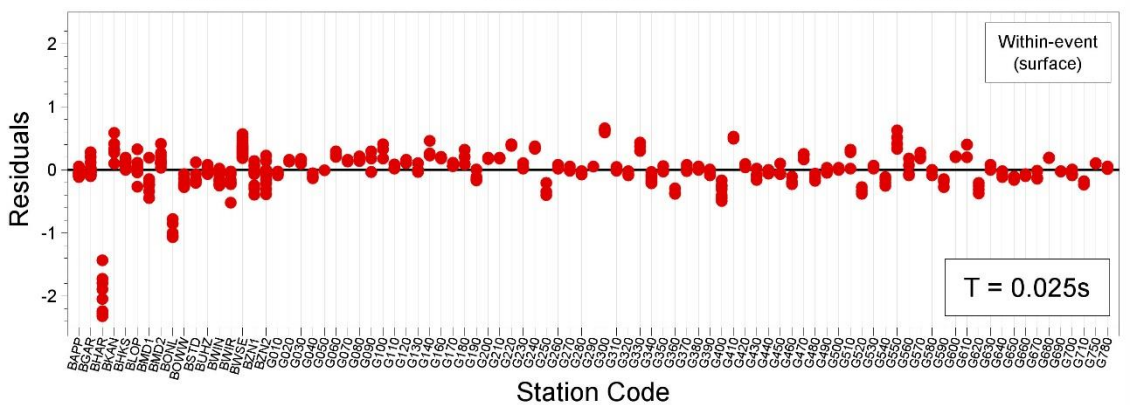
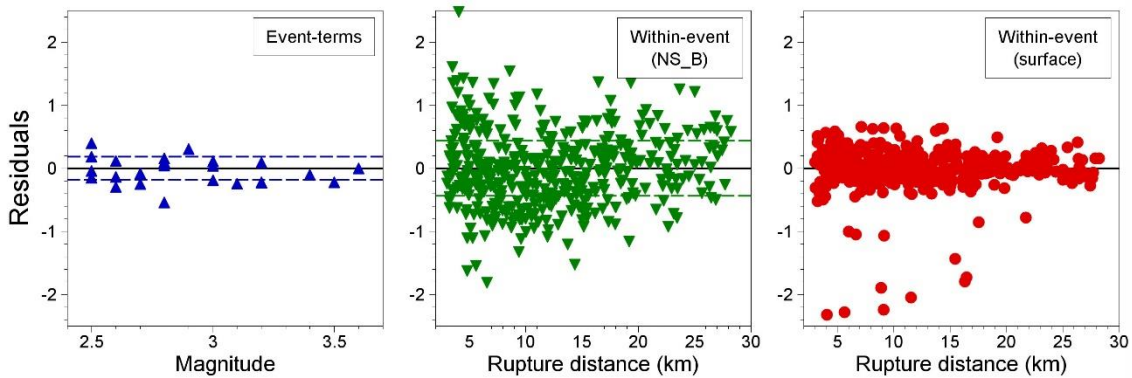
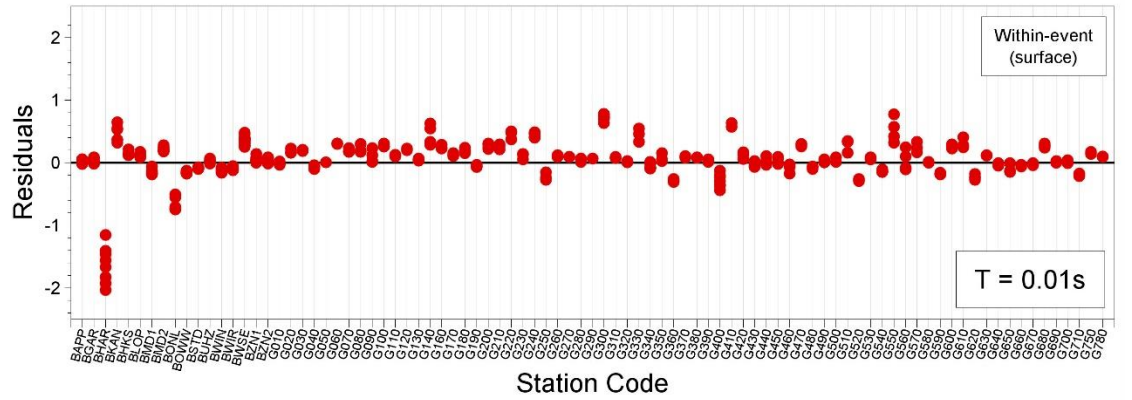
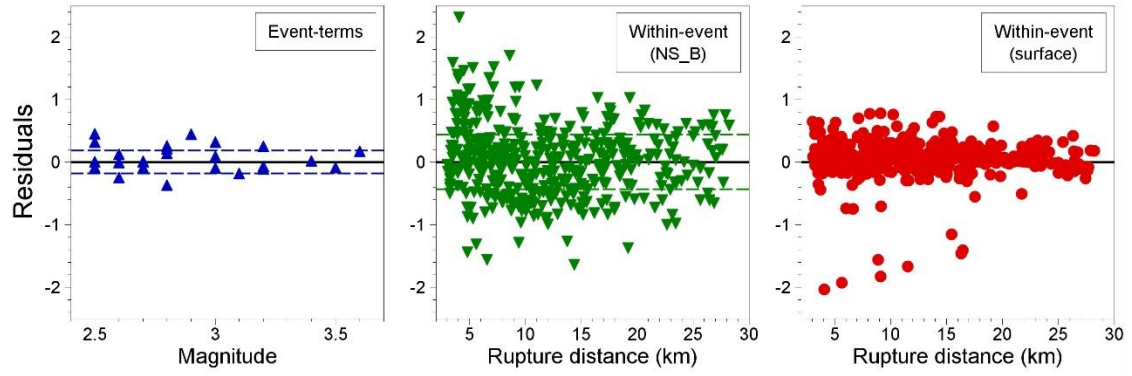


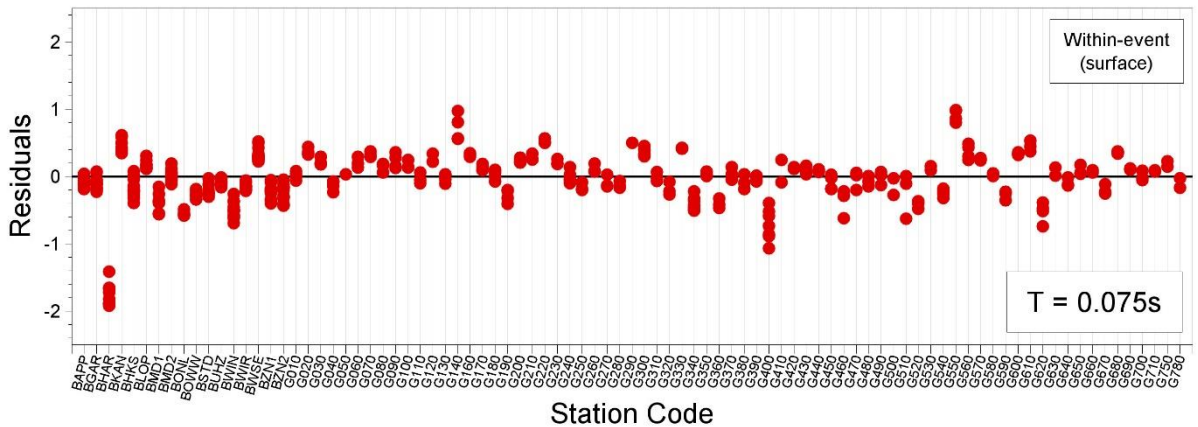
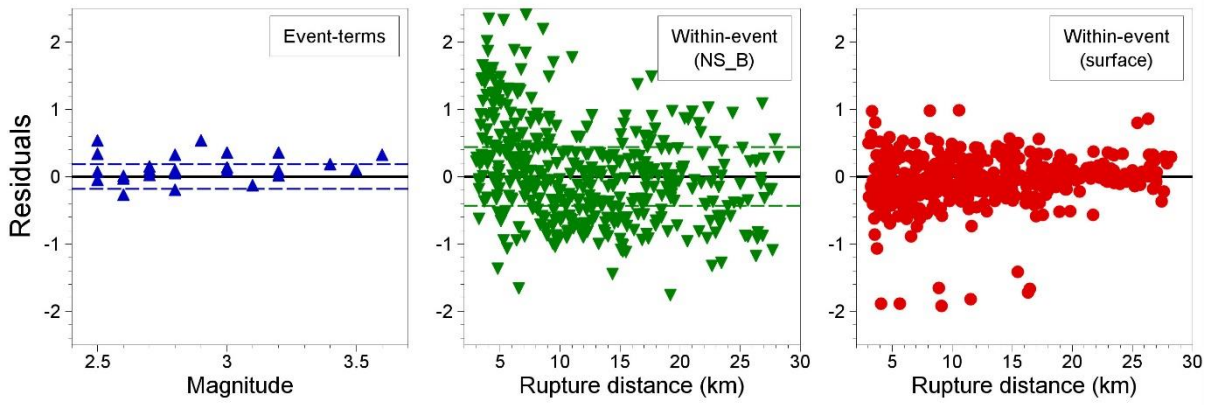
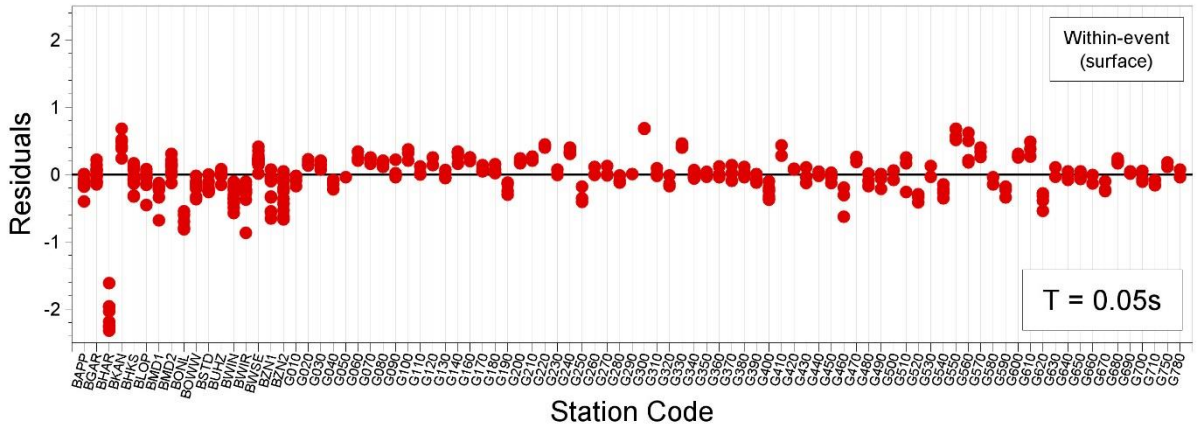
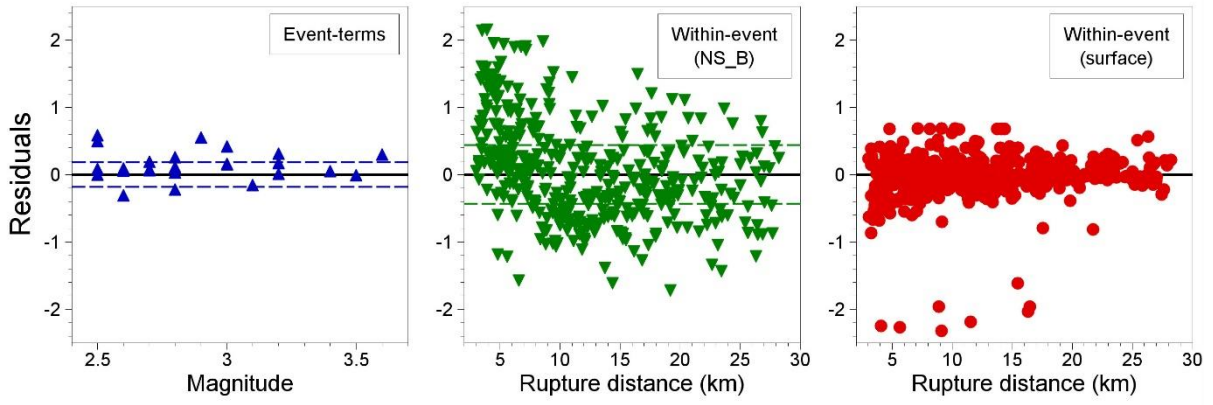


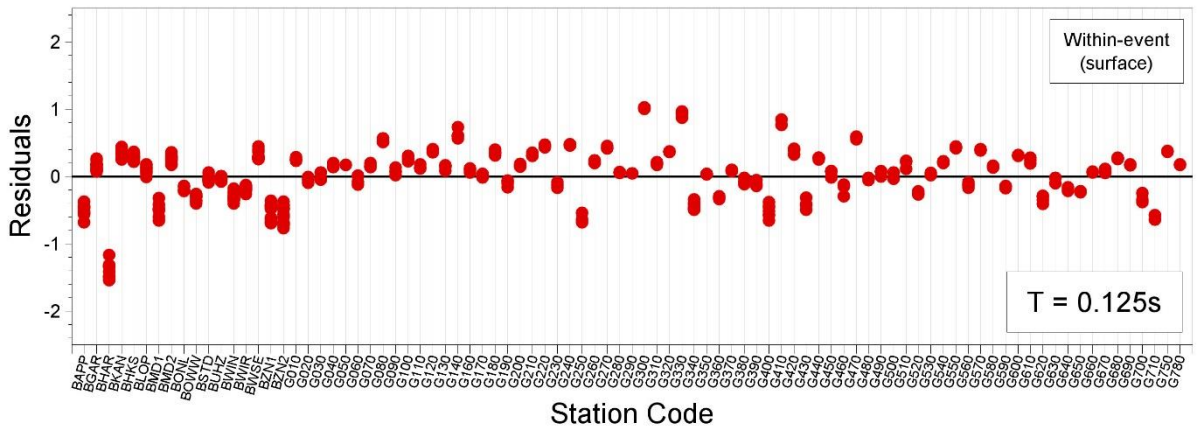
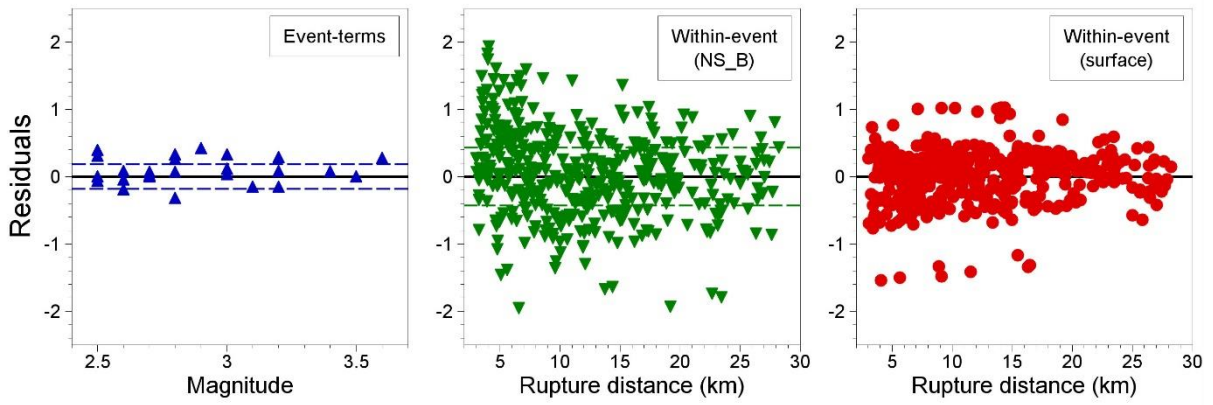
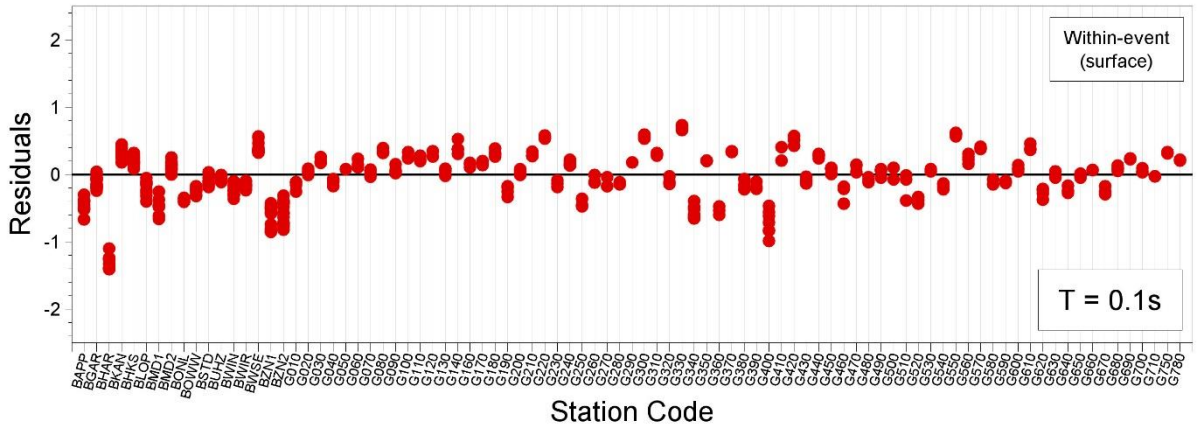
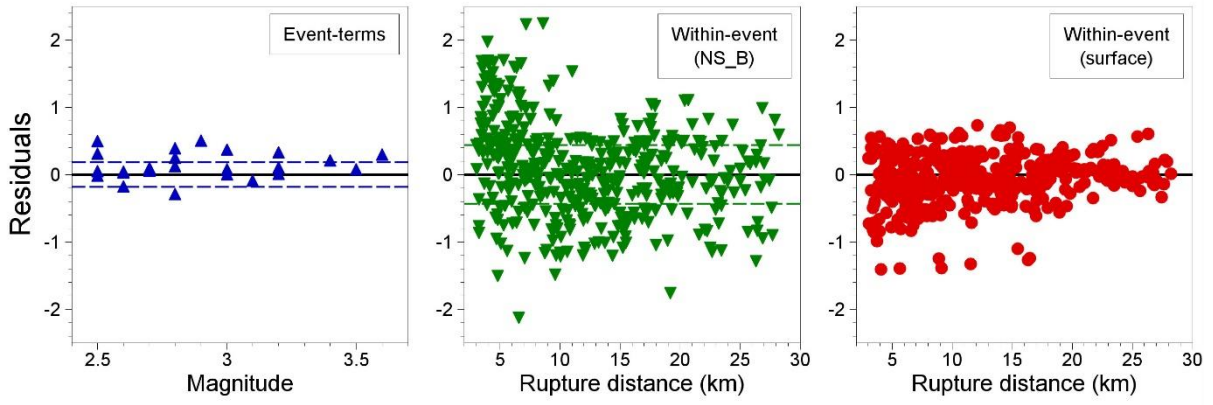
APPENDIX IV

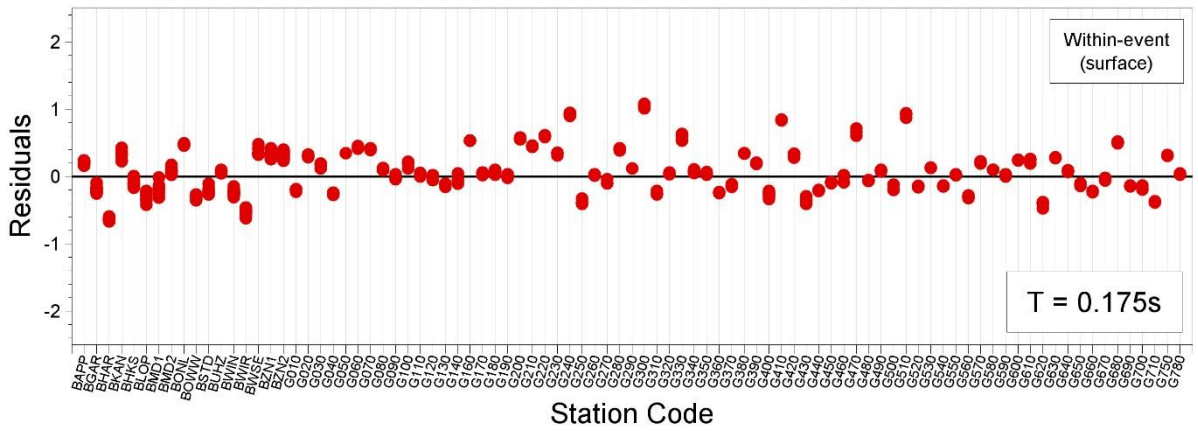
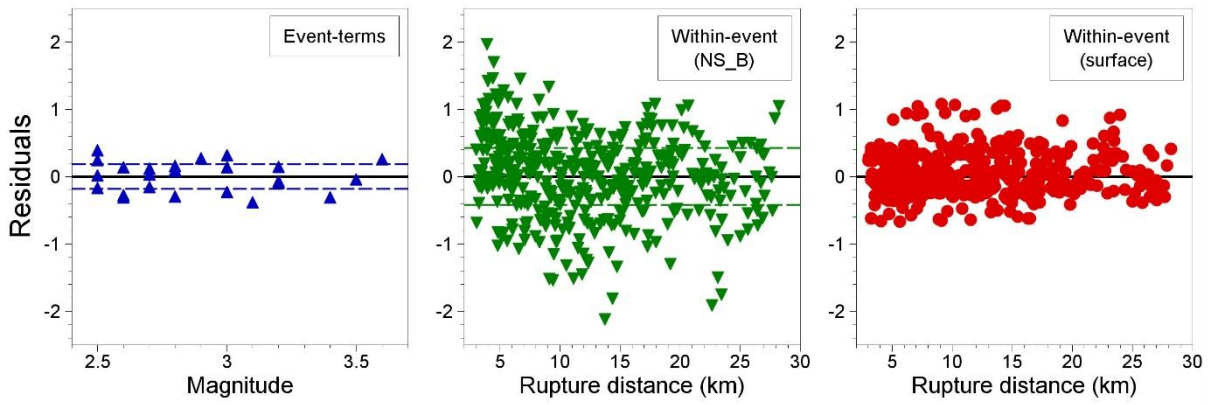
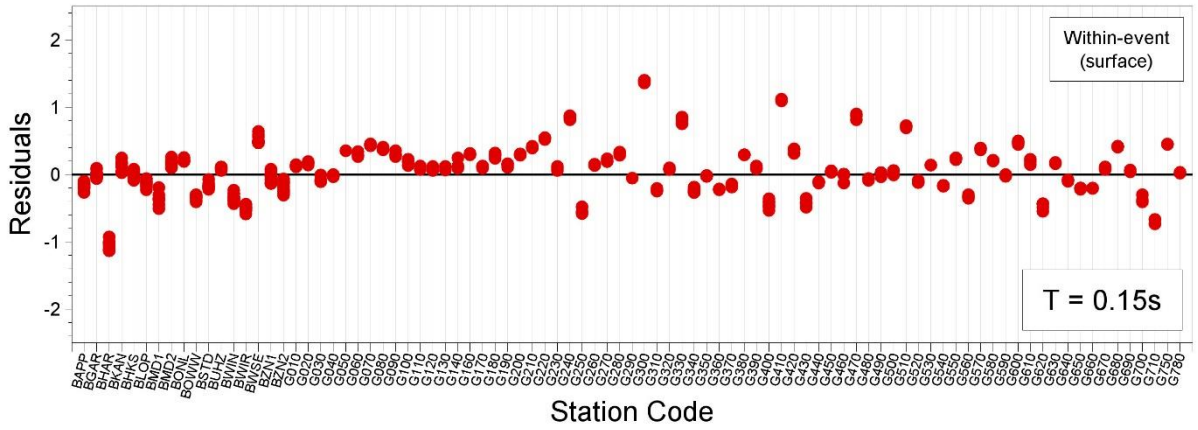
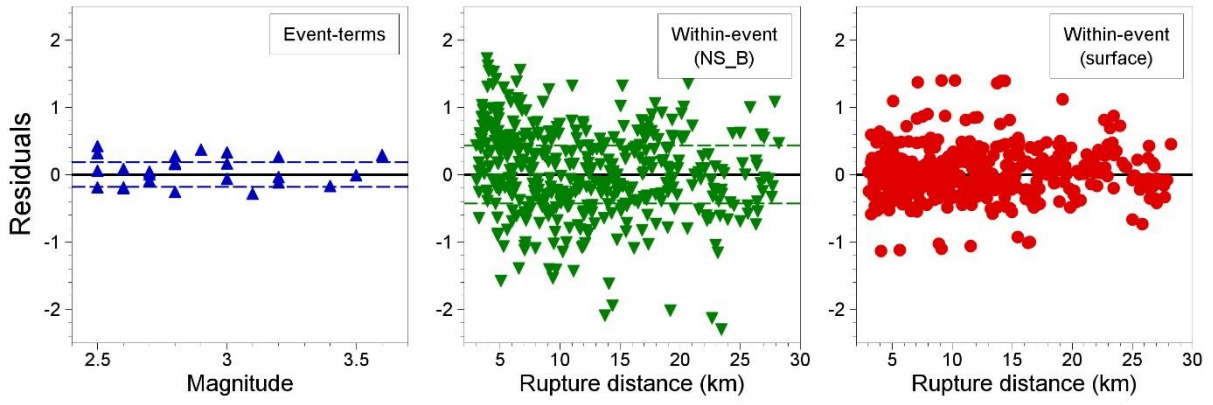
Surface Residuals of Groningen Recordings

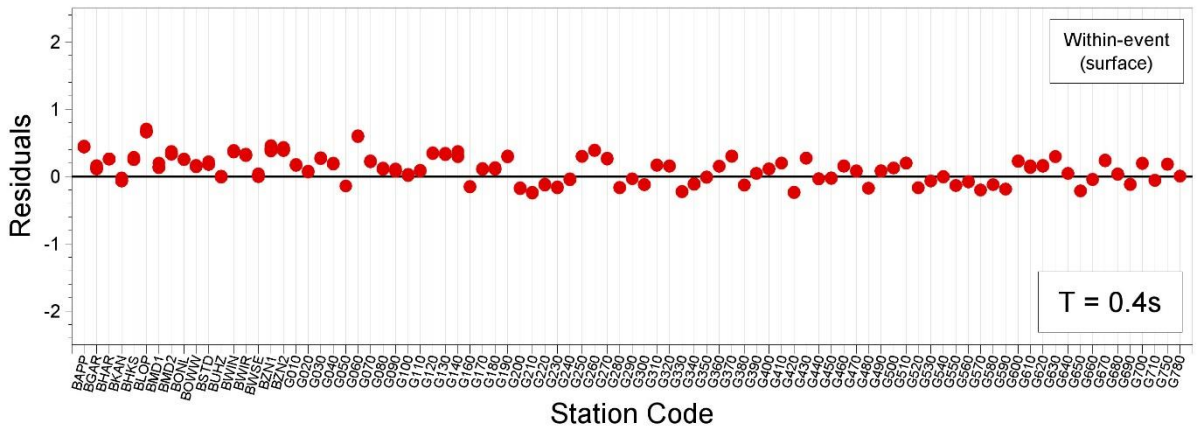
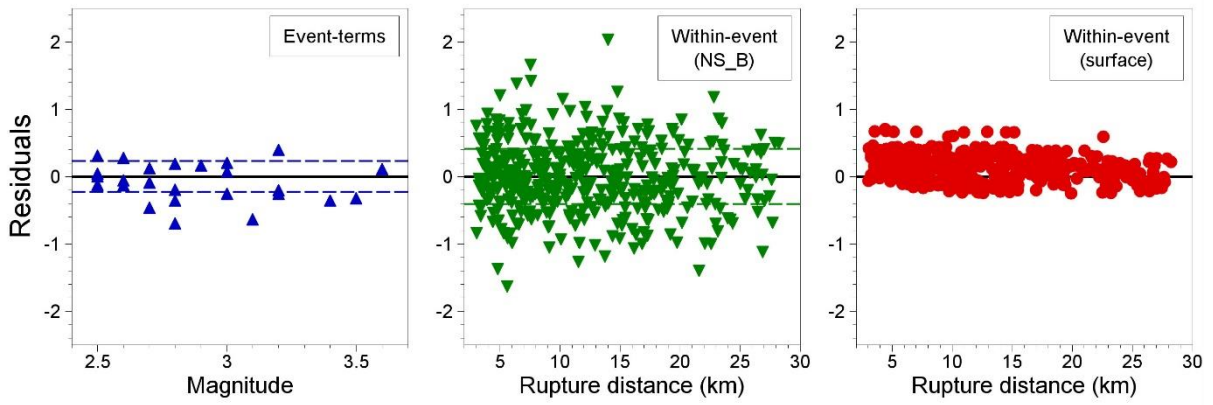
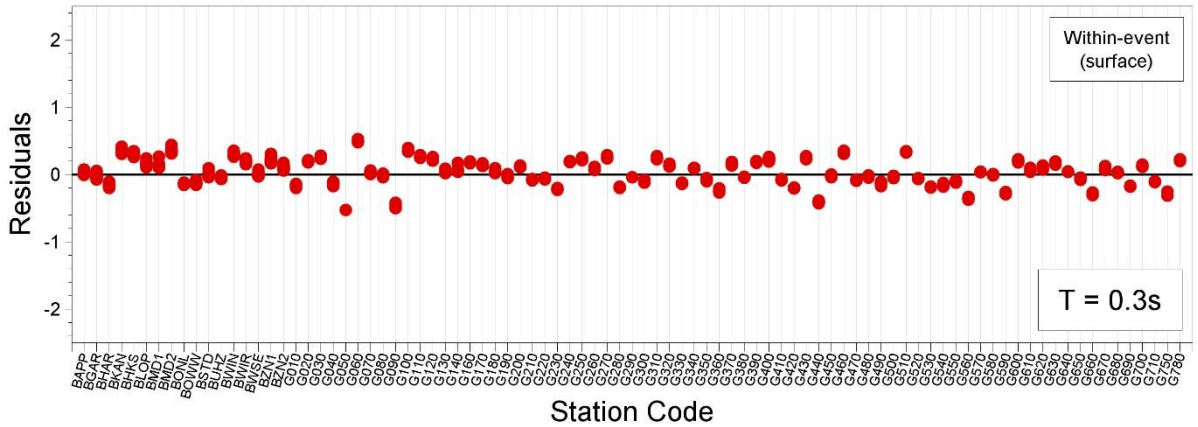
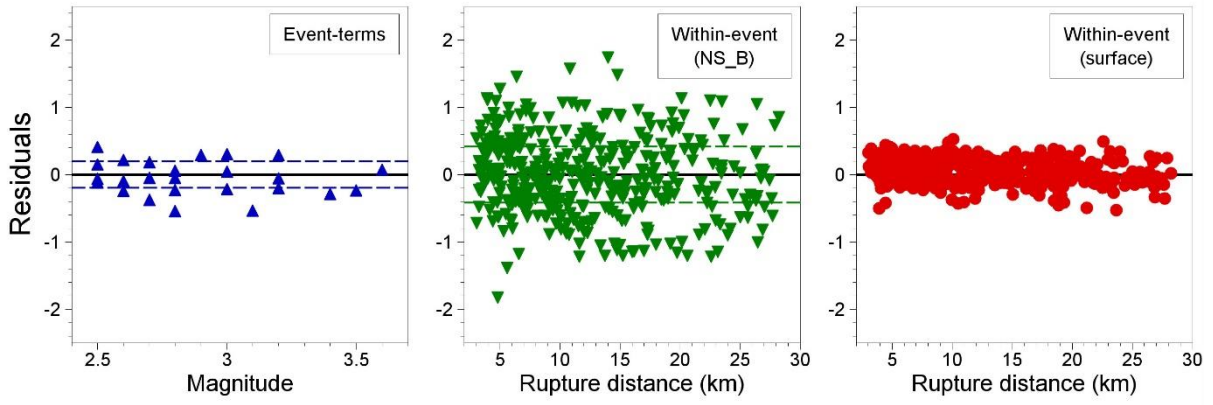
Presented in the plots are residuals of the Central-lower model obtained using $\phi_{SS,low}$.

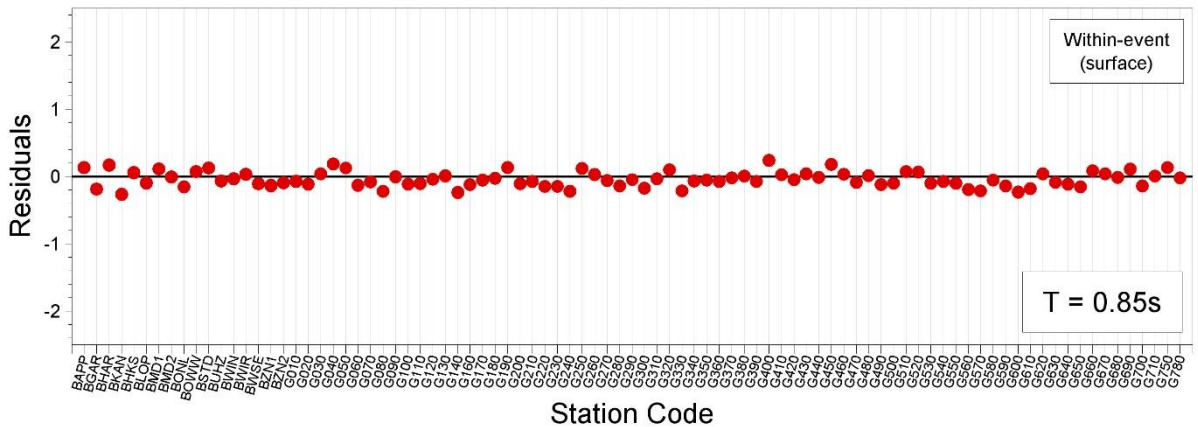
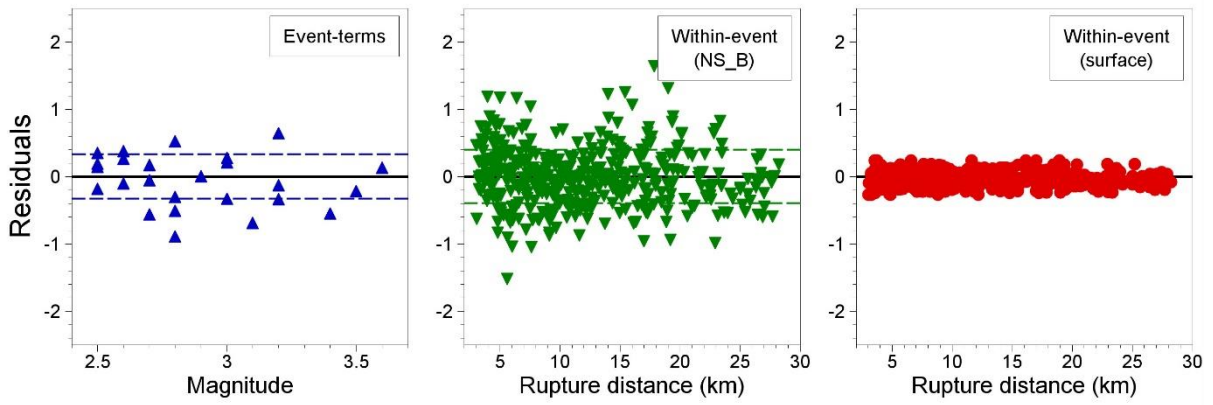
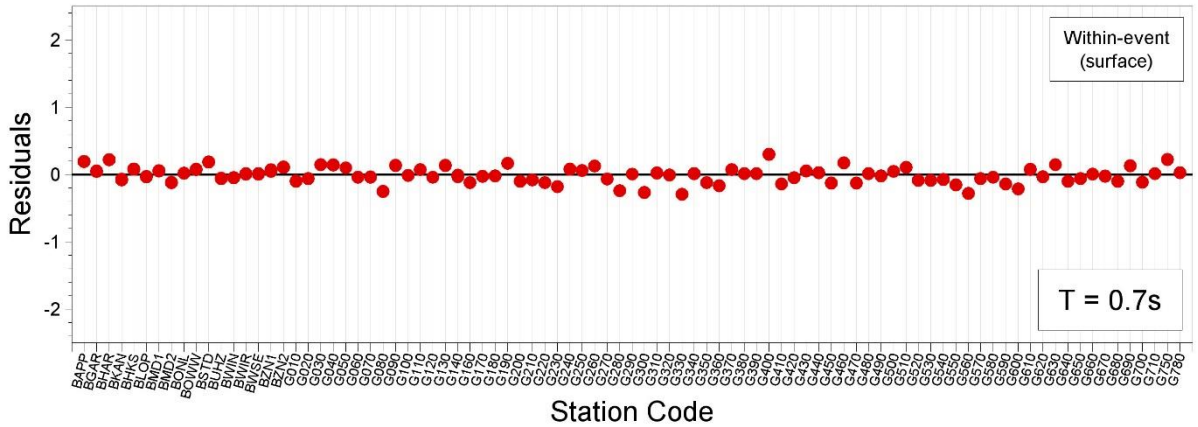
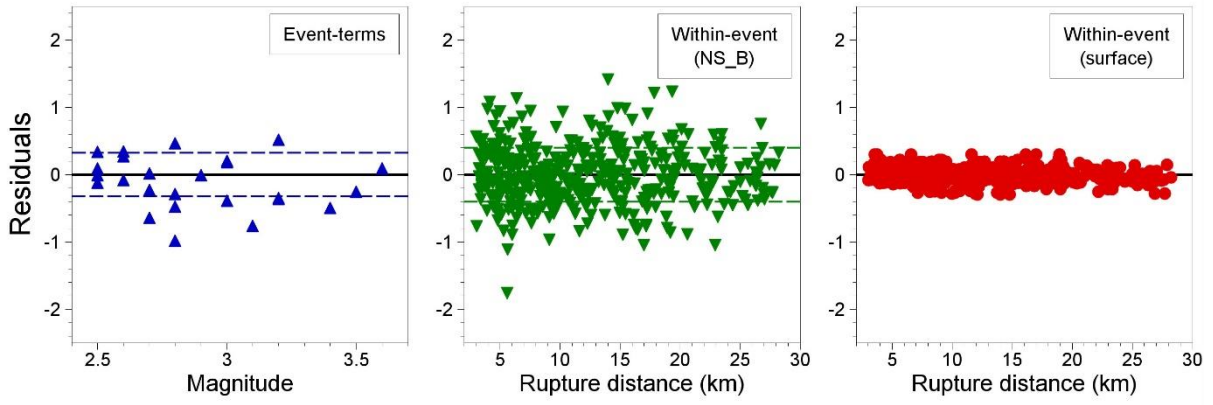


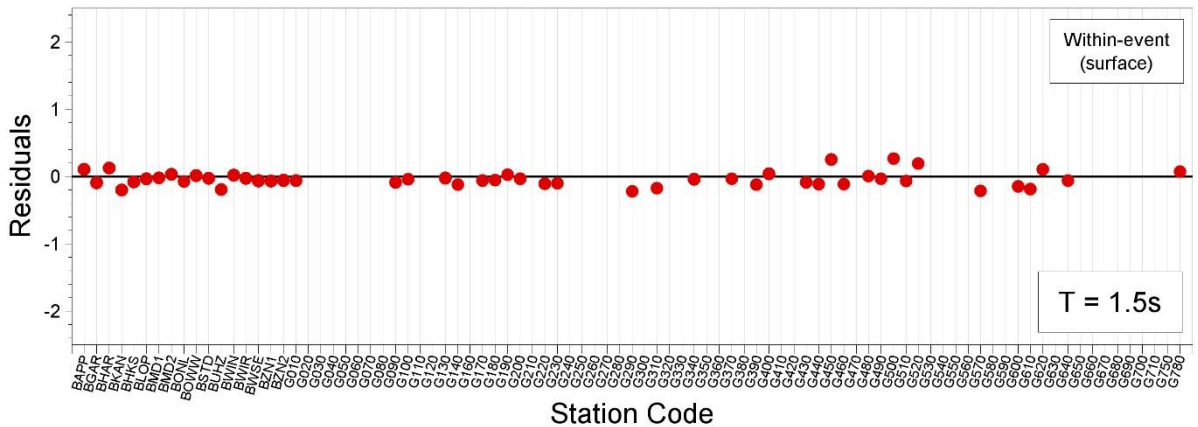
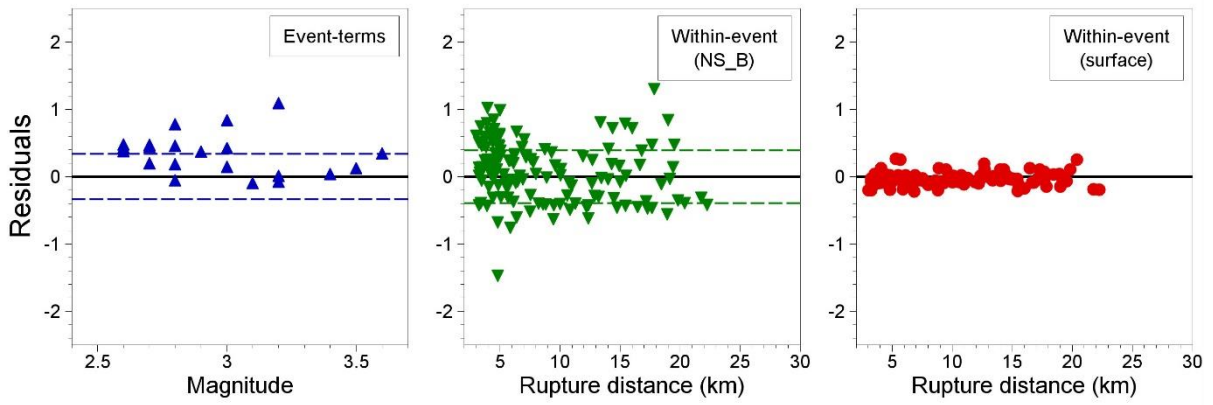
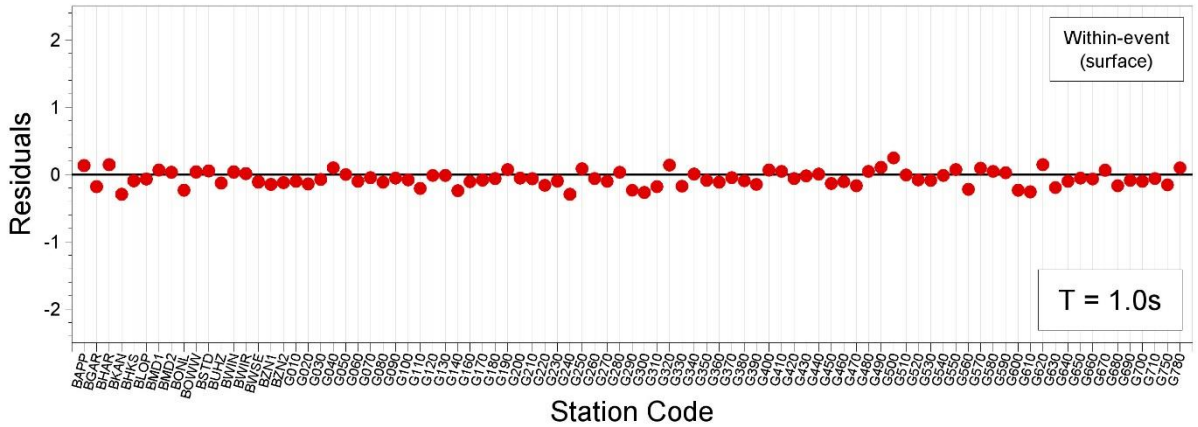
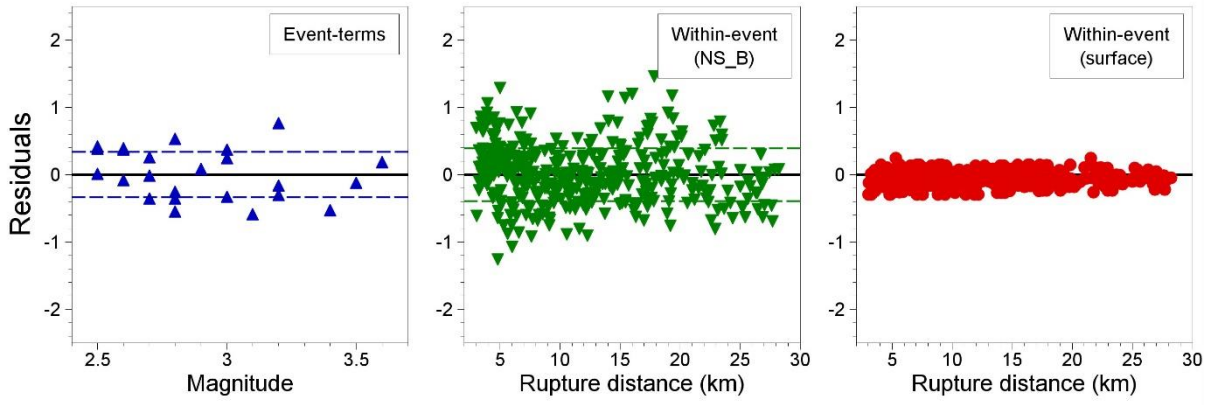








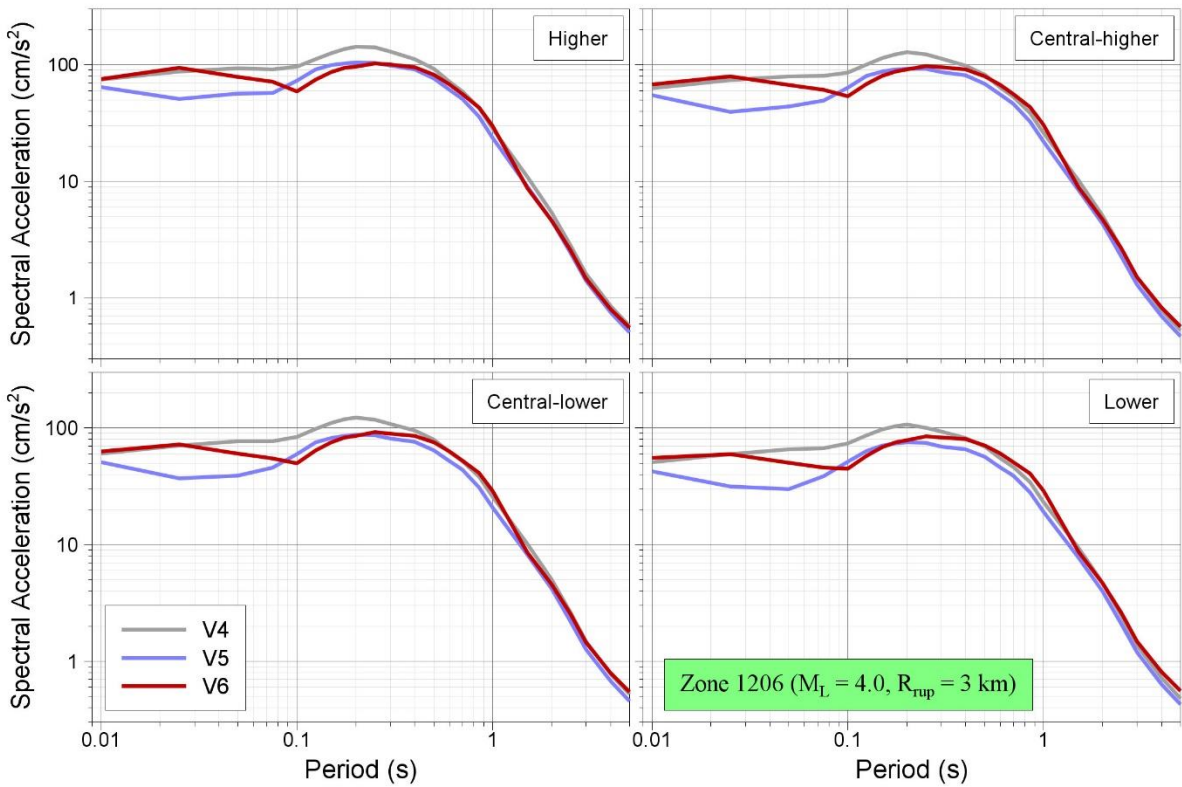
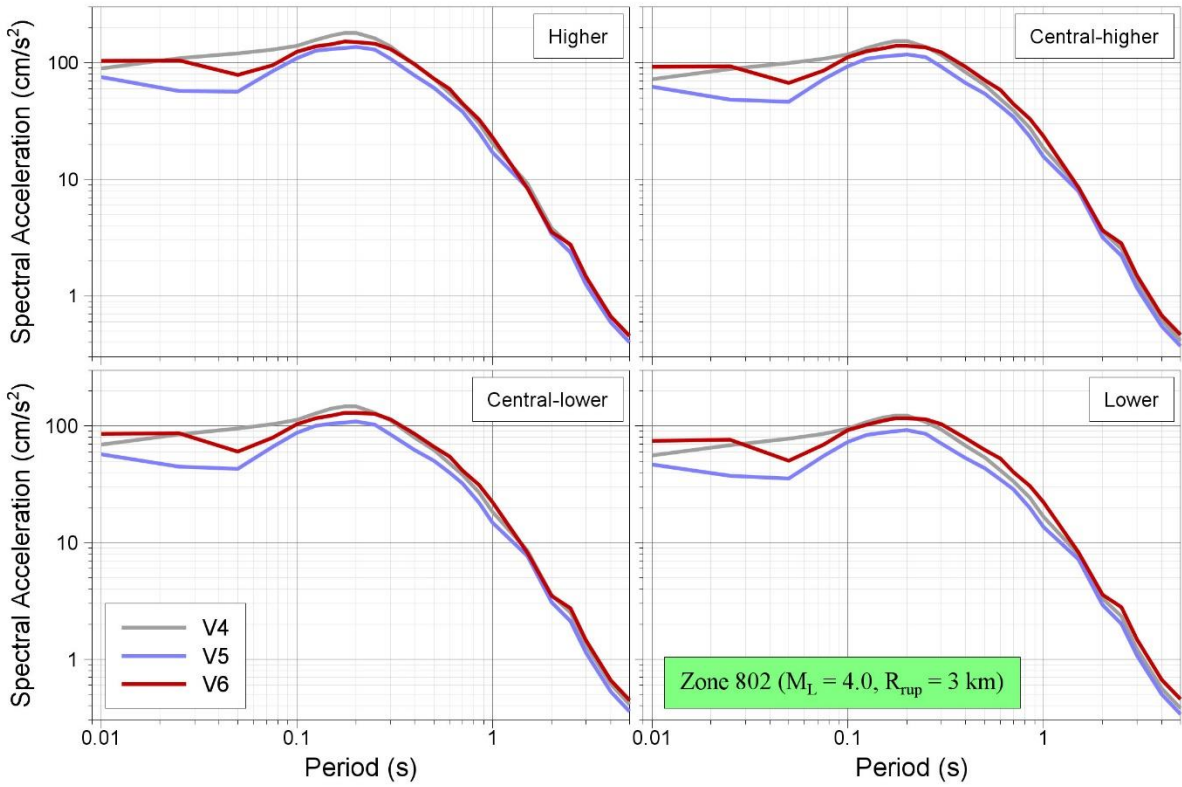


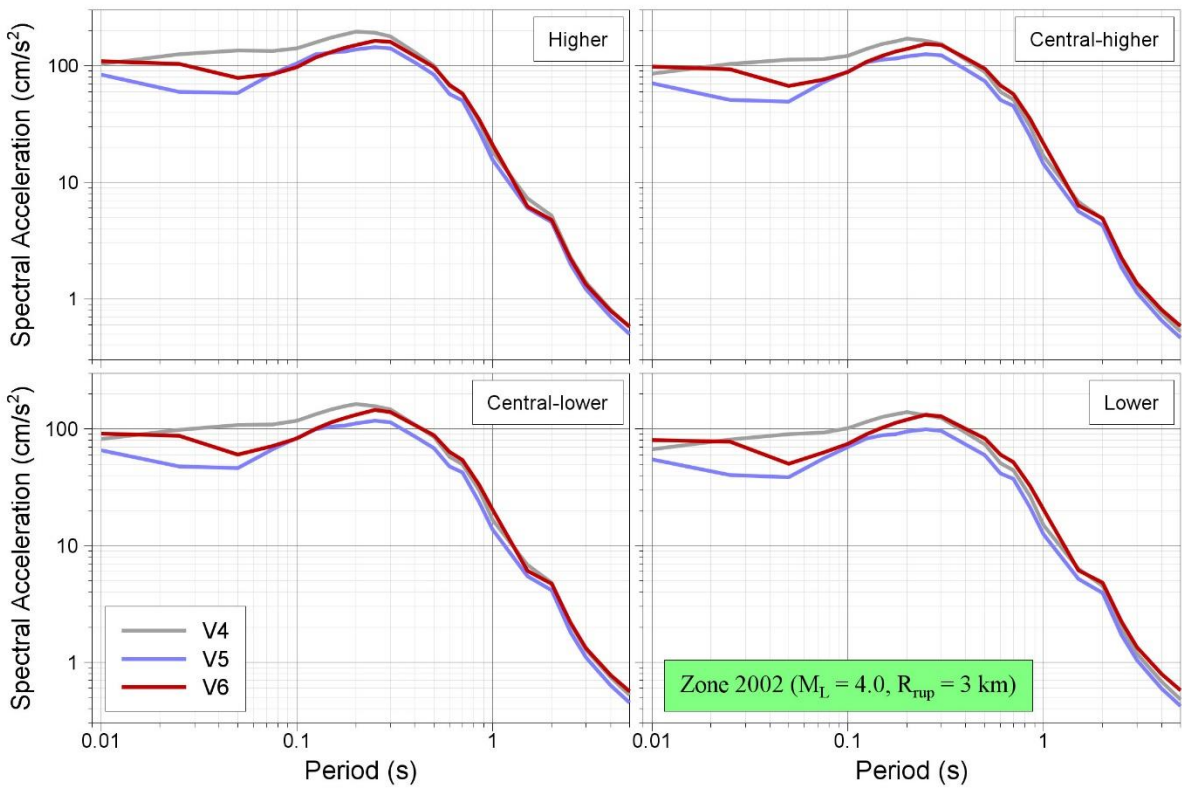
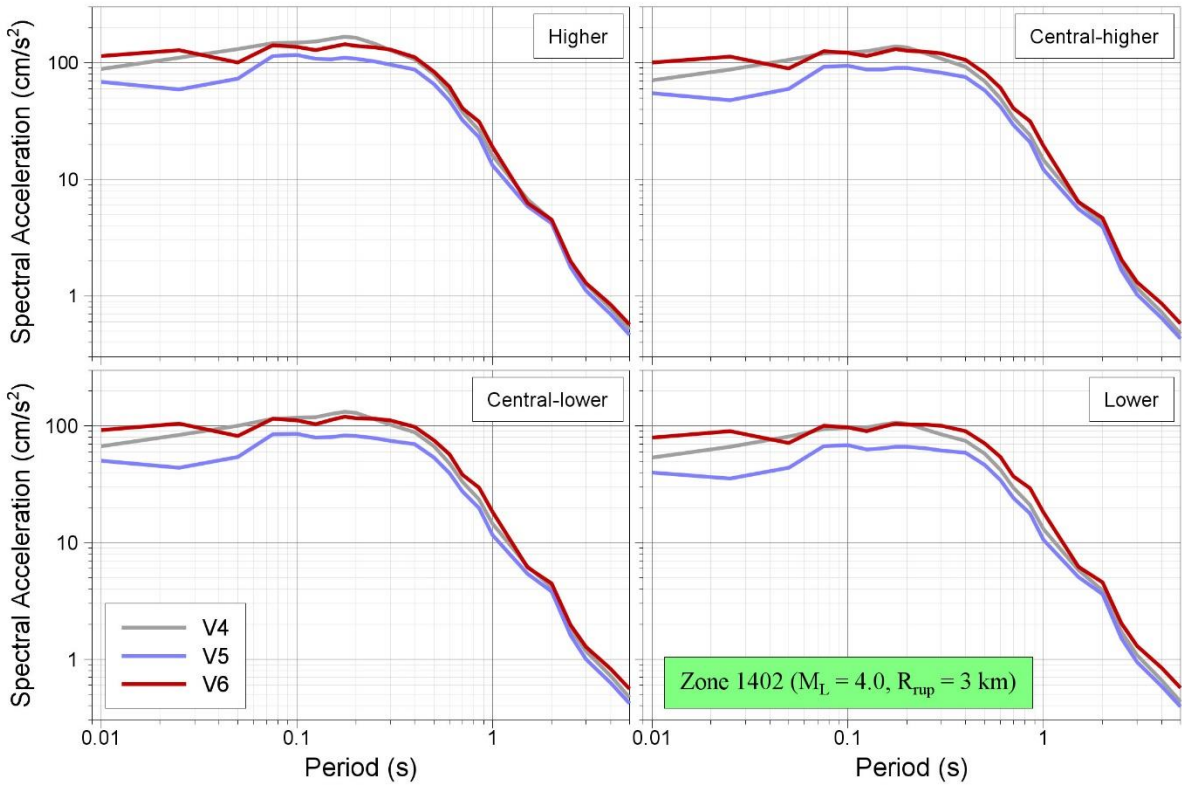


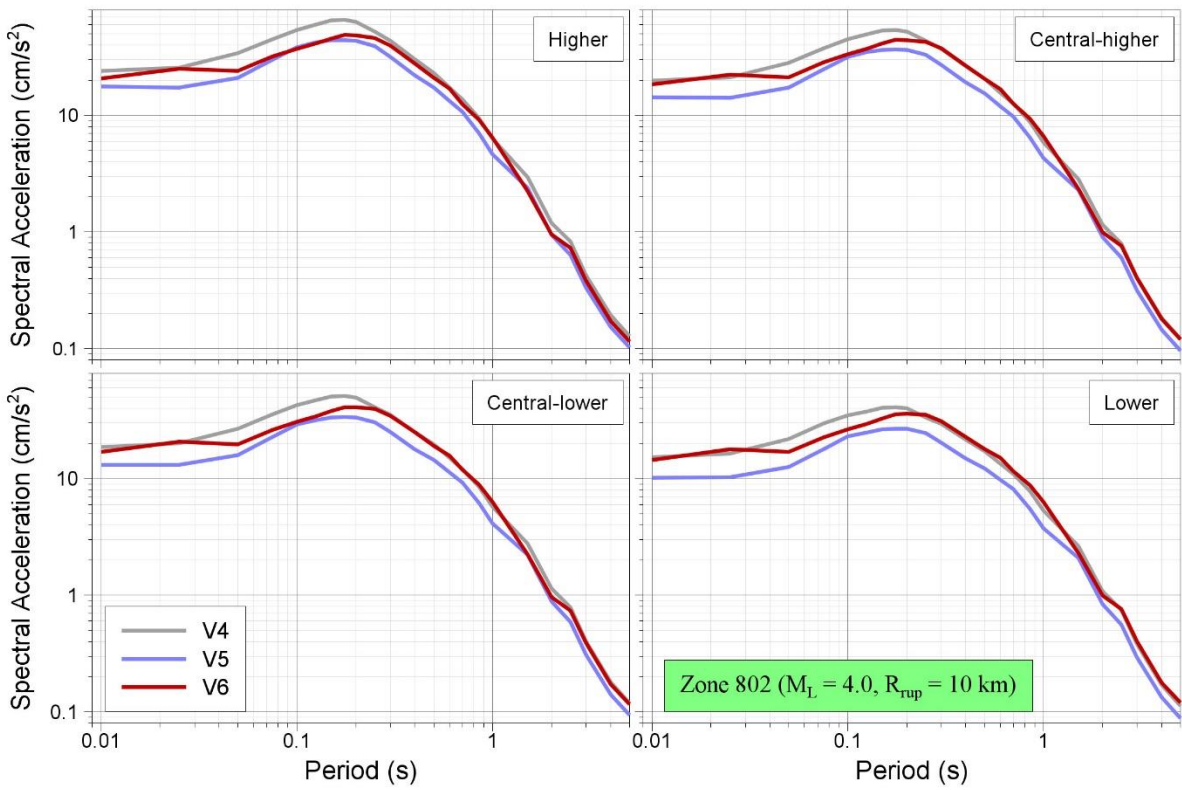
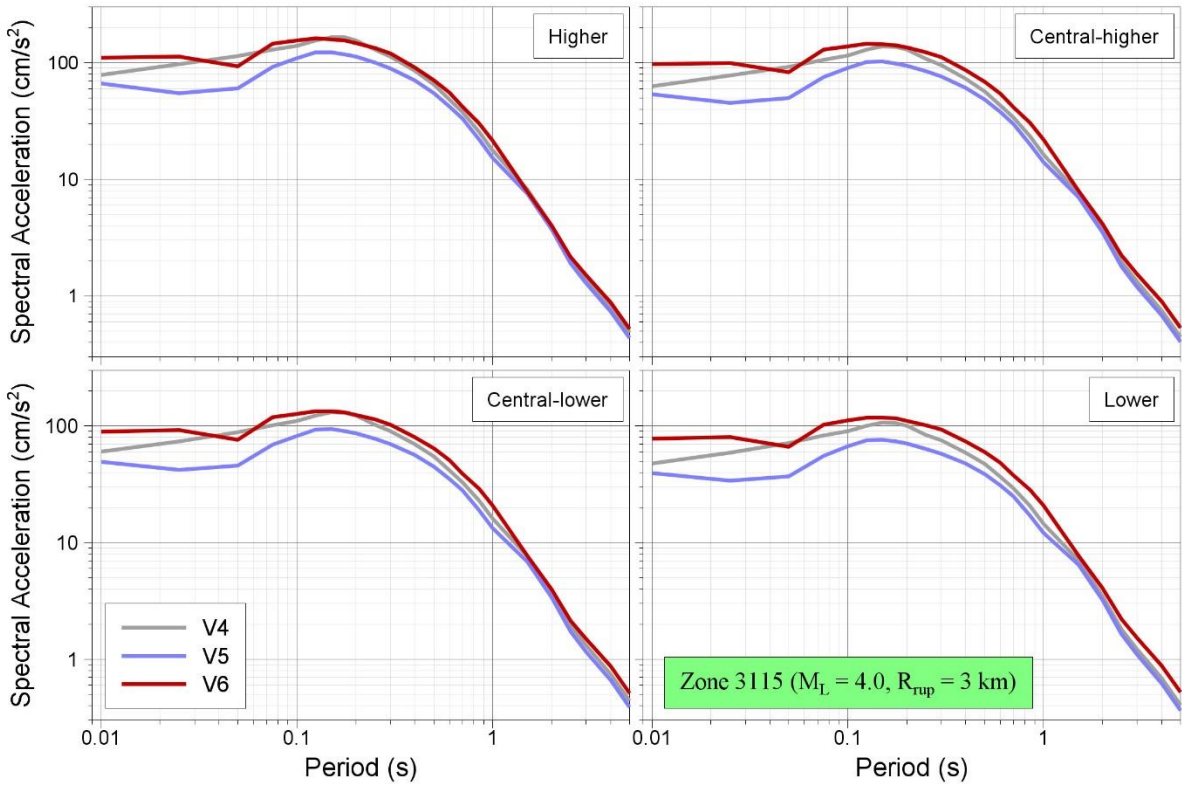
APPENDIX V

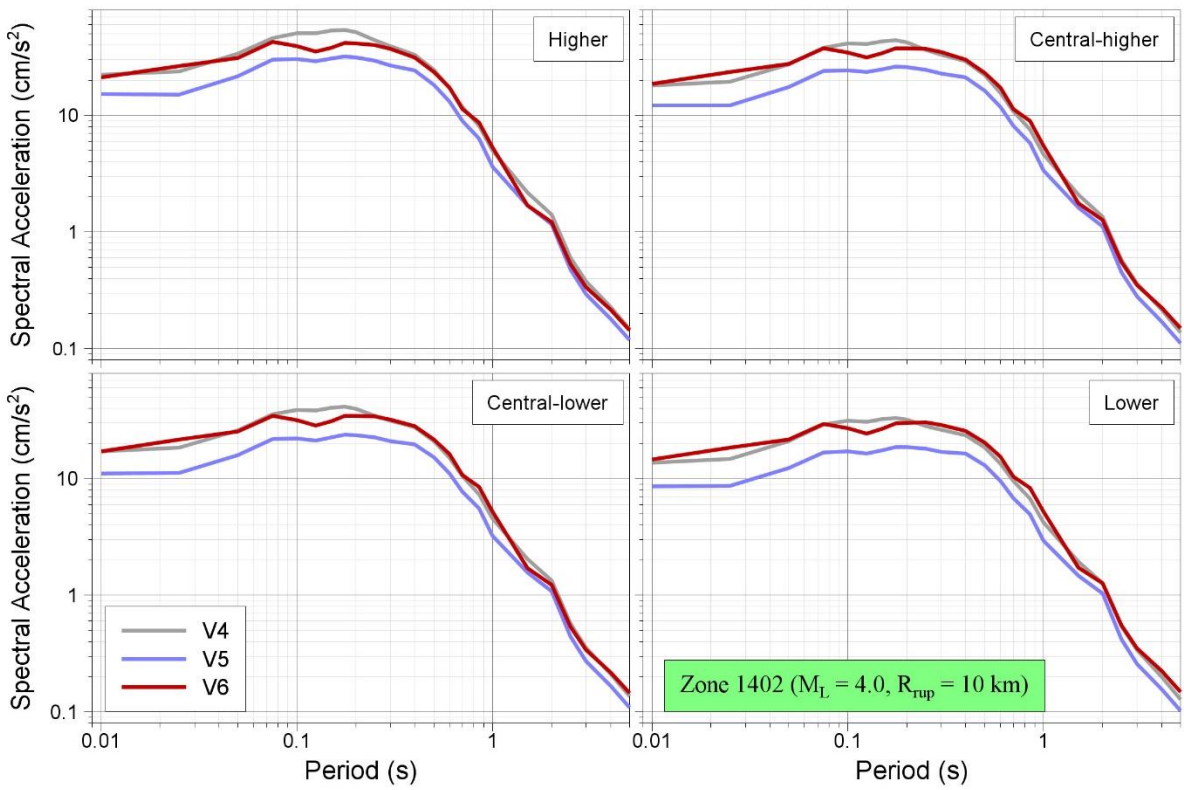
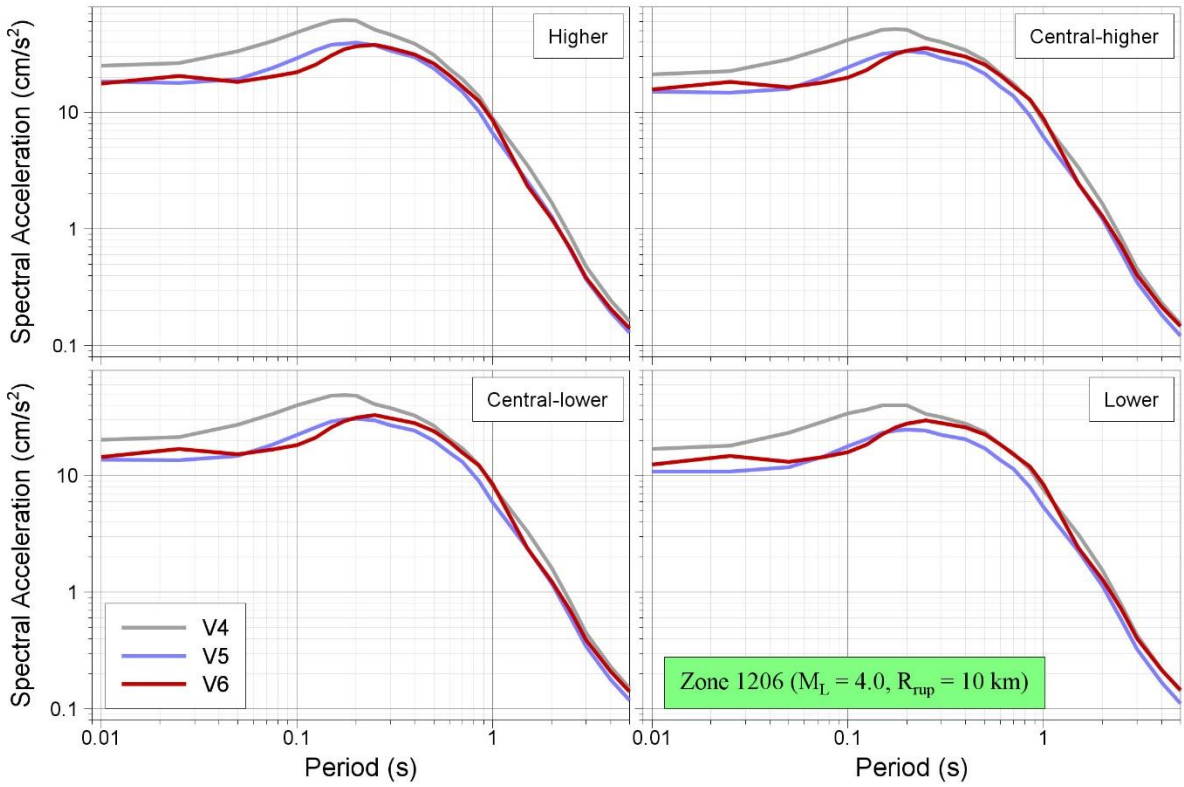
Median Predictions of Motions at Surface

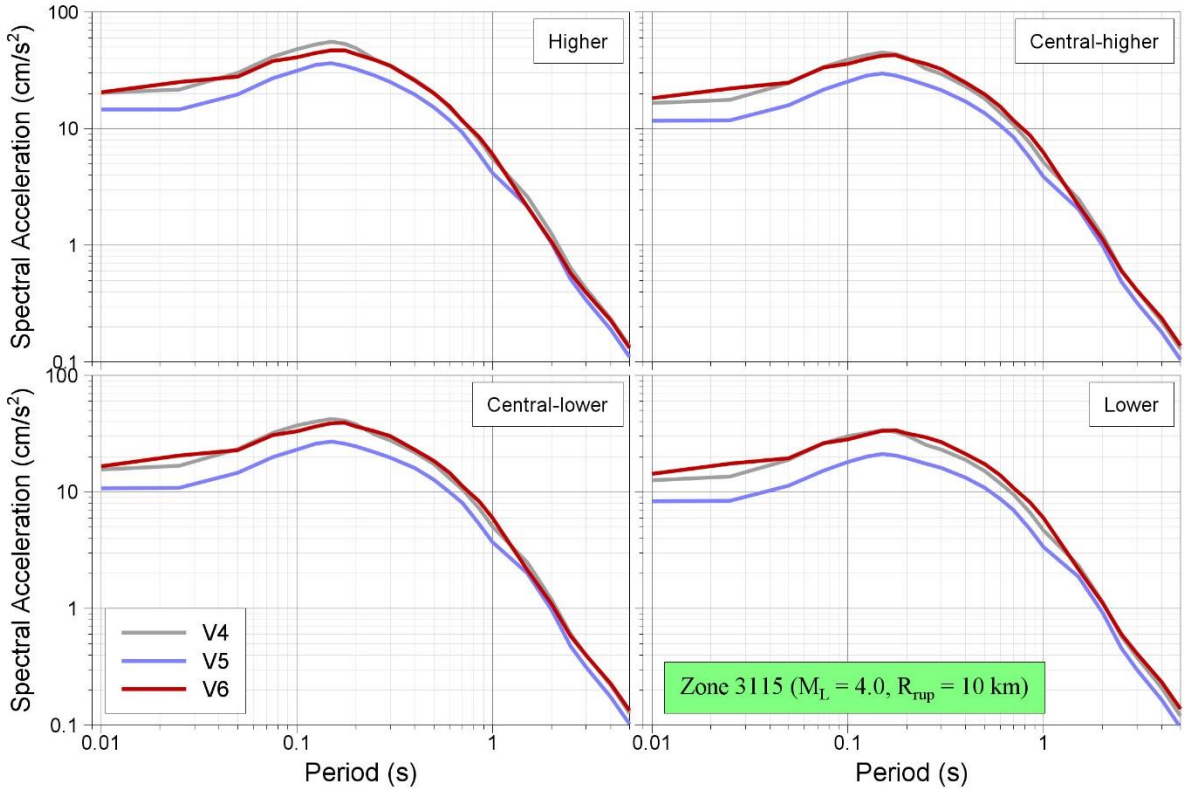
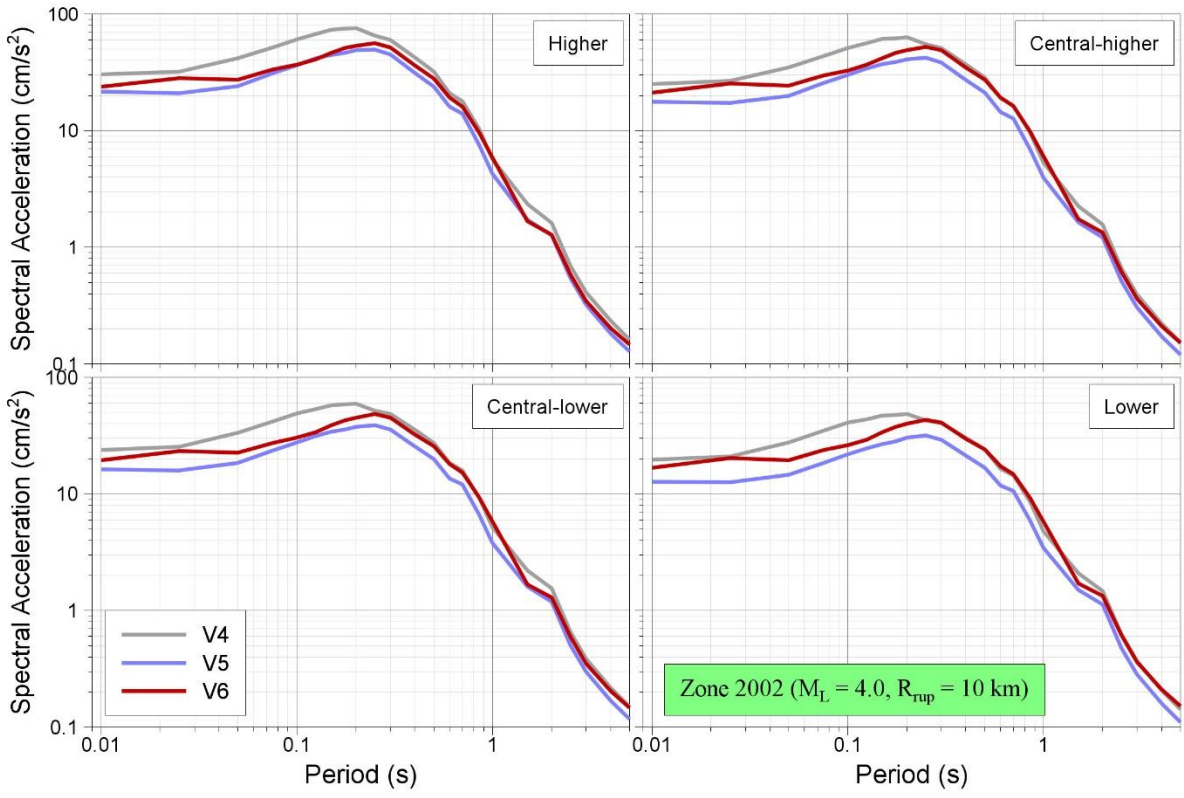
The plots on the following pages compare median predictions of response spectral ordinates at the surface (using selected zones) for various magnitude-distance combinations. In each plot, the V6 spectrum is compared with those obtained from the V5 and V4 models.

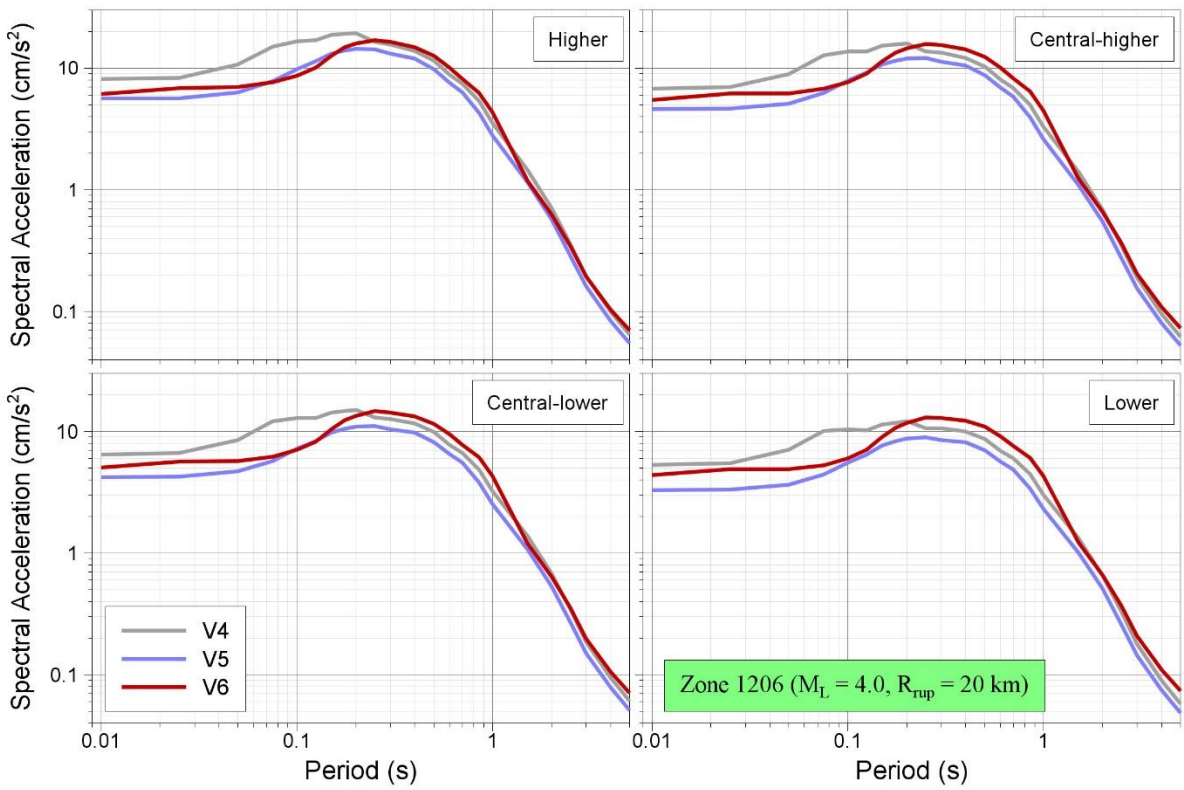
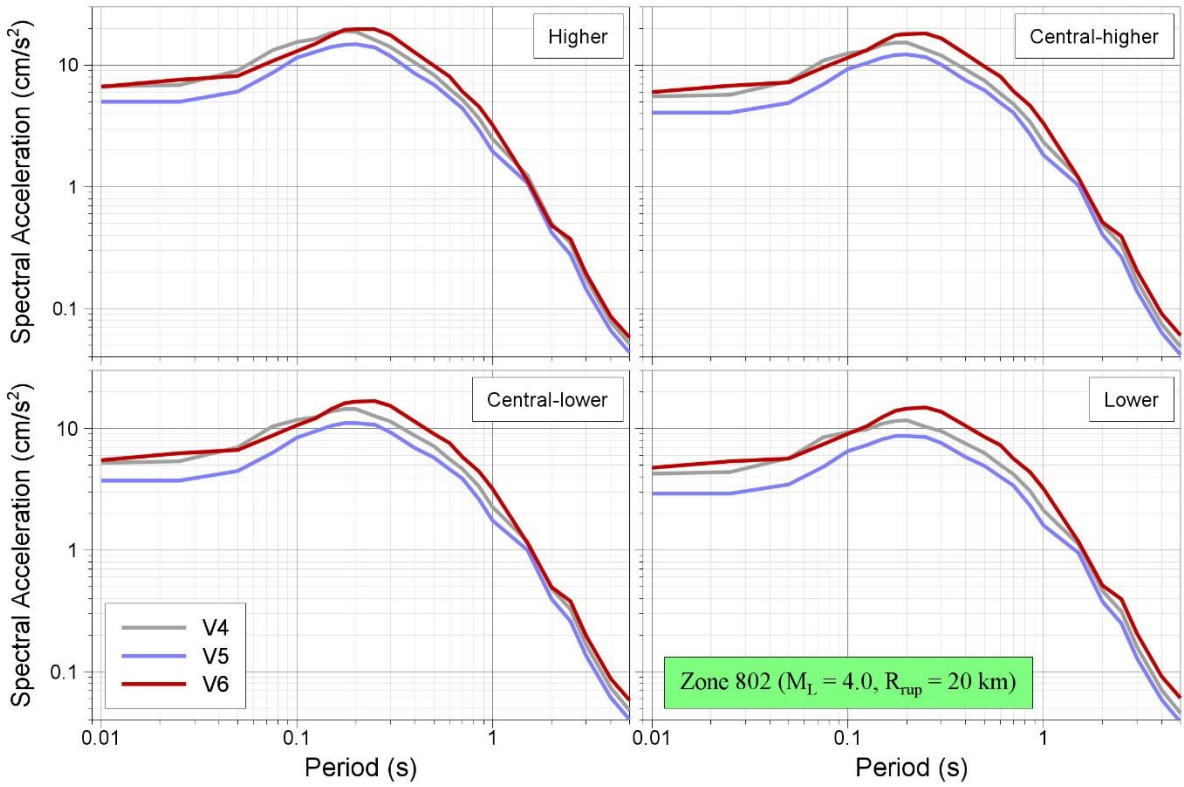


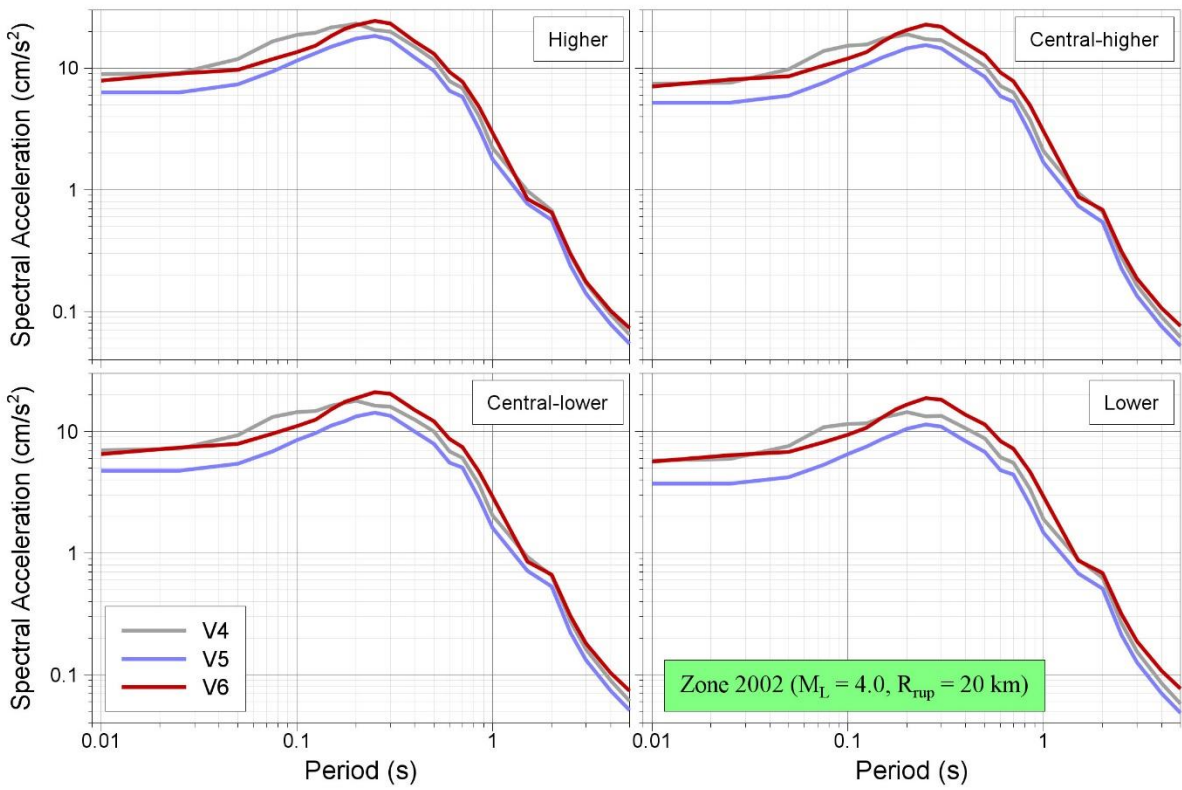
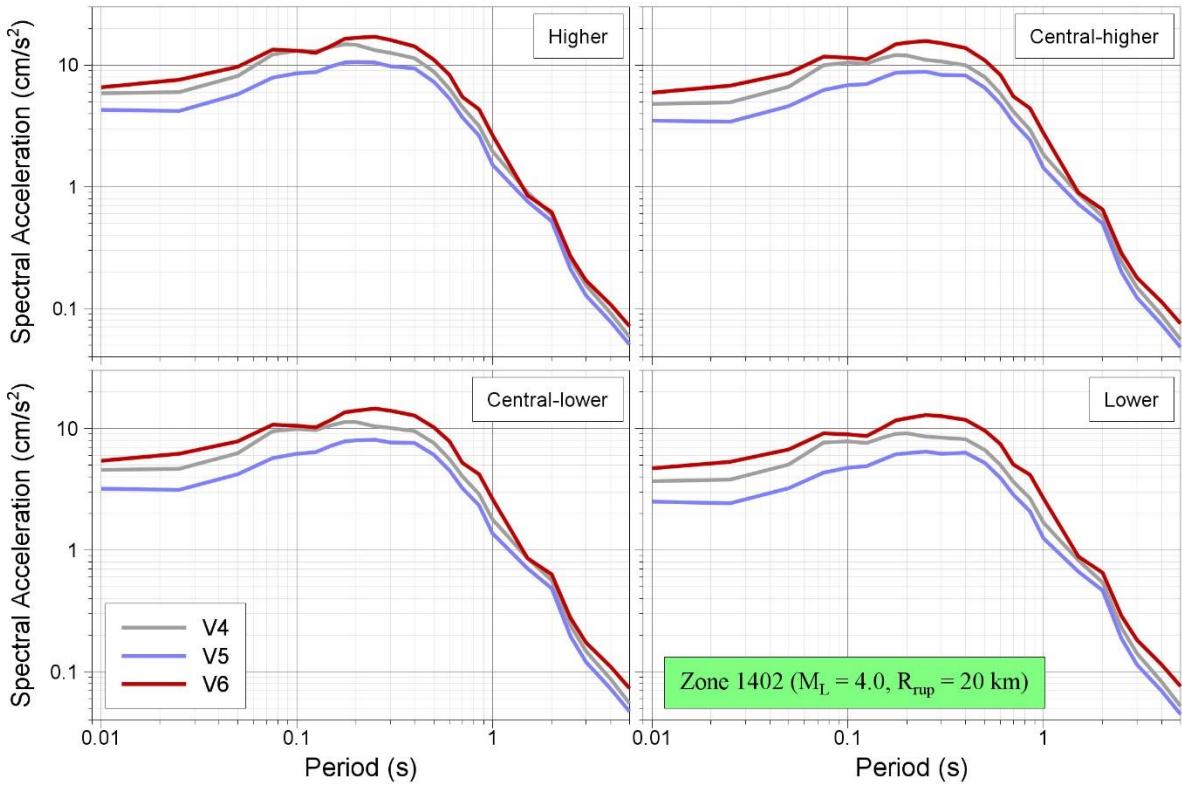


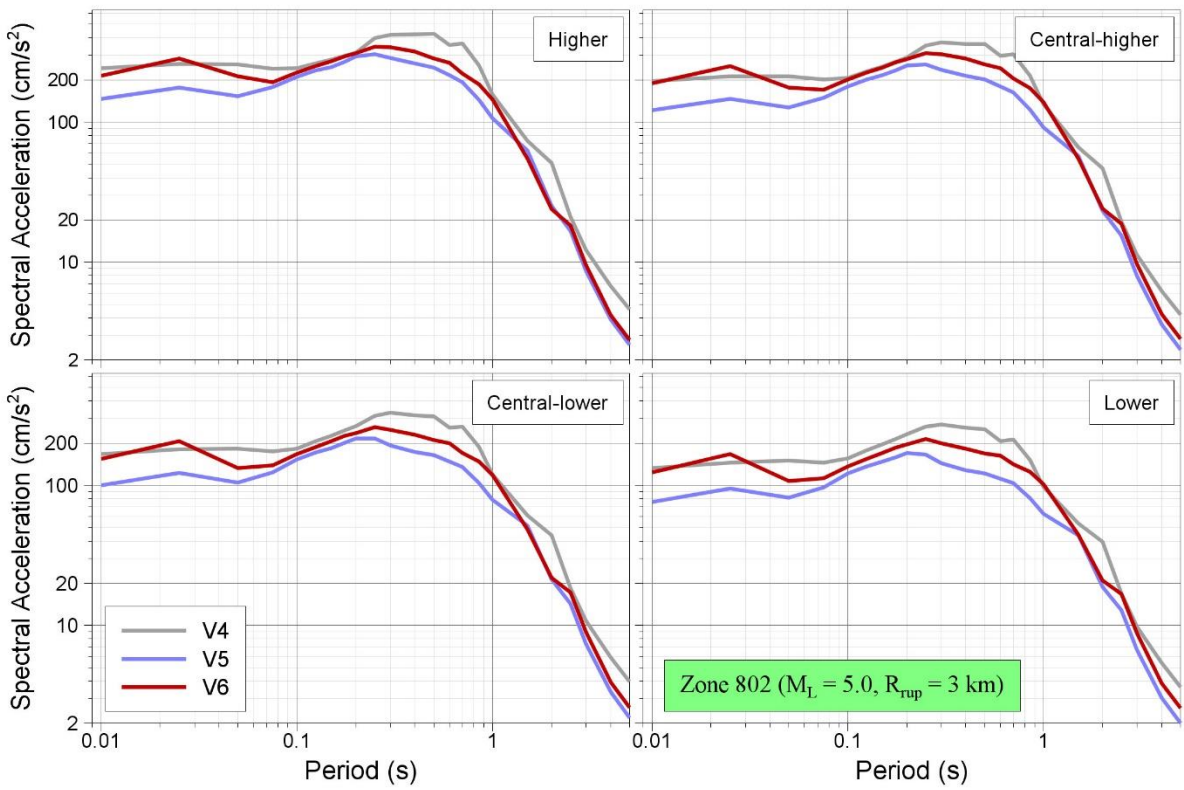
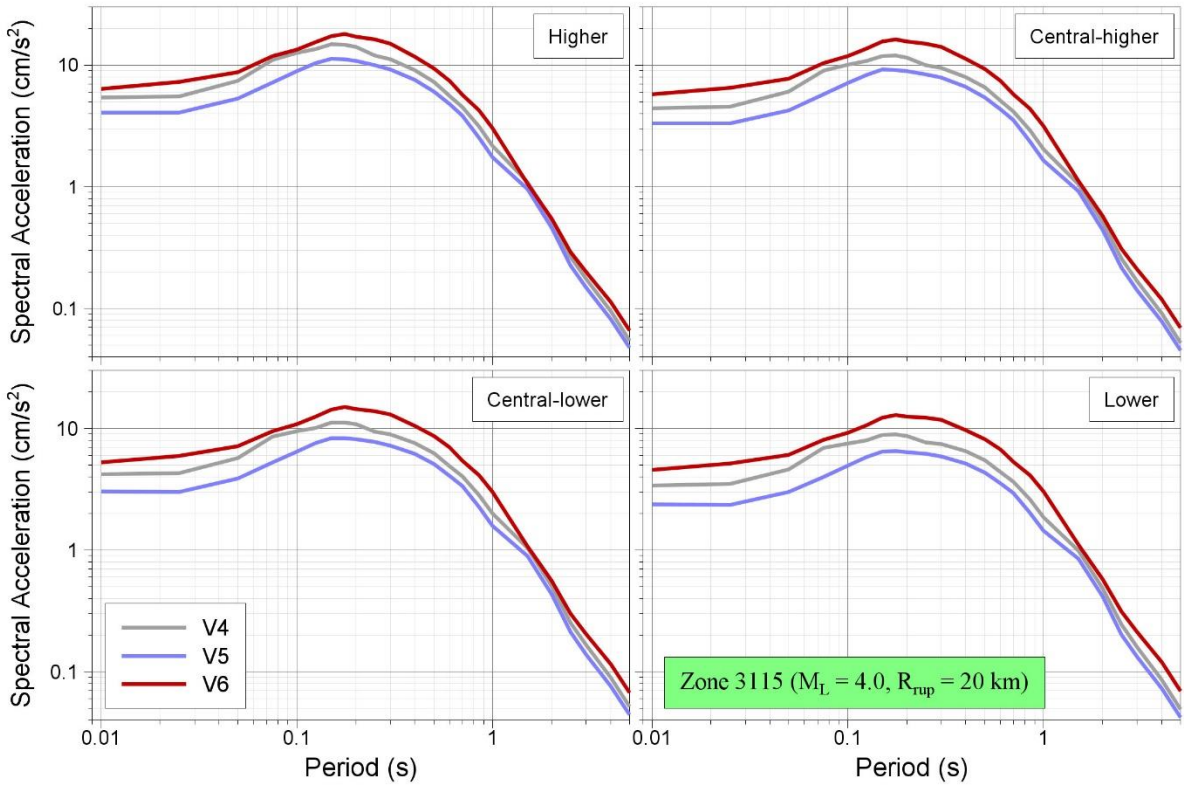


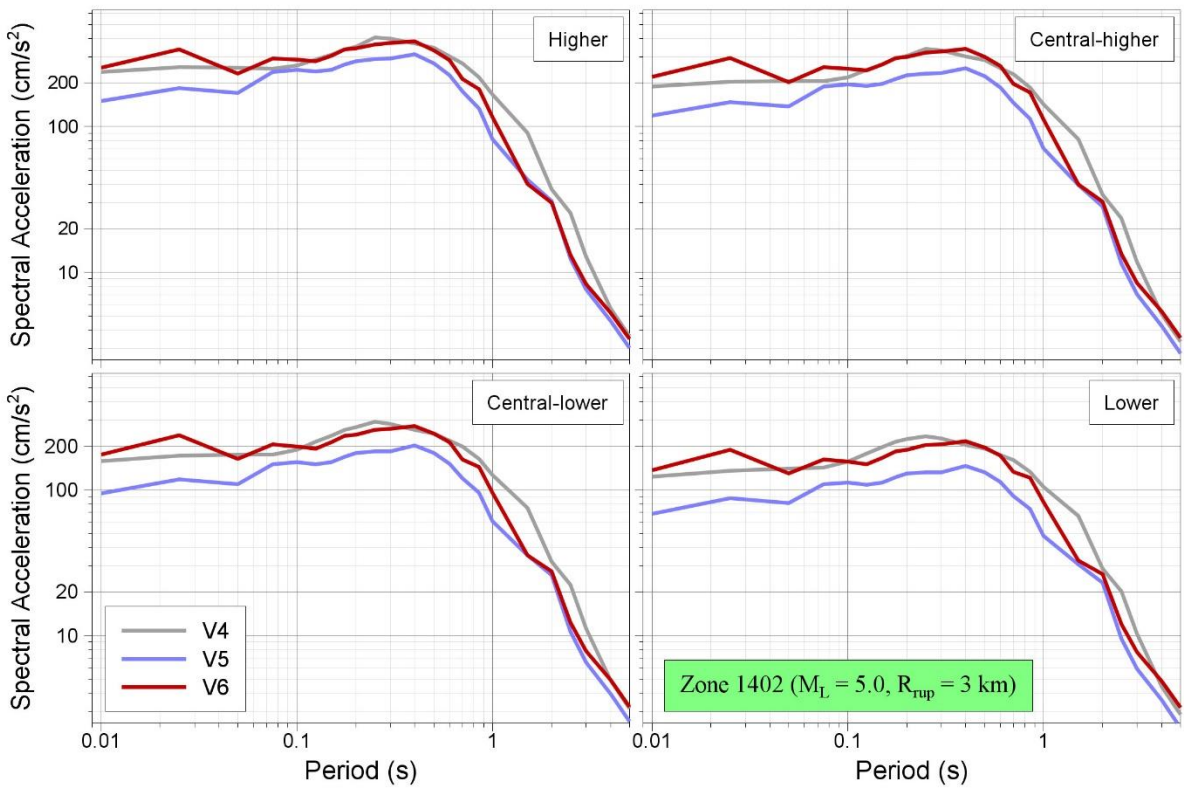
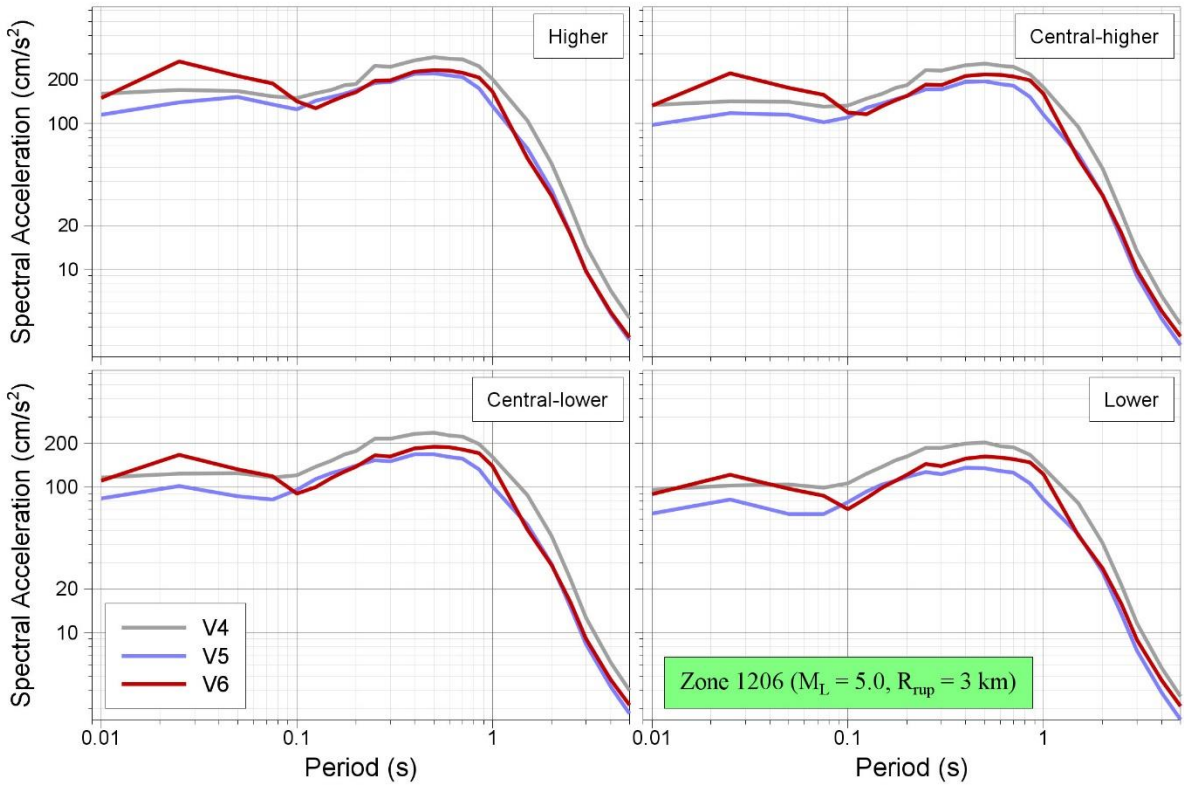


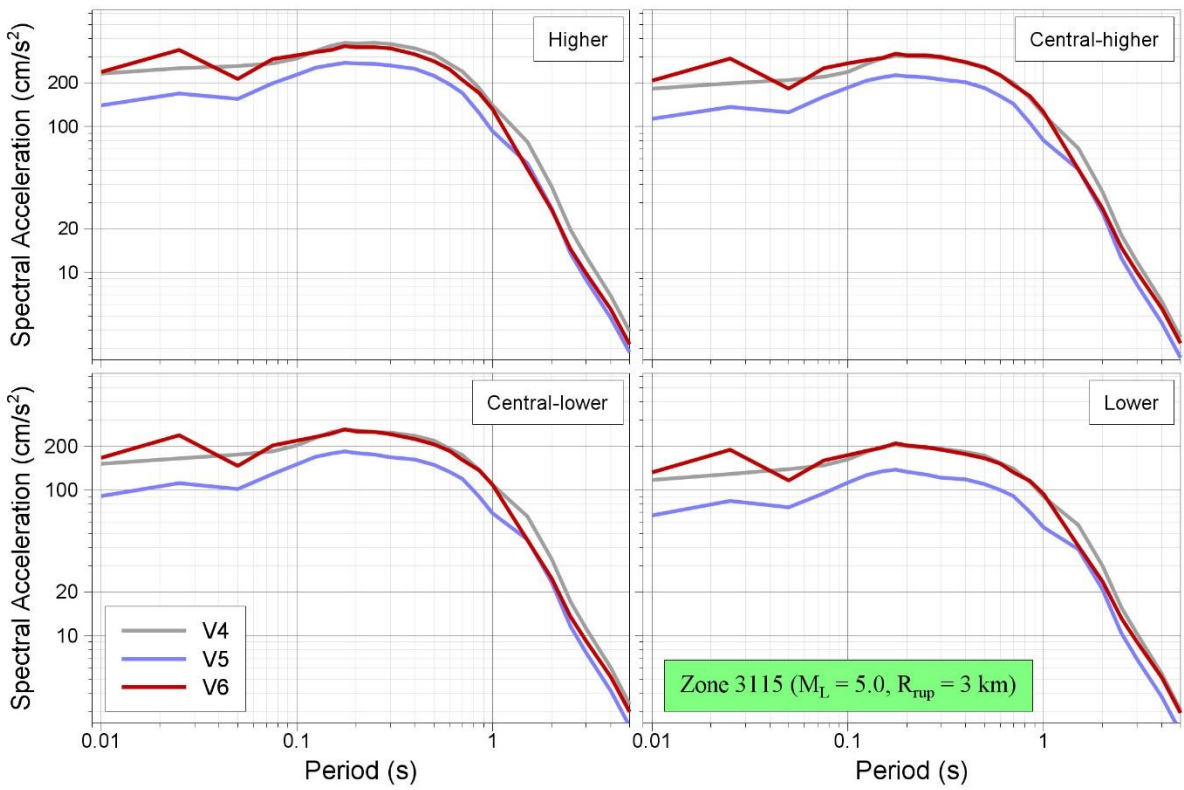
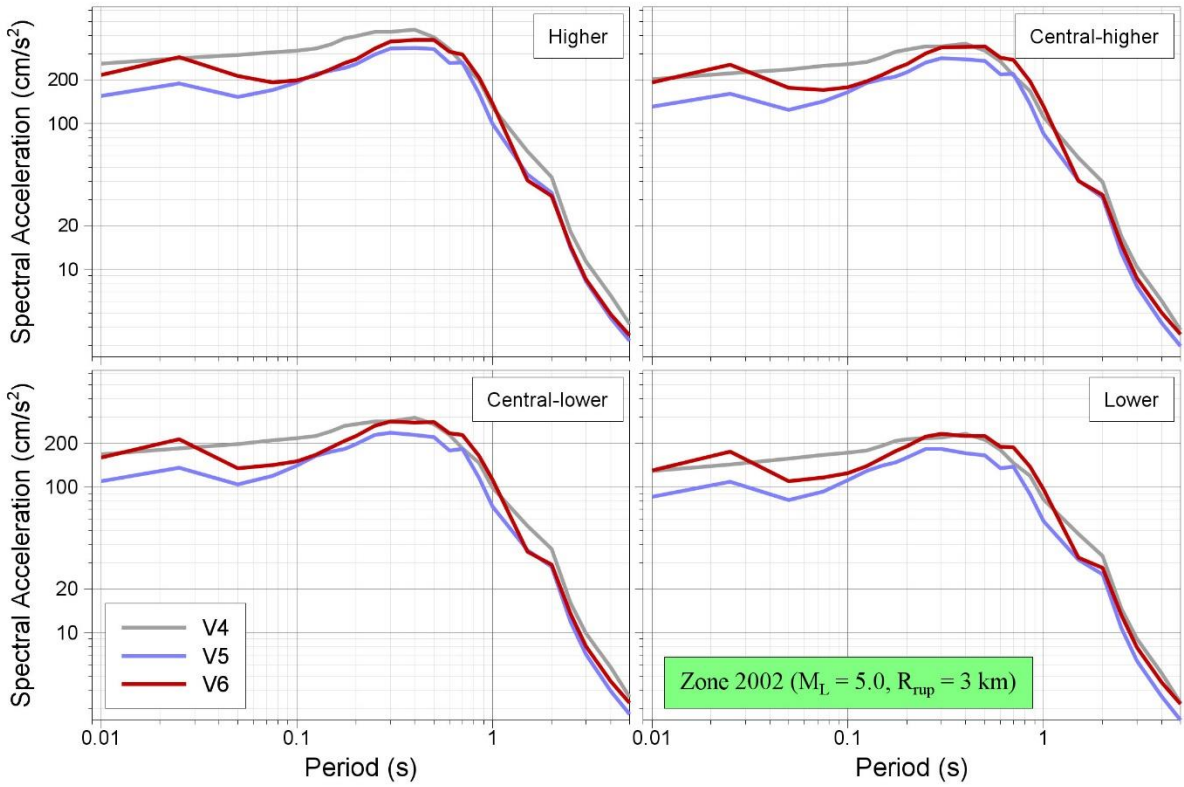


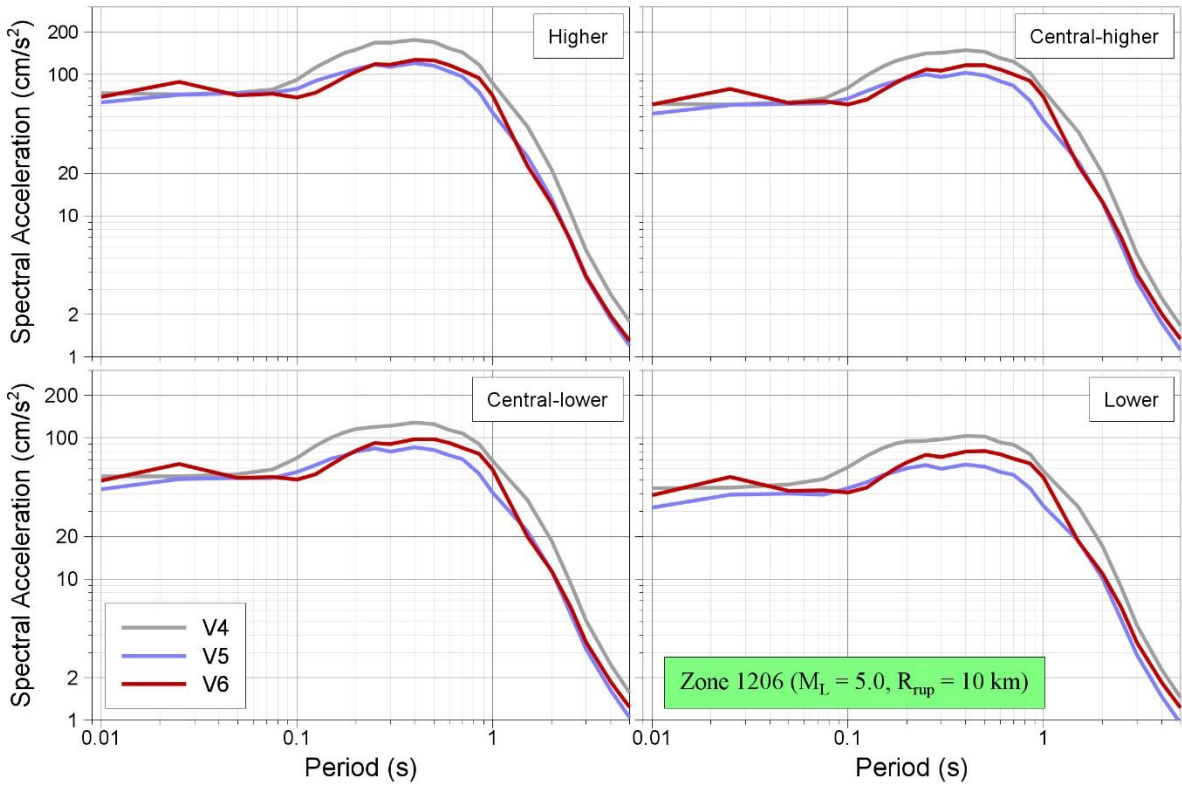
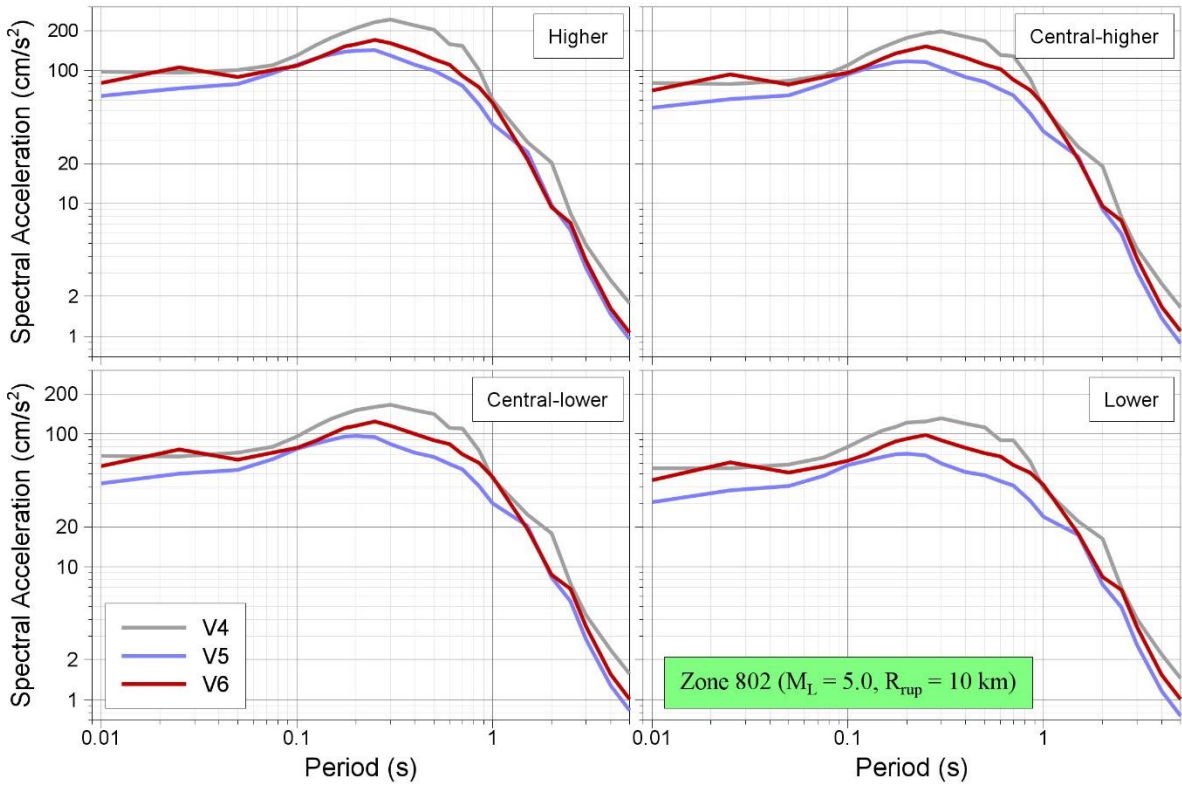


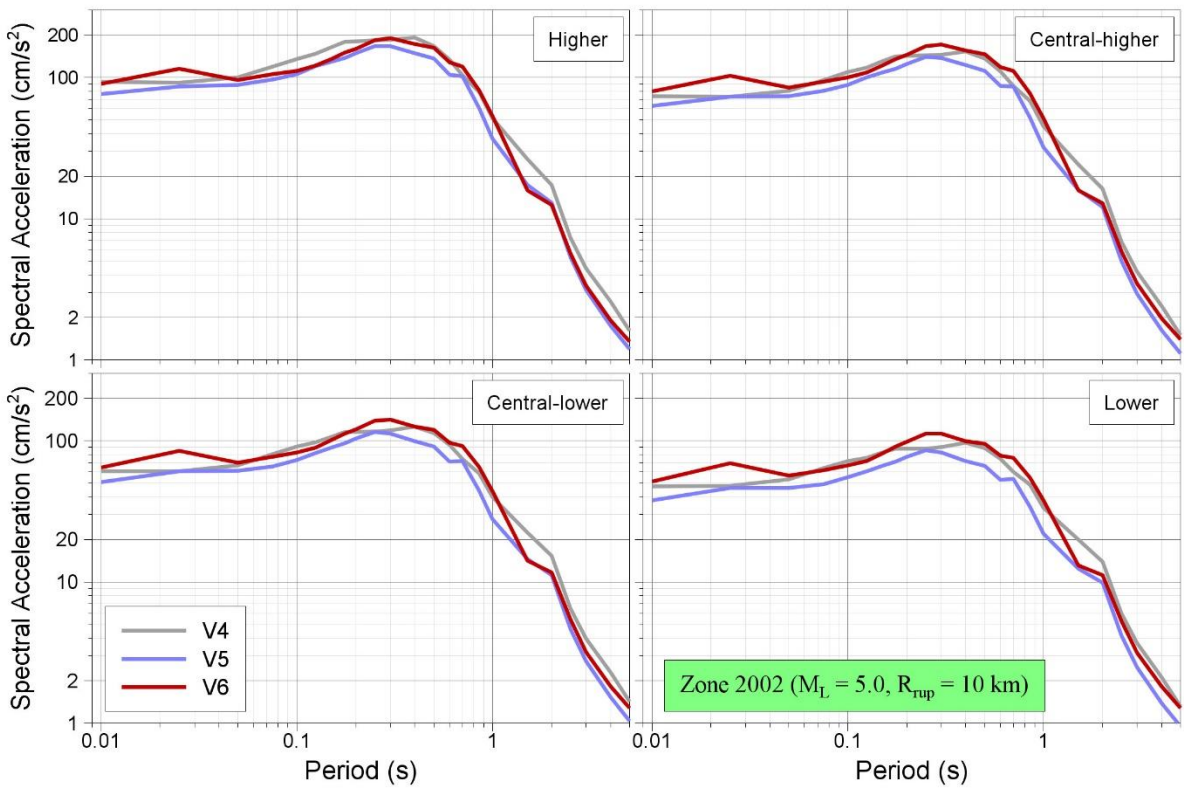
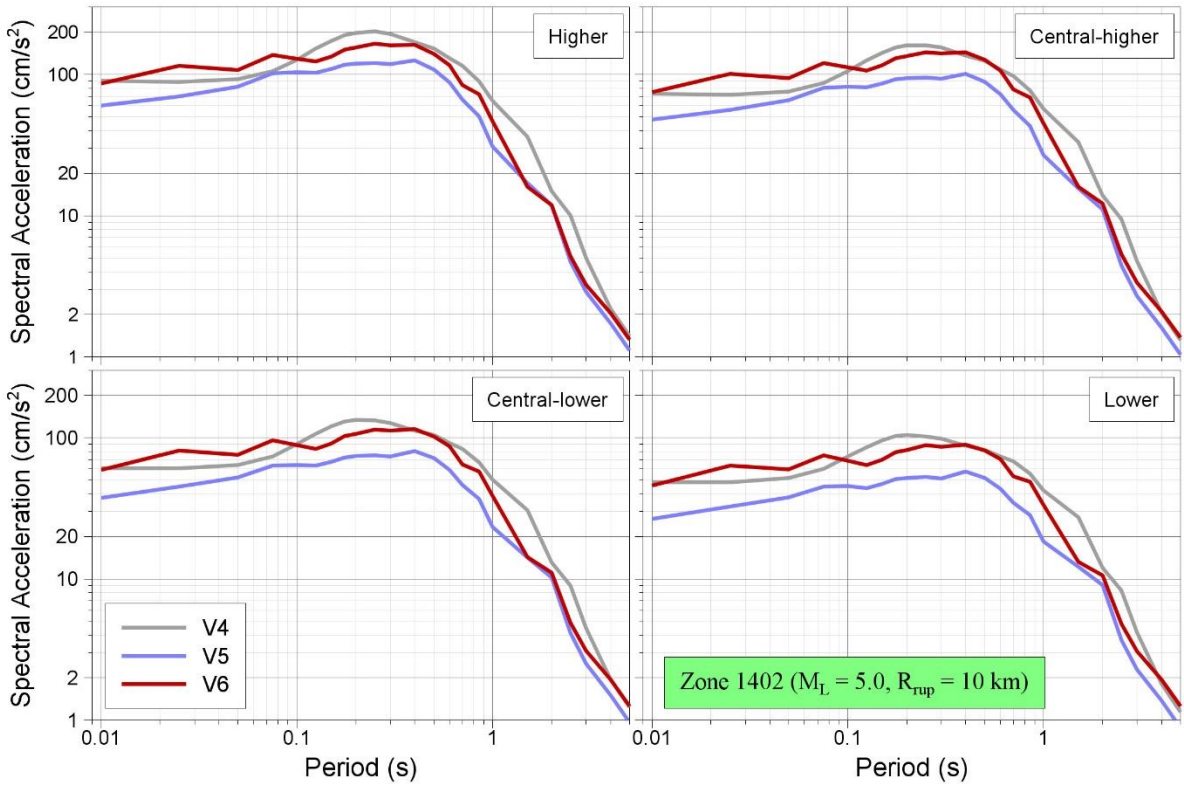


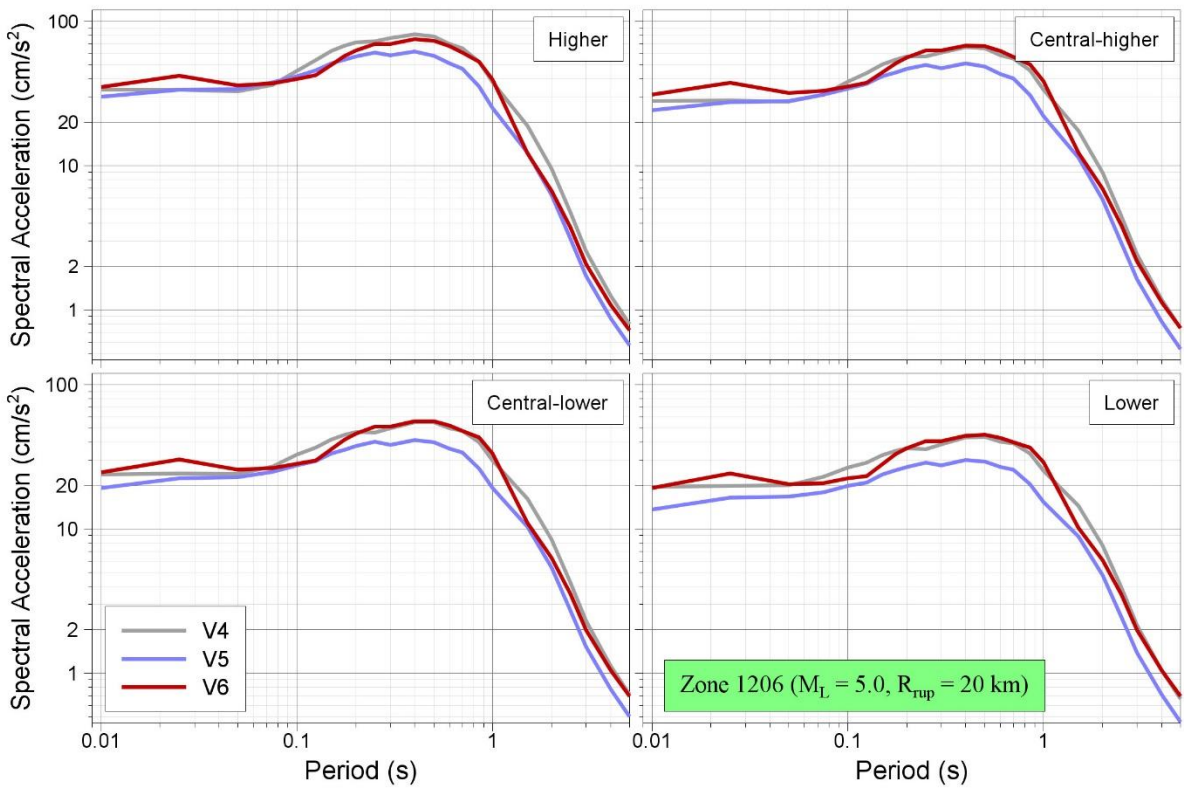
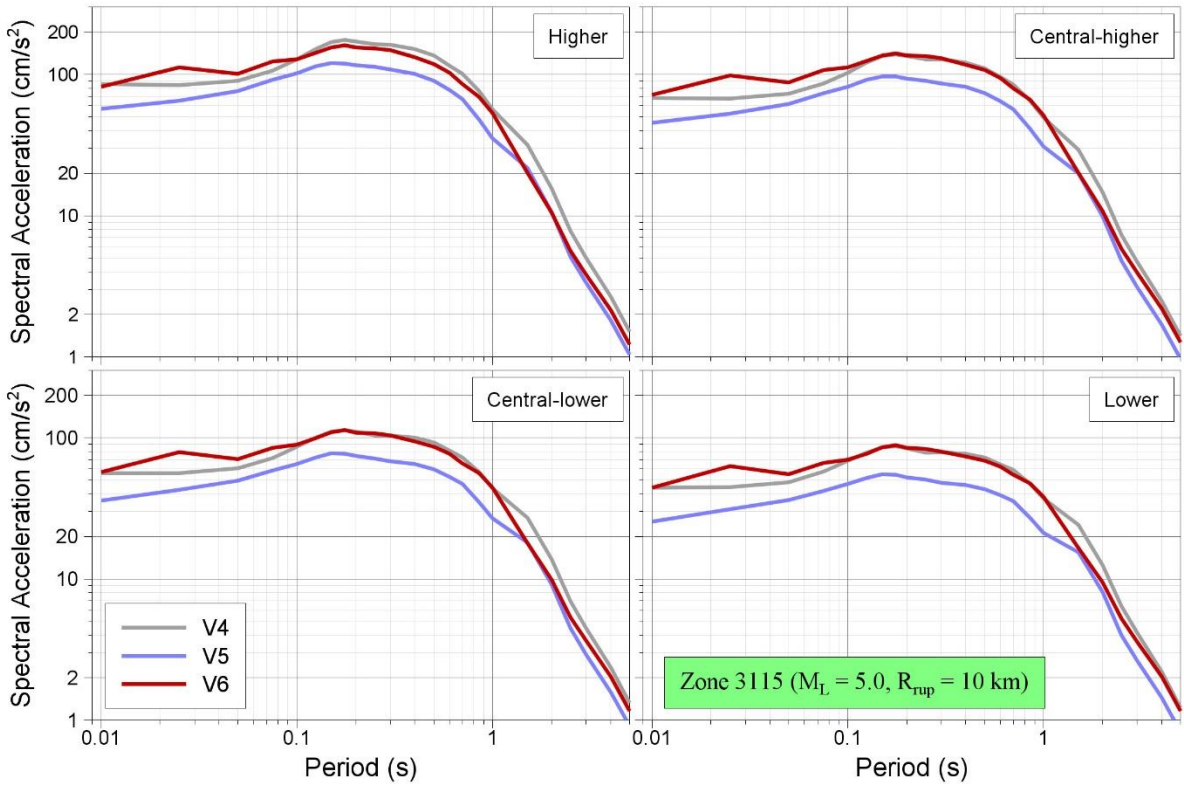


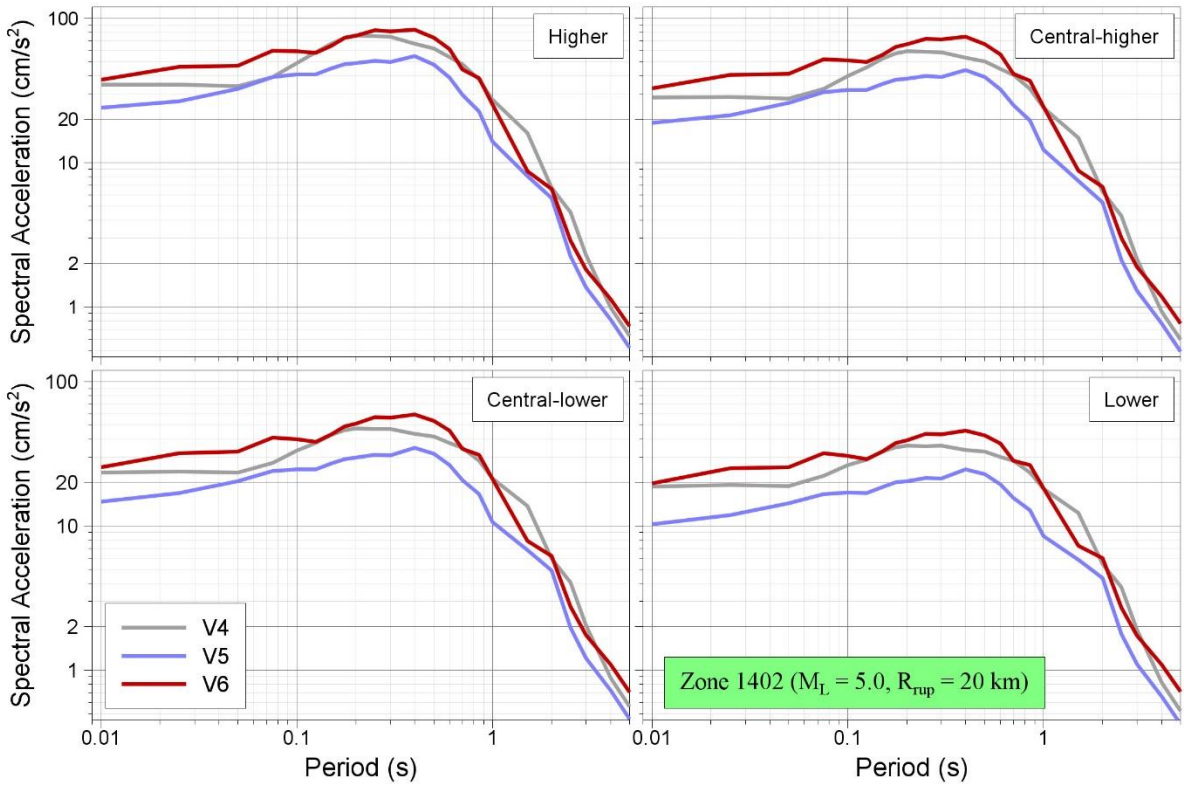
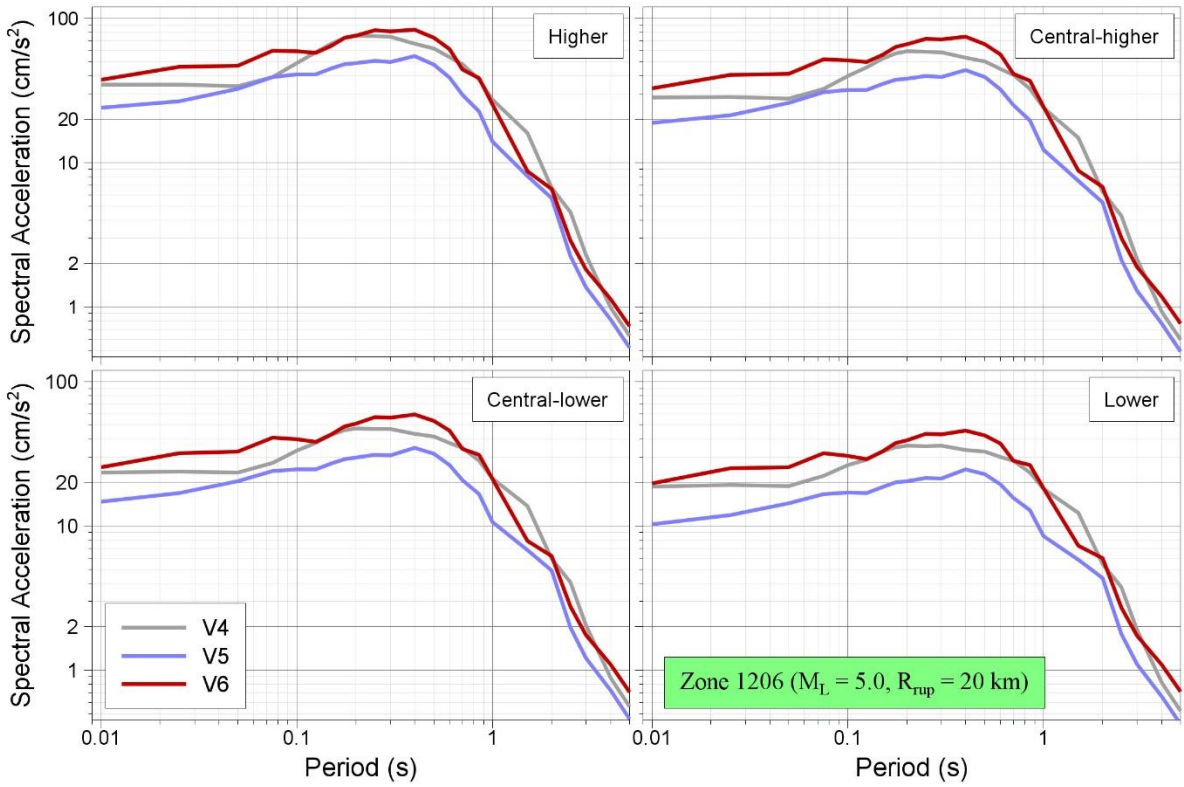


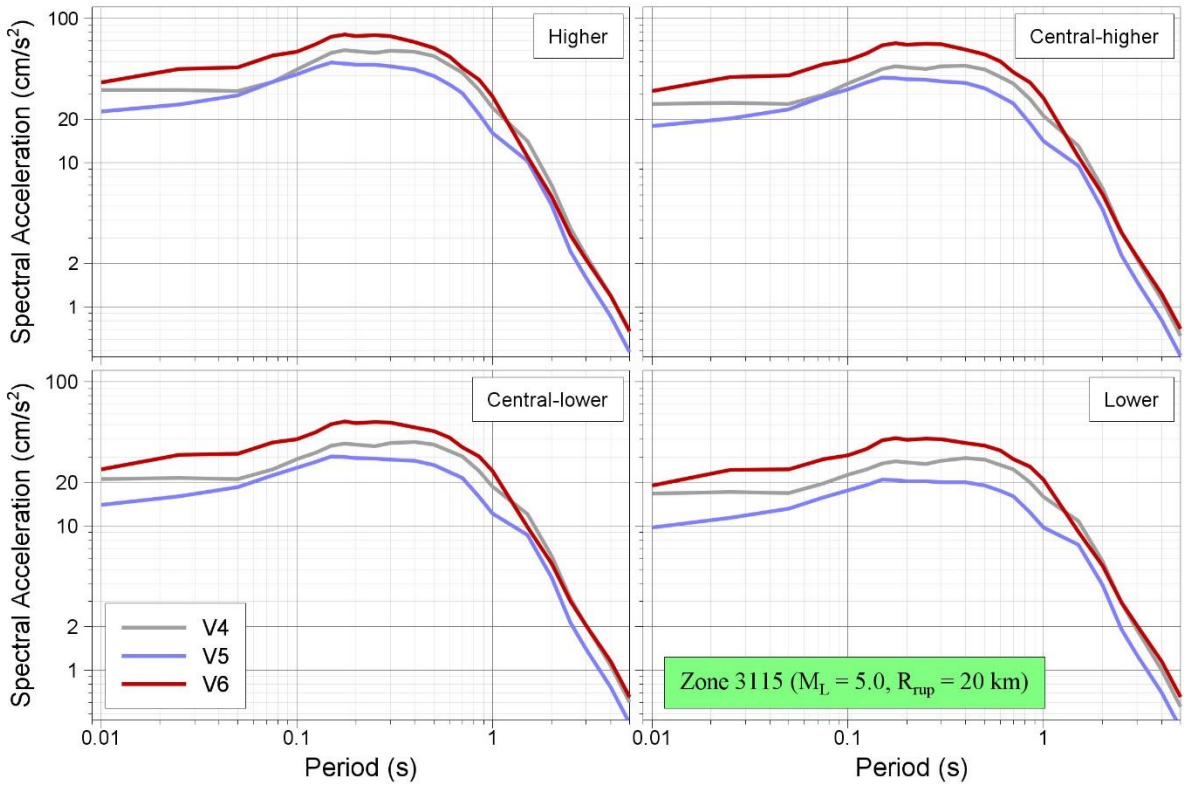
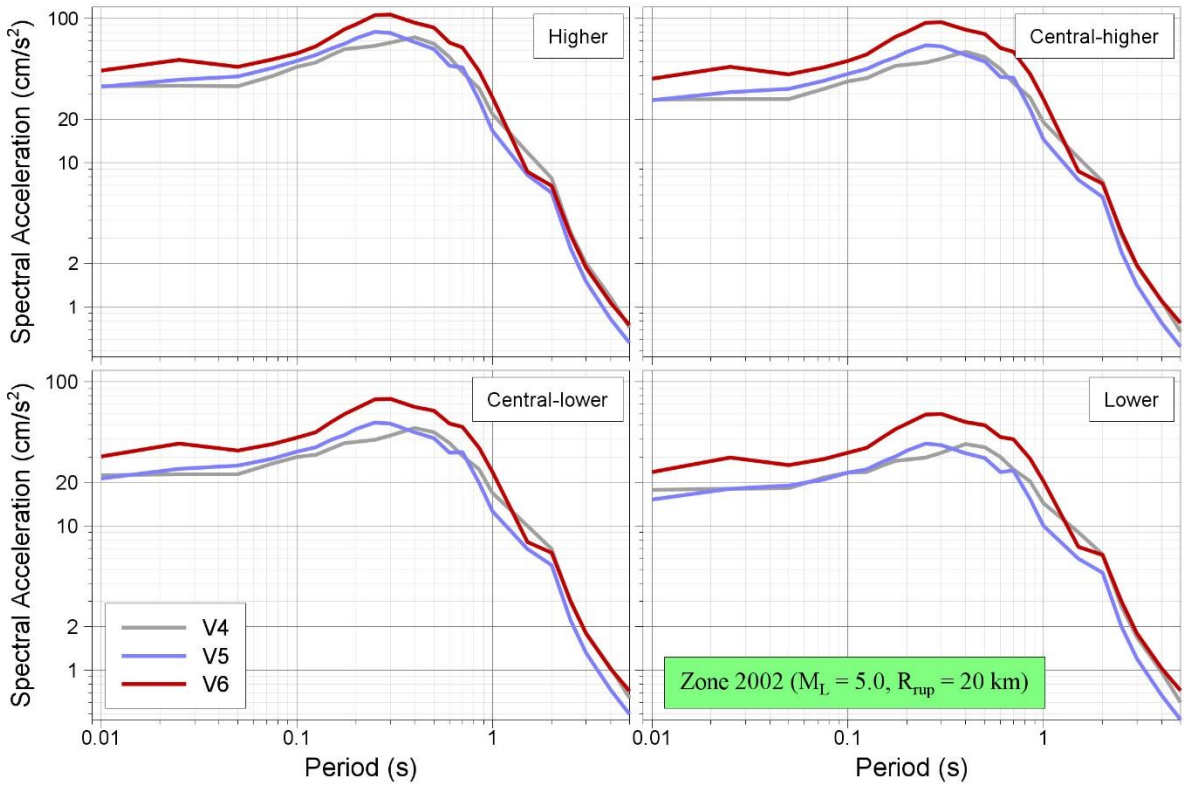


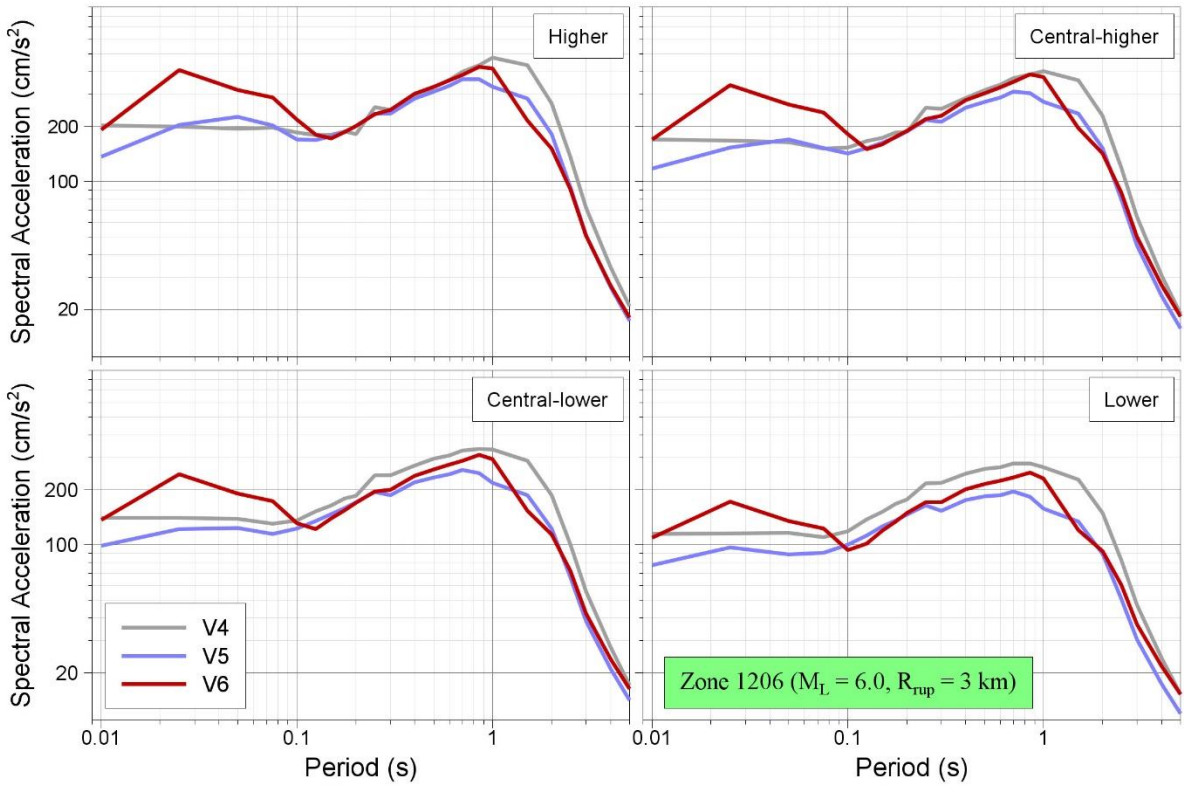
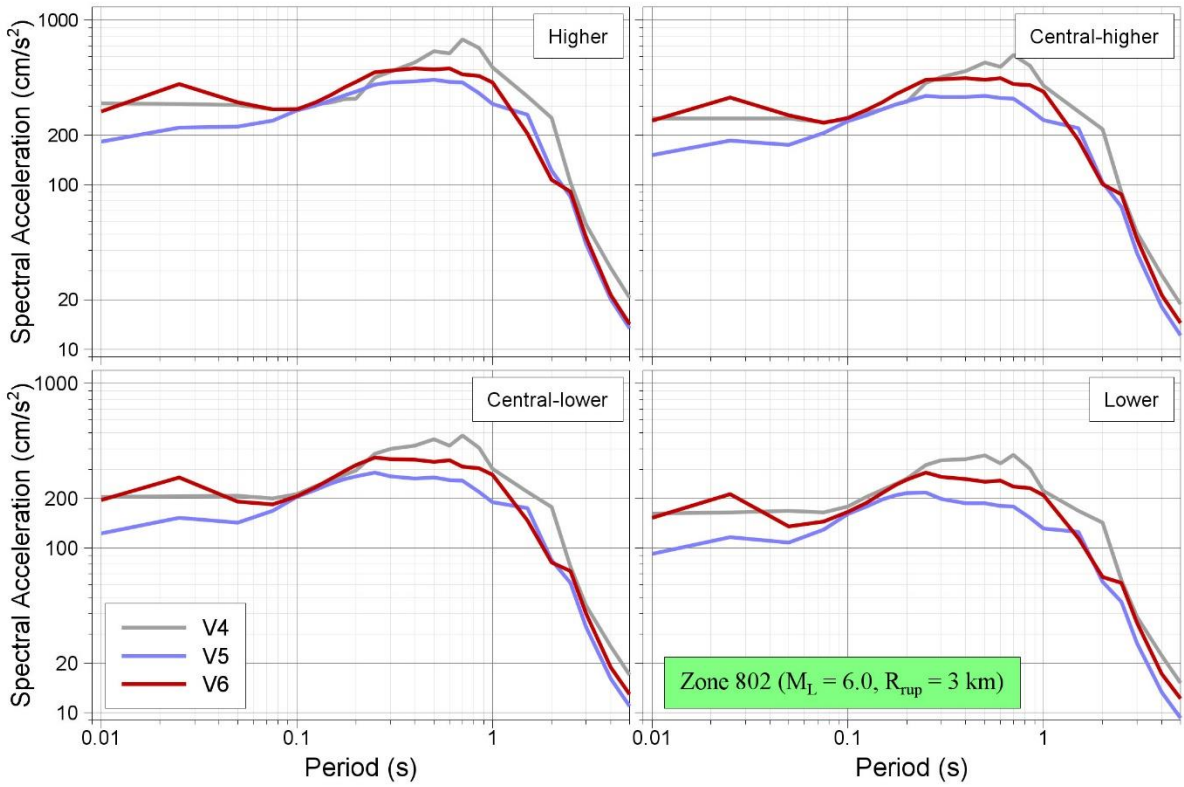


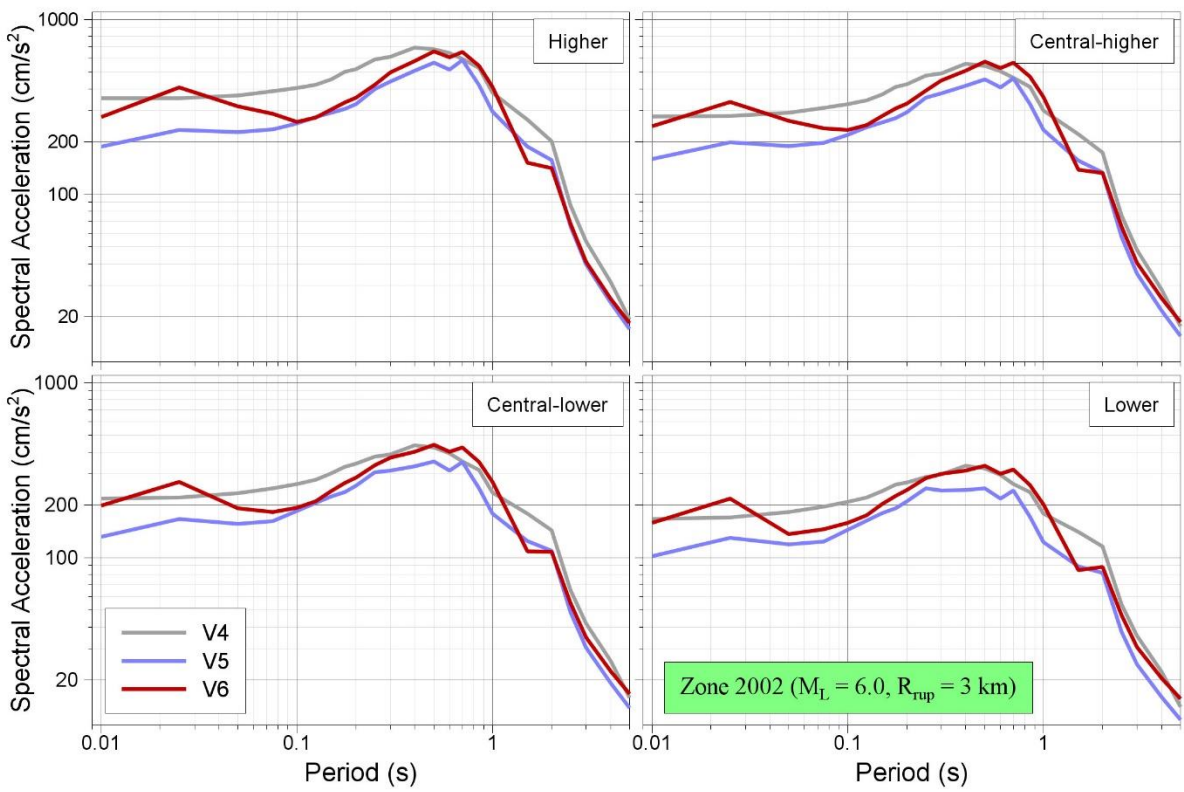
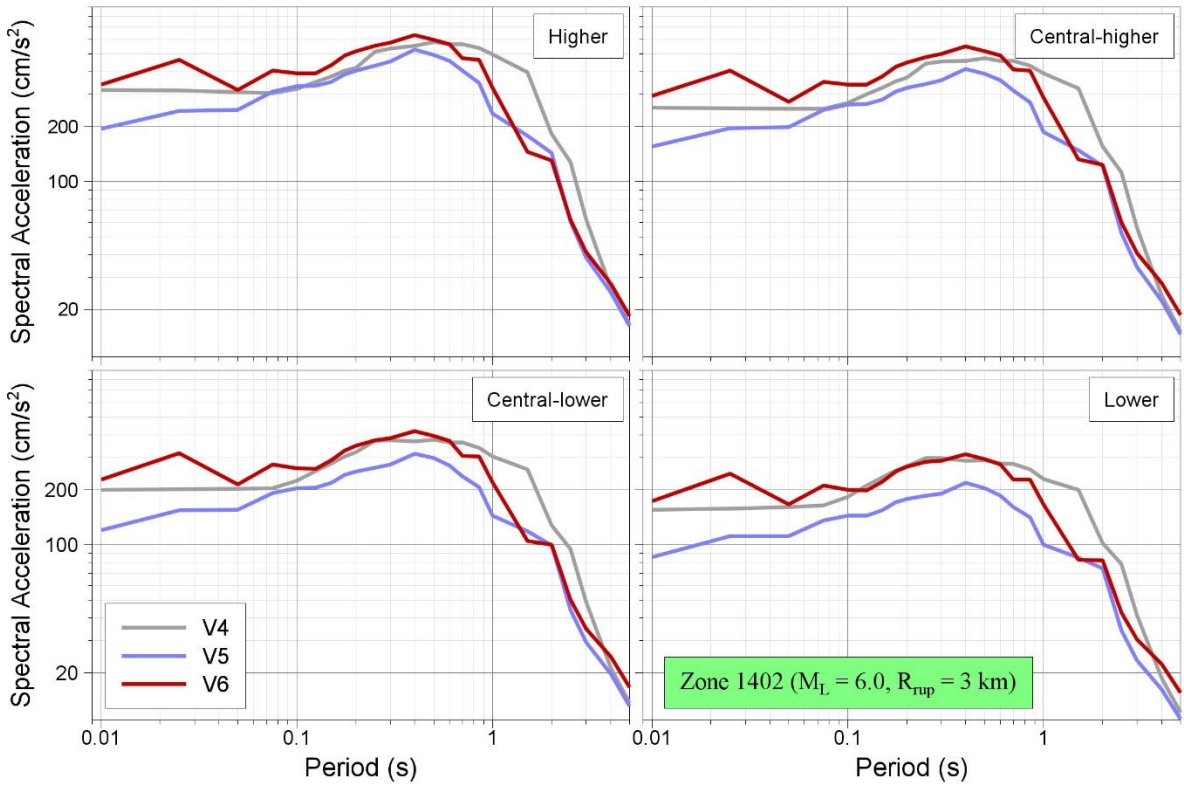


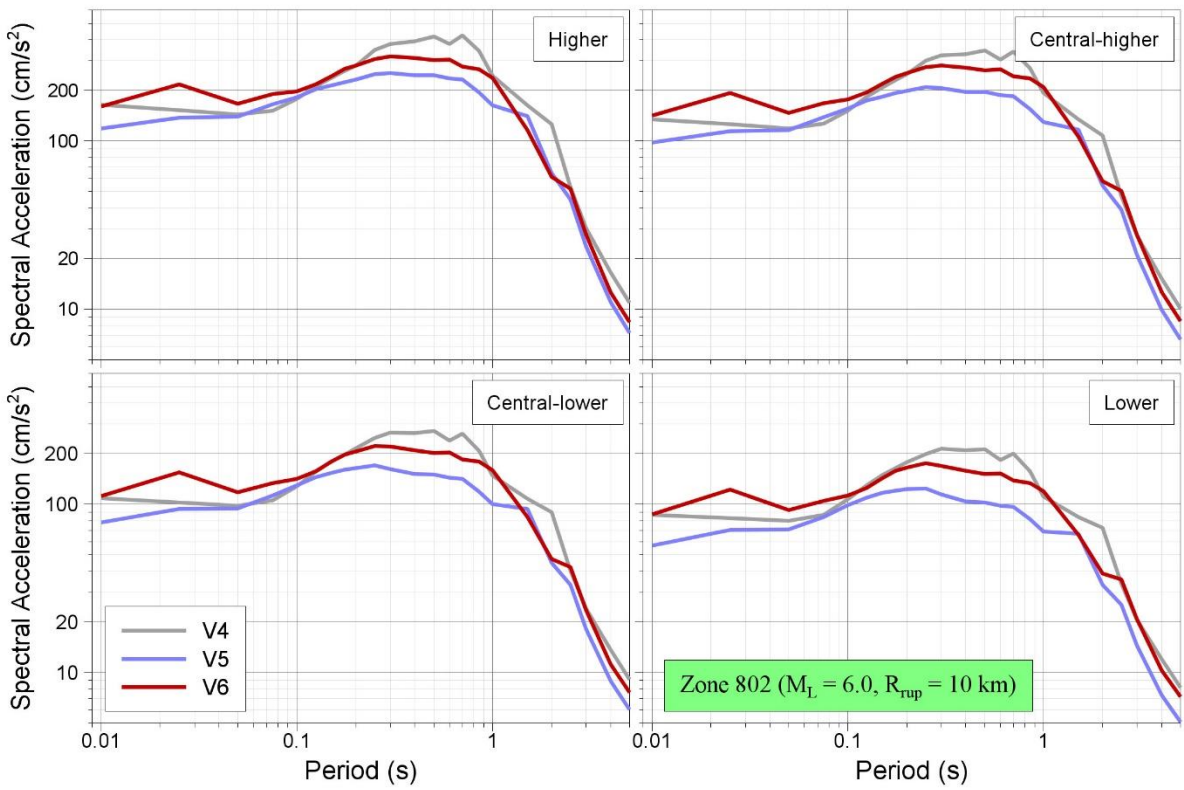
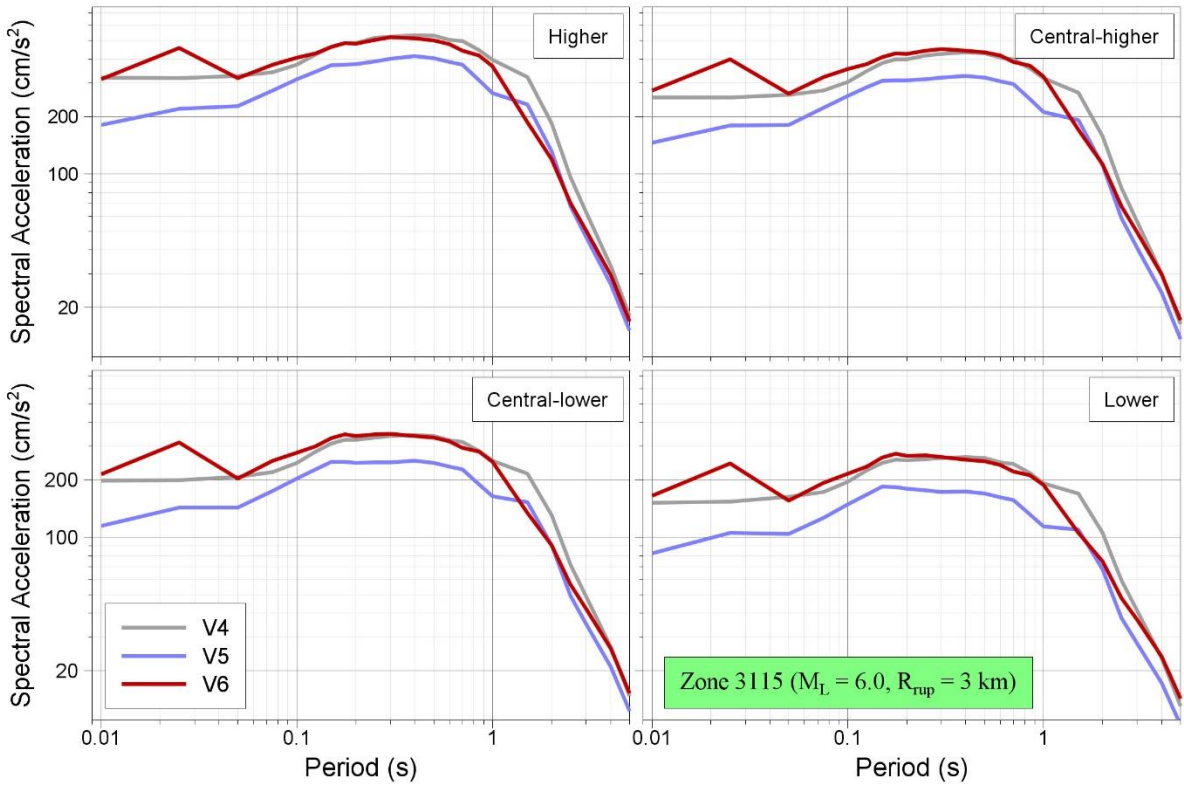


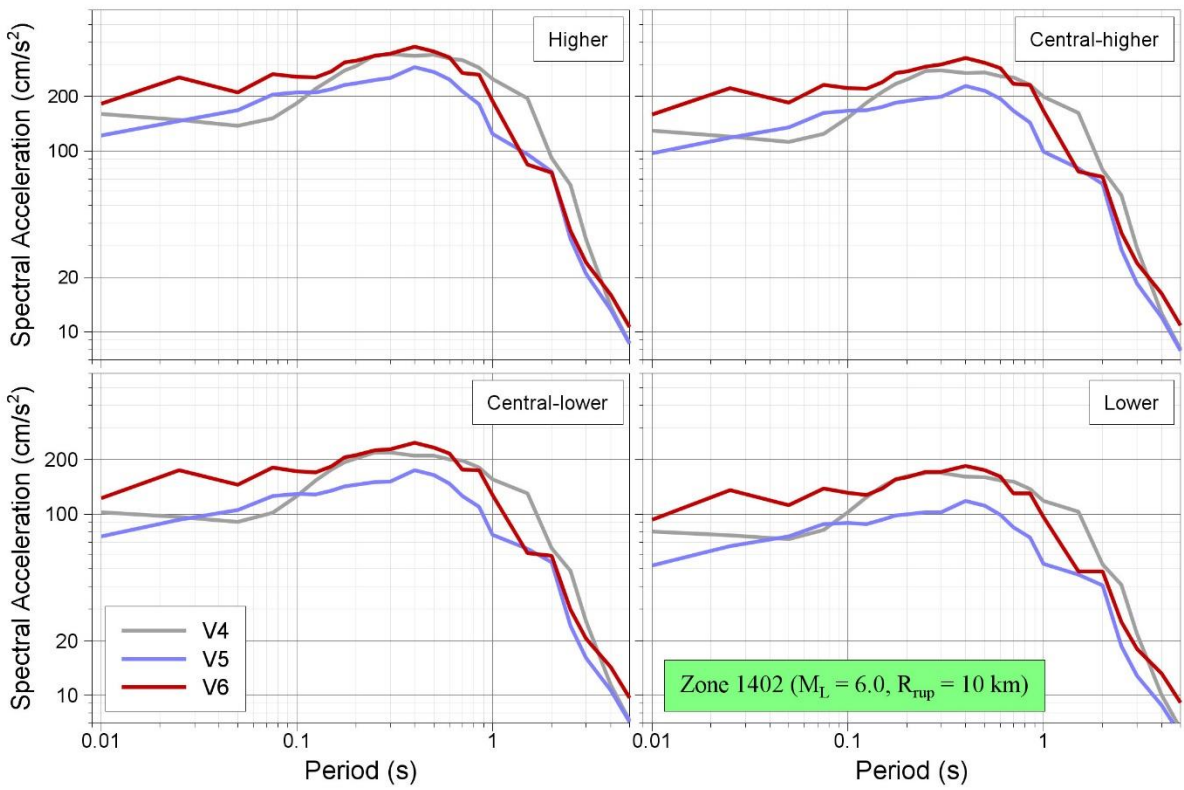
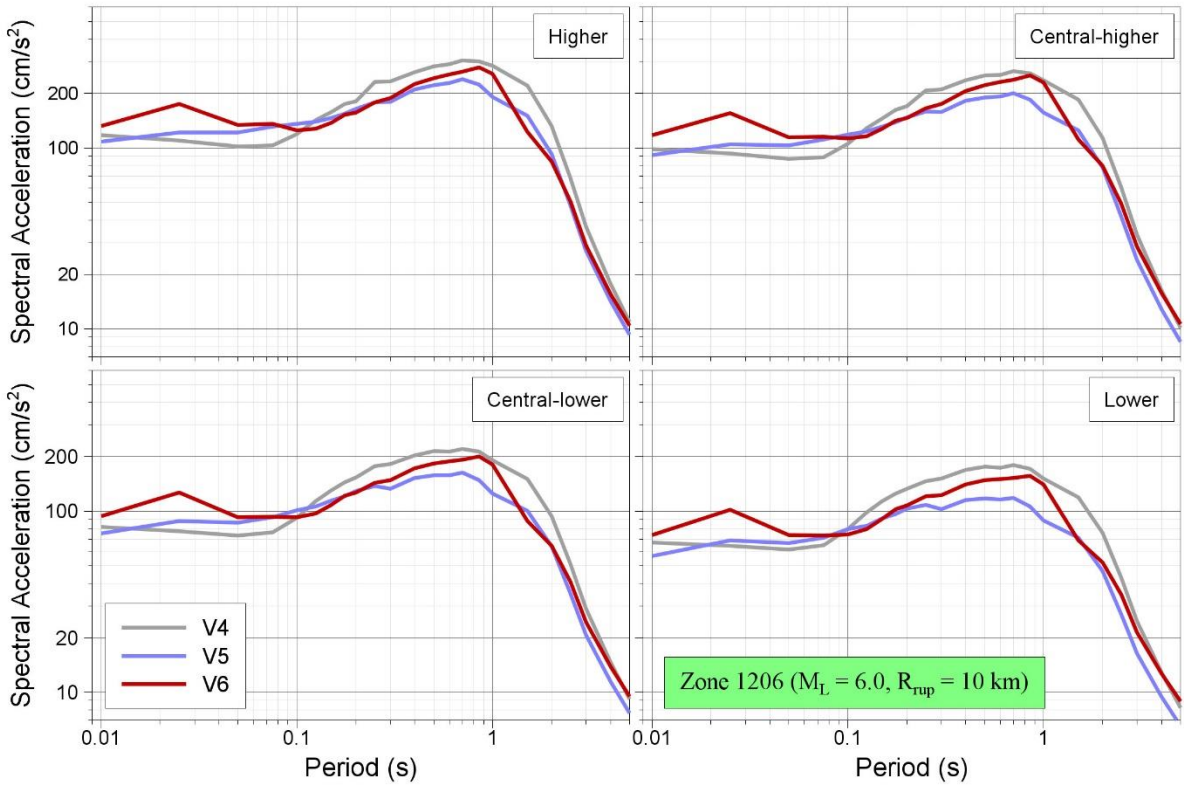


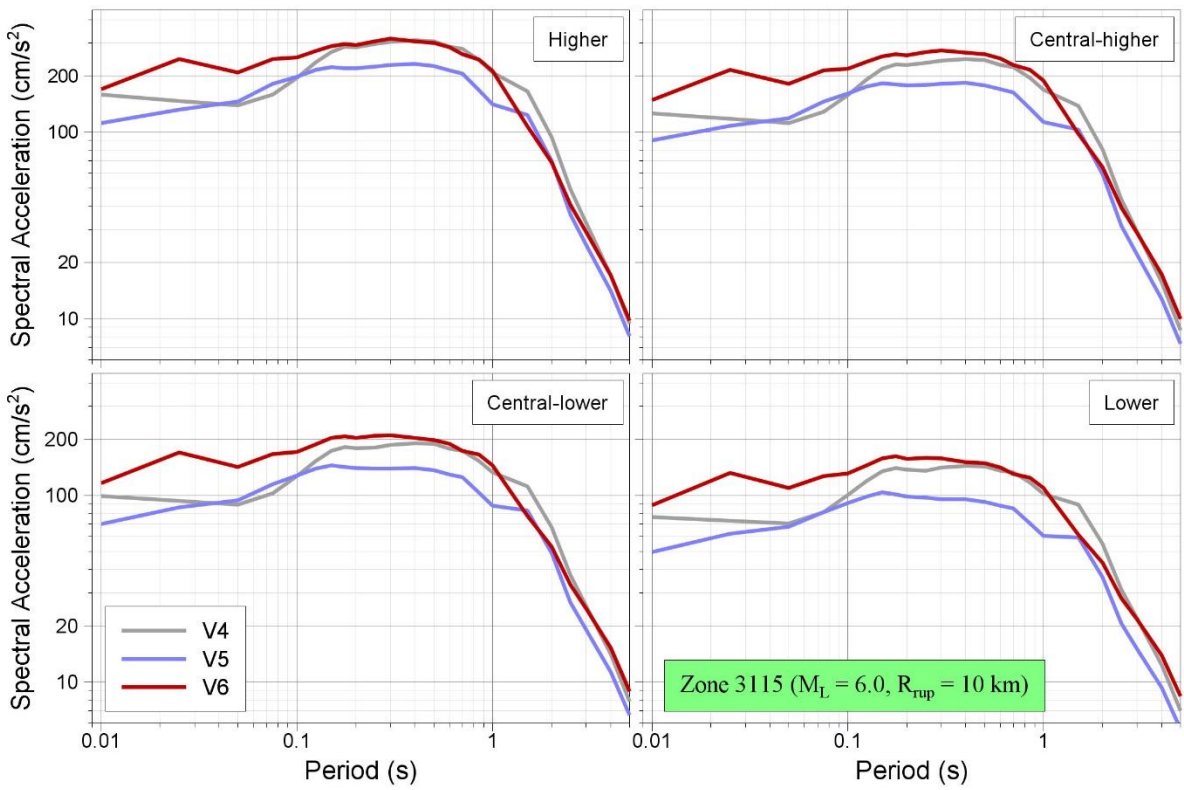
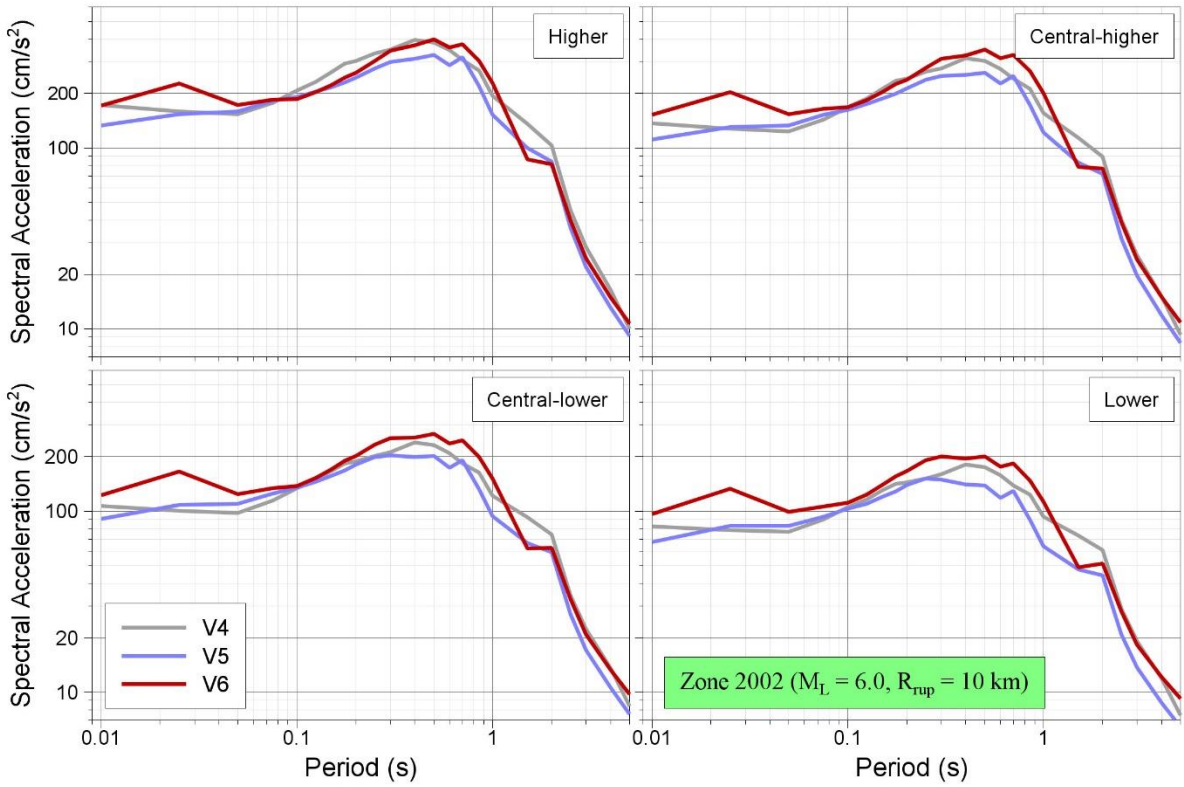


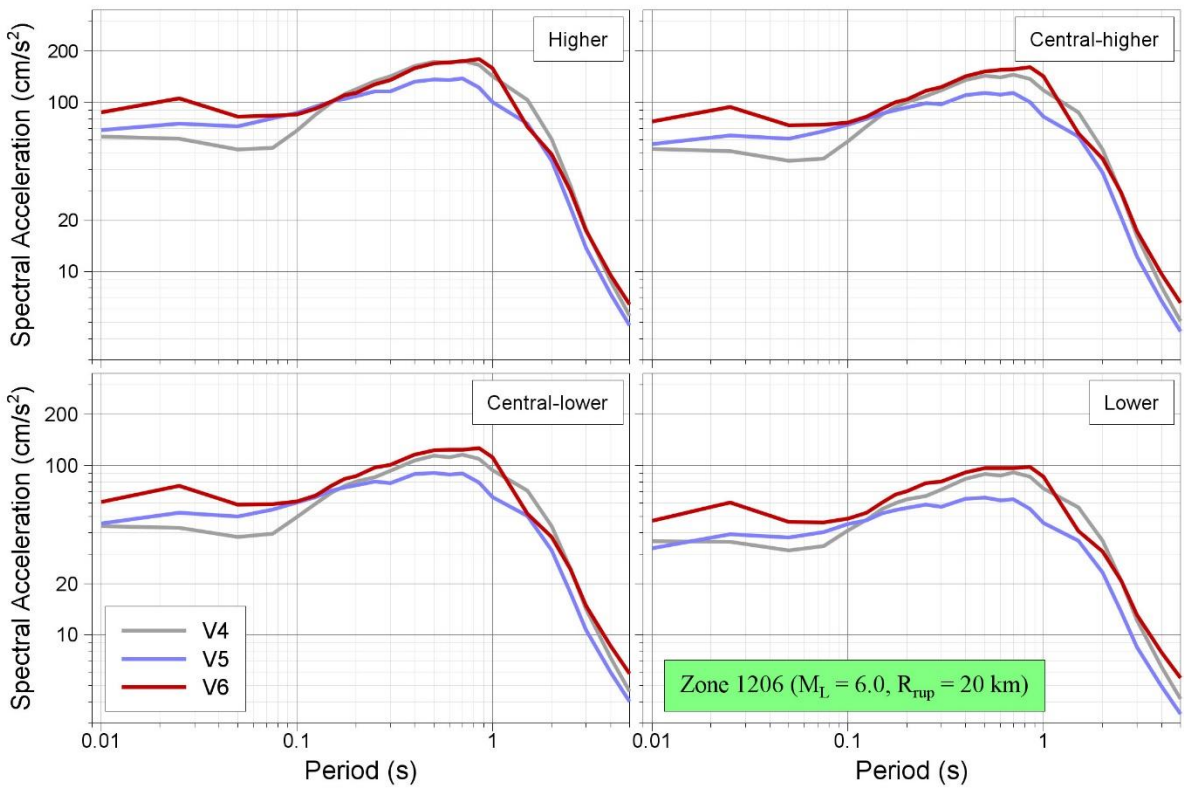
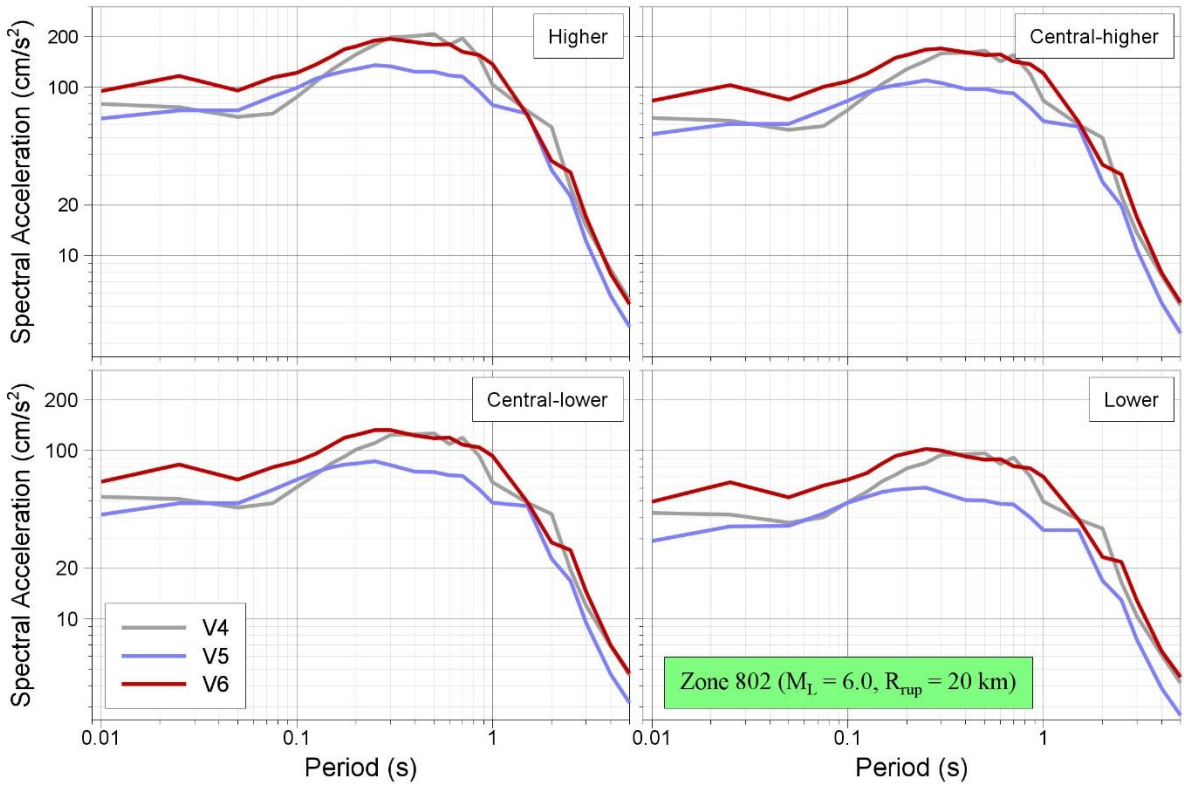


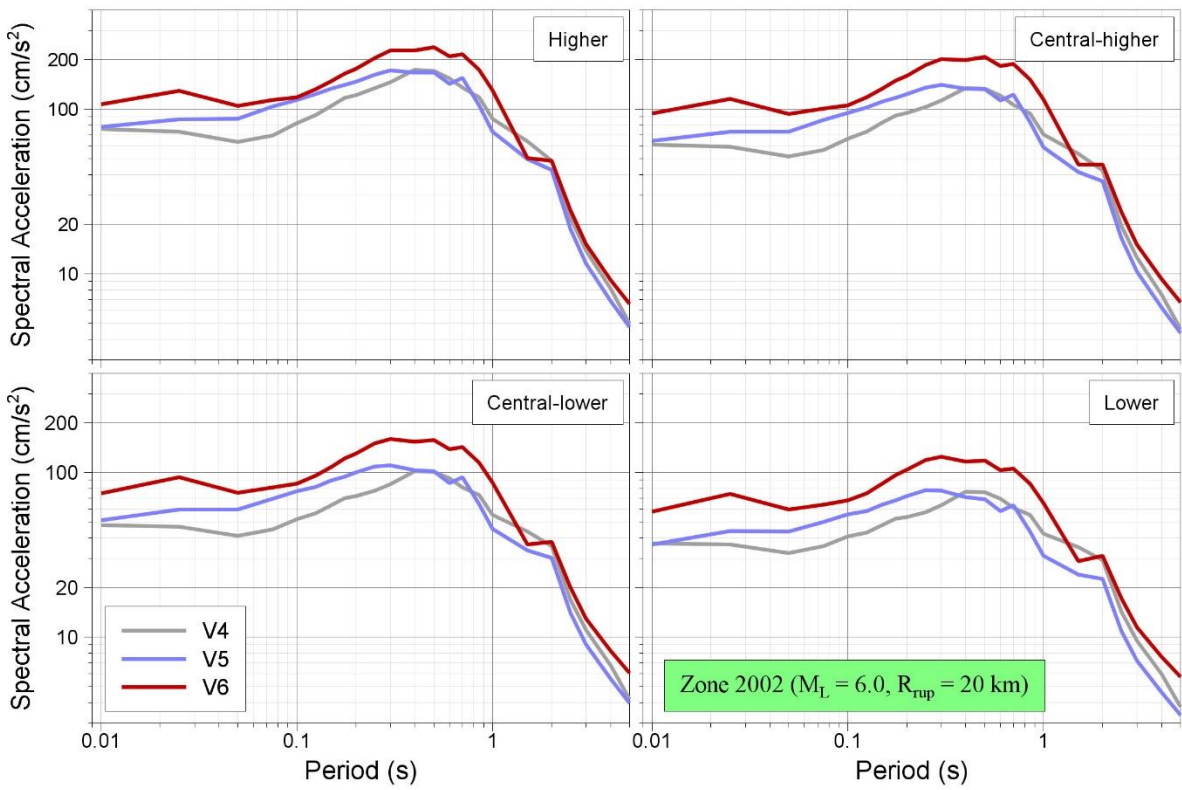
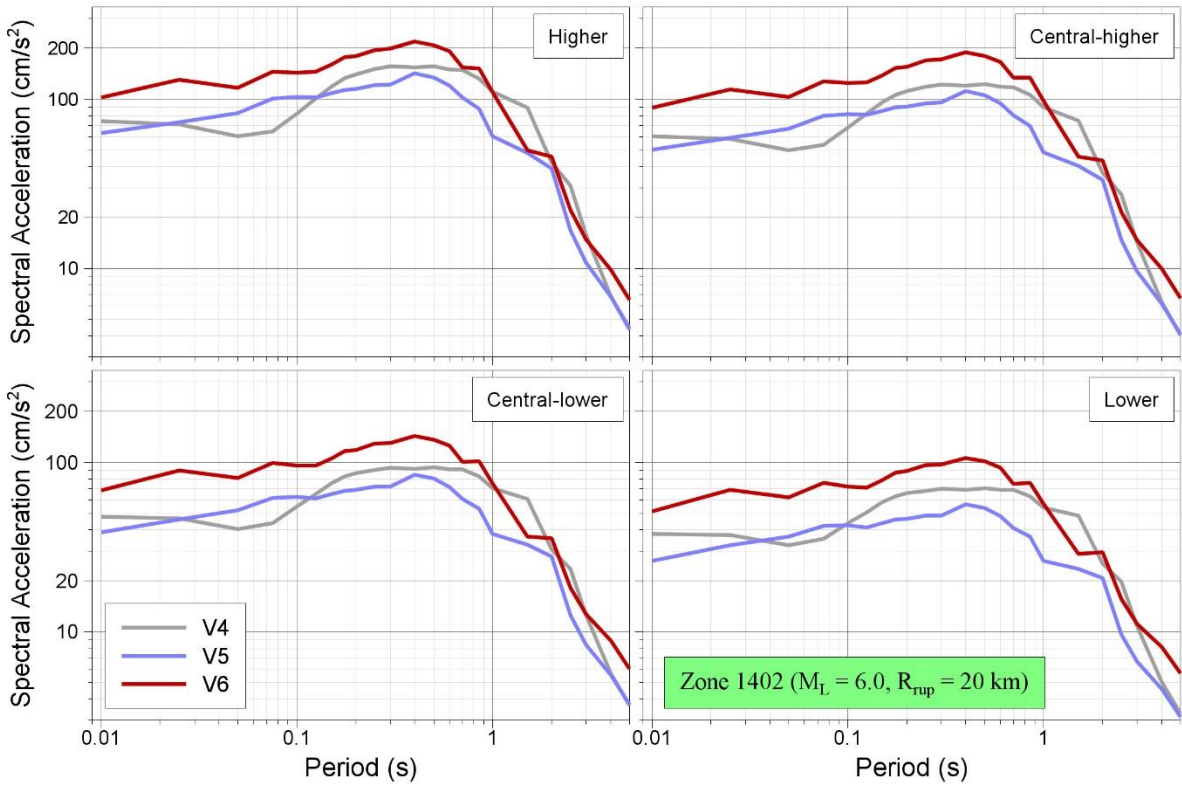


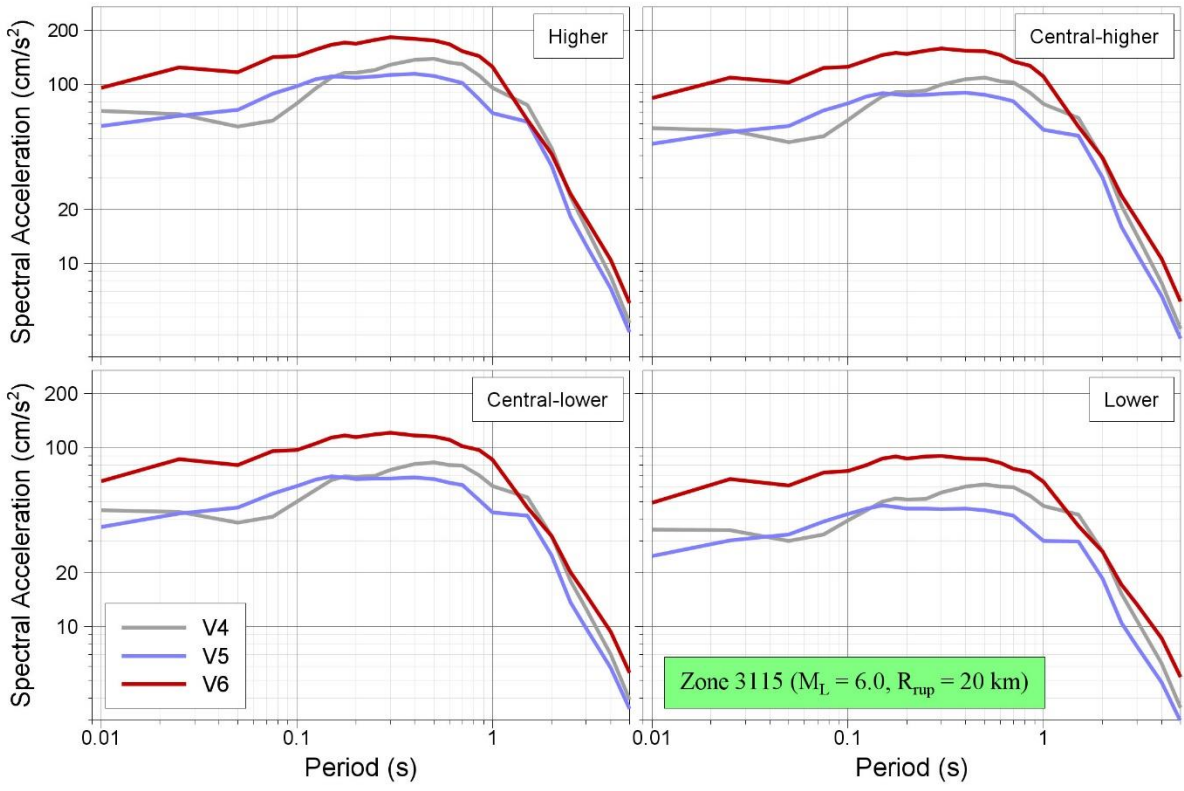












APPENDIX VI

Geophone Amplitudes

This appendix contains a short document produced by KNMI on the work undertaken to confirm the calibration—and hence the recorded amplitudes—from the G-network borehole geophones.

To monitor induced seismicity of the Groningen gas field and surrounding fields, the northeast of the Netherlands is covered with a dense seismic network. Figure A6.1 shows the KNMI borehole network in the area, and its development from 1991 until 2016. The area has soft-soil and high seismic noise conditions. As a remedy, most of the seismic sensors have been installed in boreholes.

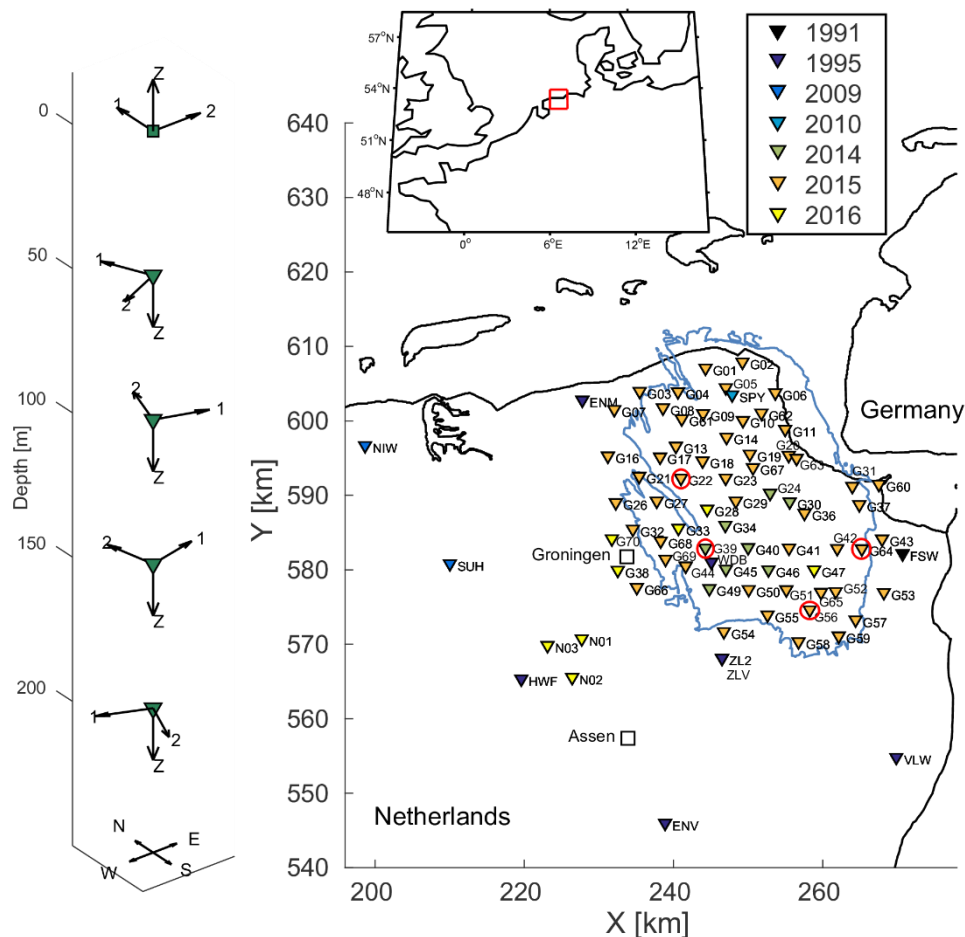


Figure A6.1. Development of the permanent borehole seismic network around the Groningen gas field in northwestern Europe. Triangles denote borehole stations and the blue line depicts the border of the Groningen gas field. Coordinates are shown in the Dutch National Triangulation Grid (Rijksdriehoekstelsel). All (borehole) stations since 2014 have a setup as shown on the left-hand figure. Red circles highlight stations where a broadband sensor has been added in 2018.

All stations installed since 2014 have a uniform setup: a 3-component accelerometer at the Earth's surface and 3-component geophones at 50, 100, 150 and 200 m depth [Figure A6.1(left)]. These newer stations are either part of the G-network (station names starting with 'G'), or the N-network (station names starting with 'N'). The G-network is tailored to monitor seismicity from the Groningen field, the N-network has been constructed to monitor a gas storage plant in Norg, but also contributes to location and characterization of events at the southwestern edge of the Groningen

field (Dost *et al.*, 2017). The geophones in the G- and N-network are IO SM-6 3-component sensors with a corner frequency of 4.5 Hz. At each station, all data streams are fed into a 16-channel datalogger (Kinometrics Granite). Below we compare recordings of teleseismic and local seismicity, to find out whether issues might exist with the geophone amplitudes after re-calibration at the end of 2018.

Recordings of local earthquakes in Groningen can be highly complicated. There may be large amplitude variations from station to station due to radiation effects, complex propagation effects and laterally varying site effects. Using regional or teleseismic arrivals, the amplitude variations are expected to be small. For distant sources, the Groningen array approximately experiences the same source radiation. Moreover, a single phase can be selected that is consistently recorded over the entire array. The main amplitude variations remaining are basin-scale focusing and defocusing effects and local site effects.

Figure A6.2 shows the maximum amplitudes of a PKP phase recording over Groningen, due to an earthquake in Fiji (20180819, 00:19:37, M=8.2).

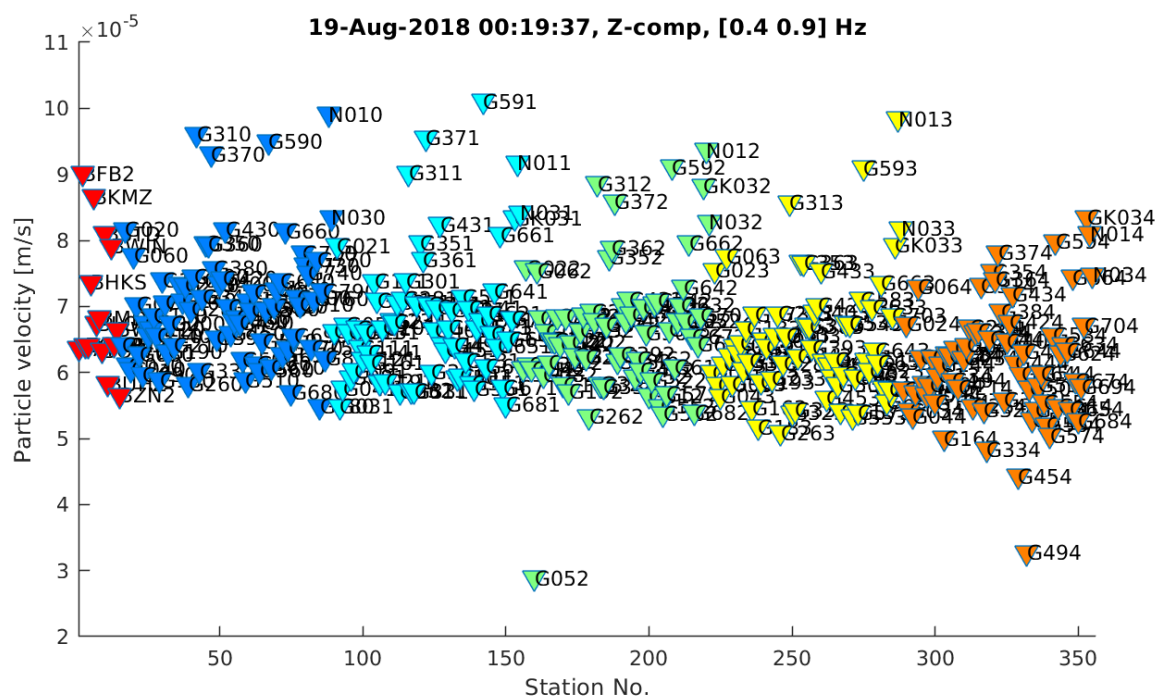


Figure A6.2. Maximum amplitudes recorded on the vertical component for an earthquake in Fiji. A time window is taken around the PKP-phase. The stations are alphabetically ordered and color-coded based on network and depth: B-network (red), 0 m depth G-network accelerometers (blue), 50 m depth geophones (cyan), 100 m depth geophones (green), 150 m depth geophones (yellow) and 200 m depth geophones (orange).

This is a P-wave that traverses the Earth's outer core before traveling through the mantle and crust at the receiver side. Because of its steep angle of incidence, most energy of this longitudinal wave resides on the vertical component. The data has

been bandpass filtered between 0.4 and 0.9 Hz. The maximum amplitudes are expressed in particle velocity. Due to the large depth (558 km) and large magnitude (8.2) of the Fiji earthquake, the PKP arrival has high signal-to-noise ratio (SNR) and is recorded with significant amplitudes over Groningen. Figure A6.2 shows that similar amplitudes are observed over Groningen, irrespective of sensor used. From left to right, sensors are shown with increasing depth. It can be seen that especially this depth influences the maximum amplitude. There is a minor decay in amplitude from the Earth's surface (red and blue triangles) to 200 m depth (orange triangles). There are a few outliers, e.g. geophone G052 and G494, that are to be checked on their overall performance.

In Figure A6.3 the maximum amplitudes are shown for two horizontal components. The maximum amplitudes are extracted from an S-wave arrival due to a large earthquake in Mexico (20170908, 04:49:21, M=8.1). The data is bandpass filtered between 0.1 and 2.0 Hz. It can be seen that especially the depth influences the recorded maximum amplitude. The geophone amplitudes show a natural trend with depth and there are no signs of consistent geophone amplitude errors. Also the smooth amplitude decay from higher levels at accelerometers at the Earth's surface to somewhat lower levels at the geophones at 50 m depth, looks realistic.

Comparing Figure A6.2 with Figure A6.1, it can be seen that the horizontal components show a much larger amplitude decay with depth over the top 150 metres. This can be understood from the amplification that is much larger for S-waves than for P-waves. Moreover, the free-surface effect diminishes more rapidly with depth for S-waves due to the much shorter wavelengths. P/S velocity ratios are up till 5 in the near surface (Hofman *et al.*, 2017).

In the summer of 2018 the G-network has been expanded with 4 broadband sensors: G81B, G82B, G83B and G84B. These are STS-5A borehole sensors, which have a flat ground-velocity response between 120 seconds and 50 Hz. The sensors have been installed at 100 depth, near stations G22, G39, G56 and G64, respectively and are highlighted with red circles in Figure A6.1. The distances from the broadbands to geophones at 100m depth are 12.4, 31.1, 10.0 and 19.7 m, respectively. The near co-location of geophones and broadband sensors allows a check on the amplitude performance of the geophones, directly in the frequency band that is relevant for induced seismicity.

Figure A6.4 shows local seismicity detected at both the broadband sensors and geophones at the same depth. For each sensor couple, records are overlain of nearby events. A time window is shown which last from earthquake origin time until 6 seconds after. The data is bandpass filtered between 3 and 20 Hz. It can be seen that that both the pre-event noise and the earthquake response match quite well. Most broadband station have slightly higher amplitudes (in the order of a few percent). For the sensor couple shown in Figure A6.4(b), arrivals between 5 and 6 seconds are larger on the geophone than on the broadbands.

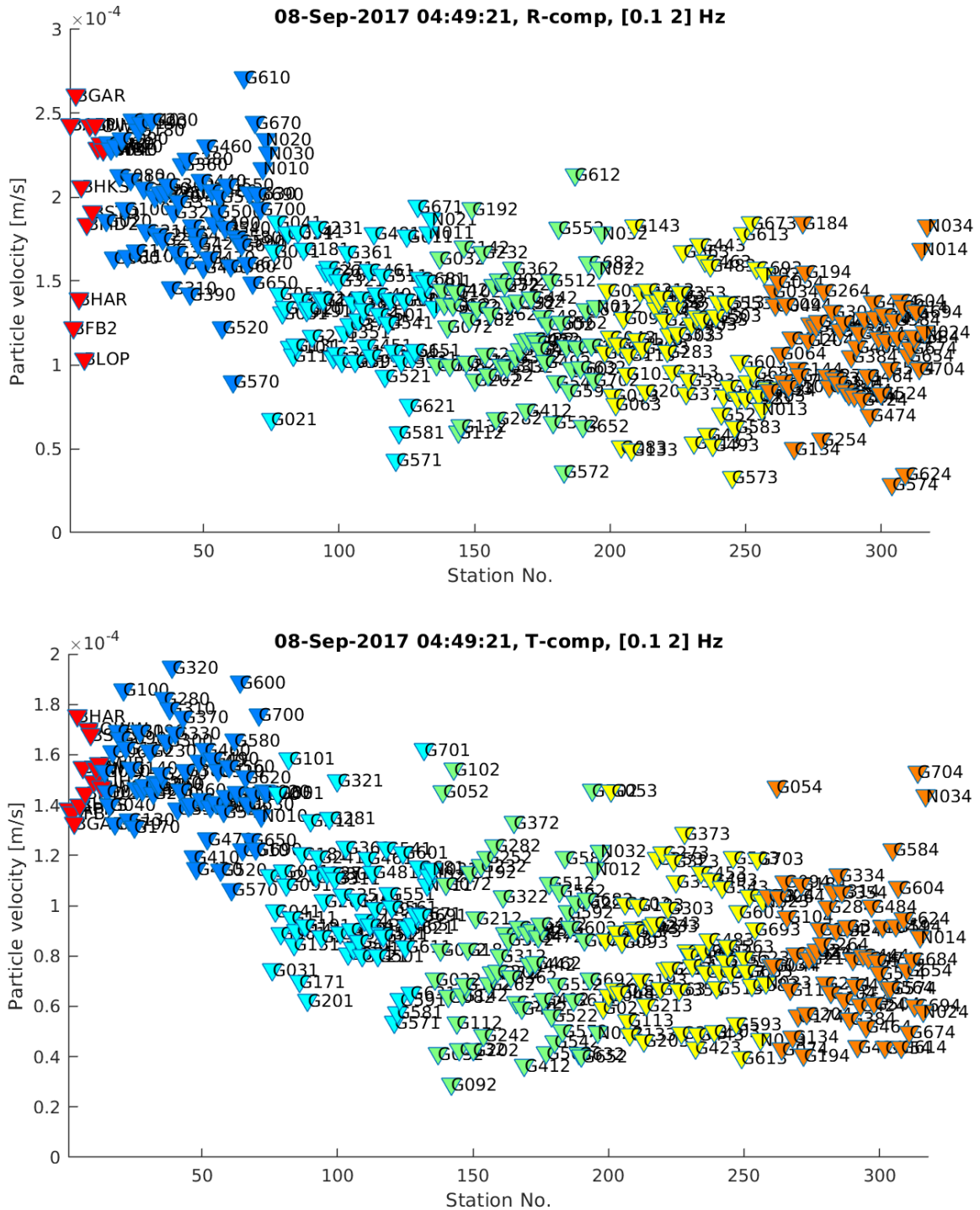


Figure A6.3. Maximum amplitudes recorded on the (upper panel) radial component and (lower panel) transverse component, for an earthquake in Mexico. A time window is taken around the S-phase. The stations are alphabetically ordered and color-coded based on network and depth: B-network (red), broadband stations (green), 0 m depth accelerometers (blue), 50 m depth geophones (cyan), 100 m depth geophones (green), 150 m depth geophones (yellow) and 200 m depth geophones (orange).

The broadbands are in a dry hole, whereas the geophones have been buried. This difference in installation could potentially explain the small differences in amplitudes observed. Moreover, geophone G392 is potentially slightly tilted. This would lead to S-wave leakage to the vertical component and could explain the larger geophone amplitudes between 5 and 6 second in Figure A6.4(b).

In summary, there are no signs of errors in the station metadata, or a degradation of the functioning of the geophones, though there are a few geophones that need further inspection. From a comparison of teleseismic arrivals, it could be concluded that consistent amplitude levels are conveyed over the G- and N-network, and the surface accelerometers and buried geophones. By a further comparison of 4 pairs of near co-located geophones and well-calibrated broadband stations, it could be concluded that actual ground motions are conveyed.

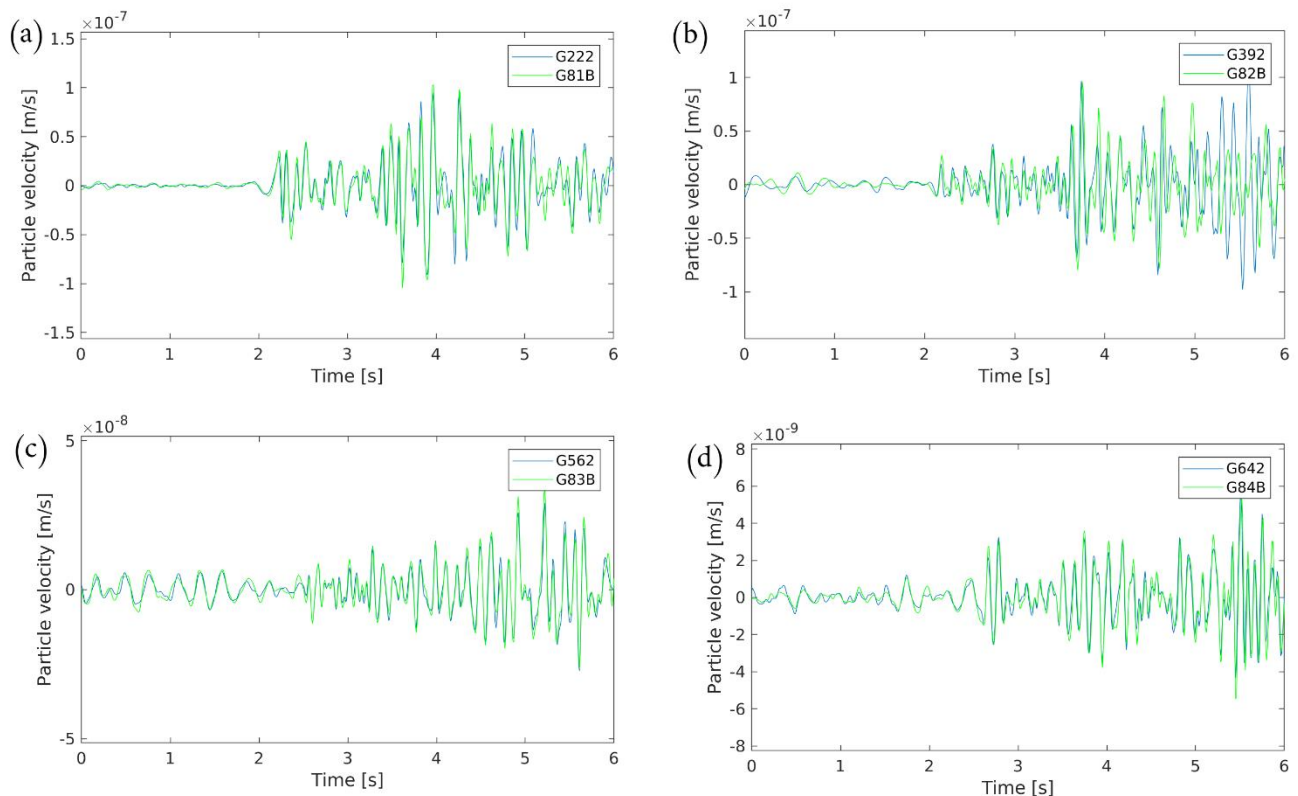


Figure A6.4. Comparison of earthquake records at buried geophones (blue seismograms) and near co-located dry-hole broadbands (green seismograms). Times are with respect to the earthquake origin time. (a) Schildwolde event, 20181107, M=1.6, recorded at 6.3 km distance; (b) Sappemeer event, 20180917, M=1.2, recorded at 7.0 km distance; (c) Borgercompagnie event, 20181116, M=1.2, recorded at 10.0 km distance; (d) Meeden event, 20190119, M=0.6, recorded at 8.8 km distance.

APPENDIX VII

Review Panel Report on V6-to-V7 Workshop

This appendix contains the consensus letter issued by the international review panel following a Workshop to discuss the V6 GMM and the changes and improvements that could be made in the development of the V7 GMM. The Workshop was held at the World Trade Center, Schiphol Amsterdam Airport, on 9-10 September 2019.

September 16, 2019

Mr. Jan van Elk
Nederlandse Aardolie Maatschappij B.V. (NAM)
Schepersmaat 2,
9405 TA Assen, The Netherlands

Dear Mr. van Elk:

This letter is to provide recommendations regarding future directions in ground-motion modelling for earthquake hazard and risk studies in the Groningen field, the Netherlands. These recommendations are being made by an international panel of experts in earthquake ground motion modelling, which has been engaged at various times since July 2015 to review the development of ground-motion models for the Groningen field. Panel reports presenting our assessments have been submitted for the Version 4 model (May 2017) and the Version 5 model (January 2018). We issued a letter endorsing the Version 5 model in January 2018.

Since our last review, documents produced by the NAM ground motion modeling team that have been provided to the panel include a revised Version 5 model report (including Appendix X, which responds to our comments) and a report on Version 6 of the model. On 9-10 September 2019, the panel, minus member Fabrice Cotton, attended a workshop with you, the ground-motion modeling team, and others in Amsterdam to attend presentations on the Version 6 model and to discuss future work, including tasks potentially leading to a Version 7 model. At the conclusion of that meeting, we discussed our preliminary recommendations with you and the ground-motion modeling team, which are described further in the remainder of this letter. Specific comments on the Version 6 report will be provided separately from this memo.

Strategy for Next Phase of Work

While the development of a Version 7 model had been envisioned, with a delivery date in December 2019, we recommend against proceeding to Version 7 model development at this time. Instead, we recommend that the ground-motion team work through technical issues that were raised in the workshop (and are discussed below), which are likely to affect the ground motion model. Following panel review of the findings, the next phase of model development can commence. Attempting to complete all of this before the end of 2019 would likely lead to rushed work products without adequate review, and as such, a Version 7 model developed under such conditions would not necessarily improve upon the existing Version 6 model. We believe that Version 6 is a significant advance on the Version 5 model that we have previously endorsed and is suitable for use in hazard and risk assessments.

Work Coordination

The September 2019 workshop was attended by representatives of a regulatory agency (SodM) and researchers working on various KEM projects. The panel is not aware of all the different KEM projects that have been undertaken in connection with Groningen ground motions, but the workshop did include presentations from investigators involved in two projects (KEM-02 and KEM-04). It was clear from the discussion at the workshop that the KEM researchers had not been in communication with the NAM ground motion modeling team prior to the workshop.

While we understand that this lack of communication may have been a strategic objective intended to maintain independence of the KEM investigators, we anticipate that continuation of this practice would diminish the value of the work. As a result, we recommend that the two teams more regularly communicate in the future: first, so that the KEM researchers can better understand particular conditions at the Groningen field that are of critical importance for ground-motion modeling, and, second, so that the NAM ground motion team is informed of the KEM work products, allowing their findings to be considered in subsequent versions of the ground-motion model. Communications that achieve such objectives need not compromise the independence of technical work products and documentation from KEM research projects.

Epistemic Uncertainty in Ground Motion Model

Epistemic uncertainty in the Groningen ground motions model has been formulated using the same logic tree structure since Version 2 of the model. The panel is concerned that this structure may be incomplete in its consideration of the level of uncertainty in the median and aleatory variability models. Moreover, the existing framework does not adequately distinguish aleatory variability from epistemic uncertainty in certain elements of the model. Tasks that can be undertaken to address these issues in Version 7 include:

1. Develop plots showing epistemic uncertainty in the median and aleatory variability models for different model versions. We anticipate this would be for model Version 2 onwards, but defer to the modeling team on which model to begin with. This would be done for the NS_B and soil surface (for specific zones that have remained essentially unchanged over time) for several scenarios (magnitude, distance) critical to hazard. Seeing how uncertainties have changed over time, as more data and knowledge of Groningen ground motions has been developed, will be insightful.
2. In the site response model, it would be useful to more clearly separate aleatory variability and epistemic uncertainties. We encourage the modeling team to consider each of the inputs to ground response analysis procedures and to identify sources of variability and uncertainty. For example, there is considerable uncertainty in the small strain damping (D_{min}) model, which is clearly epistemic. The categorization for other soil properties is somewhat more subjective, but undertaking this exercise, and expanding the logic tree as needed for epistemic uncertainties, is recommended.

3. In the aleatory variability model, we encourage consideration of alternate versions of the tau component in new logic tree branches, to supplement existing branches for ϕ_{SS} . The issue of tau model uncertainty is discussed in more detail in our comments on the Version 5 report.

Once the above has been completed, a new logic tree will have been formulated for the Version 7 model, likely with additional branches relative to the Version 6 model. The impact of the new logic tree on epistemic uncertainty can then be assessed. For hazard-critical scenarios of magnitude and distance, the uncertainty on the median can be quantified with standard error terms for different intensity measures. At that stage, a judgment will need to be made regarding whether the level of uncertainty provided by the model is sufficient and whether adjustments to uncertainty levels are needed. We encourage consideration of the following in making these judgments:

- Is the upper branch of the stress-drop logic tree leading to ground-motion levels comparable to that expected based on global models?
- Does the range (e.g. 16th to 84th percentile) encompass the range of medians across model versions (from item 1 above).
- How does the total amount of epistemic uncertainty for Groningen compare to that used for previous projects in more data-rich areas, like the western US, or other data-sparse areas, like the central and eastern US and South Africa?

Similar comparisons should be made for the aleatory variability model.

Other Topics

In addition to re-consideration of the model's epistemic uncertainty, additional issues that should be resolved before commencing Version 7 model development include:

- Identify the cause of systematically different NS_B ground motions deconvolved from G0 (ground surface) versus G4 (200 m depth) recordings. At present, estimates derived using these two motions differ by approximately a factor of 2 over a wide frequency range.
- Conduct additional residuals analyses to evaluate performance of the Version 6 model, using data from TNO stations and downhole stations G1-G4.
- Validate the performance of the site amplification model using the G0/G4 transfer function, emphasizing data from sites with measured V_s profiles.
- The flexible array at Loppersum indicates significant spatial variability in V_s (Kruiver presentation). This variability may not be adequately captured in the way the V_s zonation model was developed. We suggest to investigate flexible array results for other areas to compare the variability revealed by these results with the V_s zonation model.

- Continue the currently evolving work on soil damping. Develop alternative defensible models that can be considered, including models in which D_{min} derived from geotechnical models is not modified.
- Re-visit the fitting of the nonlinear model – plots of how parameters f_2 and f_3 change with period, and how this compares to ergodic models in the literature, would be insightful.
- Investigate potential impacts of soil-structure interaction at B stations by documenting conditions at the sites, and removing stations in basements or on the ground floor of large structures (similar to criteria used in NGA projects).
- Consider the merits and potential drawbacks of discontinuing the development of models (and plots) for pseudo-spectral accelerations at periods between 0.01 and 0.1 sec; we understand that is period range is not critical for risk applications, and its consideration may needlessly complicate model development and interpretation.

Our endorsement of the Version 5 model continues to apply for the Version 6 model, which we consider to be suitable for seismic hazard and risk studies of the Groningen field. We look forward to re-convening with the modeling team once the issues described here have been addressed, and commend the team for their considerable accomplishments in advancing the model to its present form.

Respectfully submitted,



Jonathan P. Stewart (Chair)



Norman A. Abrahamson



Gail M. Atkinson



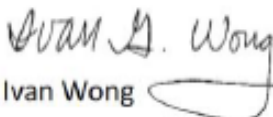
Hilmar Bungum



Fabrice Cotton



John Douglas



Ivan Wong



Robert R Youngs